Exploring novel spin and charge transport mechanisms in ferromagnetic and antiferromagnetic spin structures and spin textures

Rafael Lopes Seeger

Université Grenoble Alpes

THÈSE

Pour obtenir le grade de

DOCTEUR DE L'UNIVERSITE GRENOBLE ALPES

Spécialité : **Physique**

Arrêté ministériel : 25 mai 2016

Présentée par

Rafael LOPES SEEGER

Thèse dirigée par **Vincent BALTZ, Chargé de recherche CNRS au Laboratoire SPINTEC**

préparée au sein du **Laboratoire Spintronique et Technologie des Composants (SPINTEC)**
dans **l'École Doctorale de Physique de Grenoble**

Etude de nouveaux mécanismes de transport de spin et de charge dans des structures et textures de spin ferromagnétiques et antiferromagnétiques

Thèse soutenue publiquement le **30 novembre 2021**,
devant le jury composé de :

M^me^ Nora DEMPSEY - Présidente
Directrice de recherche, CNRS
M. Sebastian T. B. GOENNENWEIN
Professeur, Université de Constance
M. Stéphane MANGIN
Professeur, Université de Lorraine
M^me^ Lisa MICHEZ
Maîtresse de conférence, Université d'Aix-Marseille
M. Henri JAFFRES
Directeur de recherche, CNRS

Acknowledgments

After 3 years of preparation working with many exceptional people, I have no more than words to thank everyone I have worked with and those whom I have shared this fascinating moments.

I would like first to sincerely thank my supervisor, Vincent Baltz, for the opportunity to do my thesis work in your group and for sharing with me your knowledge and ideas. For always having an open door for discussions and for your continuous support, advice and encouragement. For letting me join your scientific family and for providing me the means to work with several fields of spintronics. It has been an extraordinary time, thank you!

Thanks to my jury committee members: Nora Dempsey, Sebastian T. B. Goennenwein, Stéphane Mangin, Henry Jaffres, and Lisa Michez.

Without many people from the staff keeping all the facilities alive, this work would not be possible. In particular, I am thankfull to Stéphane Auffret for growing many high quality samples for me and for sharing his knowledge in materials science. I am grateful to Isabelle Joumard, for the trainings and assistance with PPMS and VSM experiments. I would like also to thank Serge Gambarelli, Christian Lombard, and Vincent Maurel for allowing me to use their cavity resonator. Many thanks for Ursula Ebels for letting me use the broadband CPW-FMR. Thanks also for Jean-François Jacquot for allowing me to use the SQUID.

Special thanks go to Olga Gladii and Guillaume Forestier, for their enormous help with experiments and cleanroom in the early stages of my work and for all rich discussions. You are a big part of this work! Adittionally I would like to thank Miina Leiviskä and Floris Van Duijn for the help with experiments and valuable discussions. I am also gratefull to many PhD students and Post-docs at SPINTEC for all the fruitfull and interesting discussions.

I am grateful to Sebastian T. B. Goennenwein, Helena Reichlová, Richard Schlitz, and Dominik Kriegner at the Technical University Dresden for their kind reception. For performing magnetotransport experiments and for valuable scientific discussions. Thanks also for Eva Schmoranzerová and Antonín Baďura who have participated on the measurements in Dresden.

Thanks to Catherine Broisin, Celine Conche, Adriana Stoenescu for keeping everything in order and helping me to complete all the administrative work.

Most of all, I want to thank my family. Mom, dad, and brother, thanks for the encouragement and support during these years. Last but not least, Paola, thanks for being such a smart, fun, and loving partner! I am so gratefull to share the ups and downs of life with you.

Contents

Introduction

Spintronics utilises the spin degree of freedom of electrons, instead of their charge, to create novel devices with increased memory and processing capabilities [9,10]. The spin of the electrons can be seen as an elementary magnetic moment carried by each electron which has a quantum mechanical origin. Spintronics relies on the intimate interaction of the electrons' spins in a current with atomic magnetic moments in nanostructures that allow novel ways of processing information and store data. Remarkably, the remanence state of the magnetization in ferromagnets and the possibility of switching it in hundreds of picoseconds opened the door to obtain non-volatile and fast devices, respectively. Since the data remain stored even in absence of a power input, it make possible to reduce the energy required for information storage [11]. For this reasons, most spintronic devices combine magnetic and nonmagnetic material (metals, semiconductors, or insulators).

Efforts on the understanding of various magnetoresistive effects, such as the anisotropic magnetoresistance and anomalous Hall effect, have permeated the history of fundamental research on condensed matter physics. Such effects are characterized by a change of resistance upon application of a magnetic field in a magnetic material. Often the discovery and understading of new magnetoresistive effects led to applications in sensors of magnetic fields. The first observation of a magnetoresistive effect was reported in Ni and Fe [12], where it was observed that the resistance of these ferromagnetic metals depends on the orientation of the applied electric current with respect to the magnetization (variation of only a few percent at room temperature). Due to this existing anisotropy on the resistance, the effect was named anisotropic magnetoresistance (AMR). Essentially, the discovery of AMR was a major breakthrough for further magnetotranport studies. Another magnetoresistivive effect is the Hall effect, in which a conductor develops a transverse voltage when it is placed in a magnetic field due to the Lorentz force acting on the electron charge current [13]. In ferromagnetic materials, there is an additional contribution to the transverse voltage related to the magnetization, known as the anomalous Hall effect (AHE) [14].

The birth of modern spintronics is usually associated with the discovey of the giant magnetoresistance (GMR) which was done independently by the groups of Albert Fert [15] and Peter Gründberg [16] in 1988. This magnetoresistive effect is observed in films of two ferromagnetic layers separated by a layer of a non-magnetic metal. As a consequence of spin-dependent scattering, a GMR device shows two resistance states depending on the relative orientation of the magnetization of the two ferromagnetic layers [17] and it shows larger magnetoresistance compared to AMR (variation of 15-20% in GMR structures). This increase in sensitivity permitted the development of spin valves sensors that are now widely used as read-heads of hard-disk drives and in magnetic random access memories (MRAM) [11,17]. It is noteworthy that in a spin valve, the magnetization of one layer, called reference layer, is

pinned in one direction by using exchange bias between the ferromagnetic and an antiferromagnetic layer. The magnetization of the other layer, called free layer, follow the direction of an external magnetic field. It results in a control of the resistance with small magnetic fields suitable for applications. Further improvements on sensitivity were achieved by using magnetic tunnel junctions (MTJ), where the metallic layer of a GMR is replaced by an insulator [18]. In these junctions, tunneling margnetoresistance (TMR) is caused by spin-dependent tunneling. In this case, the magnetoresistance amplitude can reach values as high as 150-600% in crystalline MgO barriers at room temperature.

While TMR represents an efficient read-out mechanism for MRAMs, MTJs can also operate as an active element to write information by switching the magnezation by using spin transfer torque (STT) [19–21]. In this effect, a spin-polarized current transfer angular momentum from one ferromagnetic layer to other, exerting torque on the magnetization that eventually can lead to switching of the magnetization. A spin polarized current can be obtained by passing a current through the reference layer (or through a polarizing layer). The disadvantage of the STT switching mechanism is that it requires large current to pass through a fragile tunnel barrier [22]. An alternative mechanism is to use spin-orbit torque (SOT) switching, where the accumulation of spin-polarized electrons at the interface of a ferromagnetic layer results in a transfer of angular momentum [23]. Combined with a small in-plane magnetic field might result in a spin torque capable of reversing the magnetization direction [24]. In SOT-based device, the writing and reading path are separated, thus the MTJ is not damaged during the writing process [25]. It results in lower power consumption than in the STT counterparts, with faster writing speeds.

There exists a constant demand for speed acceleration and size reduction in nowadays spintronic devices. Intrinsically, ferromagnetic-based devices offers limiting factors in terms of device performane: i) instability due to spurious magnetic fields, ii) limit to high storage density due to magnetic field cross-talks, and iii) power consumption required to write information. Aiming to overcome the drawbacks of ferromagnets, researchers recently have turned their attention toward alternative structures.

Antiferromagnets started to be explored for spin-dependent transport recently. In the simplest case, an antiferromagnet can be seen as containing two sublattices with magnetic moments pointing in opposite directions, leading to a zero net magnetization. In terms of device performance, using antiferromagnets for spintroncis potentially offers a number of advantages [26]: i) stability to external magnetic field, i.e. typically antiferromagnets can only be manipulated by strong magnetic fields, ii) possibility of higher density memory devices thanks to the zero net magnetization in antiferromagnets which produces no stray field, and iii) faster dynamics as the resonances in antiferromagnets are found close to THz frequencies. Whereas this points makes antiferromagnets attractive for spintronic applications, it also introduces new problems when it comes for writing and reading the state of an antiferromagnet-based device. This led to an intense research effort to elucidate these problems, stablishing recently a field known as antiferromagnetic spintronics [26,27]. This emerging field aims to exploit the physical properties of antiferromagnets beyond its secondary role as pinning of the reference layer for spin valves.

Besides the interesting features mentioned above, antiferromagnets are found to show a wide variety of properties. As far as electrical properties are concerned, they can be metals,

insulators, semimetals, semiconductors and also superconductors. In addition, depending on the energies into play, the antiferromagnetic ordering can take different forms. For example, it might favor the magnetic moments to form an angle. Depending on the energy landscape, collinear, non-collinear, and even non-coplanar spin structures, with compensated or uncompensated structure, can be found in antiferromagnets. Interestingly, the interplay between the crystal structure and magnetic order opened the path for novel magnetotransport properties in antiferromagnets [28,29].

The central topic under investigation during my PhD consisted in the study of antiferromagnets systems. In the course of the work we have also explored its ferromagnets counterparts. We have dealt with spin and charge transport mechanisms in ferromagnetic and antiferromagnetic spin structures and spin textures using different experimental approaches. In order to present a clear manuscript this thesis is split in four chapters, outlined below, that can be read independently. Each chapter contains an introduction, a discussion of the theoretical and experimental framework of the subject, followed by a discussion of the experimental results obtained in the frame of my PhD thesis.

Chapter I is devoted to the study of spin transport in ferro- and antiferromagnets. Here we have used the spin pumping technique to probe the magnetization dynamics of a ferromagnetic layer. It allows accessing information about the dissipation of energy due to spin absorption in adjacent layers, i.e. the layer we want to study. The results have revealed that the spin pumping enhancement associated with ordering transition is independent on the electrical states, regardless of the electronic or magnonic nature of the spin current probe.

Chapter II explores the spin-charge conversion in ferro- and antiferromagnets. Experimentally, we discuss distinct set of results. Concerning spin-charge conversion in ferromagnets, we have observed and exploited a self-induced inverse spin Hall effect in FMR experiments, showing its non-monotonous temperature-dependence. Specific related to spin-charge conversion in antiferromagnets, we discuss experiments comparing spin transport and spin-charge conversion in the GHz and THz frequency ranges and searched for the impact of ordering transition in the spin-charge conversion.

Chapter III deals with charge transport in antiferromagnets. We discuss magnetrotransport in epitaxial thin films of Mn_5Si_3 where we have observed a spontaneous Hall effect that relies in crystal and magnetic symmetries. The experimental results were interpreted in terms of a novel time revesal ($\boldsymbol{\mathcal{T}}$) symmetry breaking mechanism arising in a collinear and coplanar antiferromagnet with a staggered Zeeman spin-splitting.

Chapter IV is devoted to the study of charge transport specific to magnetic textures. We discuss systematic experiments performed with ferromagnet/spacer/superconductor heterostructures to observe the recovery of the superconducting critical temperature when the ferromagnetic layer is set to a multi-domain state. Particularly, we have used the proximity effect to study Cooper pair characteristic lengths in antiferromagnets. We also explored the replication of spin textures from ferromagnets in antiferromagnets using exchange bias while searching for antiferromagnetic skyrmions.

Chapter I

Spin transport in ferro- and antiferromagnets

This chapter deals with spin transport in ferromagnets and antiferromagnets. Here, we used the ferromagnetic resonance via the spin pumping technique to probe the magnetization dynamics and study the dissipation of energy. We were in particular interested on the dissipation by spin absorption in adjacent layers, called spin-sink.

In § I.1 I recall the conceptual and experimental framework of spin current generation by the spin pumping effect, followed by the extraction of the relevant physical parameters from experiments. At the end of this paragraph, I show how interpretation of some of these parameters extended our understanding of the impact of eddy currents below the microwave magnetic skin-depth and explained the line shape asymmetry and phase lags reported in stripline experiments.

§ I.2 is devoted to results that have revealed that the spin pumping enhancement associated with ordering transitions is independent of the metallic and insulating nature of the spin-sink, and is observed whether the spin current probe involves electronic or magnonic transport, facilitating advances in material characterization and engineering for spintronic applications.

I.1 Spin current generation by spin pumping

I.1.1 Magnetization dynamics and relaxation mechanisms

We start by giving a short overview of magnetization dynamics in thin ferromagnetic films. In ferromagnets, the exchange interaction couples magnetic moments. Thus, they can remain parallel even in small external magnetic fields. In such a case, the magnetic moments can be described with the macrospin approximation, i.e. by a net magnetization $\boldsymbol{M}$. In a magnetic field $\boldsymbol{H}$, a force acts to align $\boldsymbol{M}$ along the direction of $\boldsymbol{H}$. An angular momentum is then associated with the magnetization: $\boldsymbol{L} = -\boldsymbol{M}V/\gamma$, where γ is the gyromagnetic ratio and V is the volume of the ferromagnet. According to the model proposed by Landau and Lifshitz (LL) [30], the force that tries to align the magnetization with the external field generates a (field-)torque on the angular momentum of the ferromagnet, causing the magnetization to precess with a constant cone angle around the field axis (see Figure 1(a)). The most common statement of the equation of motion describing the undamped precession of magnetization $\boldsymbol{M}$ in an effective field $\boldsymbol{H}_{\text{eff}}$ is:

$$\frac{d\boldsymbol{M}}{dt} = -\gamma(\boldsymbol{M} \times \boldsymbol{H}_{eff}). \qquad \text{Eq. I-1}$$

The precession frequency of the system is $\omega = \gamma H_{\text{eff}}$. Note that an effective field $\boldsymbol{H}_{\text{eff}}$ has to be considered instead of just a bias field $\boldsymbol{H}$. The effective field typically contains several terms describing magnetic anisotropies, the demagnetizing field, the exchange interaction, and the Zeeman contribution due to $\boldsymbol{H}$. It is noteworthy that when the magnetization precess about $\boldsymbol{H}_{\text{eff}}$, only $\boldsymbol{M}$ when has a component perpendicular to the field and that the precession frequency does not depend on the angle between $\boldsymbol{H}_{\text{eff}}$ and $\boldsymbol{M}$.

As stated in Eq. I-1, the magnetization precesses about an effective field indefinitely. In experimental observations, this is not the case, and the magnetization dissipates energy. In fact, the magnetization spirals in toward the effective field direction. In order to describe such a damped precession, an additional (damping-)torque term was included to the LL equation (Eq. I-1). This is described by the following phenomenological equation:

$$\frac{d\boldsymbol{M}}{dt} = -\gamma(\boldsymbol{M} \times \boldsymbol{H}_{eff}) - \frac{\lambda}{M_S^2}\boldsymbol{M} \times (\boldsymbol{M} \times \boldsymbol{H}_{eff}), \qquad \text{Eq. I-2}$$

where λ, is a phenomenological damping constant specific to the stack. It has dimensions of inverse time and is the relaxation frequency which parametrises the dissipative process.

Gilbert derived a similar phenomenological equation describing damping as a 'viscuous' force proportional to the time derivative of the magnetization, resulting in the well-known Landau-Lifshitz-Gilbert (LLG) equation [31]:

$$\frac{d\boldsymbol{M}}{dt} = -\gamma(\boldsymbol{M} \times \boldsymbol{H}_{eff}) + \frac{\alpha}{M_S}\left(\boldsymbol{M} \times \frac{d\boldsymbol{M}}{dt}\right), \qquad \text{Eq. I-3}$$

where the dimensionless parameter α is called Gilbert damping term. The second term in Eq. I-3 is a change in magnetization direction perpendicular to both $\boldsymbol{M}$ and $d\boldsymbol{M}/dt$, causing the magnetization to spiral to a position along $\boldsymbol{H}_{\text{eff}}$ (see Figure 1(b)) and changing its angular momentum. However, according to the law of conservation of total angular momentum, this difference in angular momentum has to be transferred to another reservoir, which I will discuss in the next paragraphs.

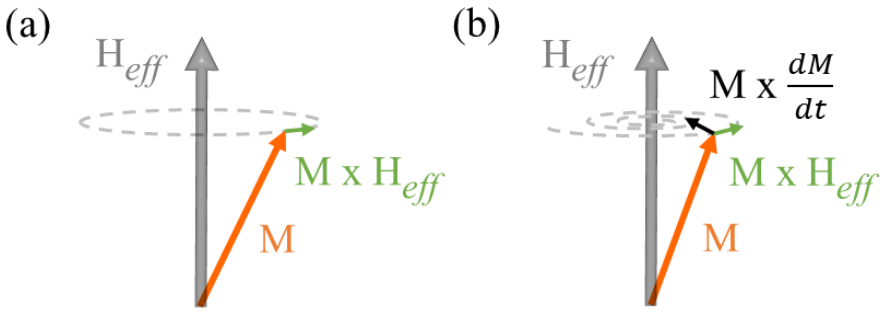

Figure 1 : Schematic illustration of (a) the uniform precession of magnetization described by the Landau-Lifschitz (LL) equation (Eq. I-1) and (b) damping acting perpendicularly to the direction of motion of the magnetization described by the Landau-Lifshitz-Gilbert (LLG) equation (Eq. I-3).

The damped precessional motion governs the process of relaxation of magnetization. The technological impact of precessional dynamics is crucial in high frequency applications of

magnetic materials. Moreover, damped precession dynamics also controls magnetization rotation and the dynamical propagation of domain walls, which are the essential modes of magnetization reversal in ferromagnets [32–34]. Therefore, the study of damped precessional motion is key for understanding and controlling magnetization processes. The most common measure of damping is given by the parameter α of Eq. I-3. The ferromagnetic resonance technique gives information on the dissipation of energy and thus is well suited for determination of α, as will be further discussed in § I.1.2.1.

As introduced in this section up to now, damping was phenomenological. However, there is still considerable physics with regard to the origin of damping in metallic systems, where there are many phenomena leading to dissipation of energy [35]. In the following, I will go through the main physical concepts contributing to damping. It should be emphasized that damping is sample dependent. Therefore, it does not reflect intrinsic properties of materials. The intrinsic damping comes from unavoidable contributions, while the contributions that could be prevented are considered to be extrinsic [36].

I.1.1.1 Intrinsic mechanisms

Intrinsic damping depends on the ferromagnetic material. It has contributions coming from interactions of magnons with conduction electrons, magnons with phonons, and eddy currents circulating in the material.

Magnon-electron interaction

The interaction between magnons and itinerant conduction electrons causes dissipation of energy, which is the most important contribution to damping in metallic ferromagnets. The presence of itinerant conduction electrons in metallic ferromagnets justifies why they have higher values of damping when compared to their insulating counterparts ($\sim 10^{-3}$ for the permalloy metal vs. $\sim 10^{-5}$ for the yttrium ion garnet insulator). There are two mechanisms that could give rise to magnon scattering with itinerant electrons: (i) *s*-*d* exchange interaction, as proposed by Heinrich *et al.* [37]; and (ii) spin-orbit interaction, as proposed in the works of Kambersky *et al.* [38] and Gilmore *et al.* [39]. These two mechanisms depend on whether incoherent scattering of electron-hole pair excitation by magnons gives rise to spin-flip or non-spin-flip interactions.

We start by introducing the mechanism proposed by Heinrich *et al.* [37] where the intrinsic damping can be treated by using the exchange interactions between the *d*-localized moments ant the *s* itinerant electrons. As presented in Figure 2, due to the *s*-*d* exchange interaction, magnons and itinerant electrons are coherently scattered resulting in creation and annihilation of electron-hole pairs. Since the total angular momentum in the *s*-*d* interaction is conserved, the electron spin flips during the scattering with magnons. Successive three particle scattering eventually lead to the emission of a magnon. Magnetic relaxation is expected when the spin flip hole-electron pairs scatter incoherently by thermally excited phonons or magnons.

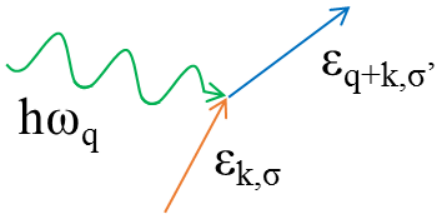

Figure 2 : Diagram of the spin-flip excitation. A magnon collides with an electron with energy $\varepsilon_{q,\sigma}$, changing its spin and momentum state to $\varepsilon_{q+k,\sigma'}$.

According to the *s-d* model, the damping depends on the spin-flip lifetime (τ_{sf}) and it is given by [36]:

$$\alpha^{el} = \frac{\chi_{Pauli}}{\gamma M_S \tau_{sf}}, \qquad \text{Eq. I-4}$$

where χ_{Pauli} corresponds to Pauli's susceptibility for the itinerant electrons. At high temperature, the damping described in Eq. I-4 is seen as resistivity-like, since it increases with increasing temperature. Contrarily, at low temperature a conductivity-like behavior is expected. It will be be further discussed in the frame of the mechanism based on spin-orbit interaction.

Kambersky *et al.* [38] showed that a more general treatment can be given to the intrinsic damping in metallic ferromagnets by using the spin-orbit interaction Hamiltonian. In this process, the effect caused by precessing magnetization on the Fermi-surface is taken into account. The relaxation rate is determined by the decay of the magnons into electron-hole pairs and the scattering of those electron-hole pairs with phonons or lattice defects. The electron-hole pair creation has to be distinguished between intraband transitions that occur within a single band and interband transitions that occur between two different bands [39,40]. In such case, the density of states governs the damping, meaning that the process depends strongly on the spin-orbit coupling. Since the temperature dependence of the damping associated with the two transitions is different, they were described in analogy with the temperature dependence of conductivity and resistivity.

As illustrated in Figure 3(a), due to change in magnetization, the Fermi-surface varies in time [40]. Some states that were below the Fermi surface at *t-dt* jumps above the Fermi surface for time *t*, and other states that were above are pushed below. This mechanism provides the creation of electron-hole pairs near the Fermi level. The timescale for the repopulation of the energy levels with the magnetization precession before it relaxes towards the instantaneous equilibrium is given by the momentum relaxation, τ_m. Depending on τ_m, at *t* some of the equilibrium states which were originally occupied at time $t - dt$ and which would be empty in an equilibrium situation may still be occupied, whereas some other states which should be occupied may still be empty. The intraband relaxation of these electron-hole pairs leads to the transfer of angular momentum from the spin system to the lattice. The so-called intraband or breathing Fermi-surface contribution in this case is proportional to the relaxation time τ_m, and thus scales with conductivity (conductivity-like term), i.e., it decreases with increasing temperature.

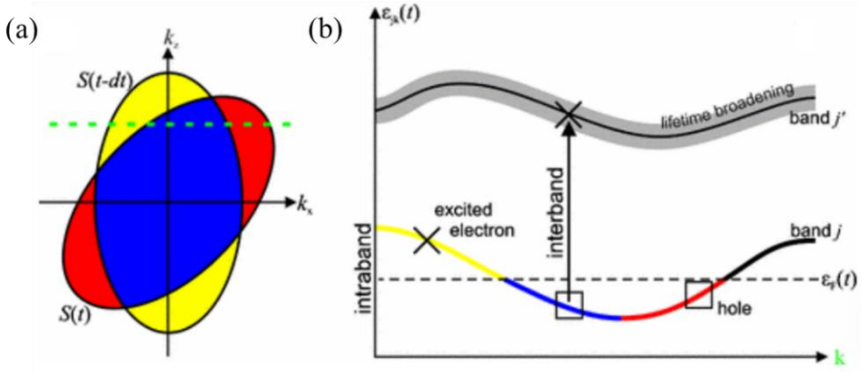

Figure 3 : Illustration of (a) the equilibrium Fermi-surface S for time *t-dt* and *t* and (b) the equilibrium band structure along the direction in *k*-space indicated in (a). From Ref. [40]

The time-dependent perturbation in the spin-orbit interaction generates interband electron-hole pairs (Figure 3(b)). The number of final states accessible by the perturbation depends on τ_m, due to the lifetime broadening of the states. The so called interband or bubbling Fermi-surface increases with $1/\tau_m$ and thus scales with resistivity (resistivity-like term). It is noteworthy that for this spin-orbit limit, the damping coefficient is similar to that found in the frame of the *s-d* exchange interaction model, see Eq. I-4.

In summary, the temperature dependence of the magnetic damping depends on the nature of the corresponding transitions. For intraband transitions the magnetic damping increases linearly with the relaxation time τ_m, following a conductivity-like behavior at low temperatures. On the other hand, interband transitions dominate at high temperatures, where the Gilbert damping is roughly inversely proportional to the electron relaxation time (proportional to $1/\tau_m$) which results in a resistivity-like behavior. This behavior can lead to a minimum in the spin–orbit damping as a function of temperature. An experimental measurement of that kind will be shown at § I.2.2.1 (see Figure 19(a)).

Magnon-phonon interaction

At finite temperatures thermally excited lattice vibrations (phonons) are unavoidable and thus can lead to a contribution to the damping of a material known as magnon-phonon interaction (or phonon drag). The physical origin of the effect is the direct coupling between the spins. Thus, a precessing spin exerts attractive or repulsive forces to the neighbor atoms, which leads to lattice vibrations (phonons). The reciprocal effect also occurs and it involves decoherence of the spin waves due to the propagation of phonons.

Suhl investigated the damping caused by the direct magnon-phonon coupling [41]. The mechanisms can be divides into direct relaxation to the lattice and indirect relaxation via excitation of many magnetic modes (see Figure 4). The results are limited to small geometries where the magnetization and lattice strain are homogeneous and it gives the following equation for the phonon damping:

$$\alpha^{ph} = 2\eta\left(\gamma\frac{B_2(1+\nu)}{E}\right)^2, \qquad \text{Eq. I-5}$$

where η is the phonon viscosity, B_2 is the magneto-elastic shear constant, ν the Poisson ratio, and E constitutes the Young's modulus. Experimentally α^{ph} was found to take small values

(~10^{-4}) [36]. While Eq. I-5 is of the form of the damping term in the LLG equation of motion, it is noteworthy that Suhl also derived terms that do not have the LLG form [41].

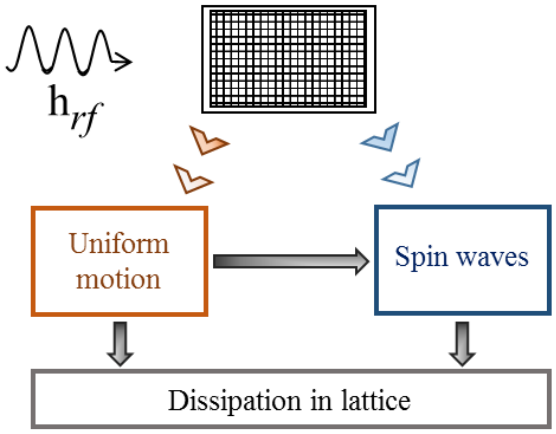

Figure 4 : Illustration of two possible dissipation processes of uniform motion: direct relaxation to the lattice and indirect relaxation mediated by decay into non-uniform motion (spin waves). Adapted from Ref. [41].

Eddy currents in ferromagnets

In metals, time-varying magnetic fields causes time-varying magnetization, which induces eddy currents. In metallic films, the dissipation of eddy currents in the sample gives rise to a contribution to damping, especially relevant for thick films. The contribution starts to be relevant when the thickness of the ferromagnetic layer (t_F) is comparable to the skin depth (δ). The contribution of eddy currents to damping in the LLG equation (Eq. I-3) is calculated by integrating the Maxwell equations across the film thickness and it is given by [42]:

$$\alpha^{eddy} = \frac{1}{6}\left(\frac{4\pi}{c}\right)2\sigma(M_S\gamma t_F)^2, \qquad \text{Eq. I-6}$$

where σ is the conductivity and c is the velocity of light in free space. Note that this type of contribution to damping depends very much on the material properties of the ferromagnet. In the case of Fe, α^{eddy} contribution is comparable to the intrinsic damping only for a film thickness of 70 nm [36]. For NiFe Permalloy, α^{eddy} has to be taken into account for thicknesses above 100 nm [36]. Therefore, the role of intrinsic eddy currents can be neglected for sufficiently thin films, like in our case.

However, when metallic layers surround the ferromagnet, eddy currents flowing in the metallic neighbors can also influence the magnetization dynamics. This will be further discussed in § I.1.2.2, where experimental demonstration of the impact of eddy currents in Cu/NiFe and NiFe/Cu bilayers will be shown.

I.1.1.2 Extrinsic mechanisms - including spin pumping

In this section, I will introduce extrinsic dissipative processes which contribution could, in principle, be avoided. Those contributions are mainly related to interfacial and structural defects, inhomogeneity of the magnetic properties or to the presence of adjacent layers. For our studies, extrinsic contributions such as two-magnon scattering, slow-relaxer, and magnetic inhomogeneities [35] are too small compared to intrinsic damping and they will not be further discussed here. The following paragraphs will be devoted the extrinsic dissipative processes which are mostly studied in this work.

Radiative damping and eddy currents in neighboring metals

The potential damping contribution from the dissipation of energy through eddy currents inside the ferromagnetic layer was discussed above, in the frame of intrinsic damping (see § I.1.1.1). I will now comment on the flow of energy transferred to the stripline and giving rise to (extrinsic) damping [43,44]. The precession of magnetization produces a net magnetic flux that spreads across the surrounding metallic layers, including the stripline, therefore leading to power dissipation. This power dissipation away from the sample to the stripline leads to a radiative damping contribution. When the dissipation occurs within the stripline center conductor, the radiative damping contribution is given by [43]:

$$\alpha^{rad} = \mu_0^2 \kappa \gamma M_S t_F L/(2 Z_0 W), \qquad \text{Eq. I-7}$$

where κ is a dimensionless parameter that accounts for the propagation mode profile in the sample, t_F is the ferromagnetic film thickness, L is the length of the sample, Z_0 is the waveguide impedance, and W is width of the stripline center conductor. Note that radiative damping depends on sample dimensions and several waveguide properties. Moreover, unlike eddy current damping given by Eq. I-6, α^{rad} is independent on the conductivity of the ferromagnet. This relaxation mechanism is thus also present in ferromagnetic insulators. We will discuss experimental data in search for radiative damping contribution at the end of § I.1.2.2.

It is noteworthy that eddy currents generated in adjacent metallic layers surrounding the ferromagnet, also influence magnetization dynamics for specific experimental configurations [45,46]. In fact, eddy currents generate a feedback radiofrequency magnetic field that contributes to the dephasing of the magnetization dynamics of the ferromagnet. Rather than acting on the damping itself, this dephasing translates into an asymmetry of the resonance lineshape of the ferromagnet. An extensive discussion along with experimental findings on the impact of eddy currents specific to stripline experimetns in Cu/NiFe and NiFe/Cu bilayers will be shown in § I.1.2.2.

Spin pumping

In ferromagnetic experiments performed with structures in which the ferromagnet is surrounded by different layers, additional energy may be dissipated in the form of a spin-current, resulting in a rise of damping. In fact, it was observed that this contribution to damping depends on the nature of the adjacent layer [47]. It was also shown that it displays a $1/t_F$ dependence, [48,49] indicating an interfacial effect. The so-called spin pumping effect describes such a process. The precessing magnetization dissipates energy via the transmission of a spin current from the ferromagnetic layer towards the adjacent material [50], followed by a subsequent relaxation of the non-equilibrium spin population.

The generation of a spin current due to the spin pumping effect in ferromagnetic (F)/normal metal (N) bilayers is illustrated in Figure 5. Let's start by considering a ferromanet at equilibrium, where there is a large population of spins in the direction of the magnetization compared to antiparallel, i.e., the two bands for up and down spins are shifted with respect to each other by the exchange energy. A chemical potential imbalance is induced at the interface due to the different magnetic nature of the two materials. This imbalance creates a spin accumulation, i.e. an out of equilibrium distribution of spins. In the case of static magnetization this translates into a dc chemical imbalance in the non-magnetic metal. An excited state for the

system can be obtained by changing the magnetization direction, the bands immediately shift in energy. In order to turn back to equilibrium state the spin relaxation process takes place, in other words, there has to be a spin transfer from one band to the other [51]. The process can either be in the ferromagnet or in the adjacent layers. In the last situation, the adjacent layer acts as a spin sink to which the spin can be transferred. In ferromagnetic resonance experiments, the magnetization direction can be changed continuously in time and eventually emits ac spin current ($\boldsymbol{I}_S^{pump}$) into the adjacent layer through the F/N interface (see Figure 5). Depending on the spin sink properties the spin current will either relax by spin-flip scattering and spin-dephasing mechanisms or it will flow back to the ferromagnet, $\boldsymbol{I}_S^{back}$. For the case of a perfect spin-sink, i.e. for a material with infinite spin-flip rate, one has $\boldsymbol{I}_S^{back} \sim 0$, which gives maximum increase in damping due to spin pumping. For the opposite case of a poor spin sink, one has ($\boldsymbol{I}_S^{pump} \sim \boldsymbol{I}_S^{back}$) and there will be very little effect of the adjacent layer on the damping of the ferromagnet.

The spin current $\boldsymbol{I}_S^{pump}$ pumped by the precessing magnetization of a ferromagnet into an adjacent layer was derived by Tserkovnyak *et al* [48]:

$$\boldsymbol{I}_S^{pump} = \frac{\hbar}{4\pi}\left[g_r^{\uparrow\downarrow}\left(\boldsymbol{M}\times\frac{d\boldsymbol{M}}{dt}\right) + g_i^{\uparrow\downarrow}\frac{d\boldsymbol{M}}{dt}\right], \qquad \text{Eq. I-8}$$

where $g_r^{\uparrow\downarrow}$ and $g_i^{\uparrow\downarrow}$ refer to the real and imaginary part of the spin mixing conductance which is a dimensionless interfacial quantity. The real and imaginary parts account for absorption/transmission of angular momentum along two orthogonal directions. In metallic interfaces, the imaginary part of the spin mixing conductance ($g_i^{\uparrow\downarrow}$) was found to be very small and can likely be neglected in most of the time [48,52]. The part of Eq. I-8 linked to the real part of the spin mixing conductace ($g_r^{\uparrow\downarrow}$ or $g_{eff}^{\uparrow\downarrow}$) has the same form as the damping term in the LLG equation (Eq. I-3) and will thus lead to an increased damping of magnetization. Since the spin mixing conductance $g_{eff}^{\uparrow\downarrow}$ governs how much spin current is passed through the interface, it was shown by using Onsager's reciprocity relations that spin pumping and spin transfer torque are reciprocal effects [53].

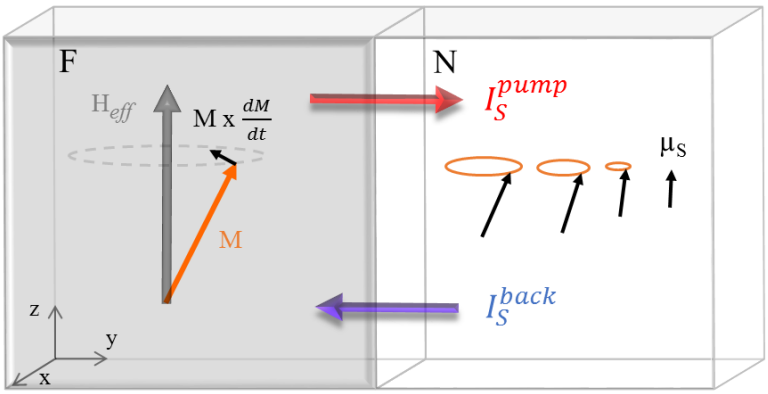

Figure 5 : Schematic illustration of the spin pumping effect in ferromagnetic (F)/normal metal (N) bilayers. The magnetization precession drives a time-varying spin current $\boldsymbol{I}_S^{pump}$ into N, causing a non equilibrium spin accumulation. It either relaxes by spin flip scattering and dephasing or flows back into the F, $\boldsymbol{I}_S^{back}$.

The absorption of spin current leads to the permanent loss of spin angular momentum and results in an increase of damping. Thus the damping may be described by $\alpha = \alpha^{ref}+\alpha^{p}$, where α^{ref} is the reference of the ferromagnetic layer damping, i.e, without spin sink. This extrinsic damping contribution can be derived from $\boldsymbol{\imath}_S^{pump}$, and is given by [48]:

$$\alpha^{p} = \frac{g_{eff}^{\uparrow\downarrow}}{S}\frac{\gamma\hbar}{4\pi M_S}\frac{1}{t_F}. \qquad \text{Eq. I-9}$$

This additional nonlocal damping is Gilbert-like and follows an inverse dependence with the ferromagnet thickness ($1/t_F$). It contains the physics of the spin absorption/transmission at the various interfaces.

I.1.2 Typical experimental procedure

I.1.2.1 Ferromagnetic resonance (FMR) condition and physical outputs

So far I have discussed about the precession of the magnetization and its relaxation governed by the damping term in the equation of motion. In order to study this relaxation experimentally, an oscillating *rf* field ($\boldsymbol{h}_{rf}$) in the radiofrequency range ($\omega=2\pi f$) is applied perpendicular to the direction of the external dc field ($\boldsymbol{H}$) in order to pull the magnetization out of its equilibrium position, causing it to precess around an effective field (see Figure 6). Damping can be obtained from corroborating the absorption spectrum measured at resonance to calculations of the resonance condition. I will now discuss how to calculate the resonance condition, i. e. when the imaginary part of the magnetic susceptibility of the system (χ'') is maximum, with $\boldsymbol{M}=\chi\boldsymbol{H}$.

In order to define the resonance condition the magnetization is written as: $\boldsymbol{M} = m_x\boldsymbol{x}+m_y\boldsymbol{y}+m_z\boldsymbol{z}$, where $m_z \sim M_S$ ($m_z >> m_x, m_y$, see Figure 6). The expression for the effective field ($\boldsymbol{H}_{eff}$) takes the following form:

$$\boldsymbol{H}_{eff} = h_{rf}\,\boldsymbol{x} - \frac{M_{eff}}{M_S}m_y\,\boldsymbol{y} + (H+H_u)\boldsymbol{z} \qquad \text{Eq. I-10}$$

Where H_u represents the uniaxial anisotropy field, $H_u = 2K_a^u/(\mu_0 M_S)$ (K_a^u corresponds to the uniaxial anisotropy constant), and $M_{eff} = M_S - 2K_a^S/(\mu_0 M_S t_F)$ (K_a^S corresponds to the surface anisotropy constant). One has to use the above form of the magnetization $\boldsymbol{M}$ and the effective field acting on it (given by Eq. I-10) to solve the LLG equation (Eq. I-3), which is the equation of motion of a system of two coupled equations for the magnetization components, m_x and m_y. As represented in Figure 6, the microwave field is applied along the *x* axis. Thus, we are interested in χ_{xx}. The magnetization components and h_{rf} are related to the susceptibility tensor. It results in the following relation:

$$\chi_{xx} = \chi'_{xx} + i\chi''_{xx} = \frac{m_x}{h_{rf}} = M_S\frac{\left(A+i\alpha\frac{\omega}{\gamma}\right)\left[AB-\left(\frac{\omega}{\gamma}\right)^2(\alpha^2+1)-i\alpha\frac{\omega}{\gamma}(A+B)\right]}{\left[AB-\left(\frac{\omega}{\gamma}\right)^2(\alpha^2+1)\right]^2+\left[\alpha\frac{\omega}{\gamma}(A+B)\right]^2}, \qquad \text{Eq. I-11}$$

where χ'_{xx} and χ''_{xx} are the dispersive and absorptive parts of the *rf* susceptibility, respectively. One set $A = M_{eff}+H+H_u$ and $B = H+H_u$ in order to simplify Eq. I-11.

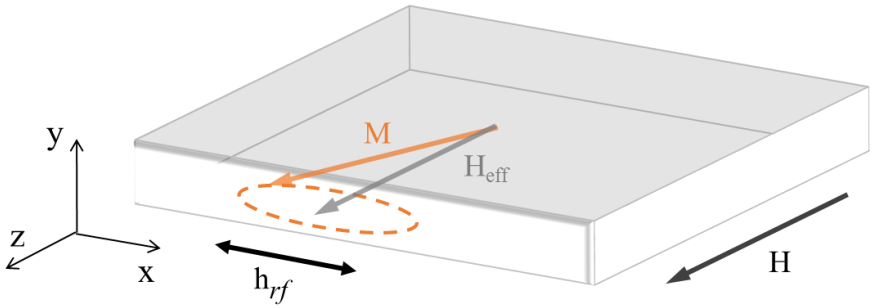

Figure 6 : Schematic representation of the ferromagnetic resonance configuration in a thin film. The magnetic field ***H*** is applied in the film plane perpendicularly to the microwave field $\boldsymbol{h}_{rf}$.

The resonance condition for the magnetization is obtained when the denominator of Eq. I-11 is minimum, i.e., when m_z becomes maximum for a given h_{rf}. Therefore, one can write:

$$AB-\left(\frac{\omega_{res}}{\gamma}\right)^2\left(\alpha^2+1\right)=0\,. \qquad \text{Eq. I-12}$$

It gives χ''_{xx} in the following form:

$$\chi''_{xx}=-M_S\frac{1}{\left[\frac{\omega_{res}}{\gamma}\left(M_{eff}+2\left(H+H_u\right)\right)\right]^2}\,. \qquad \text{Eq. I-13}$$

Note that it has the form of a conventional Lorentzian function. Since we have determined the resonance condition, we now look to the power absorbed in a ferromagnetic resonance experiment, which is given by the following relation:

$$P=\frac{1}{2}\omega\chi''\boldsymbol{h}_{rf}^2\,. \qquad \text{Eq. I-14}$$

Therefore, the absorbed power also has the form of a Lorentzian function. Eq. I-14 describes the absorption of the incident microwave radiation in ferromagnetic resonance experiments.

A typical FMR spectra as measured fora 8 nm thick NiFe layer is shown in Figure 7. As will be further discussed in § I.1.2.2 and I.1.2.3 when describing the experimental setups, lock-in detection is employed to improve the signal to noise ratio. As consequence, the signal measured experimentally corresponds to the derivative of χ''_{xx} with respect to *H*, i.e., the derivative of a Lorentzian function.

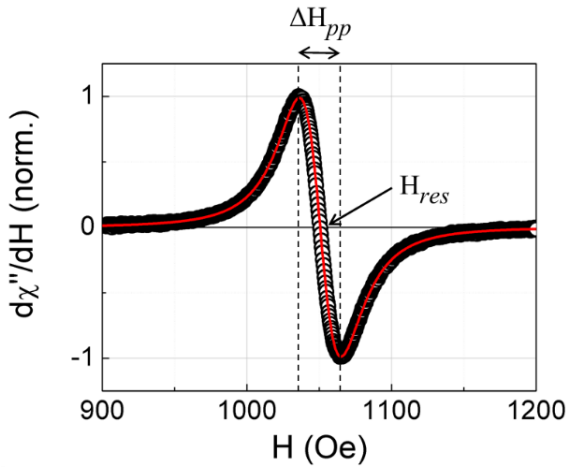

Figure 7 : Representative differential absorption spectra ($d\chi''/dH$ vs. H), related to the magnetic susceptibility (χ), as measured for a typical sample with a 8 nm thick NiFe layer. The x-intercept gives the resonance field H_{res} and peak-to-peak resonance linewidth is ΔH_{pp}.

We can rewrite Eq. I-12, which describes the resonance condition for the magnetization taking into account $\alpha << 1$. In such a case, α^2 can be neglected and the resonance condition is given by $(\omega_{res}/\gamma)^2 = AB$. Replacing A and B with their original form and neglecting the anisotropy contributions, we get the Kittel equation [54]:

$$(2\pi f)^2 = |\gamma| H_{res}(H_{res} + 4\pi M_{eff}). \qquad \text{Eq. I-15}$$

A study where such anisotropy contributions matter will be presented in § I.2.2 and I.2.3 along with a modified Kittel equation. By recording FMR spectra at selected frequencies, 4 to 20 GHz, one can fit the experimental data to the Kittel formula (see Figure 8(a)). The effective saturation magnetization is extracted from the fitting line, M_{eff} = 7785 Oe (620 emu.cm^{-3}).

From the peak-to-peak linewidth (ΔH_{pp}) it is possible to extract the total damping (α) using the following relation [55]:

$$\Delta H_{pp} = \Delta H_0 + \frac{4\pi}{\sqrt{3}|\gamma|}\alpha f \ , \qquad \text{Eq. I-16}$$

where ΔH_0 is the inhomogeneous broadening associated with the spatial dispersion of magnetic parameters, like saturation magnetization and anisotropy [56]. Figure 8(b) shows ΔH_{pp} as a function of frequency. The red line is a fit to Eq. I-16. From the corresponding slope, the total damping α is found to be 7.5 x 10^{-3} for a 8 nm thick NiFe sample. The y-intercept gives ΔH_0, which is found to be 2.71 Oe.

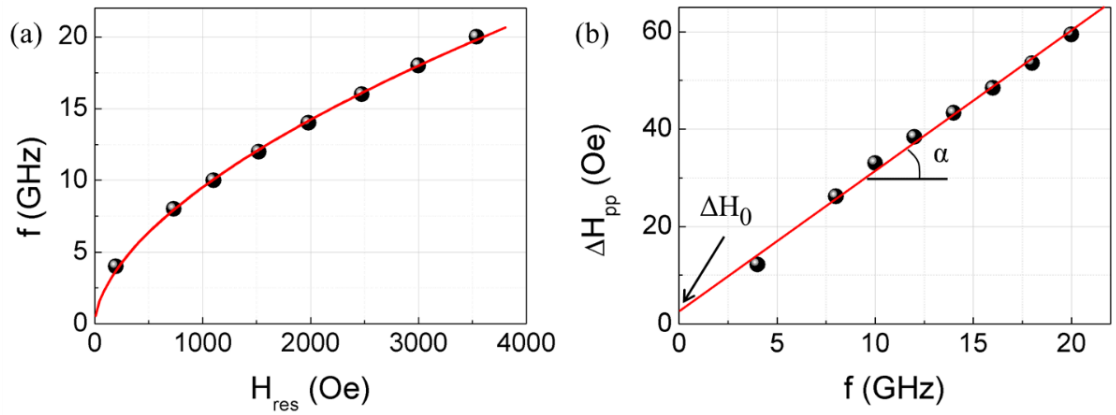

Figure 8 : (a) Typical frequency-field resonance diagram. The red line is a fit to the Kittel equation, see Eq. I-15. (b) Frequency dependence of the resonance linewidth, ΔH_{pp}. The red line is a fit to Eq. I-16. The slope of the linear fit gives the damping parameter α, while the y-intercept gives the inhomogeneous broadening, ΔH_0. The data corresponds to a series of measurements for a typical 8 nm thick NiFe layer.

I.1.2.2 Coplanar stripline for broadband measurements - eddy current related effects in Cu/NiFe and NiFe/Cu bilayers [1]

Figure 9(a) is a schematic illustration of the inductive FMR spectrometer based on a coplanar waveguide (CPW) [57]. The spectrometer was home build by Bill Bailey *et al*, back in 2010. It operates at room temperature. A vector network analyzer (VNA) is used as a source of a microwave signal (h_{rf}) of variable frequencies (10 MHz to 24 GHz). This microwave signal is transmitted through a double ground plane CPW. The sample is placed on top (up side down) of the CPW, which is placed between the poles of the magnet in a region where the field is homogeneous. The static magnetic field was applied in the plane of the film, perpendicular to the microwave field, as shown in Figure 6. The width of the central conductor strip was 375 μm and the gap between the lines was 140 μm. The transmitted signal is converted into voltage by using a Schottky diode detector. To increase the signal to noise ratio, a lock-in detection is employed. Two coils in Helmholtz configuration have been used to modulate the dc applied field. The typical modulation field amplitudes varies from 2 to 20 Oe at a constant frequency of 201 Hz. The processed signal as received from the lock-in amplifier is a derivative of the absorbed power versus the applied field. Figure 9(b) shows a picture of the experimental setup. Representative spectra are shown in Figure 10 and will be further discussed in the following paragraphs. From this plot the resonant field H_{res} corresponding to the fixed frequency and the linewidth ΔH_{pp} are extracted.

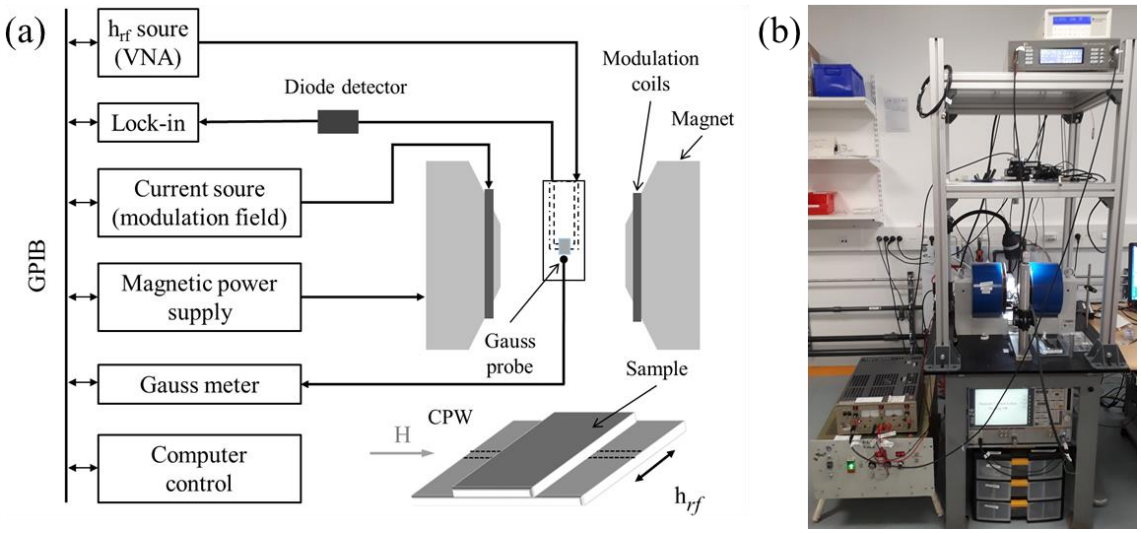

Figure 9 : (a) Schematic illustration of the FMR spectrometer based on a coplanar waveguide (CPW). CPW and sample geometry are shown in the bottom right. (b) Picture of the experimental setup. (a) is adapted from Ref. [57].

The following of the section is adapted from Ref. [1] where the main findings were published. It should be noted here that the results in this section were obtained in the frame of the PhD thesis of Lamprini Frangou (2014-2017), the Post-doctoral projects of Guillaume Forestier (2016-2018) and Olga Gladii (2017-2019) and the beginning of my PhD thesis in 2018 in the antiferromagnetic team led by Vincent Baltz - Ref. [1]: R. L. Seeger (equal first), O. Gladii (equal first), L. Frangou (equal first), G. Forestier, U. Ebels, S. Auffret, and V. Baltz, Appl. Phys. Lett. **115**, 032403 (2019).

Commonly in FMR experiments performed with stripline setups (such as CPW) line shape asymmetries are observed [58–62]. The part of the stripline inductively coupled to the sample is equivalent to a device circuit defining a complex microwave impedance [58,63,64]. The resulting phase of the microwave excitation leads to an absorption-dispersion admixture and produces asymmetric lineshapes. Although a phenomenological parameter accounting for such asymmetry is considered to extract the resonance field and linewidth from data fitting, it is usually not commented on. The reason for this is because in most cases, asymmetry, linewidth and resonance field are not related, and because for most geometries, the absorption component prevails [58] and this type of experiment-related asymmetry is therefore small.

Other effects such as eddy currents may produce unusual lineshapes. This type of effect has been thoroughly studied for film thicknesses above the skin-depth limit [65]. In contrast, below this limit, the effects of eddy currents were most often neglected, except for a study on ac charge currents, including currents produced by spin pumping and spin-charge conversion [66] and for series of comprehensive studies focused on microwave screening/shielding, [58,64,67,68] e.g. leading to layer-transducer ordering-dependent standing spin wave modes in sufficiently thick layers [58,67] and to depth-dependent dephasing [68]. As we will further discuss below, eddy currents need to be carefully considered to accurately determine damping [43,44] and other related spintronic properties [69], especially when characterizing low-damping materials. Some recent experimental studies on F-NiFe(10nm)/NM-(Au,Cu) bilayers [45,46] revealed how the Oersted field - due to eddy currents in the non-magnetic (NM) layer - affects the dynamics of F magnetization, and more specifically, how it distorts the resonance lineshape. The experiments were performed in a cavity setup and corroborated the results of analytical calculations. The scenario considered in Refs. [45,46] involved eddy currents in the NM

conductor, generated by an homogeneous excitation radiofrequency magnetic field ($\boldsymbol{h}_{rf}$) applied out-of-plane. The phaseshift (φ) between $\boldsymbol{h}_{rf}$ and the eddy current-induced field out-of-plane ($\boldsymbol{h}_{ind}=\mu\boldsymbol{h}_{rf}e^{i\varphi}$) resulted in an absorption(A)-dispersion(D) admixture of the signal. It produced an asymmetric resonance line, related to the absorbed power, $P \propto A+\beta D$ with:

$$\beta = \frac{\mu \sin(\varphi)}{1+\mu\cos(\varphi)} + \beta_0 , \qquad \text{Eq. I-17}$$

where β_0 is the empirical residual "experiment-related" phase shift. P can be calculated from: $P \propto \mathrm{Re}\left[i\omega(\chi h_{rf})h_{rf}^{*}\right]$, where the magnetic susceptibility χ is deduced from the Landau-Lifshitz-Gilbert equation (see § I.1.2 for more details on the power absorbed in resonant experiments). In this scenario relying on the use of an homogeneous $\boldsymbol{h}_{rf}$ out-of-plane, experiments conducted with stripline setups, with $\boldsymbol{h}_{rf}$ in the sample plane, should not generate eddy currents in the conductive layers. However, it has been suggested that sample tilting would lead to an out-of-plane component, [45] thus creating the conditions for eddy current-related asymmetry. According to this hypothesis, the sign of the asymmetry should be independent of the stacking order for the layers, because the homogeneous $\boldsymbol{h}_{rf}$ generates eddy currents with the same directed $\boldsymbol{h}_{ind}$ above and below the NM conductor. The data show that this assumption fails to completely describe experimental results.

In the following paragraphs, the impact of eddy currents is investigated and a contribution to lineshape asymmetry in stripline experiments is unraveled. Notably a stacking order-dependent sign change of microwave phase due to eddy currents in NiFe/Cu heterostructures is observed.

Spectra asymmetry

The full stacks used in this study were (from substrate to surface): Cu(t_{Cu})/NiFe(t_{NiFe})/Al(2)O_x and NiFe(t_{NiFe})/Cu(t_{Cu})/Al(2)O_x (nm) multilayers. t_{Cu} is the thicknesses of the Cu layer and was varied between 1 and 14 nm; t_{NiFe} is the thicknesses of the NiFe layer: t_{NiFe} = 4, 8, or 12 nm. Stacks were deposited at room temperature by dc-magnetron sputtering on Si/SiO_2(500) substrates at a pressure of argon of 2.3 x 10^{-3} mbar. Unless specified otherwise, the stacks were deposited at SPINTEC by Stéphane Auffret. The NiFe layer was deposited from a $Ni_{81}Fe_{19}$ (at. %) permalloy target. A 2-nm-thick Al cap was deposited to form a protective Al(2)O_x film after oxidation in air. This insulating film also prevented electrical contact between the samples and the waveguide (Figure 10(a,b)). Unless specified otherwise, the sample dimensions were: l = 4 mm, w = 3 mm. FMR experiments and the corresponding differential absorption spectra, $d\chi''/dH \propto dP/dH$ vs. H (Figure 10(c-h)), were recorded at room temperature at frequencies ranging between 4 and 20 GHz with the CPW based spectrometer, described in Figure 9.

First, we discuss the spectrum asymmetry which gradually built up as the t_{Cu} increased (Figure 10(c-h)). This behavior revealed a non-negligible impact of eddy currents circulating in the Cu layers. Most importantly, the sign of the asymmetry depended on the ordering of the Cu and NiFe layers, i.e., whether the Cu layer was the buffer or capping layer. Figure 11(a) illustrates a mechanism where the inhomogeneous field of the coplanar waveguide, with strong out-of-plane components, generates eddy currents with oppositely directed induced in-plane fields ($\boldsymbol{h}_{ind}$) above and below a Cu layer. Further considering a phaseshift between $\boldsymbol{h}_{rf}$ and $\boldsymbol{h}_{ind}$, we obtained $\boldsymbol{h}_{ind}^{\pm} = \mu \boldsymbol{h}_{rf} e^{i\varphi^{\pm}}$. The superscripts '+' and '-' relate to the 'capping' and 'buffer' cases respectively. We get a situation similar to Ref. [45], described by Eq. I-17, but considering

that the dominant coupling accurs between the FMR mode and in-plane fields. To extract the asymmetry and quantify the findings, the differential resonance spectra were fitted using the following equation [45]:

$$\frac{d\chi''}{dH} \propto \frac{d}{dH}\left[\frac{1+\beta(H-Hres)/\sqrt{3}\Delta Hpp}{(H-Hres)^2+(\sqrt{3}\Delta Hpp/2)^2}\right], \qquad \text{Eq. I-18}$$

where H_{res} is the resonance field, ΔH_{pp} is the peak-to-peak linewidth.

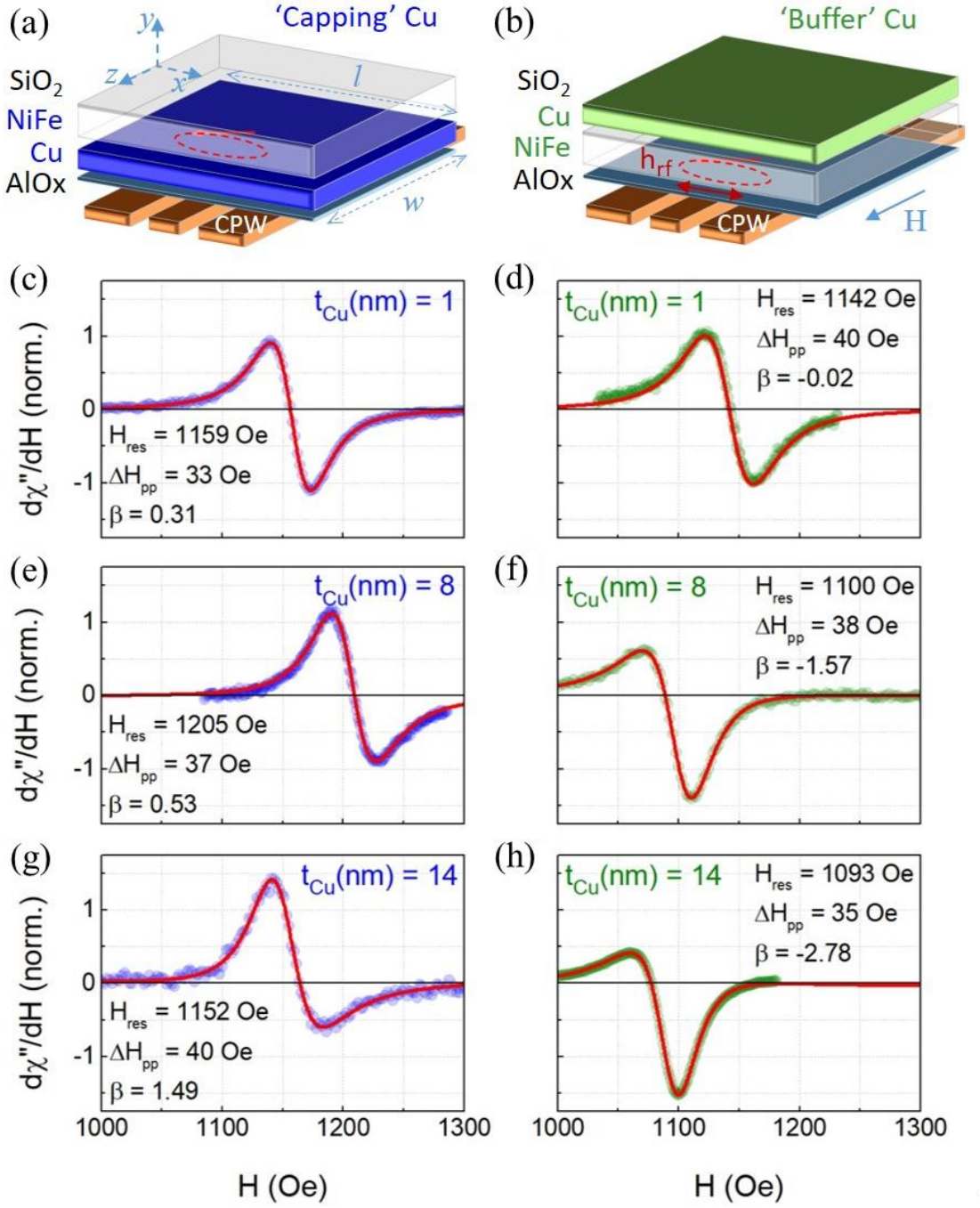

Figure 10 : (a,b) Schematic representations of the coplanar waveguide (CPW) – FMR experiment. Samples were placed face-down on the waveguide. The in-plane dc bias field (***H***), and the in-plane component of the excitation magnetic field from the waveguide ($\boldsymbol{h}_{rf}$) are represented. (c-h) Representative differential absorption spectra ($d\chi''/dH$ vs. H) measured for Si/SiO_2/NiFe(8)/Cu(t_{Cu})/Al(2)O_x and Si/SiO_2/Cu(t_{Cu})/NiFe(8)/Al(2)O_x (nm) stacks. The straight lines were fitted to the data using Eq. I-18, derived from Ref. [45] Data-fitting allowed the resonance field (H_{res}), the peak-to-peak linewidth (ΔH_{pp}), and the asymmetry parameter (β) to be determined.

Figure 11(b) shows β plotted as a function of t_{Cu} for series of Cu(t_{Cu})/NiFe(t_{NiFe}=4;8;12)/Al(2)O_x ('buffer') and NiFe(t_{NiFe}=4;8;12)/Cu(t_{Cu})/Al(2)O_x (nm) ('capping') multilayers. The gradual increase in $|\beta|$ with t_{Cu} agrees with the fact that eddy currents relate to the conductance of the Cu layers, which increases with t_{Cu}. The above deductions can be correlated by using Eq. I-17. The field $\boldsymbol{h}_{\mathbf{ind}}$ relates to the rate of change of magnetic flux through the area, S, delimited by the eddy current loop. It can be expressed as $h_{ind} = \mu_0 2\pi f(t_{Cu}/\rho)a(l,w,g)h_{rf}$. We considered that the eddy current was given by $I = S2\pi h_{rf}/R$, where the numerator corresponds to the electromotive force due to variations of $\boldsymbol{h}_{rf}$ over time. The resistance of the loop of length P, is given by $R = \rho P/t_{Cu}\zeta$, where ζ is the width of the loop, the spatial profile of which depends on the sample's geometry in a non-trivial manner [70]. The averaged magnetic field acting on the NiFe layer is expressed as $h_{FB} = \mu_0 I/b$, where b is a function of the geometry of the sample. The geometry-dependence of the parameters, including $S\zeta/(bP) \equiv a(l,w,g)$ (dimension of length) will be discussed further below. Over the thickness range investigated (1-14 nm), the Cu layer's resistivity is given by $\rho_{Cu}^{\pm} = \rho_0^{\pm} + \eta^{\pm}/t_{Cu}$, where $\eta^{\pm} = 3\lambda_{mfp}^{\pm}/8$ according to the Fuchs-Sondheimer model [71,72]. From separate 4-point electrical measurements, we obtained $\rho_{Cu}^{+}[\mu\Omega\cdot cm] = 7 + 53/t_{Cu}[nm]$ for the capping layers and $\rho_{Cu}^{-}[\mu\Omega\cdot cm] = 5 + 35/t_{Cu}[nm]$ for the buffer layers (Figure 11(c)), which produce reasonable values for the electron mean free path: $\lambda_{mfp}^{\pm} = 14$ nm and $\lambda_{mfp}^{\pm} = 9$ nm. With regard to the phaseshift (φ) in Eq. I-17, we neglected the contribution of the skin effect, which is proportional to t_{Cu}/δ_{Cu}, because t_{Cu}=1-14 nm, and the skin-depth δ_{Cu} ~ 1000-500 nm for f = 4-20 GHz. In the ideal situation of a negligible inductive contribution to the complex impedance, $\varphi^+ = \pi/2$ for the 'capping' layer case (quadrature phase shift because $\boldsymbol{h}_{ind}$ is related to the time derivative of $\boldsymbol{h}_{rf}$), and $\varphi^- = -\pi/2$ for the 'buffer' layer case (in antiphase to the 'capping' layer case). Developing the different terms in Eq. I-17 produced a predictable non-linear dependence of β on t_{Cu}, and a linear dependence on f:

$$\beta^{\pm} = \pm\mu_0 2\pi f \frac{t_{Cu}}{\rho_0^{\pm} + \eta^{\pm}/t_{Cu}} a(l,w,g) + \beta_0 . \qquad \text{Eq. I-19}$$

The two straight lines in Figure 11(b) were fitted with Eq. I-19; $a(l,w,g)$ and β_0 were the only free parameters. It can be seen that the simplified model captures the physics of the phenomenon observed experimentally. Data fitting returned $\beta_0 = -0.3$ and $a(l,w,g) = 185\pm3$ µm in both cases, in agreement with the constant sample dimensions in these sets of experiments. Remarkably, the model can account for the difference in the thickness-dependence of Cu-resistivity due to the inversion of the growth order. To emphasize this, the dashed line in Figure 11(b) corresponds to a simulation using Eq. I-19, considering the fictitious case of $\rho_{Cu}^{+} = \rho_{Cu}^{-}$. From Figure 11(b), we note that slight deviations between predictions and experimental data can still be observed for the 'buffer' layer case. Most importantly for thick Cu layers - as for example experimentally shown in Ref. [45] in the 10-50 nm range - and high frequencies, inductive contributions to the complex impedance are very likely to affect the ideal thickness-dependence of β in a non-trivial manner. Considering such a term, the phase shift becomes: $\varphi = \pm\pi/2 + \theta(f,t_{Cu},l,w,g)$, where θ shows a non-linear dependence on several parameters, thus producing non-linear dependences of β (from Eq. I-17).

The non-trivial influence of the inductive contributions to the complex impedance can clearly be seen for f-dependent measurements. Figure 11(d) shows β vs. f, for series of

Cu(t_{Cu}=1;8;14)/NiFe(8)/Al(2)O_x 'buffer' and NiFe(8)/Cu(t_{Cu}=1;8;14)/Al(2)O_x (nm) 'capping' multilayers. Data for t_{Cu} = 1 nm, in the absence of eddy current, correspond to β_0 and superimpose for the 'buffer' and 'capping' cases. The *f*-dependence of β_0 is weak, ruling out any *f*-dependent impedance contribution of the NiFe layer to the phaseshift. The straight lines in Figure 11(d) were produced by calculations using Eq. I-19. The same set of parameters as that returned from Figure 11(b) was used. It concurrently described the thickness- and *f*-dependences of β for the 'capping' case (Figure 11(d)), confirming that the simplified model reflects the physics behind the phenomenon observed. The overall linear increase of $|\beta|$ with *f*, driven by the fact that eddy currents increase when the rate of change of flux rises, may be altered by complex inductive contributions, which are known to increase for higher frequencies and thicker films. In agreement with this information, we observe in Figure 11(d) that data depart from a linear dependence above 10 GHz for the 14-nm-thick layers, a result that contrasts with those obtained for the 8-nm-thick ones, which follow a linear dependence throughout. The 14-nm-thick buffer layer case typically illustrates how non-trivial contributions can drastically distort and bend the initially linear *f*-dependence.

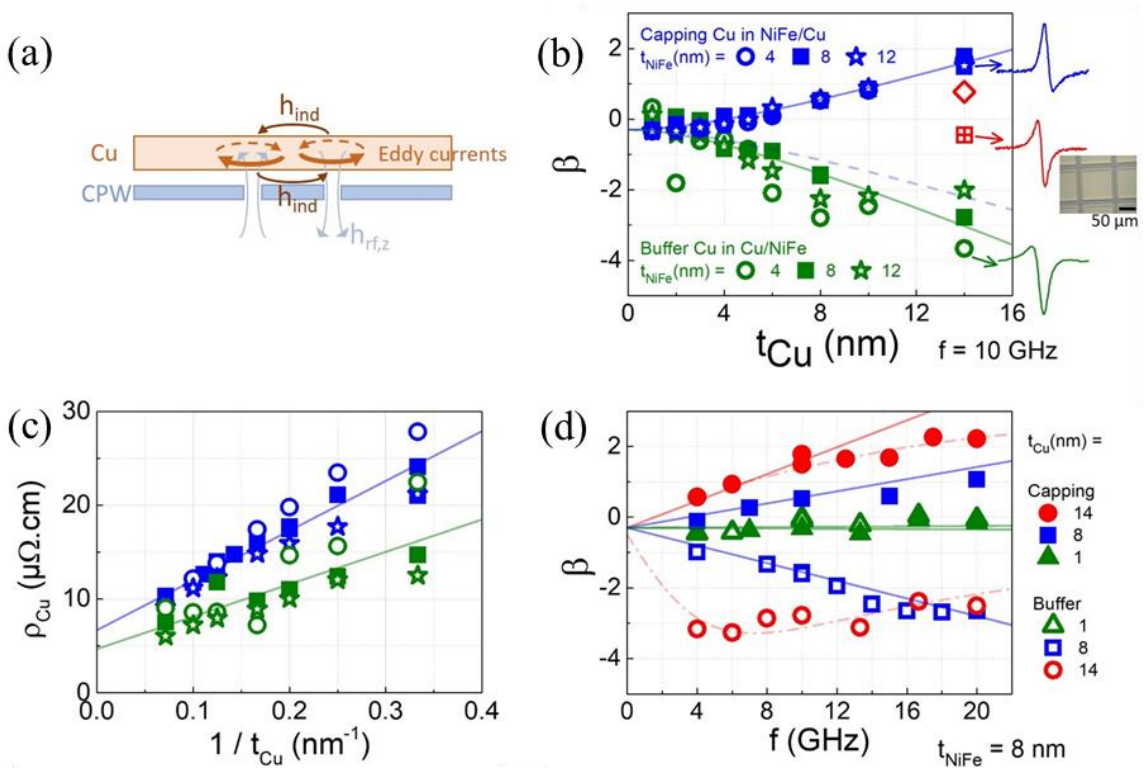

Figure 11 : (a) Illustration of a mechanism where the inhomogeneous field ($\boldsymbol{h}_{rf}$) of the coplanar waveguide, with strong out-of-plane components, generates eddy currents with oppositely directed induced in-plane fields ($\boldsymbol{h}_{ind}$) above and below a Cu layer. (b) Representative series of dependences of β on 'capping' and 'buffer' Cu-layer thickness (t_{Cu}) for Si/SiO_2/Cu(t_{Cu})/NiFe(t_{NiFe}=4;8;12)/Al(2)O_x and Si/SiO_2/NiFe(t_{NiFe}=4;8;12)/Cu(t_{Cu})/Al(2)O_x (nm) stacks. Data were recorded at 10 GHz. The square crossed symbol corresponds to data recorded after patterning (inset) the Cu(14)/Al(2)O_x bilayer in a Si/SiO_2/NiFe(8)/Cu(14)/Al(2)O_x (nm) stack. The open square symbol corresponds to data for the same stack on which the whole etching process was performed, as these samples were protected by a resist they remained unpatterned. (c) Corresponding dependences of Cu-layer resistivity (ρ_{Cu}) on t_{Cu}, obtained separately using standard 4-point electrical measurements. The lines were obtained using linear fits. (d) Representative series of dependences of on frequency (*f*) for Si/SiO_2/Cu(t_{Cu}=1;8;14)/NiFe(8)/Al(2)O_x and Si/SiO_2/NiFe(8)/Cu(t_{Cu}=1;8;14)/Al(2)O_x (nm) stacks. The straight lines in (b) and (d) were obtained using Eq. I-19. The dashed and dash-dotted lines are visual guides.

To rule out any contribution of the Si/SiO_2(500) substrate on the sign-change of β, we compared a Cu(14)/NiFe(4)/Al(2)O_x to a NiFe(4)/Cu(14)/Al(2)O_x (nm) stack deposited on glass

substrates (not shown). The same trend of a positive vs. negative value of β for the 'capping' vs. 'buffer' case was obtained.

Finite-sizes effects

We will now consider finite-size effects. Once again using Figure 11(b), we will briefly comment on the square crossed symbol corresponding to data recorded after patterning only the Cu(14)/Al(2)O_x capping layers in a Si/SiO_2/NiFe(8)/Cu(14)/Al(2)O_x (nm) stack (inset of Figure 11(b)). A 4x3 mm^2 array of square dots with lateral size of 100 µm was fabricated. Following patterning, two effects compete with one another. First, the number of eddy current loops increases, and simultaneously, the path of each loop is constrained. The fact that patterning significantly reduced β to a value close to β_0 (Figure 11(b)) shows that eddy currents cannot develop in the dots. This result indicates that the dot size (100 µm) was smaller than the width of the eddy current loop. We further assessed the dependence of β on the sample's geometry in Figure 12(a). We considered geometry-dependent parameters, $S\zeta/(bP) \equiv a(l,w,g)$ to account for the fact that the spatial profile of the eddy currents depends on the sample's geometry in a non-trivial manner. In particular, the width (ζ) and the circulation (determining S and P) are unknown.

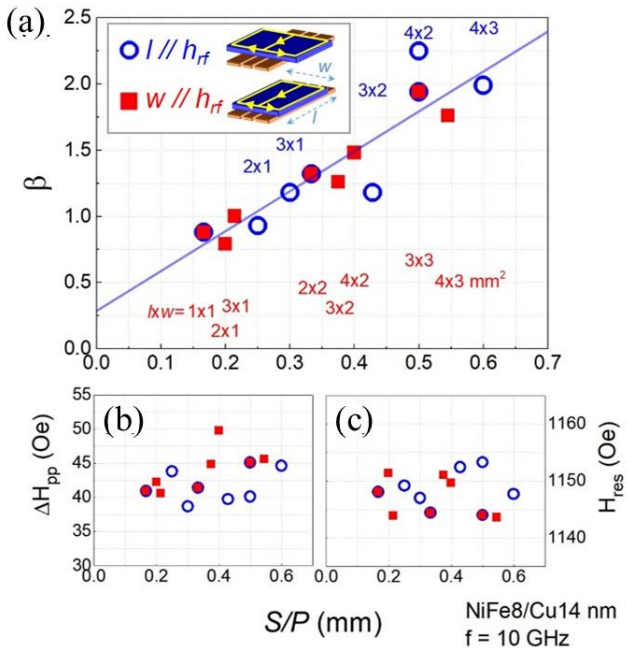

Figure 12 : (a) Dependences of β on the ratio S/P for Si/SiO_2/NiFe(8)/Cu(14)/Al(2)O_x (nm) stacks for two sample's orientations: l // h_{rf} and w // h_{rf}. S is the area delimited by the eddy current loop and P is the length of the current path, considering that currents extend over the sample (see inset). For l // h_{rf} $S/P=(wl/2)/[2(w+l/2)]$, and for w // h_{rf} $S/P=(lw/2)/[2(l+w/2]$. Data were recorded at 10 GHz. The line in (a) is a visual guide. (b,c) Corresponding dependences of H_{res} and ΔH_{pp}.

In addition, the amplitude of I is likely inhomogeneous along the width, making it difficult to obtain an analytical expression for the parameter b relating to the magnetic field created by I. Considering the limit case when eddy currents extend over the sample (see inset in Figure 12(a)), we obtained a linear dependence on S/P (Figure 12(a)), meaning that ζ/b seems to be almost independent of the sample's geometry. The discrepancy for the β_0 value is probably related to a geometry-dependence close to the smallest dimensions, that is likely to result in curve-binding. The results also show that rotating the sample in the plane of the stripline had no impact on the data (Figure 12(a)), demonstrating that both the length and the width of the current path contribute to h_{ind}. The most relevant insight is that stacking order-, thickness-, and

f-dependent measurements (Figure 11) returned the same value of *a(l,w,g)*, in agreement with the constant sample dimensions in these sets of experiments. The value of $\alpha \sim 185$ µm is also in agreement with the order of magnitude that can be estimated from Ref. [45]. Figure 12(b,c) present control data showing that the sample vs. stripline dimensions remained within a range where the linewidth and resonance field were unaffected by geometrical effects.

Magnetic properties

We next investigated the position (H_{res}) and the linewidth (ΔH_{pp}) of the spectra. The total Gilbert damping, α, was calculated from the slope of *f*-dependent measurements (ΔH_{pp} vs. *f*), from Eq. I-16, [55]. The inhomogeneous broadening [56] ΔH_0 due to spatial variations in the magnetic properties presents values of a few Oe in our experiments. The gyromagnetic ratio γ was derived from the fit of the curve representing H_{res} vs. *f*, see Eq. I-15. Plots representing H_{res} vs. t_{Cu} and α vs. t_{Cu} are shown in Figure 13(a,b) and Figure 13(c,d), respectively. The data showed no obvious link between eddy currents in the Cu layers (spectrum asymmetry in Figure 11), and the spectrum position, H_{res}.

We finally note from Figure 13(b) that, for $t_{NiFe} = 4$ nm, a non-monotonous dependence of H_{res} was observed. This behavior supports non-monotonous dependence of the effective NiFe magnetization, M_{eff}, (Figure 13(e,f)) which can be extracted from H_{res} vs. *f* using the Kittel formula, Eq. I-15. We recall that $M_{eff} = M_S - 2K_S/(4\pi M_S t_{NiFe})$. The values of M_S (Figure 13(g,h)), measured independently by magnetometry, were monotonous and thus confirmed that the non-monotonous behavior of M_{eff} seems to primarily relate to the properties of the Cu/NiFe interface. A similar non-monotonous dependence of α was observed. Cu wets poorly on SiO_2 compared to NiFe on SiO_2 and Cu, and as a result may create rougher thin Cu films. Consequently, spatially inhomogeneous stray fields may lead to incoherent dephasing of the spin current [49,73] injected from the NiFe to the buffer Cu layer, and thus to enhanced damping.

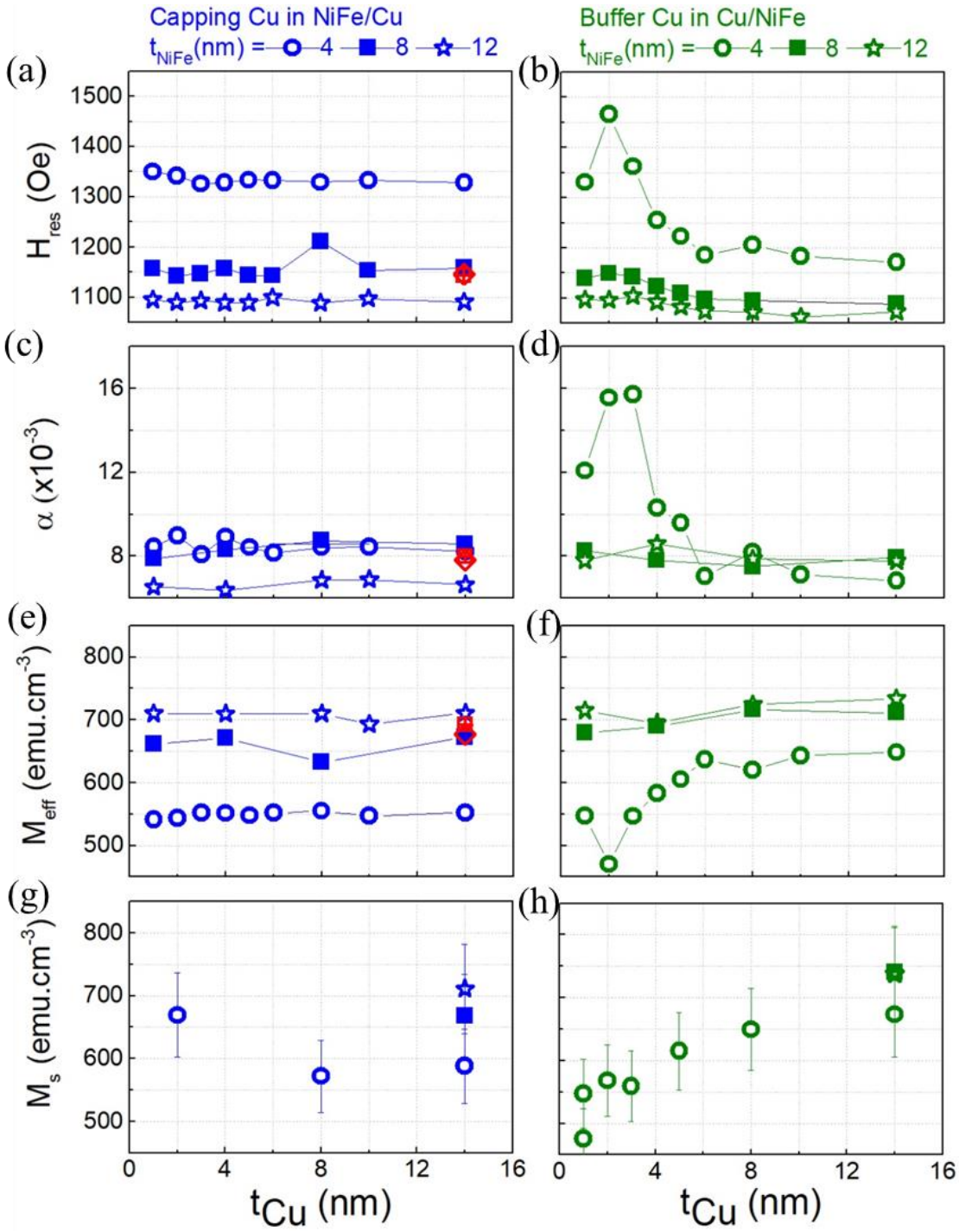

Figure 13 : Dependences of (a,b) H_{res}, (c,d) α, (e,f) M_{eff}, and (g,h) M_S on t_{Cu} for Si/SiO_2/Cu(t_{Cu})/NiFe(t_{NiFe}=4;8;12)/Al(2)O_x and Si/SiO_2/NiFe(t_{NiFe}=4;8;12)/Cu(t_{Cu})/Al(2)O_x (nm) stacks. The square crossed symbols correspond to the patterned sample. (a-b) correspond to data recorded at 10 GHz. (c-d) were deduced from *f*-dependences of ΔH_{pp} (e,f) were deduced from *f*-dependences of H_{res} by fitting the data to Eq. I-16 and Eq. I-15, respectively (see § I.1.2.1 for more details on determination of physical parameters from experiments). (g,h) were measured independently by magnetometry, using a superconducting quantum interference device.

In the search for the radiative damping contribution

Regarding α, eddy currents in conductors adjacent to a resonator, including the waveguide, were shown to contribute to a damping process due to losses via inductive coupling [43,44,74]. This phenomenon is referred to as radiative damping and was introduced in § I.1.1.2. Considering the case where the dissipation occurs within the waveguide, the radiative

contribution to damping can be expressed by Eq. I-7 that we recall here [43]: $\alpha^{rad} = \mu_0^2 \kappa\gamma M_S t_F L/(2 Z_0 W)$. For YIG(200)/$Al_2O_3$(30)/Pt(5-20) (nm) samples with M_S ~ 121 emu.cm^{-3} and dimensions of 2x5 mm^2, in-plane stripline FMR measurements showed that α^{rad} due to eddy currents in the Pt capping layer can be up to 3×10^{-4} - for the 20 nm thick 35-Ω Pt layer [44]. From this value, considering the dependence of α^{rad} on M_S, t_F, Z_0 and the sample dimensions, and extrapolating to our case, we estimate a maximum value of α^{rad} of 1×10^{-4} for the NiFe(12)/Cu(14) (nm) with M_S ~ 700 emu.cm^{-3}, dimensions of 3x4 mm^2 and a resistance of the Cu layer of 10 Ω. This value of α^{rad} is too small to influence the damping of our NiFe layers (α~6-8$\times10^{-3}$). In fact, no obvious contribution of eddy currents to α can be inferred from the measurement discussed so far. Nevertheless, an α^{rad} of the order of few 10^{-4} is already significant for materials exhibiting low intrinsic damping, such as the YIG insulator ($\alpha \sim 6\times10^{-5}$), [44] the $Co_{1.9}Mn_{1.1}Si$ half metal Heusler alloy (7×10^{-4}) [75], and the $Co_{25}Fe_{75}$ bcc alloy (5×10^{-4}) [76].

Given the orders of magnitude indicated above, radiation contribution due to eddy currents in NM layers will need to be carefully considered when extracting α in several cases. In the search for a radiative contribution to damping, we have grown the following stacks (from substrate to surface): NiFe(40)/Al(2)O_x/Cu(t_{Cu})/Al(2)O_x (nm) multilayers. t_{Cu} is the thicknesses of the Cu layer: t_{Cu}=0, 10, 20, or 40 nm. The sample dimensions were 1x3, 2x3, and 4x3 mm^2 (see inset in Figure 14(a)). We expected α^{rad} due to eddy currents in the Cu neighbor layer might become sizeable. According to Eq. I-7, α^{rad} increases by increasing the NiFe layer thickness (now 40 nm compared to 12 nm). Note, however, that the NiFe thickness has to be sufficiently small to avoid: i) intrinsic damping contributions arising from eddy currents circulating inside the ferromagnetic layer in thick NiFe layers (see Eq. I-6 in § I.1.1.1) and ii) perpendicular standing spin wave modes [58]. In addition, by evaluating α as function of the Cu layer thickness, we search for small increase on α due to the α^{rad} while the Cu thickness increases. Finally, by increasing the spacing between the ferromagnetic and the adjacent metallic layers α^{rad} is strongly reduced and, thus, we use a thin Al(2)O_x (nm) spacing layer.

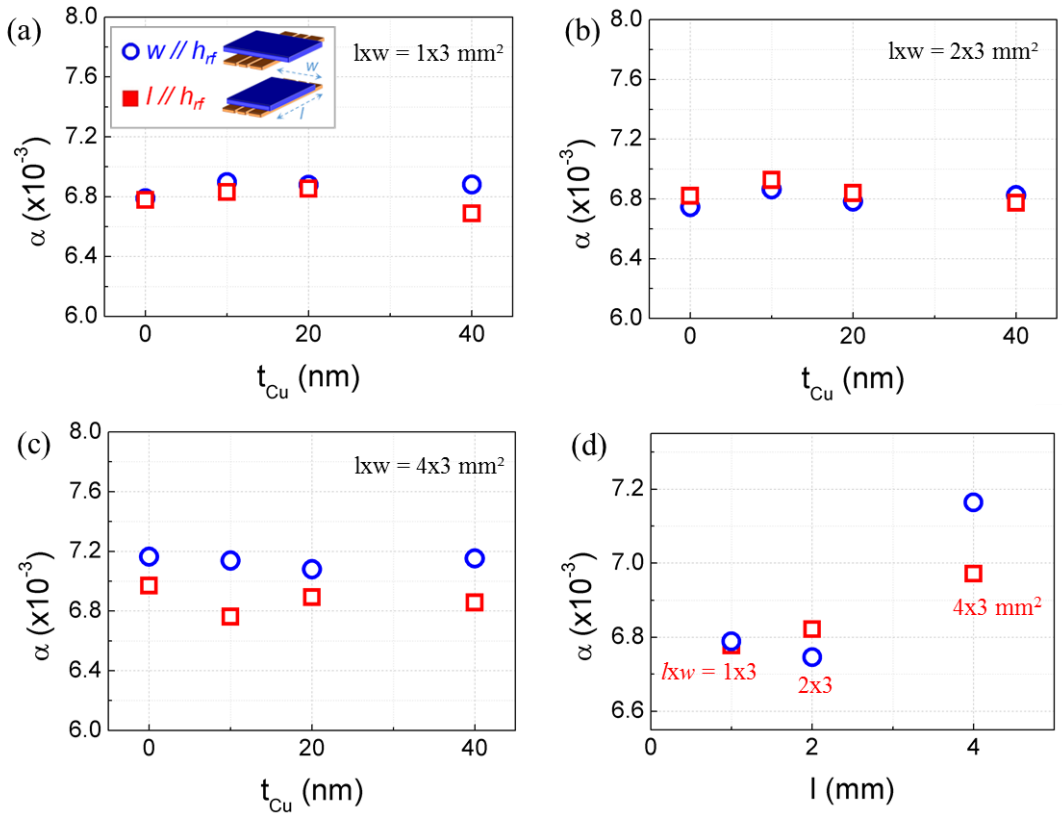

Figure 14 : Dependences of α on t_{Cu} for Si/SiO$_2$/NiFe(40)/Al(2)O$_x$/Cu(t_{Cu}=0;10;20;40)/Al(2)O$_x$ (nm) stacks for different sample geometry lxw = 1x3 (a), 2x3 (b) and 4x3 (c) mm². (d) Dependence of α on l as measured for Si/SiO$_2$/NiFe(40)/Al(2)O$_x$. The measurements were carried out for two sample's orientations: w // h_{rf} (circles) and l // h_{rf} (squares).

Figure 14(a,b,c) summarizes the dependence of α on t_{Cu} as measured for the NiFe(40)/Al(2)O$_x$/Cu(t_{Cu})/Al(2)O$_x$ (nm) multilayers. We first note that there is no evidence of α enhancement with increasing the Cu layer thickness and, thus, we can rule out the possibility of energy dissipation by eddy currents in the Cu adjacent layer. We will now discuss whether the dissipation by eddy currents within the waveguide can be at stake. As shown in Figure 14(a,b) (sample geometry: lxw = 1x3 and 2x3 mm^2) there is no dependence of α on t_{Cu}, regardless of the sample orientation with respect to h_{rf} (l // h_{rf} or w // h_{rf}). For the sample geometry lxw = 4x3 mm^2, depending on the orientation with respect to h_{rf} a variation on α is observed. According to Eq. I-7, α^{rad} depends on the sample length along to the stripline axis. Since rotating the sample in the plane of the stripline had impact on the data, it may indicate that α^{rad} is measurable for sufficiently large samples (as expected α is bigger when the longer sample length is along the stripline axis or when w // h_{rf}). Figure 14(d) shows the α dependence on l for various sample geometry as measured for a sample without the Cu layer. Despite the fact that the trend is as expected for radiative damping, we cannot exclude that inhomogeneity of the magnetization dynamics emerging in large samples are the responsible mechanism for the observed enhancement in damping. It may also be that the α^{rad} was still below of the order 10^{-4}, contrary to our crude estimation, i.e. negligible for materials such as NiFe which exhibit intrinsic damping of the order of few 10^{-3}.

Summary

In summary, the above discussed results represents systematic experimental evidence of a stacking-order-dependent sign-change of the microwave phase in nanometer-scale NiFe/Cu bilayers. The effect could be ascribed to eddy currents generated in the Cu layer in the sub-skin-

depth regime by the time varying magnetic fields in the experiment. Distinct sets of experimental data were consistent with a simple quantitative analysis encompassing the main features of the phenomenon. These results contribute to our understanding of the impact of eddy currents below the microwave magnetic skin-depth and explain the contributions to lineshape asymmetry and phase lags reported in stripline experiments commonly used to characterize and engineer materials for spintronic applications. They support a rational explanation to the use of the 'phenomenological' parameter accounting for lineshape asymmetry when extracting the spectral resonance field and linewidth from FMR data-fitting. The results also provide a straightforward way to detect the contributions of eddy currents from NM-adjacent conductors, as a caveat for the need in some cases to take these contributions into account when attempting to accurately determine damping [43,44] and other related spintronic properties such as spin-mixing conductance and the spin-Hall angle in spin-pumping experiments [69].

I.1.2.3 Resonant cavity for variable temperature measurements

So far, I have described the broadband coplanar stripline and provided typical results obtained with this setup. In the frame of this work, some of the studies necessitated variable temperature measurements and stripline experiments at low temperature are challenging due to the high loss of power to bring long cables inside of a cryostat. In fact, for variable temperature measurements we had access to another setup based on a resonant cavity, which will be further described below (Figure 15). The main reason for the scarce amount of studies using variable temperature in a resonant cavity is that the experiments cannot be easily automatized since manual retuning is usually needed after each temperature increment.

Figure 15(a) is a schematic illustration of the FMR spectrometer based on a cavity resonator [49]. It consists of a continuous wave electron paramagnetic resonance spectrometer that operates at 9.6 GHz fitted with a dual-model rectangular cavity. The system belongs to the team of Serge Gambaralli (SYMMES laboratory) and is made available to SPINTEC almost full time. It is equipped with a helium cryostat for measurements in the temperature range from 5 to 300 K. Same as the system described in Figure 9, lock-in detection is employed in order to increase the signal to noise ratio (the dc applied field is modulated with typical field amplitudes of few Oe at a constant frequency of 201 Hz). The waveguide is used to supply microwave power to the cavity and to return the reflected signal from the cavity to the diode detector. The cavity and waveguide are impedance matched and it provides maximum coupling. A circulator is employed to direct the reflected signal to the diode and protect the generator from the reflected power. A diode detector placed at the end of the cavity records the microwaves.

Before conducting a measurement the generator frequency is tuned to the resonant frequency of the cavity. The sample is placed in the cavity, between the poles of the magnet. The magnetic field is swept while the resonant absorption intensity is measured and a change in the cavity impedance is detected when the ferromagnetic resonance condition is satisfied. It results in reflection of microwaves detected by the diode, giving rise to the FMR signal.

Figure 15(c) shows a picture of the experimental setup. This experimental setup is also equipped with wires that can eventually be used to contact the sample edges and extract electrical signals concomitant to the FMR characterization, as shown in Figure 15(b). This case will be presented in § II, where experimental measurements of this kind will be discussed. For more details on the three-loop-two-gap resonator used in our studies the reader is refered to Refs. [77,78].

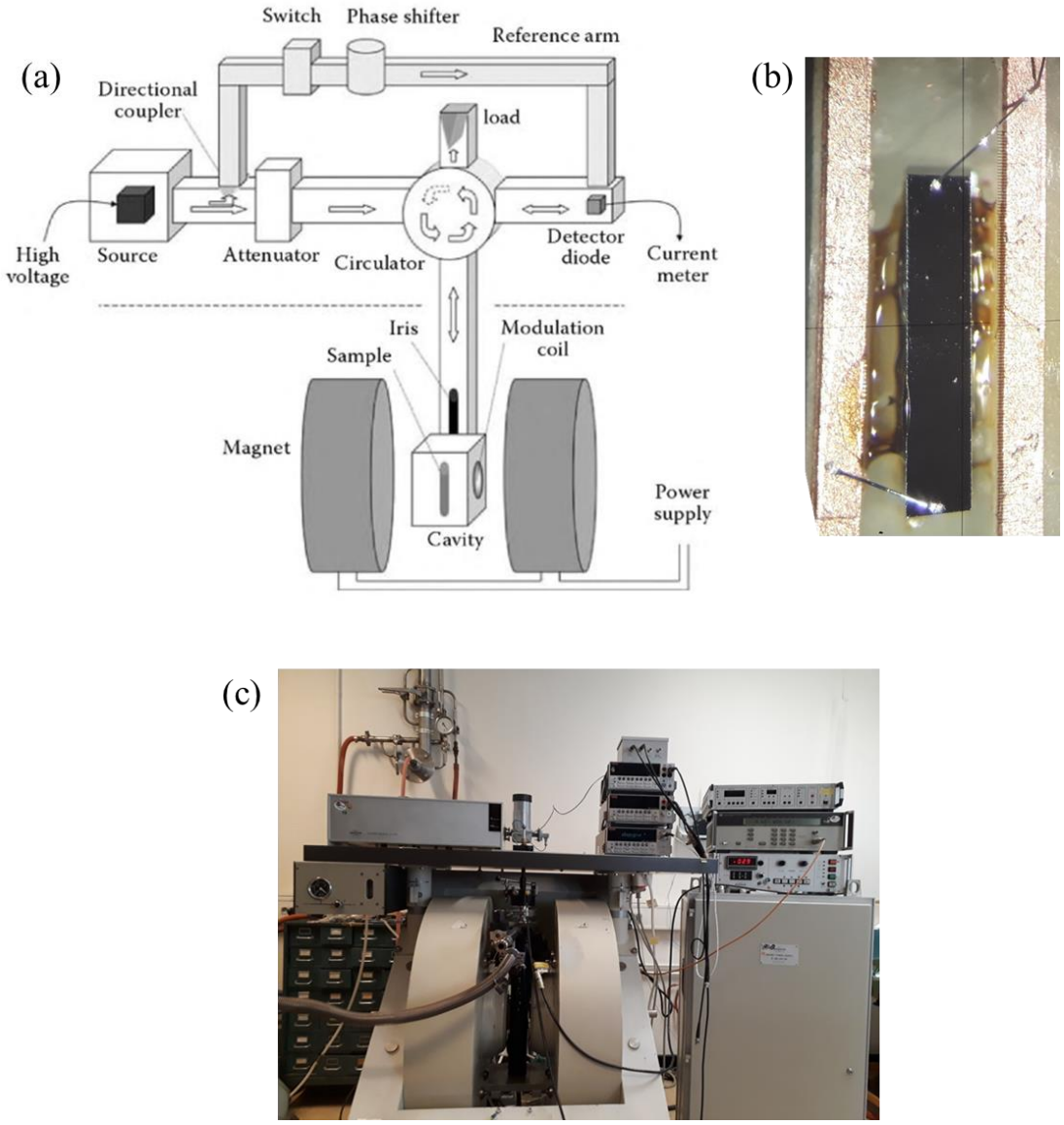

Figure 15 : (a) Schematic illustration of the FMR spectrometer based on a cavity resonator. (b) Picture of the sample connected to Cu electrodes on a printed circuit board (PCB), using Al-wire-bonding. The sample dimensions are: l = 2.46 mm and w = 0.46 mm. (c) Picture of the experimental setup. (a) From Ref. [79]

I.2 Spin pumping as a generic probe for linear spin fluctuations

I.2.1 Enhanced spin pumping efficiency around a magnetic phase transition

Originally, the theoretical framework for spin pumping is formulated by Tserkovnyak *et al* [48,49] in an analogy to a theory of adiabatic charge pumping. The spin injection method based on spin pumping is governed by the interfacial quantity called spin mixing conductance, as introduced above in § I.1.1.2. This model describes spin pumping at thermal equilibrium and does not consider spin fluctuations in the spin sink.

In the following paragraphs, I will briefly discuss a more recent theoretical model from the literature describing spin pumping near thermal equilibrium, in particular near a magnetic phase transition. I will then show the pioneering experimental foundations for complementary studies that I will describe further down, in § I.2.2 and I.2.3.

I.2.1.1 Spin-mixing conductance and linear magnetic susceptibility

In this section, I start by addressing the theory described by Ohnuma *et al* [80]. The system for observing spin pumping is composed a spin injector (SI) with precessing magnetization and an adjacent spin sink (SS), as shown in the inset of Figure 16. Ohnuma *et al* [80] investigate theoretically the effect of critical spin fluctuations of the spin sink on the spin pumping. As early pointed out in the theoretical description of spin pumping formulated by Tserkovnyak *et al* [48,49], see also § I.1.1.2, the pumped spin current efficiency depends on the spin mixing conductance $g_{eff}^{\uparrow\downarrow}$. Accordingly, the non-local damping contribution arising from the spin injection is also connected to this quantity ($\alpha^p \propto g_{eff}^{\uparrow\downarrow}$), see Eq. I-9. Ohnuma *et al* [80] have presented $g_{eff}^{\uparrow\downarrow}$ using a linear-response formalism describing spin pumping near thermal equilibrium. They found $g_{eff}^{\uparrow\downarrow}$ to be linked to the linear contribution of the dynamical transverse spin susceptibility (χ_k^R, with $\boldsymbol{M} = \chi_k^R \boldsymbol{H}$) of the spin-sink through the following expression:

$$g_{eff}^{\uparrow\downarrow}(T) \propto \sum_k \frac{1}{\Omega_{rf}} \mathrm{Im}\,\chi_k^R(\Omega_{rf}, T), \qquad \text{Eq. I-20}$$

where k is the wave vector, and Ω_{rf} is the angular frequency of the ferromagnetic spin-injector at resonance. Consequently, α^p is connected to the dynamical linear transverse spin susceptibility of the spin sink. Since this spin susceptibility is enhanced around most ordering transitions, spin pumping should generically result in the temperature (T)-dependence of α^p owing the enhancement of $g_{eff}^{\uparrow\downarrow}$.

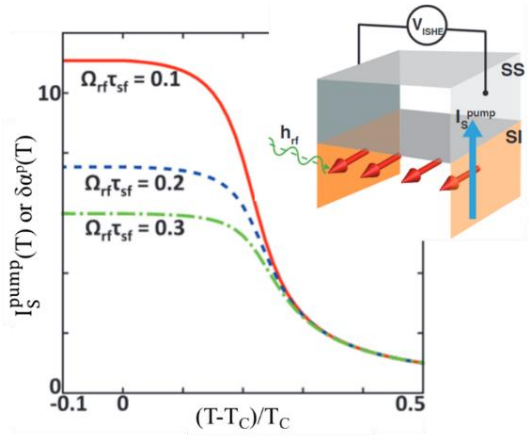

Figure 16 : Reduced temperature (T-T_C)/T_C dependence of the extra contribution to damping of the spin-injector due to spin fluctuations of the spin sink ($\delta\alpha^p$), calculated for a spin-injector (SI)/spin sink (SS) bilayer. Inset: Schematic illustration of a bilayer considered in the theoretical description. Adapted from Ref. [80].

In fact, the formalism was formulated for a ferromagnetic spin-sink [80]. It was shown that the spin pumping into a fluctuating ferromagnet near the Curie temperature (T_C) show an enhancement due to the fluctuation enhancement of the interface spin conductance, governed by $g_{eff}^{\uparrow\downarrow}$. Figure 16 shows the T-dependence of calculated the pumped spin current ($\boldsymbol{I}_S^{pump}$) and

the spin injection enhancement ($\delta\alpha^p$), which are intimately related through Eq. I-8. One can see that $\boldsymbol{I}_S^{pump}$ and $\delta\alpha^p$ are enhanced near the Curie temperature of the ferromagnetic spin sink layer for various values of the parameter $\Omega_{rf}l_{sf}$, where l_{sf} represents the spin-flip relaxation time. As indicated in Figure 16, the spin injection enhancement is larger for smaller values of $\Omega_{rf}l_{sf}$, meaning that the enhancement is more visible in a material with a larger spin-orbit coupling.

I.2.1.2 Experimental state of the art and open questions

Following the theoretical description of spin pumping near thermal equilibrium, some experimental works found that enhanced spin pumping can be achieved by using a fluctuating antiferromagnetic spin sink close to its Néel temperature (T_N) [81–83]. These studies demonstrated that the spin current injection by spin pumping has an enhancement close to the magnetic ordering transition of the spin sink. The spin absorption within the spin sink depends on the spin-dependent properties of the material. Pioneering experimental results on this subject were obtained by the antiferromagnetic spintronic team at SPINTEC [81](see Figure 17(a). Note that in the NiFe/Cu/IrMn structures, the spin injector (NiFe) and the spin sink (IrMn) are separated by an efficient spin conductor (Cu). The Cu spacer also eliminate direct exchange interactions and focus on the effects due to the spin current injection towards the spin sink. The aforementioned model was in fact developed for SS/SI bilayers, however, it can be applied for SS/Cu/SI structures because the spin absorption for a thin Cu layer is negligible and the contribution of the SS/Cu is cancelled out in the α^p calculation [81].

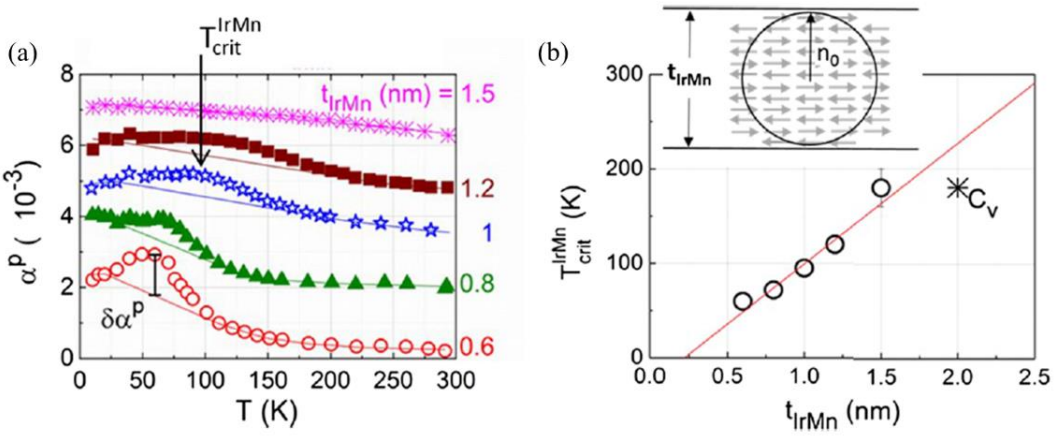

Figure 17 : (a) IrMn spin pumping contribution to NiFe damping (α_p) as function of temperature measured for a range of IrMn layer thicknesses, t_{IrMn}. $\delta\alpha^p$ represents the enhanced spin pumping occurring during the IrMn magnetic phase transition. (b) Dependence of the critical temperature for the IrMn phase transition (T_{IrMn}) on t_{IrMn}. The line is a fit that returns the phenomenological spin-spin correlation length (n_0) and will be further discussed in § I.2.2.1. Adapted from Refs. [26,81].

It is noteworthy that other experimental techniques (such as susceptibility, neutron diffraction, calorimetry) are usually volume sensitive, while the method based on spin pumping is surface sensitive. Besides that, these works open the possibility for novel investigations in other magnetic ordering. For instance, the dependence of the IrMn critical temperature on the thickness of this layer was experimentally determined by spotting the spin pumping peak, as shown in Figure 17(b) [26,81]. This information provided access to a fundamental parameter, the characteristic length for spin-spin interactions (the spin-spin correlation length, n_0), which will be further discussed in § I.2.2.

As written in Ref. [3]: although the initial description of spin pumping near thermal equilibrium was formulated for a ferromagnetic (F) spin sink [80], the experimental application of the method proved to be more useful for antiferromagnetic (AF) spin sinks [26,81–83], due to the

absence until then of a benchtop technique to access paramagnetic(P)-to-AF transitions in thin films, as for example pointed out early in Ref. [84]. While a paramagnetic-ferromagnetic phase transition can be recorded from simple magnetometry experiments, by measuring the *T*-dependence of magnetization, the magnetic phase transition of an antiferromagnet is not accessible in this way. Alternative techniques using local probes such as neutron [85] are also unsuitable for films of AF a few nanometers thick, since their signal is limited by the small volume. The first experimental demonstrations of spin pumping as a spin fluctuation probe were presented for the case of an uncoupled IrMn AF metal in a fully metallic stack [81] and for the case of coupled and uncoupled (through a Cu spacer) CoO and NiO AF insulators [82,83]. Published studies can be split into three cases: [26] first, in F/non-magnet/AF metallic trilayers, spin transport is purely electronic through the non-magnetic metal, i.e., spins are carried by conduction electrons; second, in exchange-biased F/AF–insulator bilayers, transport is purely magnonic, i.e., due to excitation of localized-magnetic-moments; and third, in exchange-biased F/AF metallic bilayers, both electronic and magnonic transport regimes may coexist since transport by conduction electrons is permitted while magnons produced simultaneously by the oscillating ferromagnet feed directly into the antiferromagnet due to exchange bias interactions.Whether the nature of the probe, i.e., the magnonic vs. electronic nature of the spin current injected and absorbed in the spin-sink, influences the efficiency of damping enhancement near the magnetic phase transition is still a subject of debate. The initial formalism of spin pumping near a phase transition was recently theoretically extended to the case of normal to superconducting transitions [86] reinforcing interest in investigating various types of ordering. Those questions provided the foundations for the studies that will be discussed in the following of the sub-chapter.

I.2.2 Electronic nature of the spin current probe from NiFe/Cu/IrMn and NiFe/IrMn multilayers [2]

This section is adapted from Refs. [2] and [3] where the main findings were published. It should be noted here that the results in this section were also obtained in the frame of the PhDs and Post-doctoral projects detailed for § I.1.2.2. The purpose of inserting these findings here is to introduce the path to the subjects to which I contributed to a main extend, see e.g. data reported in § I.1.2.2; II.3; II.4; III.2; and IV. - Ref. [2]: O. Gladii, L. Frangou, G. Forestier, R. L. Seeger, S. Auffret, I. Joumard, M. Rubio-Roy, S. Gambarelli, and V. Baltz, Phys. Rev. B **98**, 094422 (2018); and Ref. [3]: O. Gladii, L. Frangou, G. Forestier, R. L. Seeger, S. Auffret, M. Rubio-Roy, R. Weil, A. Mougin, C. Gomez, W. Jahjah, J. P. Jay, D. Dekadjevi, D. Spenato, S. Gambarelli, and V. Baltz, Appl. Phys. Express **12**, 023001 (2019).

The full stacks used in this study were (from substrate to surface): NiFe(8)/IrMn(t_{IrMn})/Al(2)O_x (nm) (short name: NiFe/IrMn bilayer), NiFe(8)/Cu(3)/IrMn(t_{IrMn})/Al(2)O_x (nm) (short name: NiFe/Cu/IrMn trilayers), and NiFe(t_{NiFe})/IrMn(t_{IrMn})/Al(2)O_x (nm) stacks. t_{IrMn} is the thicknesses of the IrMn layer: t_{IrMn} = 0, 0.6, 0.8, 1 or 1.2 nm; t_{NiFe} is the thicknesses of the NiFe layer: t_{NiFe} = 8, 10, 12, 16, 25, or 50 nm. Similar to § I.1.2.2, the stacks were deposited at room temperature by dc-magnetron sputtering on Si/SiO_2(500) (nm) substrates. The NiFe layer was deposited from a $Ni_{81}Fe_{19}$ (at. %) permalloy target and the IrMn layer was deposited from an $Ir_{20}Mn_{80}$ (at. %) target. An Al cap was deposited to form a protective passivating AlO_x film.

Spin currents were generated by the spin-pumping mechanism (already introduced in § I.1.1.2). The technique involves inducing resonance (see Figure 5) in a ferromagnetic spin injector,

here a NiFe layer, which is adjacent to a spin sink, here an IrMn layer. We first compared two series of samples consisting of: NiFe/IrMn bilayer, where mostly magnonic transport is observed, as detailed below, and NiFe/Cu/IrMn trilayer, in which mostly electronic transport occurs. It should be noted that data for the NiFe/Cu/IrMn trilayer were adapted from our previous study [81] to make comparison possible. In the NiFe/IrMn bilayers, the IrMn spin-sink can be fed with magnons through direct magnetic coupling with the NiFe spin-injector (see Figure 18(a)). In contrast, in NiFe/Cu/IrMn trilayers, the Cu layer prevents direct magnetic interaction between the IrMn and NiFe layers. The potential magnonic contribution to the spin current in the IrMn layer is therefore the result of electron-magnon conversion mechanisms and is probably less efficient than direct feeding (see Figure 18(b)). We also investigated how spin transport near the ordering transition is influenced by exchange coupling using in the series of NiFe(t_{NiFe})/IrMn(t_{IrMn}) stacks. For this series, the amplitude of the exchange interactions, specifically of the rotational anisotropy contribution to exchange bias (as will be further discussed in § I.2.2.2), can be tuned by altering the thicknesses of the different layers.

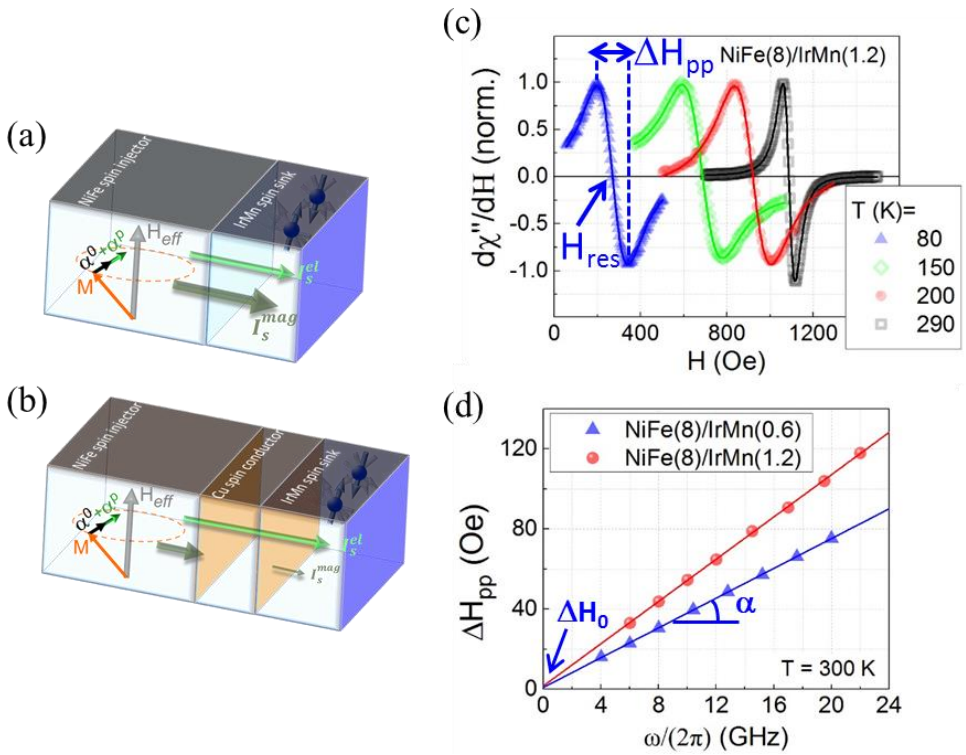

Figure 18 : (a,b) Spin-pumping experiments: out-of-equilibrium magnetization (M) dynamics of the NiFe ferromagnet pumps electronic (I_s^{el}) and magnonic spin currents (I_s^{mag}). Compared to a NiFe/IrMn bilayer (a), potential transmission of the magnonic spin current in a NiFe/Cu/IrMn trilayer (b) involves additional electron-magnon conversion at interfaces since the non-magnetic Cu only allows electronic transport. (c) Representative series of differential absorption spectra ($d\chi''/dH$ vs. H) measured at different temperatures (T). The data correspond to a series of measurements for a NiFe(8)/IrMn(1.2) bilayer (nm). The lines were fitted to the data using a Lorentzian derivative, as described in § I.1.2.1. The peak-to-peak linewidth (ΔH_{pp}) provides information on the amount of spin current transmitted and absorbed by the IrMn antiferromagnet (α^p). (d) Representative frequency (f)-dependence of ΔH_{pp} measured at 300K. The lines are fit using Eq. I-16 which return the damping parameter α and the inhomogeneous broadening ΔH_0. The data correspond to measurements for NiFe(8)/IrMn(0.6) and NiFe(8)/IrMn(1.2) bilayers (nm).

As part of the NiFe damping enhancement (α^p) is a reciprocal effect of spin injection, damping enhancement can be used to investigate spin injection. Spin-pumping experiments (Figure 18(a,b)) and the corresponding series of ferromagnetic resonance spectra (Figure 18(c)) were therefore recorded at temperatures (T) ranging between 5 and 300 K, using a continuous-wave electron paramagnetic resonance spectrometer operating at 9.6 GHz and fitted with a cavity, described in § I.1.2.3 (see Figure 15). When not specified, the varying bias field was applied

in the plane of the sample. For each temperature tested, the peak-to-peak linewidth, ΔH_{pp}, and the resonance field, H_{res}, were determined by fitting the NiFe differential resonance spectrum to a Lorentzian derivative (Figure 18(c)). The total Gilbert damping, α, was calculated from $\alpha(T)=\left[\Delta H_{pp}(T)-\Delta H_0(T)\right]\sqrt{3}|\gamma|/(2\omega)$ (see Eq. I-9 in § I.1.1.2), where ΔH_0 is the inhomogeneous broadening due to spatial variations in the magnetic properties [56], γ is the gyromagnetic ratio, and ω is the angular frequency. The frequency-independent inhomogeneous broadening was determined from frequency dependent spin-pumping experiments using a separate broadband coplanar waveguide at room temperature (described in § I.1.2.2, see Figure 18(d)). For all samples, ΔH_0 was one order of magnitude smaller than ΔH_{pp}.We took $\Delta H_0(T)$ = ΔH_0(300 K) since ΔH_0 has been shown to be a temperature-independent parameter [81].

I.2.2.1 Unravelling electronic and magnonic transport regimes

Figure 19(a,b) show α plotted as a function of temperature for series of NiFe/Cu/IrMn trilayers and NiFe/IrMn bilayers with various IrMn spin-sink thicknesses. The reference temperature(T)-dependence of the NiFe Gilbert damping, $\alpha^{ref}(T)$, i.e., in the absence of influence of the IrMn spin-sink, was directly deduced from the measurements performed on the samples with t_{IrMn} = 0. α^{ref} can be described as the sum of local intrinsic damping due to intraband and interband scattering [39,40] (already discussed in § I.1.1.1) and non-local damping mostly associated with the loss of angular momentum due to spin pumping by an ultra-thin $NiFeO_x$ layer [87]. This layer formed naturally at the SiO_2/NiFe interface during sputter deposition. The increase of α^{ref} at low temperature was associated with the onset of paramagnetic to antiferromagnetic transition of the $NiFeO_x$ layer [87]. Addition of the IrMn layer on top of the NiFe and NiFe/Cu stacks opened another relaxation channel, resulting in an additional contribution to damping, α^P. The temperature-dependence of the IrMn contribution to NiFe damping can be directly determined from: $\alpha^P(T)$ = $\alpha(T)$+ $\alpha^{ref}(T)$ (Figure 19(c,d)). With the NiFe/Cu/IrMn trilayers, the IrMn-thickness-dependence of α and α^P tended to increase at room temperature, with oscillation observed near saturation. This behavior can mostly be related to the finite electronic spin diffusion length (approximately 0.7 nm), as extensively discussed in an earlier work [84]. For the NiFe/IrMn bilayer, it is impossible to accurately extract the IrMn-thickness-dependence of α and α^P at room temperature since it superimposes on the tail of pronounced peaks in the temperature-dependent data.

From the data presented in Figure 19(a,b) we observe that all the temperature-dependences of α show a bump. This is because α^P reaches a maximum (Figure 19(c,d)), which itself is the direct consequence of the enhanced dynamical transverse spin susceptibility of IrMn when spins fluctuate near the paramagnetic-to-antiferromagnetic phase transition for the IrMn layer. More precisely, the non-local damping α^P is connected to a quality known as spin mixing conductance, as $\alpha^P=\left(g_{eff}^{\uparrow\downarrow}/S\right)|\gamma|\hbar/\left(4\pi M_{S,NiFe}t_{NiFe}\right)$ [49]. This quality has been presented in a linear-response formalism [80] describing spin pumping near thermal equilibrium (see Eq. I-20), and was found to be linked to the dynamical transverse spin susceptibility of the spin-sink, χ_k^R, through $g_{eff}^{\uparrow\downarrow}(T)\propto\sum_k\frac{1}{\Omega_{rf}}\mathrm{Im}\,\chi_k^R(\Omega_{rf},T)$, where k is the wave vector, and Ω_{rf} is the angular frequency of the ferromagnetic spin-injector at resonance. Consequently, the non-local damping is directly connected to the dynamical transverse spin susceptibility of the spin-sink which is enhanced around ordering transitions, i.e., near the critical temperatures (T_{crit}^{IrMn}). The results presented here show that spin pumping enhancement near the antiferromagnetic phase

transition functions regardless of whether the probe involves spin-wave-like or electronic-like transport. Peak broadening may indicate the formation of short range correlation in the antiferromagnet close to T_{crit}^{IrMn}. We note that some early debates suggested that the two-magnon scattering mechanism was at the origin of the bump in temperature-dependence observed for α vs. T. It is now acknowledged that the spin injection enhancement mechanism is at stake, and that two-magnon scattering can be ruled out. More specifically, it was shown for NiFe/CoO bilayers that the position of the bump in α as a function of temperature is frequency-independent and that it corroborates with the ordering transition temperature, which can be measured separately by X-ray magnetic linear dichroism [83]. Similarly, for NiFe/Cu/IrMn trilayers, the bump in α correlated with the ordering transition, measured separately by calorimetry [81,88].

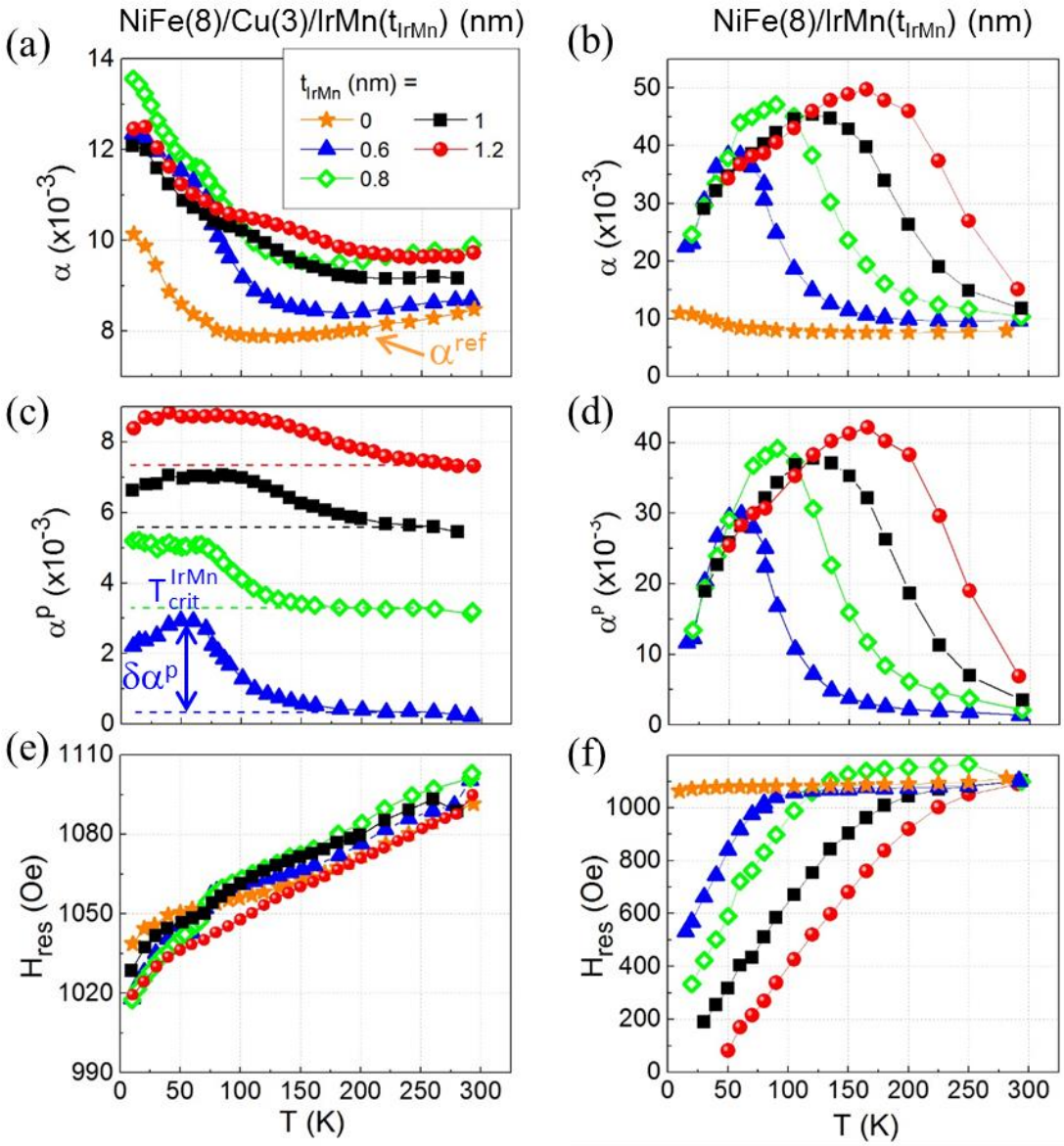

Figure 19 : Temperature (T)-dependence of (a,b) the NiFe layer's Gilbert damping (α), (c,d) the IrMn antiferromagnet contribution to NiFe damping ($\alpha^p=\alpha-\alpha^{ref}$), and (e,f) the NiFe resonance field (H_{res}) as a function of the IrMn antiferromagnet's thickness (t_{IrMn}) for two representative series of samples: NiFe(8)/Cu(3)/IrMn(t_{IrMn}) trilayers and NiFe(8)/IrMn(t_{IrMn}) bilayers (nm). (a) and (c) are adapted from Ref. [81] to allow comparison, see also Figure 17 of the present manuscript. $\delta\alpha^p$ denotes the extra contribution to damping due to the magnetic phase transition of the IrMn antiferromagnet and T_{crit}^{IrMn} stands for the corresponding critical temperature. In (c), data were shifted vertically to facilitate reading, the native values are (0.2, 1.4, 0.75, and 1.25) x 10^{-3} for t_{IrMn} = 0.6, 0.8, 1, and 1.2 nm.

Initially, the amplitude of the enhancement appears to be consistently much smaller in the electronic case (through a Cu spacer) compared to the magnonic one (no Cu spacer) (Figure 19(a,b)). However, this first impression may be misleading. For example, if we consider t_{IrMn} = 0.6 nm, we have $[\alpha^p(300K);\alpha^p(T_{crit}^{IrMn})] \cong [0.2\text{x}10^{-3}; 2.9\text{x}10^{-3}]$ for the NiFe/Cu/IrMn trilayer and $\cong [2\text{x}10^{-3}; 31\text{x}10^{-3}]$ for the NiFe/IrMn bilayer. Thus, although spin injection in the IrMn layer strongly depends on the transport regime at room temperature - being more efficient in the case of the bilayer ($2\text{x}10^{-3}$ vs. $0.2\text{x}10^{-3}$) - the spin injection enhancement due to spin fluctuations near the ordering temperature can be equally efficient for both types of transport regimes (here, the enhancement is about 15-fold since $\alpha^p(T_{crit}^{IrMn})/\alpha^p(300K) \cong 15$ in both cases). The relative spin injection enhancement, $\delta\alpha^p$, is specified in Figure 19(c). The plot of the IrMn-thickness-dependence of $\delta\alpha^p$ is shown in Figure 20(a), showing a clear difference for spin injection enhancement, as $\delta\alpha^p$ is independent of t_{IrMn} in the bilayers but not the trilayers, where it scales as $1/t_{IrMn}$ in line with the predictions proposed by Ohnuma *et al.* [80]. This result is probably a direct consequence of deeper penetration of the spin current carried by magnons in IrMn compared to that transported by conduction electrons (~0.7 nm, i.e., of the same order as the IrMn thickness in this case, thus explaining the decreased enhancement) [89]. This observation further supports the hypothesis that the transport regime is mostly magnonic for the bilayer and electronic for the trilayer. Note that although the penetration of the spin current in the magnonic regime has yet to be reported for IrMn, it seems reasonable to expect similar electronic vs. magnonic behavior to that reported for FeMn [90]: a magnonic spin current propagates over 9 nm whereas its electronic counterpart propagates over less than 2 nm.

The position of the spin pumping maximum can be deduced from Figure 19(a,b) and Figure 19(c,d), and the resulting IrMn-thickness-dependence of the ordering temperature is plotted in Figure 20(b). Data for NiFe/Cu/IrMn trilayers were adapted from our previous study [81], where the position of the spin pumping maximum was initially determined by subtraction of a baseline following the natural trend of the signal. This is equivalent to considering α vs. T Figure 19((a)) when determining the maximum and accounting for any slight dispersion in the values of the reference α^{ref}, e.g. due to the possible differences in growth reproducibility between samples. However, although reading of the spin pumping maximum may appear clear from α vs. T (Figure 19(a)), some samples do not show a clear peak in α^p vs. T (Figure 19(c)), i.e., after subtraction of the same α^{ref} from α for all samples. To further clarify this point, data determined from α^p vs. T (Figure 19(c)), and considering a constant baseline are also provided in Figure 20(b). Satisfactory agreement was obtained for all but the thickest sample with the smallest signal amplitude. It should be remembered that the thickness-dependence of the ordering temperature is well described by theoretical models [91,92]. The phenomenological model presented in Zhang and Willis [92] is suitable for use in the thin-layer regime, i.e., when the layer is thinner than the spin-spin correlation length. Here, curve fits using:

$$T_{crit}^{IrMn}(t_{IrMn}) = T_N^{IrMn}(bulk)\frac{(t_{IrMn}-d)}{2n_0} \qquad \text{Eq. I-21}$$

returns a phenomenological spin-spin correlation length of n_0 = 2.7 nm and an interatomic distance of d = 0.22 nm for the NiFe/Cu/IrMn trilayer [81]; and of n_0 = 1.9 nm and d = 0.29 nm for the NiFe/IrMn bilayer. To achieve these fits, we took $T_{N,bulk}$ = 700 K [85]. X-ray diffraction measurements performed on similar but thicker (9 nm) samples revealed a (111) growth direction and a related interatomic distance, d, of about 0.22 nm, similar to that measured for bulk IrMn [85]. The level of discrepancy observed on n_0 between the trilayer and

the bilayer may be explained by the fact that IrMn in these samples was grown on different 'buffer' layers (IrMn was grown on a Cu layer in the case of the trilayer whereas it was grown on NiFe in the bilayer). Improvement of the phenomenological spin-spin correlation length (i.e., steeper slope) suggests better growth quality for the bilayers. The small IrMn thicknesses were not compatible with x-ray diffraction experiments to further support this point. However, we note that exchange coupling between the IrMn and NiFe layers cannot be the reason for the improvement in the critical temperature of IrMn with the NiFe/IrMn bilayers compared to the NiFe/Cu/IrMn trilayers. Indeed, an interfacial mechanism of this type would result in a greater enhancement of T_{crit}^{IrMn} for thin layers than for thick ones, which contradicts the results presented in Figure 20(b). Finally, for t_{IrMn} = 0.6 nm, the position of the peak can be seen to be the same for the NiFe/IrMn bilayer and the NiFe/Cu/IrMn trilayer, meaning that this position is not altered by exchange coupling. This observation clearly agrees with the hypothesis that the peak can be used as an indicator of the ordering transition temperature - which is specific to the IrMn antiferromagnet - unlike the exchange bias blocking temperature - which is linked to the interaction between the properties of both the NiFe and the IrMn layers (see § I.2.2.2 for discussion).

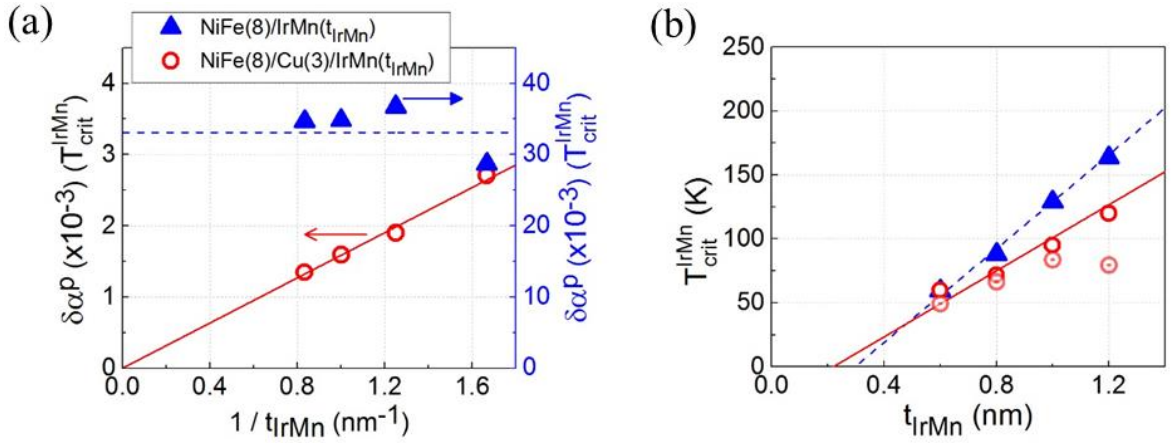

Figure 20 : IrMn thickness (t_{IrMn})-dependence of (a) the contribution to damping due to the magnetic phase transition of the IrMn antiferromagnet ($\delta\alpha^p$), and (b) the corresponding critical temperature (T_{crit}^{IrMn}) for NiFe(8)/IrMn(t_{IrMn}) bilayers (nm) and NiFe(8)/Cu(3)/IrMn(t_{IrMn}) trilayers (determined after subtraction of a baseline in a way that it follows the natural trend of the signal [81], open symbol, or considering a constant baseline, dotted signal). In (a), the dashed line corresponds to a constant fit and the straight line to a linear fit of the data constrained to pass through (0,0). In (b), line fitting was based on the equation presented in Ref. [92] in the thin-layer regime, also Eq. I-21 of the present manuscript.

We feel it is important to first briefly comment on the temperature-dependence of the resonance field, H_{res}. If we return to Figure 19(e,f), it emerges that for the uncoupled NiFe/Cu/IrMn trilayers the temperature-dependence of the resonance field of the samples containing an IrMn spin-sink is unchanged compared to the reference sample (with no spin-sink), whereas it is significantly altered for the exchange-coupled NiFe/IrMn bilayers. This behavior is known to result from rotational anisotropy [93], i.e., from the presence of uncompensated spins in the IrMn antiferromagnet. These uncompensated spins have a longer relaxation time than the characteristic time for ferromagnetic resonance in the NiFe layer (~10 ns). Due to interfacial coupling, these spins are dragged by the NiFe ferromagnet in a quasi-static experiment (~10 min) but stay still in a dynamic experiment, adding to the anisotropy of the NiFe layer and altering its resonance field. Since interfacial coupling is a temperature-dependent parameter, rotational anisotropy is also temperature-dependent as is the alteration of the resonant field. This situation will be discussed in more detail below. Although damping maxima are observed,

the relatively monotonous temperature-dependent behavior of H_{res} for the NiFe/Cu/IrMn samples is a good indication that the process does not involve paramagnetic relaxation [94].

I.2.2.2 Influence of interfacial exchange coupling

Since there is currently no clear experimental evidence of whether spin transport near the ordering transition of an antiferromagnet is influenced by exchange coupling to a ferromagnet, we further investigated series of NiFe(t_{NiFe})/IrMn(t_{IrMn}) stacks for which the amplitude of interfacial coupling between the NiFe and the IrMn layers, and in particular that of the rotational anisotropy contribution is tuned through changes to the thicknesses of the different layers. Figure 21(a-d) show the temperature-dependence of the NiFe layer's Gilbert damping and resonance field, for a range of NiFe ferromagnet thicknesses (t_{NiFe}) in two representative series of samples: NiFe(t_{NiFe})/IrMn(0.6) and NiFe(t_{NiFe})/IrMn(1.2) bilayers (nm). The results confirm that the resonant field is altered due to coupling. The influence of temperature on the resonant field can in fact be described using the modified Kittel formula [54,93]:

Eq. I-22

$$\omega = |\gamma| \sqrt{\left(H_{res}(T) + H_{E,st}(T) + H_{rot}(T)\right)\left(H_{res}(T) + H_{E,st}(T) + H_{rot}(T) + 4\pi M_S^{eff}\right)},$$

where $M_S^{eff}(T) = M_{S,NiFe}(T) - 2K_{S,NiFe}/\left(4\pi M_{S,NiFe}(T) t_{NiFe}\right)$ is the effective magnetization, $M_{S,NiFe}$ is the saturation magnetization (the temperature-dependence of which follows the Bloch equation: $M_{S,NiFe}(T) = M_{S,NiFe}(0)(1-\beta T^{3/2})$, K_S is the surface anisotropy, $H_{E,st}$ is the static hysteresis loop shift (static anisotropy contribution due to exchange bias), and H_{rot} is the rotational anisotropy (dynamic anisotropy contribution). The lines in Figure 21(c,d) clearly show how the values of H_{res} measured differ from the expected values in the absence of coupling. These lines correspond to a fit to the high-temperature data for the NiFe(8)/IrMn(0.6) bilayer (above 100 K, i.e., above the onset of coupling), using the Kittel equation and discarding the exchange bias terms. Data-fitting returned $M_{S,NiFe}(0)$ = 800 emu.cm^{-3}, β = 1 x 10^{-5} K$^{-3/2}$, and K_S =1 erg.cm^{-2}, which are in satisfactory agreement with the expected results for an uncoupled NiFe layer. To extract $H_{rot}(T)$ from $H_{res}(T)$, we recorded hysteresis loops separately at various temperatures (inset in Figure 22(b)) using a quasi-static vibrating sample magnetometer. The resulting temperature-dependence of the static hysteresis loop shift, $H_{E,st}$, and coercive field, $H_{C,st}$ are shown in Figure 22(a-d) for the NiFe(t_{NiFe})/IrMn(0.6) and NiFe(t_{NiFe})/IrMn(1.2) bilayer series. As expected, due to rotational anisotropy [93], $H_{E,st}$ starts to increase at a much lower temperature (25 and 75 K for t_{IrMn} = 0.6 and 1.2 nm, respectively) than that at which H_{res} decreases (100 and 250 K for t_{IrMn} = 0.6 and 1.2 nm, respectively, from Figure 21). The temperature-dependent increase in $H_{C,st}$ is generally thought to be the result of antiferromagnetic grains being dragged by the ferromagnet. These same grains stay still in a dynamic experiment, because they have a longer relaxation time than the characteristic time for ferromagnetic resonance, and consequently contribute to H_{rot}. For this reason, the temperature-dependent increase in $H_{C,st}$ usually mirrors the increase in $H_{E,st}$.

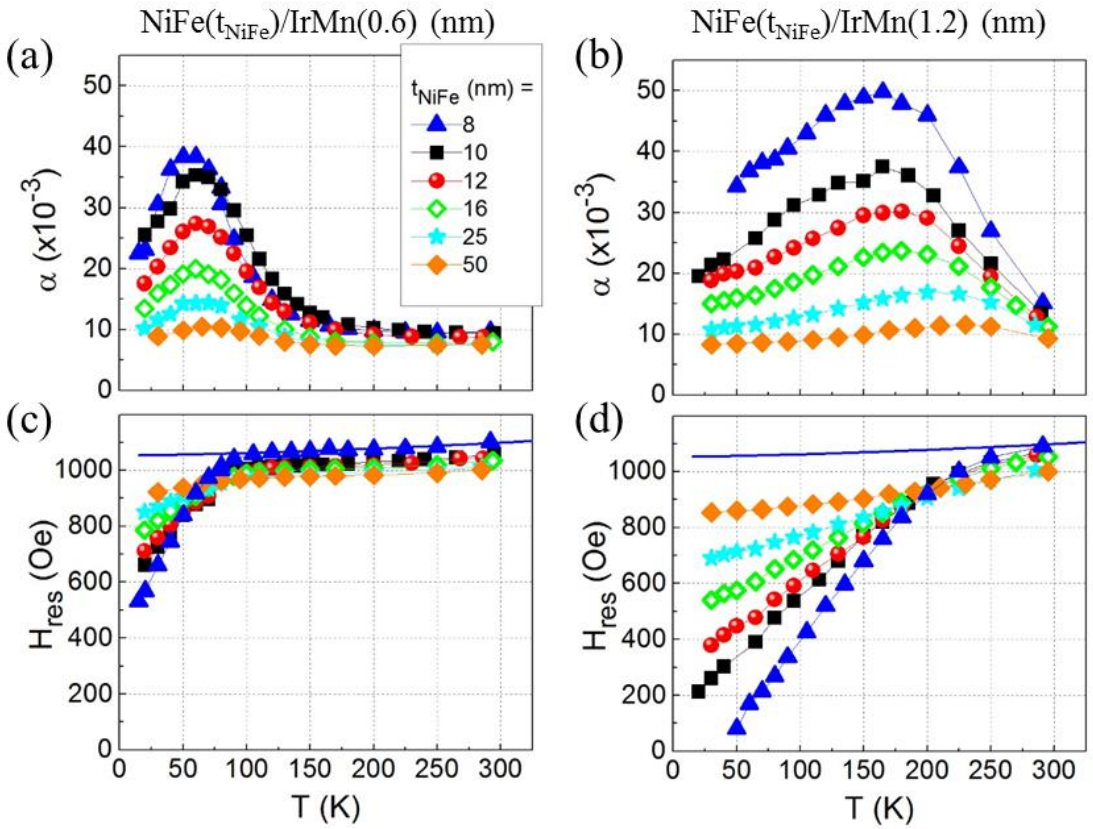

Figure 21 : *T*-dependence of (a,b) the NiFe layer's Gilbert damping (α), and (c,d) the NiFe resonance field (H_{res}), for a range of NiFe ferromagnet thicknesses (t_{NiFe}), as recorded for two representative series of samples: NiFe(t_{NiFe})/IrMn(0.6) and NiFe(t_{NiFe})/IrMn(1.2) bilayers (nm). The lines in (c,d) correspond to a fit to the high-temperature data for the NiFe(8)/IrMn(0.6) bilayer, using see Eq. I-22 (modified Kittel equation) and discarding the exchange bias terms.

However, this matching contradicts the present findings, suggesting that other factors also contribute to H_{rot}. Figure 23(a) shows the temperature-dependence of H_{rot} deduced from the modified Kittel equation (Eq. I-22). In general, H_{rot} increases when the NiFe thicknesses is reduced, confirming the interfacial nature of the rotational anisotropy contribution. The temperature-dependence of H_{rot} can in fact be described using the formula: $H_{rot}(T) = J_{int,dyn}(T)/(M_{S,NiFe}(T)t_{NiFe})$, where $J_{int,dyn}$ is the dynamic interfacial exchange constant per unit area. This parameter can be expressed as an effective volume anisotropy, $K_{IrMn,eff}$, as follows: $J_{int,dyn}(T) = K_{IrMn,eff}(T)t_{IrMn}$, with $K_{IrMn,eff}(T) = K^0_{IrMn,eff}(1-T/T_{rot})^{\lambda}$, in analogy to [95], where T_{rot} is the onset of rotational anisotropy. The temperature-dependence of H_{rot} can therefore be described as follows:

$$H_{rot}(T) = K^0_{IrMn,eff}\, t_{IrMn}\left(1-\frac{T}{T_{eff}}\right)^{\lambda} \Big/ \left(M_{S,\,NiFe}(T)t_{NiFe}\right). \qquad \text{Eq. I-23}$$

Results of data-fitting using Eq. I-23 are plotted in Figure 23(a). From this figure, we can conclude that T_{rot} ~ 100 and 300 K for t_{IrMn} = 0.6 and 1.2 nm, respectively, and that these values are independent of t_{NiFe}. $M_{S,NiFe}$ was also found to be weakly dependent on t_{NiFe}, and remains between 800 and 830 emu.cm^{-3}. The temperature-dependence of H_{rot} described above predicts that the plot of $H_{rot}(T)t_{IrMn}/t_{NiFe}$ vs. T/T_{rot} will be universal. Figure 23(b) validates this prediction. However, data for t_{NiFe} = 50 nm depart from the universal behavior, probably as a consequence of the small value of H_{rot} leading to larger errors in its determination. Overall, by averaging over the samples with variable NiFe thicknesses and discarding the values for t_{NiFe} =

50 nm, data-fitting for $H_{rot}(T)$ returned $\langle\lambda\rangle$ = 1.4 and 1.6; and $\langle K^0_{IrMn,eff}\rangle$ = (5.8 and 5.9) x 10^3 erg.cm^{-3}, corresponding to $\langle J^0_{int,dyn}\rangle$ = (3.5 and 7.1) x 10^{-4} erg.cm^{-2} for the series with t_{IrMn} = 0.6 and 1.2 nm, respectively. Figure 24(a) further shows that the notion of rotational anisotropy can also describe the findings for another measurement configuration, when the dc bias field is applied out of the sample plane, compared to the in-plane configuration previously studied. Data fitting for the out-of-plane configuration (Figure 24(a)) returned $\langle J^0_{int,dyn}\rangle$ = (3.6 and 7.8) x 10^{-4} erg.cm^{-2} for the NiFe(8)/IrMn(0.6) and NiFe(8)/IrMn(1.2) bilayers (nm), respectively. These values are in satisfactory agreement with those extracted from in-plane measurements. In Figure 24(b), we plotted the temperature-dependence of the peak-to-peak linewidth (ΔH_{pp}), which is related to the spin injection efficiency. These data superpose for the in-plane and out-of-plane configurations, a fact that is ascribed to the expected isotropic nature of the dynamic susceptibility for polycrystalline films. We also note that, as mentioned earlier, some early debates suggested that the two-magnon scattering mechanism caused the bump in temperature-dependence observed for ΔH_{pp} vs. T. However, several experiments now demonstrate that the spin injection enhancement mechanism causes this phenomenon [81–83,88]. The fact that ΔH_{pp} vs. T superpose for the in-plane and out-of-plane configurations further rules out an influence of two-magnon scattering.

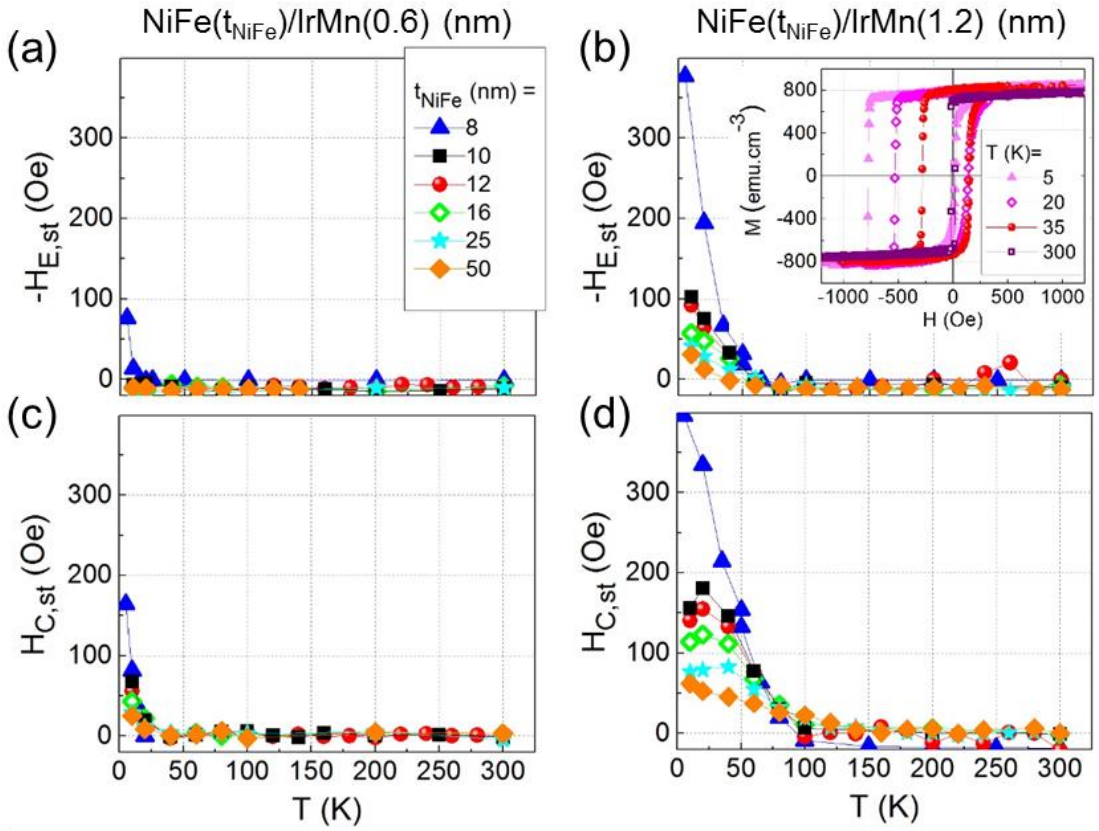

Figure 22 : T-dependence of (a,b) the exchange bias coupling field ($H_{E,st}$), and (c,d) the coercive field ($H_{C,st}$) when the NiFe ferromagnet thickness (t_{NiFe}) is varied for two representative series of samples: NiFe(t_{NiFe})/IrMn(0.6) and NiFe(t_{NiFe})/IrMn(1.2) bilayers (nm). The inset in (b) shows representative hysteresis loops at various temperatures with the example of the NiFe(8)/IrMn(1.2) bilayer.

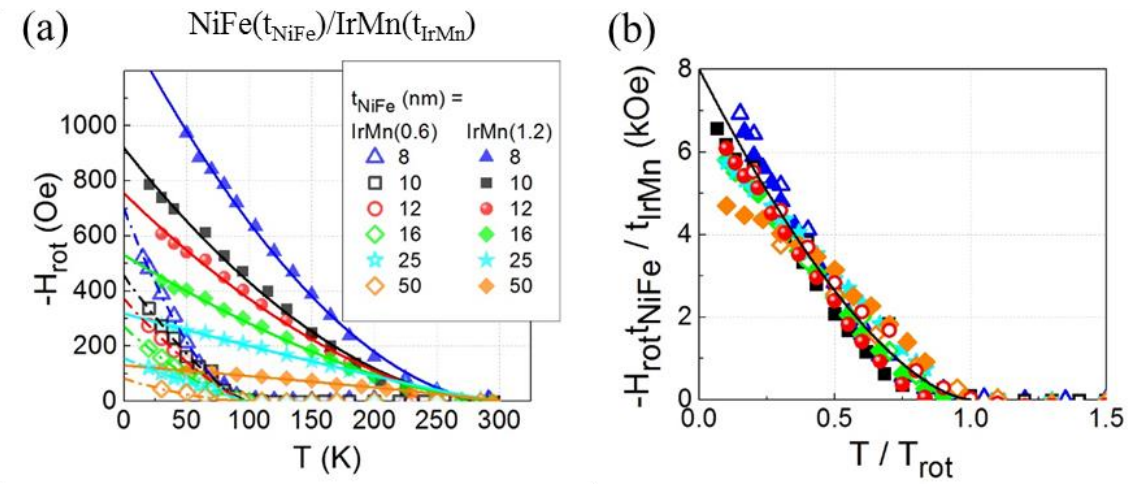

Figure 23 : *T*-dependence of (a) the rotational anisotropy (H_{rot}) calculated from the data in Figure 21 and Figure 22, for a range of NiFe ferromagnet thicknesses (t_{NiFe}), as recorded for two representative series of samples: NiFe(t_{NiFe})/IrMn(0.6) and NiFe(t_{NiFe})/IrMn(1.2) bilayers (nm). Lines in (a) are fitted to data using Eq. I-23. The corresponding universal behavior of $H_{rot}t_{NiFe}/t_{IrMn}$ with T/T_{rot} is plotted in (b). The line in (b) is a visual guide.

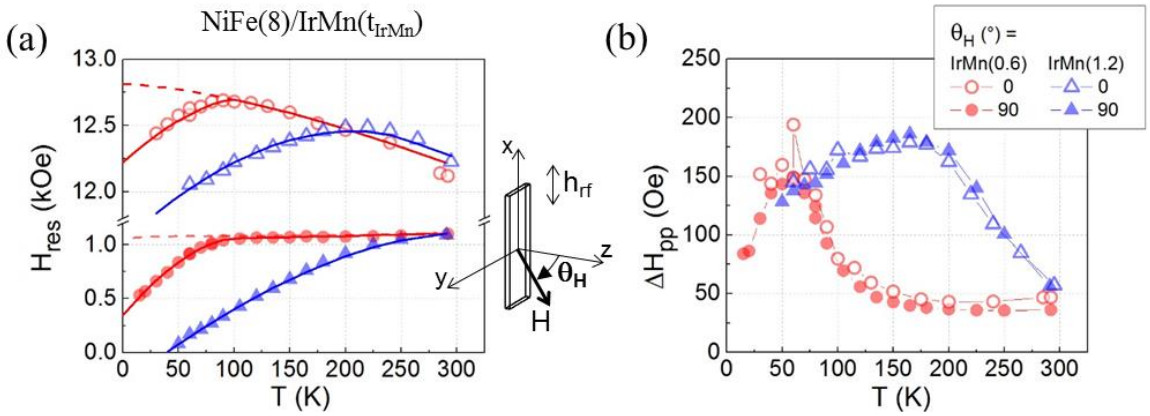

Figure 24 : *T*-dependence of (a) the NiFe layer's resonance field (H_{res}), and (b) the peak-to-peak linewidth of the NiFe absorption spectrum (ΔH_{pp}), for a bias field applied in- and out-of- the plane of the sample, as recorded for two representative samples: NiFe(8)/IrMn(0.6) and NiFe(8)/IrMn(1.2) bilayers (nm). The straight lines in (a) correspond to a fit to the data, using the modified Kittel equation and including the exchange bias terms (Eq. I-22) for the low-temperature data. For the sake of comparison, the dashed lines in (a) correspond to a fit for the NiFe(8)/IrMn(0.6) bilayer, discarding the exchange bias terms.

The impact of spin fluctuations on the efficiency of spin pumping in the IrMn antiferromagnet and whether it is influenced by coupling with the NiFe layer can now be discussed by extracting the maximum amplitude of spin pumping, $\alpha^p(T_{crit}^{IrMn})$, for all the NiFe and IrMn thicknesses (see Figure 21(a,b)). The plot of $\alpha^p(T_{crit}^{IrMn})$ vs. t_{NiFe} for the various IrMn thicknesses is given in Figure 25(a). To facilitate comparison, Figure 25(a) also shows the NiFe-thickness-dependence of spin pumping at room temperature, α^p(300 K), for t_{IrMn} = 0.6 nm. We note that the NiFe-thickness-dependence of α^p(300 K) cannot be accurately extracted for t_{IrMn} > 0.6 nm since it overlaps with the pronounced peaks in the tail of the temperature-dependence. The initial increase of α^p(300 K) observed in Figure 25(a) when the thickness of the NiFe layer is qualitatively reduced agrees with the expected ferromagnetic-thickness-dependence of spin pumping, which in this case should scale as $1/t_{NiFe}$ for Gilbert-like damping - $\alpha^p = \left(g_{eff}^{\uparrow\downarrow}/S\right)|\gamma|\hbar/\left(4\pi M_{S,NiFe}t_{NiFe}\right)$ [49]. However, fitting the data actually returns a $(1/t_{NiFe})^{\gamma}$ dependence, with γ =1.6. This level of deviation from a pure $1/t_{NiFe}$ dependence observed at room temperature can be explained by additional relaxation processes, such as two-magnon scattering, related to the interface roughness [96]. Most importantly, $\alpha^p(T_{crit}^{IrMn})$ qualitatively

shows a similar NiFe-thickness-dependence to α^p(300 K), meaning that $\alpha^p(T_{crit}^{IrMn})$ simply reproduces the room-temperature behavior. From this observation we can conclude that spin fluctuations act as a spin injection amplifier - as a consequence of the amplification of $g_{eff}^{\uparrow\downarrow}$ - and that the amplification factor is independent of the NiFe thickness and thus independent of interfacial coupling. In further support of this conclusion, we note that while the contribution of rotational anisotropy to exchange coupling scales linearly with the thickness of the IrMn layer (see discussion above), Figure 25(a) shows that $\alpha^p(T_{crit}^{IrMn})$ is virtually independent of t_{IrMn}.

In adition, we would like to comment on the NiFe thickness-dependence of T_{crit}^{IrMn} (Figure 25(b)). As expected from finite size scaling, T_{crit}^{IrMn} scales linearly with the IrMn thickness, for all NiFe thicknesses, i.e., whatever the amplitude of interfacial coupling. We note however that the slope of T_{crit}^{IrMn} vs. t_{IrMn} increases with thicker NiFe 'buffer' layers, suggesting a reduction in the phenomenological spin-spin correlation length, n_0, since we recall Eq. I-21 [92]. The plot of n_0 vs. t_{IrMn} is shown in the inset in Figure 25(b). We can once again eliminate exchange coupling between the IrMn antiferromagnet and the NiFe ferromagnet as being the reason for the improvement, because such an interfacial mechanism would result in a more extensive enhancement of T_{crit}^{IrMn} for thin compared to thick IrMn layers, which would contradict our experimental findings. Rather, as in the case of NiFe/IrMn bilayers vs. NiFe/Cu/IrMn trilayers, we infer that such a modification of n_0 relates to growth quality and more specifically to better quality growth for IrMn on thick NiFe layers. By reversing the order of the growth of the IrMn and NiFe stacks with t_{IrMn} = 1.2 nm and t_{NiFe} = 25 and 50 nm, we were able to confirm that T_{crit}^{IrMn} can recover the same value as that recorded for growth on thinner NiFe layers.

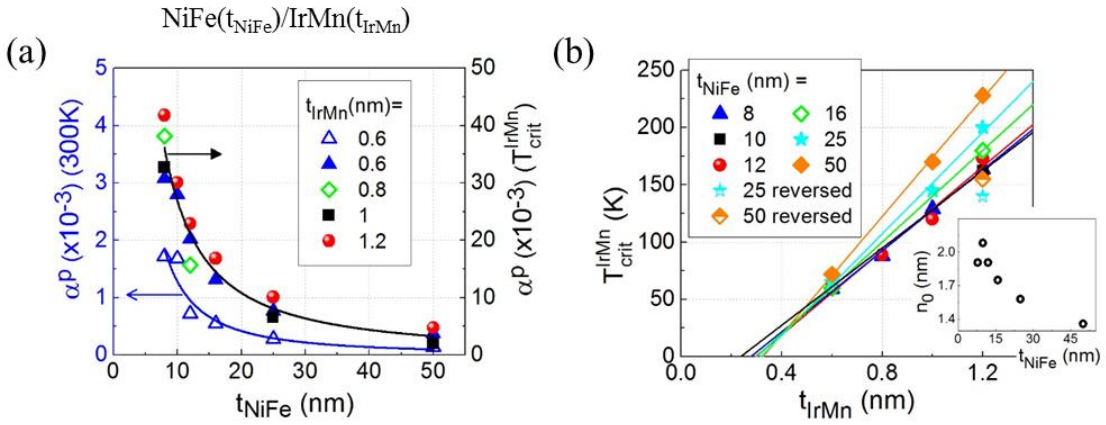

Figure 25 : (a) NiFe thickness (t_{NiFe})-dependence of (a) the IrMn antiferromagnet contribution to NiFe damping (α^p) measured at for NiFe(t_{NiFe})/IrMn(t_{IrMn}) bilayers with t_{IrMn} = 0.6, 0.8, 1 and 1.2 nm, and at T = 300 K when relevant, i.e., for t_{IrMn} = 0.6 nm. The lines are visual guides. (b) Corresponding NiFe thickness-dependence of T_{crit}^{IrMn}. Data for inverted IrMn(1.2)/NiFe(t_{NiFe}) bilayers with t_{NiFe} = 25 and 50 nm are plotted for comparison. Line fitting was based on the equation presented in Ref. [92] in the thin-layer regime (Eq. I-21), and returned a phenomenological spin-spin correlation length, n_0. Inset: n_0 vs. t_{IrMn}.

Summary

In summary, the above-mentioned results present systematic experimental demonstrations of the magnonic vs. electronic nature of the spin current in metallic antiferromagnets, and shows how it influences the efficiency of spin injection enhancement near the magnetic phase transition. It also provides information on whether this enhancement relates to the amplitude of interfacial exchange interactions. Spin currents were generated using the spin-pumping

mechanism and the systems investigated consisted of uncoupled NiFe/Cu/IrMn trilayers and coupled NiFe/IrMn bilayers, served so as to tune the relative electronic and magnonic transport contributions. Additionally, variable NiFe and IrMn layer thicknesses were used to alter the amplitude of interfacial coupling. Through temperature-dependent ferromagnetic relaxation in thin NiFe films we characterize the efficiency of spin injection and how it was affected by spin fluctuations when scanning the ordering temperatures for the IrMn antiferromagnet. Our results showed that spin injection in IrMn at room temperature strongly depends on the transport regime, and that it is more efficient in the case of magnonic transport. However, we also demonstrated that enhanced spin injection due to spin fluctuations near the ordering temperature can be equally efficient for the two types of transport regimes. In addition, we also found a clear difference in the IrMn thickness dependence of such spin injection enhancement as a direct consequence of deeper penetration of the spin current carried by magnons compared to that transported by conduction electrons. Finally, we observed that spin injection amplification near the IrMn ordering temperature is not influenced by the amplitude of interfacial exchange coupling with the adjacent NiFe layer.

I.2.3 Nature of the ordering transition from Tb, IrMn, NiO and $BiFeO_3$ films [3]

In the previous section we studied whether the magnonic vs. electronic nature of the spin current influences the efficiency of enhanced spin injection near the magnetic phase transition of metallic antiferromagnets. In the following, we will show systematic experimental results exploring all kinds of ordering and electrical states in order to evaluate the generic character of enhanced spin pumping resulting from spin fluctuations.

This section is adapted from Ref. [3] where the main findings were published, please see also introduction to § I.2.2 for more information on the frame of this work.

The full stacks used in this study were (from substrate to surface): NiFe(8)/Cu(3)/Tb(3)/Al(5) (nm), Ta(3)/NiO(1.5)/NiFe(7)/Cu(3) (nm), NiFe(8)/$NiFeO_x$(1.5) (nm), and Ta(15)/$BiFeO_3$(3)/NiFe(8)/Ta(3) (nm) multilayers. The Tb based sample was deposited by molecular beam epitaxy at LPS in Orsay by Alexandra Mougin and Raphael Weil, all others were produced by magnetron sputtering either at SPINTEC by Stéphane Auffret ($NiFeO_x$ based stacks) or at OPTIMAG in Brest by David Spenato and collaborators (NiO and $BiFeO_3$ based stacks). Same as before, the NiFe layer was deposited from a $Ni_{81}Fe_{19}$ (at%) permalloy target and an Al cap was added when necessary to block oxidization by air, it formed a protective passivating AlO_x film. Uncapped NiFe formed a passivating 1.6 nm thick $NiFeO_x$ layer [87]. A 3 nm thick Cu layer was used in some samples to break the direct magnetic interaction between the spin-injector and the spin-sink. Six stacks consisting of similar multilayers without Tb, NiO, $NiFeO_x$, and $BiFeO_3$ spin-sinks, respectively, were also deposited. They were used as references to further isolate the spin-sink contribution to Gilbert damping. The spin-sink thicknesses were chosen to give a magnetic phase transition within the temperature range accessible in our setup.

Spin pumping experiments (already described in Figure 18(a,b)) and the corresponding ferromagnetic resonance spectra (Figure 18(c)) were recorded at temperatures (T) ranging between 5 and 300 K, using the continuous-wave electron paramagnetic resonance spectrometer described in § I.1.2.3. As discussed in §I.2.2, the total Gilbert damping (α) can

be determined by fitting the NiFe differential resonance spectrum to a Lorenzian derivative (see Figure 18(c)). For every system, the temperature-dependence of the NiFe Gilbert damping in the absence of influence of the spin-sink, $\alpha^{ref}(T)$, was deduced from measurements performed with the reference sample. The temperature-dependence of $\alpha^{p}(T)$ was calculated using interpolation functions, by subtracting $\alpha^{ref}(T)$ from the value of $\alpha(T)=\alpha^{ref}(T)+\alpha^{p}(T)$ (for more details see Figure 19).

We will first discuss the results obtained for a ferromagnetic spin-sink: a 3-nm-thick Tb layer [97] in a NiFe(8)/Cu(3)/Tb(3)/Al(5)O_x (nm) multilayer. Figure 26(a) shows an enhanced spin angular momentum relaxation rate (α^{p}) near 40 K (Left axis). The link between enhancement of α^{p} and spin fluctuations in Tb due to the paramagnetic to ferromagnetic phase transition undoubtedly correlates with the onset of saturation of the Tb layer's magnetization, as measured by magnetometry (Right axis and inset). The additional smooth temperature-dependence of the saturation magnetization is related to the NiFe(8) spin-injector. Data-fitting using the Bloch equation: $M_{S,NiFe}(T) = M_{S,NiFe}(0)(1-\beta T^{3/2})$ returned $M_{S,NiFe}(0) = 785$ emu.cm^{-3}, and $\beta = 1.7 \times 10^{-5}$ K$^{-3/2}$ (see line in Figure 26(a)). These results are in satisfactory agreement with expectations. Although the initial description of spin pumping near thermal equilibrium was formulated for a ferromagnetic spin-sink, it should be remembered that clear experimental demonstration was missing until now [80,98,99]. We also note that the reduction of the Curie temperature from 200 K for bulk Tb [100] down to 40 K for a 3-nm thick layer can be ascribed to known finite-size effects [91,92]; finite-size scaling of ordering temperatures will be further discussed below in this section. The values of α^{p} at room temperature (α^{p}_{300K}) and at the ordering transition temperature ($\alpha^{p}_{T=T_C}$) are listed in Table 1. Paramagnetic Tb(3) is known to be a poor spin-sink, which explains why the value of α^{p}_{300K} is practically equal to zero [101]. Values listed in Table 1 for a number of stacks will be compared and discussed below. However, first we feel it is important to briefly comment on the temperature-dependence of the resonance field, H_{res} (Figure 26(b)). By using the same procedure as the one described earlier (see Eq. I-22 in § I.2.2.1) and using the Kittel equation with anisotropy terms, we found (line in Figure 26(b)) $M_{S,NiFe}(0) = 800$ emu.cm^{-3}, $\beta = 1.3 \times 10^{-5}$ K$^{-3/2}$, and $K_S = 0.5$ erg.cm^{-2}, which are in satisfactory agreement with the values obtained from the Bloch fit in Figure 26(a). Interestingly, the shape of the low-temperature region is not satisfactorily described by the bare formula. Dipolar coupling between the NiFe and Tb layers through the Cu spacer could explain why the NiFe resonance field deviates from the usual Kittel equation. In fact, since the ferromagnetic Tb layer is not saturated around ~1 kOe (see inset in Figure 26(a)), it contains domains and consequently results in a stray field (H_{Tb}) with a non-zero in-plane projection which is sensed by the NiFe layer. This field is related to the magnetization of the Tb layer ($H_{Tb} = 4\pi M_{1kOe,Tb}$) and it contributes as an effective field to the Kittel equation. Its influence becomes more marked when $M_{1kOe,Tb}$ increases as the temperature decreases, resulting in the gradual reduction of H_{res} observed. The inset in Figure 26(b) demonstrates that $M_{1kOe,Tb}$, deduced from hysteresis loop measurements (inset in Figure 26(a)), and the deviation from H_{res} are proportional.

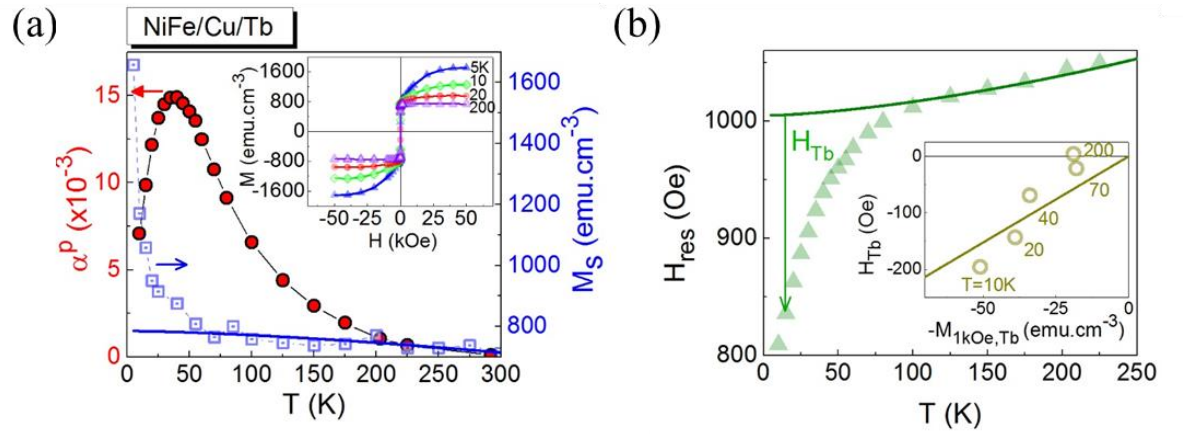

Figure 26 : (a) *T*-dependence of the extrinsic spin pumping contribution (α^p) to the NiFe layer's total Gilbert damping due to a Tb(3) metallic ferromagnetic spin-sink (Left) and temperature-dependence of the sample's saturation magnetization (M_S) (Right), for a NiFe/Cu/Tb trilayer. The line corresponds to a fit to the high-temperature data, considering only the NiFe contribution and based on a Bloch equation. Inset: corresponding typical in-plane hysteresis loops measured at several temperatures. (b) *T*-dependence of the NiFe layer resonance field (H_{res}). The line corresponds to a fit to the high-temperature data using the Kittel equation. Inset: relationship between the deviation from H_{res} (ascribed to the stray field, H_{Tb}, created by the unsaturated Tb layer) and the Tb layer's remanent magnetization ($M_{r,Tb}$). The line gives a linear fit and is constrained to pass through (0,0).

We next investigated insulating antiferromagnets, a 1.5-nm thick NiO, a 1.6-nm thick $NiFeO_x$ and a 3-nm thick $BiFeO_3$ layer (Figure 27(a)), in which spin current is carried by spin-waves. We found enhanced spin pumping near the paramagnetic-to-antiferromagnetic transition, at T = 85, 65, and 20 K, respectively. This result further underlines that spin current carried by spin-waves or by conduction electrons both efficiently reveal enhanced spin pumping due to spin fluctuations, in addition to experimentally supporting the universality of the phenomenon. It is also noteworthy from the results presented in Table 1 that, overall, the spin mixing conductance ratio stays within the same order of magnitude, regardless of the nature of the ordering transition. With regard to the position of the spin pumping maximum, it should be remembered that we purposely tuned the transition temperature to the temperature range accessible in our experimental setup by choosing appropriate spin-sink thicknesses. Indeed, the thickness-dependence of the ordering temperature is well described by theoretical models [91,92]. A typical example is plotted in Figure 27(b) for the Néel temperature of NiO, comparing data from the present study to data from the literature acquired with various experimental techniques [91,92,102–106]. Taking all data points into account, the fit using $\left(T_{N,bulk}-T_N\left(t_{NiO}\right)\right)/T_N\left(t_{NiO}\right)=\left(t_{NiO}/\xi_0\right)^{-\lambda_{eff}}$ [91,92] gave an extrapolated correlation length at T = 0 K, ξ_0 = 1.7 ± 0.1 nm (about 4 monolayers). For this fit, we took $T_{N,bulk}$ = 520 K [26] and the effective shift exponent for a three-dimensional Heisenberg antiferromagnet λ_{eff} = 3. This exponent corresponds to a critical exponent $1/\nu$ = 1.4, as predicted by theory [92]. It should be noted that data points were for non-identical stacks and recorded using different techniques. These differences may explain the level of discrepancy observed. Nevertheless, the overall thickness-dependent behavior was satisfactory. In addition, it is clear from Figure 27(b) that x-ray and calorimetry techniques are suitable for measuring T_N for thick layers, whereas spin pumping and spin Hall magnetoresistance have made it possible to explore more systematically the thin-layer regime (here sub-2 nm). Finally, if we return to the discussion in § I.2.2.2, we can see that the position of the peak is not altered by exchange bias coupling, agreeing with the idea that the peak is an indicator of the ordering transition temperature.

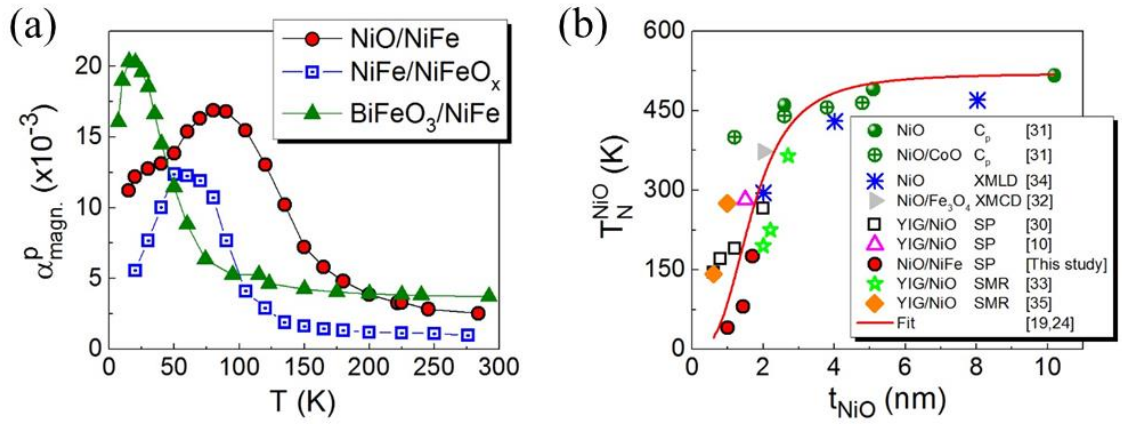

Figure 27 : (a) T-dependence of α^p due to NiO(1.5), $NiFeO_x$(1.6), and $BiFeO_3$(3) insulating antiferromagnetic spin-sinks. (b) Thickness-dependence of the Néel ordering temperature for NiO. C_p refers to calorimetry; XMCD and XMLD refer to x-ray magnetic circular and linear dichroism, respectively; SP refers to spin pumping; and SMR refers to spin-Hall magnetoresistance. Lines were fitted using the finite-size model. Note that references in (b) refer to articles cited in Ref. [3].

In order to complete the information in Table 1, we will briefly recapitulate the results discussed in §I.2.2. We compared two cases for the same metallic antiferromagnet without and with a Cu spacer. In the NiFe(8)/IrMn(t_{IrMn})/Al(2)O_x (nm) multilayer, the IrMn spin-sink is directly fed by spin-waves through direct magnetic coupling with the NiFe spin-injector, and by conduction electrons as well (see Figure 18(a)). In contrast, in the NiFe(8)/Cu(3)/IrMn(t_{IrMn})/Al(2)O_x (nm) multilayer, the spin current flows via conduction electrons through Cu and the Cu breaks the direct magnetic interaction between the IrMn and NiFe layers (see Figure 18(b)). The potential magnonic contribution to the spin current in the IrMn layer is therefore the result of electron-magnon conversion mechanisms and is probably less efficient than direct feeding. α^p reaches a maximum near the paramagnetic-to-antiferromagnetic phase transition of the IrMn layer (Figure 19(c,d)). A similar maximum is reached in both the no Cu spacer and Cu spacer cases. Since the relative amplitude of the maxima, $\alpha^p(T_{crit}^{IrMn})/\alpha^p(300\ K)$, is the same for both cases (e.g. showing a 15-fold increase for t_{IrMn}=0.6 nm, see Figure 19(c,d) and Table 1) we conclude that the phenomenon of spin pumping enhancement near a phase transition is independent of the Cu spacer, in agreement with Ref. [83]. The relative enhancement of spin mixing conductance due to spin fluctuations at the phase transition ($g_{eff}^{\uparrow\downarrow}(T_{crit}^{IrMn})/g_{eff}^{\uparrow\downarrow}(300K)$) is listed in Table 1 for several cases. This ratio can be approximated from $\alpha^p(T_{crit}^{IrMn})/\alpha^p(300\ K) = g_{eff}^{\uparrow\downarrow}(T_{crit}^{IrMn})/g_{eff}^{\uparrow\downarrow}(300K)$ [50]. We remember that α^p(300 K) is 10 times larger for the sample without Cu spacer (2 vs. 0.2, see Table 1). This effect is probably the result of direct exchange bias coupling, meaning that although the transport regime does not influence the relative enhancement due to spin fluctuations, it does influence the initial value at room temperature [26]. The data in Table 1 also show that larger α^p(300 K) are recorded with magnonic transport in several kinds of materials. This effect may be the consequence of deeper penetration of the spin current carried by magnons compared to that flowing via conduction electrons [90].

Stack (nm)	**Nature of the spin current probe**	**Nature of the ordering transition**	α_{300K}^{ref} x 10^{-3}	α_{300K}^{p} x 10^{-3}	$\alpha_{T=Tc}^{p}$ x 10^{-3}	$\frac{g_{T=Tc}^{\uparrow\downarrow}}{g_{300K}^{\uparrow\downarrow}}$
NiFe(8)/**Cu(3)/Tb(3)**	Electronic, through Cu	Para. to ferro.	10.1	~0	15	/
NiO(1.5)/NiFe(7)	Magnonic	Para. to antiferro.	7.2	2.5	16.8	6.7
$BiFeO_3$(3)/NiFe(8)	Magnonic	Para. to antiferro.	8.1	3.6	20.4	5.7
NiFe(8)/**IrMn(0.6)**	Electronic & magnonic	Para. to antiferro.	8.1	2	31	15.5
NiFe(8)/**Cu(3)/IrMn(0.6)**	Electronic, through Cu	Para. to antiferro.	8.1	0.2	2.9	14.5
NiFe(8)/**NiFeOx(1.6)**	Magnonic	Para. to antiferro.	8.1	1	12.3	12.3

Table 1 : NiFe Gilbert damping at room temperature for the reference sample, $\alpha_{300\,K}^{ref}$ (without the spin-sink), spin-sink contribution to Gilbert damping, at room temperature, $\alpha_{300\,K}^{p}$, and at the phase transition, $\alpha_{T=T_C}^{p}$, and corresponding spin mixing conductance ratio, $\frac{g_{T=T_C}^{\uparrow\downarrow}}{g_{300K}^{\uparrow\downarrow}}$. Data are listed for spin-sink layers of several magnetic and electronic kinds. Note: the samples and their respective references were deposited using three different machines (see gray separations).

Summary

In summary, the main contribution of this study is that it represents systematic experimental investigation supporting the generic character of the phenomenon of enhanced spin pumping resulting from spin fluctuations in a spin-sink layer. The phenomenon was found to apply with all kinds of ordering and electrical states, regardless of the electronic or magnonic nature of the spin current probe. These results will facilitate progress in characterization and engineering of new materials. For this manuscript, these findings set the general frame of the work carried out in the next Chapter.

Chapter II

Spin-charge conversion in ferro- and antiferromagnets

This chapter deals with spin-charge conversion in ferromagnets and antiferromagnets. Like in § I, the spin pumping method is used for spin injection.

In § II.1 I recall the conceptual framework of the inverse spin Hall effect for spin-charge conversion, discussing the different mechanism generating a Hall response. At the end of this paragraph the typical experimental procedure consisting of spin pumping and spin-charge conversion in spin injector/spin sink bilayers is described.

§ II.2 is devoted to results that have revealed a self-induced inverse spin Hall effect in FMR experiments. The experimental results were corroborated by first-principle calculations. The findings further indicates that self-induced conversion within the ferromagnet needs to be carefully considered when investigating SO-related effects in materials of interest for spintronics. These findings proved very useful for the design of samples aiming at demonstrating the link between the spin Hall effect and non-linear fluctuations in antiferromagnets (§ II.4).

§ II.3 is devoted to explore the characteristic lengths related to spin transport and spin-charge conversion in antiferromagnets comparing the GHz and THz frequency ranges. In § II.4, preliminary experimental results exploring the impact of ordering transition in the spin-charge conversion efficiency is discussed.

II.1 Introduction to the inverse spin Hall effect

A conductor develops a transverse voltage when it is placed in a magnetic field due to the Lorentz force acting on the electron charge current [13]. This transverse voltage is simply proportional to the magnetic field.

In ferromagnetic materials, there is an additional contribution related to the magnetization, known as the anomalous Hall effect (AHE) [14]. Essentially, in a ferromagnetic conductor the electrons moving acquire a spin-dependent transverse velocity. Since the magnetization in ferromagnets determines the direction for a net polarization of the charge currents, the spin-dependent transverse velocity results in a transverse voltage. Those charge related Hall effects will be further discussed in § III while studying charge transport specific to antiferromagnets.

In a non-magnetic material, the same spin dependent transverse velocity takes place, but in the absence of a net polarization it does not results in a measurable voltage. Instead, a spin accumulation with opposite spin polarity at opposite samples edges is created. Figure 28(a) illustrates such effect, the generation of a transverse spin current (I_S) by an electric charge current (I_C). This conversion from a charge current to spin current is called the spin Hall effect (SHE) [107–110]. Also, the inverse effect, namely the generation of a transverse electric charge current by a spin current exists (see Figure 28(b)). It is called the inverse spin Hall effect (ISHE). In fact charge and spin current are coupled through the spin-orbit interaction and they can be transformed into each other by making use of this coupling and scattering. One of the crucial parameters determining the conversion efficiency between charge and spin current is the spin Hall angle, θ_{SHE}, that is defined as the ratio between spin (charge) and charge (spin) current density.

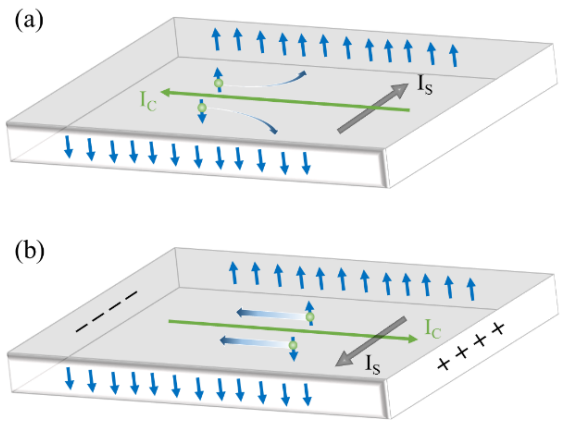

Figure 28 : Schematic illustration of: (a) the spin Hall effect (SHE) and (b) the inverse spin Hall effect (ISHE).

The following paragraphs will be devoted to a brief introduction of the physical mechanisms underlying the spin-charge conversion. It is noteworthy that those different mechanisms contribute to both the spin Hall and anomalous Hall conductivities [111,112]. The mechanisms contributing to Hall conductivity ascribed to topology of the spin structure (like chirality in kagome lattices) and topology of the band structure will be further discussed in § III.

II.1.1 Different types of mechanisms

So far, three mechanisms giving rise spin Hall effect have been recognized. First, I will discuss the intrinsic contribution that is solely determined by the electronic band structure and then I will detail, two extrinsic contributions, namely the side jump and skew scattering originated by impurity scattering. We will for example see in § II.2.2 that the competition between these two extrinsic contributions in permalloy allowed us to demonstrate non-monotonicity of the self-induced ISHE. Taking into account those three contributions, the spin Hall conductivity σ_{xy}^{z} can be expressed by:

$$\sigma_{xy}^{z} = \sigma_{xy}^{\text{int}} + \sigma_{xy}^{sk} + \sigma_{xy}^{sj} \qquad \text{Eq. II-1}$$

Where σ_{xy}^{int}, σ_{xy}^{sk}, and σ_{xy}^{sj} are the intrinsic, skew scattering and side jump contributionsis. σ_{xy}^{int} and σ_{xy}^{sj} are independent of the relaxation time τ, while σ_{xy}^{sk} is proportional to τ.

II.1.1.1 Intrinsic mechanism

The intrinsic spin Hall effect (and also linked to the intrinsic AHE) is related to the crystal structure of the material, where the spin dependent transverse velocities originate from the intrinsic spin-orbit coupling of the electronic band structure (Figure 29) [111,112]. In this case, the transverse spin current is generated in between scattering events. Such an intrinsic contribution to the spin Hall effects may be driven by the bulk band structure and has been expressed in terms of the Berry curvature. In this context, the intrinsic Hall conductivity σ_{xy}^{int} is calculated in terms of the Berry curvature of each occupied band $B_{nz}(k)$ by [113,114]:

$$\sigma_{xy}^{\text{int}} = -\frac{e^2}{2\pi\hbar}\sum_n \int_{BZ} d^2k n_F\left(\varepsilon_n(k)\right) B_{nz}(k), \qquad \text{Eq. II-2}$$

where n_F is the Fermi distribution function for the band n. In such approach, $B_n(k)$ is regarded as a "fictious" magnetic field in the k-space. The integration of the effect of $\boldsymbol{B}(k)$ into the generalized equations of motion in the presence of a electric field $\boldsymbol{E}$ results in:

$$\dot{\boldsymbol{r}} = \frac{1}{\hbar}\frac{\partial \boldsymbol{E}_n(\boldsymbol{k})}{\partial k} - \dot{\boldsymbol{k}} \times \boldsymbol{B}_n(\boldsymbol{k}) \qquad \text{Eq. II-3}$$

and,

$$\hbar\dot{\boldsymbol{k}} = -e\left[\boldsymbol{E} + \dot{\boldsymbol{x}} \times \boldsymbol{B}(\boldsymbol{k})\right]. \qquad \text{Eq. II-4}$$

The second term in Eq. II-3 and Eq. II-4 represents the transversal velocity acquired by the electrons due to the Berry phase. In simple words, the electrons moving in an electric field experience a magnetic field created by their own spin and it produces scattering perpendicularly to the electric field direction. The expected scaling of the intrinsic contribution with the resistivity is that the Hall conductivity ρ_{xy} is proportional to the square of the longitudinal resistivity ρ_{xx}.

Note that symmetry breaking at interfaces and surfaces inducing Rashba split band structure may also produce a transverse voltage, in addition to the effect originated from the bulk band structure. In certain metals such as Pt, the intrinsic effect was predicted to have a large influence on the effect [115].

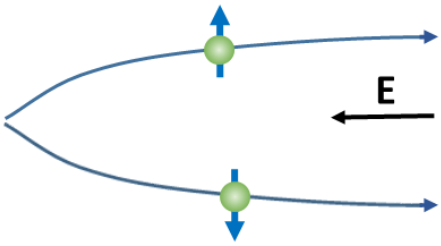

Figure 29 : Schematic illustration of the intrinsic mechanism contributing to the spin Hall and anomalous Hall conductivities. The 'topology' of the band structure break the time-reversal symmetry, resulting in a spin-dependent transverse velocity in real space. The mechanism involved has recently been reformulated in the language of the Berry phases as a geometric effect in reciprocal space.

II.1.1.2 Extrinsic mechanisms

The extrinsic contributions to the spin Hall effect (and also extrinsic AHE) occur due to spin-orbit interaction with impurities, defects and phonons, present in the materials. In the skew scattering the electrons are scattered asymmetrically via the spin-orbit coupling caused by an impurity (illustrated in Figure 30(a)), whereas in the side jump the electrons are deflected by the impurity (illustrated in Figure 30(b)). Thus in contrast to intrinsic mechanism the transverse spin current is generated during the scattering, instead of between scattering events.

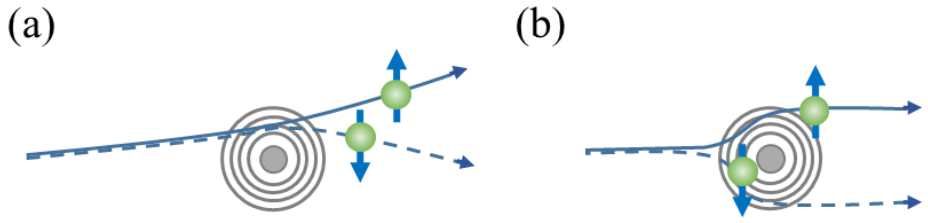

Figure 30 : Schematic illustration of the different extrinsic mechanism contributing to the spin Hall and anomalous Hall conductivities. (a) Skew scattering results in a spin dependent scattering angle. (b) Side jump results in a sideway displacement due to repeated scattering events. Although in two different ways, both mechanisms relate to spin-orbit interactions.

Skew scattering

The skew scattering mechanism is illustrated in Figure 30(a) where the trajectory of the electron after scattering is at an angle compared to the trajectory before scattering, meaning that the electron acquires tranverse momentum. Several theories have been suggested for the skew scattering (for further details see Ref. [111,116]). Essentially, the spin-orbit coupling results in an effective magnetic field gradient within the scattering plane [117,118]. As a result, depending on the spin orientation, this field gradient generates a net force toward or away from the scattering center. The sign of the effect depends on the sign of the electron-impurity interaction, in other words, whether the interaction is repulsive or attractive [116]. The skew scattering gives rise to spin Hall effects even for isotropic scattering in the presence of spin-orbit interactions, and there is no need for additional symmetry breaking (through crystal anisotropies or external magnetic fields). In the case of the skew scattering the Hall conductivity ρ_{xy} is proportional to the longitudinal resistivity ρ_{xx}.

Side jump

The side jump mechanism is illustrated in in Figure 30(b) where the electron trajectory after scattering is displaced by finite distance from the trajectory before scattering. This transverse displacement was estimated to be in the order of 10^{-11}-10^{-10} m in the case of 3*d* band electrons. The mechanism is based on spin dependent acceleration during scattering that results in an effective transverse displacement of the electron upon successive scattering [119]. Such mechanism results in a spin Hall angle proportional to the impurity concentration. Thus, in cases where the impurity concentrations is high enough this may dominate the spin Hall angle over other mechanisms [112]. The side jump scattering contribution gives a Hall conductivity ρ_{xy} which is proportional to the square of the longitudinal resistivity ρ_{xx}.

II.1.2 Typical experimental procedure

Spin pumping and spin-charge conversion experiments (Figure 31(a)) are typically conducted in spin injector/spin sink bilayers. The pumped spin current is converted into a transverse charge

current by means of the inverse spin Hall effect, resulting in a measurable voltage across the two contacts. I will now introduce how this dc voltage builds up as a result of the combination of the spin pumping and inverse spin Hall effects. As described in § I.1.1.2 the spin current is a priori ac (see Figure 5). However, in the experimental configuration we have used (Figure 31(a)) we measure the time average of the dc component. Additional information about the phase of the spin current can be inferred by using other specific experimental configuration where it is possible to measure the ac component of the spin current [120]. Those ac measurements are beyond the scope of this work. By rewriting Eq. I-8, the time average of the dc component of the spin current density at the interface (for $y = 0$) can be expressed as [121]:

$$j_S^0 = \frac{\omega}{2\pi}\int_0^{2\pi/\omega}\frac{\hbar}{4\pi}g_{eff}^{\uparrow\downarrow}\frac{1}{M_S^2}\left[\boldsymbol{M}\times\frac{d\boldsymbol{M}}{dt}\right]_z . \qquad \text{Eq. II-5}$$

Note that here $[\boldsymbol{M} \times d\boldsymbol{M}/dt]_Z$ is the z component of $\boldsymbol{M} \times d\boldsymbol{M}/dt$ and, thus, the pumped spin current is polarized along the precession of magnetization axis and flows along the y axis (see sketch in Figure 31(a)).

Due to relaxation, the spin current injected into the adjacent spin sink layer decays when flowing away from the interface. The depth dependence of the spin current density is given by:

$$j_S(y) = j_S^0\frac{\sinh\left[(d_N - y)/l_{sf,N}\right]}{\sinh\left(d_N/l_{sf,N}\right)}, \qquad \text{Eq. II-6}$$

here d_N and $l_{sf,N}$ are the thickness as spin diffusion length of the spin sink layer. The spin current density $j_S(y)$ can be obtained by using conservation of total angular momentum and boundary conditions. The spin current $j_S(y)$ is converted into a charge current $j_C(y)$ using the ISHE in the spin sink layer: $j_C(y) = \theta_{SHE}\,(2e/\hbar)\,j_S(y)$. Finally, it is possible to obtain the average charge current density as $\langle j_C\rangle = (1/d_N)\int_0^{d_N} j_C(y)dy$:

$$\langle j_c\rangle = \theta_{SHE}\left(\frac{2e}{\hbar}\right)\frac{l_{sf,N}}{d_N}\tanh\left(\frac{d_N}{2l_{sf,N}}\right)j_S^0 . \qquad \text{Eq. II-7}$$

In reality, j_C is measured through a voltage drop in an open circuit consisting of two layers in parallel [121]:

$$V_{ISHE} = \frac{w\theta_{ISHE}\,l_{sf,N}\tanh\left(d_N/2l_{sf,N}\right)}{d_N\sigma_N + d_F\sigma_F}\left(\frac{2e}{\hbar}\right)j_s^0 , \qquad \text{Eq. II-8}$$

here w denotes the sample width and σ_N and σ_F denote the layers' conductivities.

Figure 31(b) is an schematic representation of the experimental design in the resonant cavity. The measurement consists in recording the evolution of the transverse voltage as a function of a bias field. Typical V vs. H spectra as measured for a NiFe(8)/Pt(10) (nm) bilayer are shown in Figure 31(c) for two directions of the applied field: $\theta = 90°$ and $\theta = -90°$. The signal have superimposed symmetric (sym) and antisymmetric (antisym) contributions which can be disentangled by fitting data using the following equation:

$$V = V_{sym}\frac{\Delta Hpp^2}{(\Delta Hpp\sqrt{3}/2)^2 + (H - Hres)^2} - V_{antisym}\frac{(\Delta Hpp\sqrt{3}/2)(H - Hres)}{(\Delta Hpp\sqrt{3}/2)^2 + (H - Hres)^2}, \qquad \text{Eq. II-9}$$

where ΔH_{pp} is the the peak-to-peak linewidth, and H_{res} is the resonance field. V_{sym} can be produced by the ISHE combined with any contributions from the anisotropic magnetoresistance (AMR) effect - planar Hall effect (PHE) part - and the anomalous Nernst effect (ANE) [122,123]. $V_{antisym}$ generally results from the anomalous Hall [122,123]. In addition to these measurements, absorption spectra were measured. The physical origin of these contributions are attributed to the time varying change of resistance of the ferromagnet as the magnetization is changing which combines with radiofrequency currents induced by the incident electromagnetic wave giving rise to a dc voltage. This is also known as spin rectification effect (V_{SRE}) [124]. In addition to the spin rectification effect, V_{sym} also contains a contribution due to the inverse spin Hall effect (V_{ISHE}). The red and blue lines in Figure 31(c) are a fit according to Eq. II-9, from which we extracted V_{sym}, and $V_{antisym}$, for θ = 90°: - 6.45 µV and 0.61 µV and for θ = -90°: 7.04 µV and 0.66 µV, respectively. It is noteworthy that the angular dependences of V_{sym} and $V_{antisym}$ can be calculated and used to determine accurately the different contributions. It will be further discussed in this manuscript in particular to verify the inverse spin Hall effect contribution to the signal.

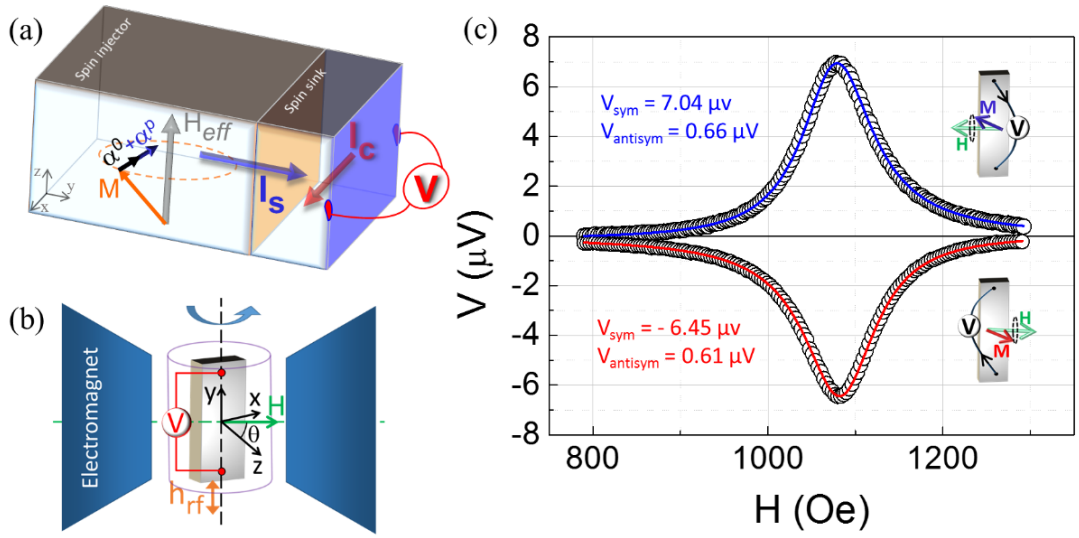

Figure 31 : (a) Schematic of spin pumping and inverse spin Hall effects in a bilayer. Compared to Figure 18(a), a voltmeter has been added to probe the voltage drop due to spin-charge conversion in the sample. (b) Schematic representation of the experiment design in the resonant cavity (see Figure 15 for more details on the experimental setup). (c) Representative data showing magnetic field dependence of the generated voltage for two directions, θ = 90° and θ = -90°. The data correspond to a series of measurements for a typical NiFe(8)/Pt(10) bilayer (nm). The open circles are the experimental data, while the lines indicate the fitting to Eq. II-9 which returns the symmetric (V_{sym}) and antisymmetric ($V_{antisym}$) contributions. Adapted from Ref. [4].

In fact, the experiments that will be discussed in the following paragraphs were conducted in the cavity resonator (described in § I.1.2.3) attaching wires to the sample edges to detect the voltage drop, see a picture of a Al-wire-bonded sample on Figure 15(b).

Besides the above mentioned experiments, we sought to perform optical spin pumping experiments. Measurements of this kind were conducted in the THz regimes by collaborators at FHI Berlin with the aim to compare findings for similar set of samples but different transport and frequency regimes. Note that the basic principle of this type of measurement will be described in § II.3.1.

II.2 Self-induced inverse spin Hall effect in ferromagnets [4]

II.2.1 Mechanisms for self-induced transverse voltage

This section is adapted from Ref. [4] where the main findings were published. Similarly to § I.2.2, the purpose of inserting these findings to which I contributed at the beginning of my PhD thesis is to introduce the path to the subjects to which I contributed to a main extend, see eg. data reported in § I.1.2.2; II.3; II.4; III.2; and IV. - Ref. [4]: O. Gladii, L. Frangou, A. Hallal, R. L. Seeger, P. Noël, G. Forestier, S. Auffret, M. Rubio-Roy, P. Warin, L. Vila, S. Wimmer, H. Ebert, S. Gambarelli, M. Chshiev, and V. Baltz, Phys. Rev. B **100**, 174409 (2019). Theoretical calculations were performed by A. Hallal and M. Chshiev from the theory team at SPINTEC on a code provided by S. Wimmer and H. Ebert from the University of Munich.

The generation of a spin current (discussed in § I in the frame of spin pumping) and its further conversion to a charge current have attracted considerable attention in the recent years [53]. The electronic transport regime considers spins carried by conduction electrons, in contrast to the magnonic transport regime, which refers to excitation of localized-magnetic-moments (in § I.2.2 we have discussed electronic and magnonic transport). Electronic spin current can be considered to occur through two distinct mechanisms: drift 'spin-polarized' current, when spins are carried by conduction electrons drifting due to the effect of an electric field; and diffusive 'pure' spin current, which is caused by diffusion of conduction electrons bearing majority spin and minority spin in opposite directions. In the case of diffusive spin current, diffusion results from non-equilibrium conditions creating a spin imbalance. This imbalance can be triggered by several mechanisms including distinct densities of states at the interface between materials of different types (e.g. ferromagnetic metals (F) and non-magnetic metals (NM)), and transfer of angular momentum between phonons, photons, and electrons [125]. In this context, an electrical current can be converted to a spin current and vice versa as a result of the spin-orbit interaction (SOI), which links the spin and the orbital angular momentum of an electron. As a result of SOI, a flow of charges (spin) causes transverse spin (charge) to accumulate (see Figure 28(a,b)) [126]. One of the related effects of this phenomenon, known as the inverse spin Hall effect (ISHE) [110,112], is commonly used to study SOI in NMs inserted into archetypal F/NM bilayers. In some of these studies, a spin current is pumped from the F spin-injector at resonance [48–50], and the ISHE ensures spin-charge conversion in the NM [121]. The contribution of the F to spin-charge conversion can be difficult to distinguish from that of the NM, and spin-charge conversion arising from the F is frequently neglected in experiments [127–134]. However, as we will further discuss below, in some cases spin-charge conversion in the F may prevail and need to be carefully considered. Some experimental studies indicated that self-induced charge current can be generated at room temperature (T), e. g. in (Ga,Mn)As [130], NiFe [129,134], Co [131] and Fe [131] ferromagnets at resonance. Self-induced charge current can be considered to occur through two distinct mechanisms: magnonic charge-pumping (MCP) [130,134–136], or ISHE. While both mechanisms are triggered by spin-orbit interactions in ferromagnets, they are fundamentally different. Refs. [130] and [134] report experimental investigation at room temperature of the reciprocal spin-orbit torques (SOT) phenomenon known as MCP [135], or inverse SOT (ISOT) [136]. This effect is dictated by lack of spatial inversion symmetry (bulk or structural). In contrast, Refs. [129] and [131]

propose a mechanism for the origin of this spin current based on spin-dependent scattering at the different interfaces. More specifically, when magnetic moments precess, the angular momentum of 3*d*-electrons is transferred to 4*s*-conduction electrons leading to a spin-polarized current in the F. Spins then flow in a diffuse manner due to non-uniform magnetization, which has been ascribed to asymmetric spin relaxation at the various interfaces. SOI in the F further ensures spin-charge conversion via the ISHE. Experimental data indicated a conversion efficiency of about 1% for NiFe [129].

In the following paragraphs, we will discuss experimental results showing a self-induced ISHE in single permalloy thin films when brought to resonance. Most importantly, our results demonstrated the bulk origin of the effect. Our experimental data revealed the self-induced transverse charge current to have a non-monotonous *T*-dependence. This finding was corroborated by the results of first-principle calculations describing the various contributions to the *T*-dependent spin Hall conductivity. These findings were further used to design specific samples in § II.4, in search for demonstrating the link between non-linear spin fluctuations and spin-charge conversion in antiferromagnets.

II.2.2 Demonstration through nonmonotonic temperature dependence in NiFe

The full stacks used in this study were (from substrate to surface): Cu(6)/NiFe(t_{NiFe}=8;12;16;24;32)/Cu(3)/Al(2)O_x (nm) multilayers. Stacks were deposited at room temperature by sputtering on Si/SiO_2(500) (nm) substrates at a pressure of 2.3 x 10^{-3} mbar under argon. The NiFe layer was deposited from a $Ni_{81}Fe_{19}$ (at. %) permalloy target. A 2-nm-thick Al cap was deposited to form a protective Al(2)O_x film after oxidation in air. The sample dimensions were: l = 2.46 mm and w = 0.46 mm. Both sides of the samples were connected to electrodes using Al-wire-bonding.

Spin pumping and spin-charge conversion experiments were described in Figure 31 for typical NiFe(8)/Pt(10) bilayer (nm). We will now discuss the experiments performed in a NiFe single layer (Figure 32(a)). An input power, P, of 40 mW was used, corresponding to an excitation magnetic field of h_{rf} ~ 0.5 Oe, along the y direction (see Figure 31(b)). The precise value of this field was determined for each data point by measuring the quality factor of the cavity Q and using the equation given for our MS5 resonator: $h_{rf}^2 = 4PQ/500$. The further normalization by h_{rf}^2 thus takes into account any variability of the *rf*-to-material coupling. A dc bias field (H) was simultaneously applied at an angle (θ) with respect to the sample normal (z) (see Figure 31(b)). For each angle tested, the amplitude of H was scanned across the resonant condition for the NiFe layer's magnetization (M). The corresponding electric potential difference (V) induced along the y direction as a result of spin pumping and spin-charge conversion was then recorded. The field-sweep-rate was 14 Oe.s^{-1}. A typical V vs H spectrum is shown in Figure 32(b). The symmetric (Sym) and the antisymmetric (Antisym) contributions were disentangled by fitting data using Eq. II-9. The linear-dependences of V_{sym} and $V_{antisym}$ with P (and thus with h_{rf}^2) were demonstrated (Figure 32(c)). In addition to these measurements, absorption spectra were measured (not shown). Lock-in detection was used to enhance the signal-to-noise ratio. Data were fitted using a Lorentzian derivative to determine ΔH_{pp} and H_{res} (see Figure 18(c)).

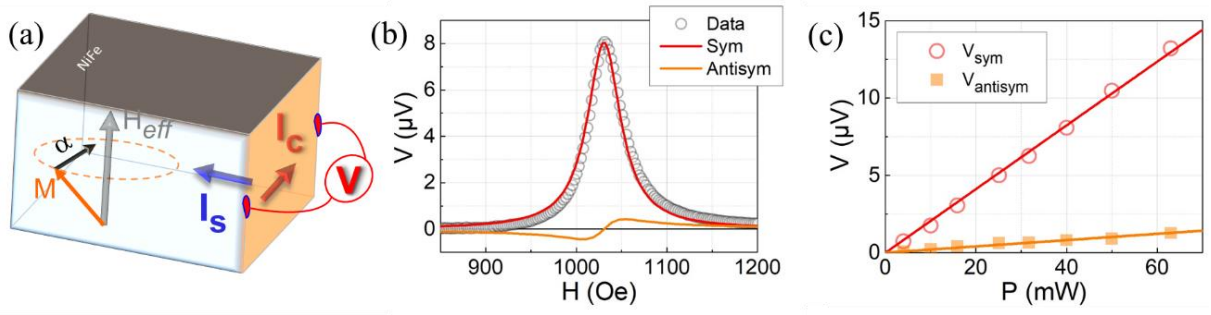

Figure 32 : (a) Schematic of spin pumping and spin-charge conversion experiments in a NiFe single layer. (b) Representative data showing H-dependence of V, as measured for a Si/SiO_2//Cu(6)/NiFe(8)/Cu(3)/Al(2)O_x (nm) stack at 95 K, when θ = + 90° and P = 40 mW. (c) Corresponding input power (P)-dependence of V_{sym} and $V_{antisym}$. The line in (b) was fitted to the data using Eq. II-9. The lines in (c) correspond to linear fits of the data constrained to pass through (0,0).

The experiments and data analysis described in above were conducted at T ranging between 50 and 300 K (Figure 33). The key novel result of our study is that, for NiFe, V_{sym} displays a non-monotonous T-dependence. From Figure 33(a), V_{sym} can be seen to flip sign upon reversal of H. This observation agrees with the time-reversal symmetry properties of the ISHE [110,112]. The PHE, which is odd in H, can be omitted. Figure 33(b) also show that the non-monotonous T-dependence of V is not related to $V_{antisym}$ nor to the possible PHE, as deduced from the AMR [137] evolution obtained separately for H = 1 kOe using standard 4-point measurements [138]. The non-monotonous T-dependence of V was also independent of ΔH_{pp} vs T, which was monotonous (Figure 33(c)) [39,40,81]. The total Gilbert damping was determined using the following equation: $\alpha(T)=\left[\Delta H_{pp}(T)-\Delta H_0(T)\right]\sqrt{3}|\gamma|/(2\omega)$. Inhomogeneous broadening (ΔH_0) due to spatial variations in the magnetic properties could reasonably be neglected when making estimations at 9.6 GHz, since T-invariant values of just a few Oe were found using similar samples and a broadband setup. The gyromagnetic ratio was determined by fitting data related to the f-dependence of H_{res} at 300 K, and a reasonable value of γ = 18.8 MHz.Oe^{-1} was obtained. In line with [139], a potential T-dependent change in the direction of anisotropy could also be ruled out from the behavior of H_{res} vs T (Figure 33(d)). Data were satisfactorily described using the usual Kittel formula [54], discarding the anisotropy terms (we have used the same procedure as the one described earlier, see Eq. I-22 in § I.2.2.1).

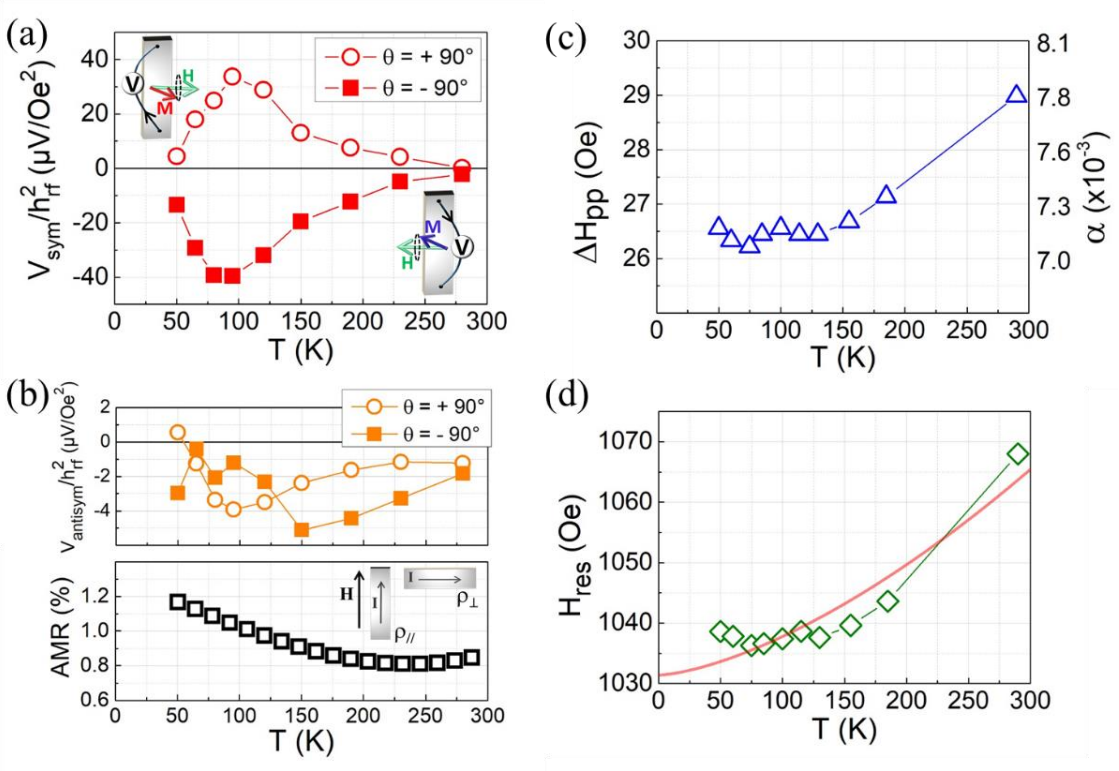

Figure 33 : (a) *T*-dependence of the symmetric contribution, V_{sym} to *V*, normalized by 'the microwave power' $\propto h_{rf}^2$. Data measured for a Si/SiO_2//Cu(6)/NiFe(8)/Cu(3)/Al(2)O_x (nm) stack, when $\theta = \pm 90°$. (b) T-dependences of the antisymmetric contribution, $V_{antisym}$ plotted along with the AMR. (c,d) *T*-dependences of ΔH_{pp} (and corresponding α) and H_{res}. The line was obtained using the Kittel equation, described in § I.2.2.2 of the present manuscript.

To gain further insight into the origins of V_{sym}, we performed angular(θ)-dependent measurements for T = 95 K (maximal signal). Experimental data were compared to numerical calculations (Figure 34(a)). The following set of equations describing equilibrium conditions was considered [121,137]: $2H_{res}\sin(\theta-\theta_M)+4\pi M_S\sin(2\theta_M)=0$; and $(\omega/\gamma)^2=[H_{res}\cos(\theta-\theta_M)-4\pi M_S\cos(2\theta_M)]\times[H_{res}\cos(\theta-\theta_M)-4\pi M_S\cos^2(\theta_M)]$, where M_S is the saturation magnetization and θ_M is the tilt in $\boldsymbol{M}$. Numerical minimization returned M_S = 700 emu.cm^{-3} and γ =18.5 MHz.Oe^{-1}. The expression $\Delta H_{pp}=(2/\sqrt{3})\alpha(\omega/\gamma)/\cos(\theta-\theta_M)+|dH_{res}/d\theta|\Delta\theta$ [137,140] was used to describe the data shown in Figure 34(b). Numerical minimization returned α = 0.008, and θ_M = 0.25°. The θ-dependence of θ_M was also determined from the calculations and is plotted in Figure 34(c). The related transverse voltage resulting from the ISHE was calculated by applying the following theoretical expression [121]:

$$V_{sym}(norm)=\frac{\sin(\theta_M)\left[4\pi M_S\gamma\sin^2(\theta_M)+\sqrt{(4\pi M_S\gamma\sin^2(\theta_M))^2+4\omega^2}\right]}{(4\pi M_S\gamma\sin^2(\theta_M))^2+4\omega^2}. \qquad \text{Eq. II-10}$$

The correspondence between experimental data and theoretical predictions (Figure 34(d)) indicates that the ISHE may be the main effect influencing the *T*-dependence observed.

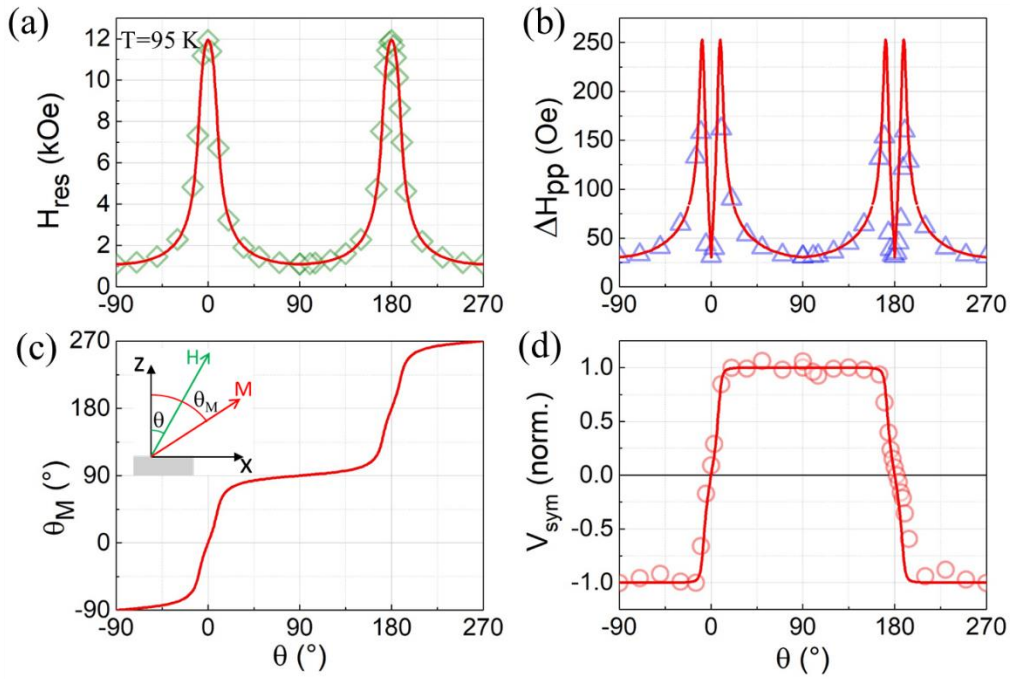

Figure 34 : θ-dependences of (a) H_{res}, (b) ΔH_{pp}, (c) the tilt in magnetization θ_M, and (d) V_{sym}. Data measured at 95 K for a Si/SiO_2//Cu(6)/NiFe(8)/Cu(3)/Al(2)O_x (nm) stack. The lines were obtained by numerical calculations using models described in the text.

We then compared the charge current deduced from our experimental data (Figure 35(a)): $I_C = [V_{sym,\theta=-90°} - V_{sym,\theta=90°})]/(2R)$, where R is the resistance of the slab, to first-principle calculations of spin Hall conductivity (Figure 35(b)). Readers should note that data are discussed in terms of charge current to take the experimental contributions of the Cu layer and contacts into account. When performing calculations, the thin film was considered a bulk material. For these calculations, the spin-polarized relativistic Korringa-Kohn-Rostoker (SPR-KKR) code was used [141,142]. In this code, the linear response Kubo formalism was implemented in a fully relativistic multiple-scattering KKR Green function method. Thermal effects were modeled by considering electron scattering due to lattice vibration to be the dominant effect, because application of H in the ferromagnetic resonance (FMR) experiments quenched spin fluctuations. The T-dependence of transversal spin Hall conductivity ($\sigma^z_{xy,NiFe}$) is in satisfactory qualitative agreement with the experimental findings, showing a non-monotonous behavior with a minimum around T =100 K. To gain more insight into the origins of the effect, we further disentangled the skew scattering ($\sigma^{sk}_{xy,NiFe}$) and side-jump plus intrinsic ($\sigma^{sj+intr}_{xy,NiFe}$) contributions, based on an approach using scaling behavior [110,112,143]. The following equation was considered: $\sigma^z_{xy,NiFe} = \sigma^{sk}_{xy,NiFe} + \sigma^{sj+intr}_{xy,NiFe} = \sigma_{xx,NiFe} S + \sigma^{sj+intr}_{xy,NiFe}$, where S is the skewness factor. For every T tested, $\sigma_{xx,NiFe}$ was varied by changing the composition of the alloy over a range from $Ni_{85}Fe_{15}$ to $Ni_{70}Fe_{30}$. S was subsequently determined from plots of $\sigma^z_{xy,NiFe}$ vs $\sigma_{xx,NiFe}$. The two contributions, $\sigma^{sk}_{xy,NiFe} = \sigma_{xx,NiFe} S$ and $\sigma^{sj+intr}_{xy,NiFe}$, were then plotted (Figure 35(c)) to determine the $Ni_{81}Fe_{19}$ composition. The non-monotonous T-dependence of $\sigma^z_{xy,NiFe}$ could clearly be ascribed to the fact that the skew scattering and the side-jump plus intrinsic contributions have opposite signs and similar amplitudes. These results can be phenomenologically understood in the light of the resonant scattering model that takes split impurity levels into

consideration [144,145]. By inserting the scattering phase shift of Fe in Ni, returned by the SPR-KKR code, into the equations for spin Hall proposed in [144], we determined the ratio between the skew scattering and side-jump contributions to be around -1.2. The same trend of opposing signs and similar amplitudes was observed. This finding also seems to infer that the intrinsic ISHE is negligible in permalloy.

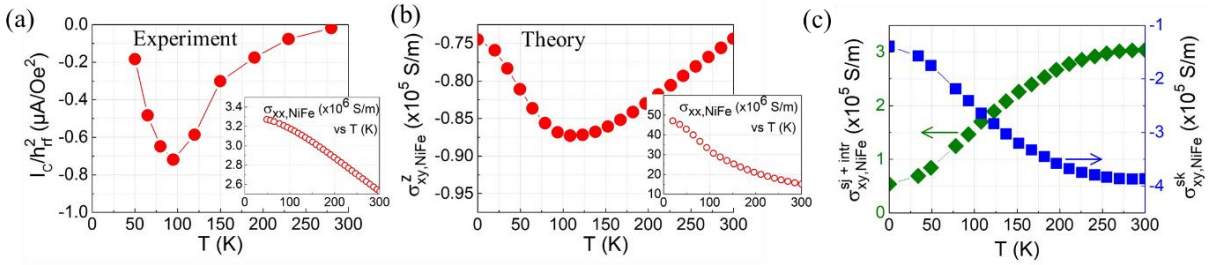

Figure 35 : (a) *T*-dependence of the charge current (I_C) generated by spin-charge conversion in an Si/SiO_2//Cu(6)/NiFe(8)/Cu(3)/Al(2)O_x (nm) stack. Inset: *T*-dependence of the NiFe layer's longitudinal conductivity ($\sigma_{xx,NiFe}$) obtained independently using 4-point measurements. (b) *T*-dependence of the spin Hall conductivity of bulk NiFe ($\sigma^z_{xy,NiFe}$) determined from first-principle calculations. Inset: *T*-dependence calculated for $\sigma_{xx,NiFe}$. (c) Skew scattering ($\sigma^{sk}_{xy,NiFe}$) and side jump plus intrinsic ($\sigma^{sj+intr}_{xy,NiFe}$) contributions (see also § II.1.1 for more details on the contributions to the spin Hall effect).

Interestingly, similar sets of experimental *T*-dependences for I_C were obtained whatever the material in contact with the permalloy: SiO_2, MgO, AlO_x oxides, Cu, and Pt metals (Figure 36). This observation further confirms the bulk origin of the effect. Figure 36(a) corresponds to the reference sample, where the NiFe layer was encapsulated between two metallic Cu layers. The data in Figure 36(b) show that replacing a Cu/NiFe interface by an SiO_2/NiFe interface does not alter the *T*-dependence profile for the charge current. For Figure 36(c,d), the NiFe/Cu and Cu/NiFe interfaces were replaced by interfaces with AlO_x and MgO. These samples were grown in a different sputter machine, which could explain the discrepancy in signal amplitude. In addition, we cannot exclude the possibility that the quality of the NiFe stack grown on AlO_x and MgO differ from that of the NiFe stack grown on SiO_2 or Cu. Nevertheless, the non-monotonous *T*-dependence of I_C was qualitatively similar for this set of samples. Figure 36(e) corresponds to a Pt/NiFe/Cu stack. With this sample, spin-charge conversion in Pt shifts the signal downwards. Figure 36(f) corresponds to the Cu/NiFe/Pt stack, where opposing spin-charge conversion occurs in the NiFe and Pt layers. Substituting a Cu/IrMn layer for the Pt spin-charge converter induced a similar effect, thus confirming the findings. Note that for this latter case, Cu was used to avoid exchange bias coupling between the NiFe and IrMn layers. The samples including buffer and capping Pt layers, and the important observations and conclusions that can be drawn from these measurements, will be discussed further below. Finally, Figure 36(g) shows that the effect was absent when the NiFe was replaced by a CoFeB layer.

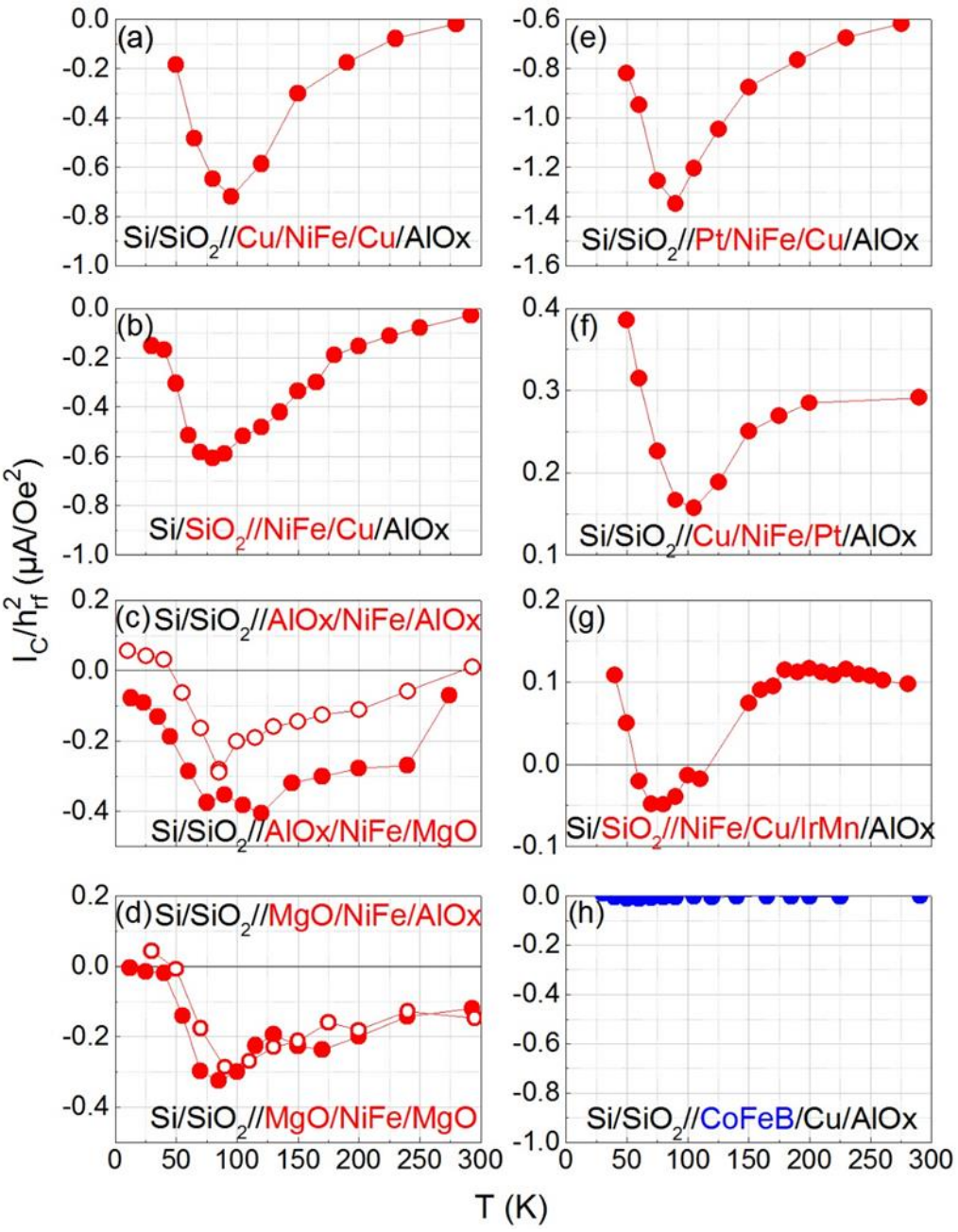

Figure 36 : *T*-dependence of I_C generated in several stacks deposited on Si/SiO2// substrates. The compositions were: (a) //Cu(6)/NiFe(8)/Cu(3)/Al(2)O_x, (b) //NiFe(8)/Cu(3)/Al(2)O_x, (c) //AlO_x(20)/NiFe(16)/AlO_x(20) and //AlO_x(20)/NiFe(16)/MgO(20), (d) //MgO(20)/NiFe(16)/AlO_x(20) and //MgO(20)/NiFe(16)/MgO(20), (e) //Pt(10)/NiFe(8)/Cu(6)/Al(2)O_x, (f) //Cu(6)/NiFe(8)/Pt(10)/Al(2)O_x, (g) //NiFe(8)/Cu(3)/IrMn(1.5)/Al(2)O_x, and (h) //CoFeB(8)/Cu(3)/Al(2)O_x (nm).

While we cannot definitively exclude that MCP [130,134–136] also occurs in our samples, our experimental and theoretical data indicated that our observations mainly relate to the self-induced ISHE. In particular, theory and the findings presented in Figure 36 support a bulk origin of the effect, obviating the need to consider the spatial inversion symmetry which is compulsory for MCP [130,134–136]. The results shown in Figure 36 also demonstrate that our observations are not linked to the ANE [146–148]. This effect could also generate a transverse charge current due to SOI, and shares the same symmetry as the ISHE. It is known to result from a *T*-gradient building up when maximum power is absorbed by the F. Because the thermal conductivity of the oxides used in our experiments is of the order of $W.m^{-1}.K^{-1}$

compared to a few hundred for the metals, significant changes in the amplitude of ANE-related observations is expected. However, our observations were independent of the heat-sinking efficiency of the stack (Figure 37). These results were also corroborated by the fact that the signal observed was independent of the field-sweep rate, over the range accessible with our experimental setup (Figure 37(a)). We have used the measurement scheme shown in the inset of Figure 37(b) to measure the change of resistance at resonance, known as the bolometric effect. As can be seen in Figure 37(b) the increase of resistance at resonance depends on the field-sweep rate, in contrast to the results shown in Figure 37(a). Figure 37(c) shows the temperature dependence of the resistance of the sample as measured inside the cavity that was used to estimate the corresponding temperature increase of the sample for the various field-sweep rates. Since thermal effects should vary with the sweep-field rate, we conclude that thermal effects can be neglected in our measurements [148]. We note that this behavior remains valid despite an estimated temperature increase of up to about 200 mK (Figure 37(d)), due to the absorption of microwave power by the sample at resonance calculated from Figure 37(b,c).

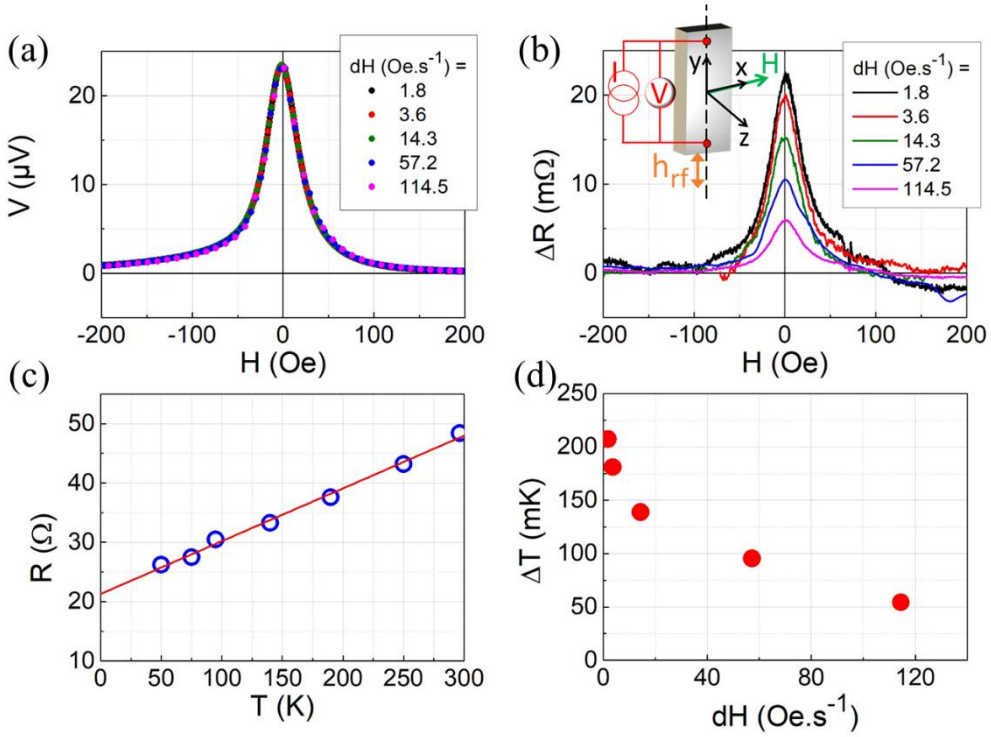

Figure 37 : (a) Representative V vs H-H_{res} for a Si/SiO_2//Cu(6)/NiFe(32)/Cu(3)/Al(2)O_x (nm) stack at T = 95 K, with θ = + 90° (no bias current). Several field-sweep rates (dH) were used for the magnetic field. (b) The same dependences as in (a) were measured when a bias current of I = 100 μA was applied across the sample (see inset). The change in the sample's resistance was estimated after removing the off-resonance voltage, as follows: $\Delta R = [V_{\text{with bias current}} - V_{\text{without bias current}})]/I$. (c) T-dependence of the off-resonance sample's resistance, measured independently. (d) dH-dependence of the increase in temperature of the sample at resonance (ΔT), deduced from (b) and (c).

We will now comment on the direction of the self-induced current ($J_{S,self}$) (Figure 38). A reference layer of Pt was added to the stack, either as a buffer or as a capping layer. In this case, spin-charge conversions produced by ISHE in the Pt and NiFe layers contribute concurrently to the total experimentally probed I_C. The Pt layer has a positive spin Hall angle $\Theta_{ISHE,Pt}$. For sufficiently thick layers, V_{sym} generated in Pt relates to $\Theta_{ISHE,Pt}$ $l_{sf,Pt}$ because $\Theta_{ISHE,Pt}$ is known to be mostly intrinsic [149–151]. $\Theta_{ISHE,Pt}$ $l_{sf,Pt}$ and V_{sym} are therefore T-independent. Furthermore, V_{sym} in Pt flips sign when the stacking order or field are reversed [110,112]. Given this fact, and considering the electrical connections in our setup, a buffer Pt layer pumps

a spin current ($J_{S,Pt}$) toward the substrate and returns a negative (positive) value of V_{sym} for a field angle θ = -90° (90°), resulting in a negative value of I_C = [$V_{sym,\ \theta=-90°}$-$V_{sym,\ \theta=90°}$)]/(2R). Conversely, when a capping Pt layer is included, a positive value of I_C is returned. The NiFe layer also has a positive Hall angle [129]. The findings presented in Figure 38 therefore indicate that, with regards to spin current direction, the NiFe layer behaves similarly to a buffer Pt layer, as it induces a negative I_C. In this scenario, spin- and subsequent charge-currents in the Pt and NiFe layers add up for the buffer Pt layer case, and subtract for the capping case (Figure 38). Similar to previous experiments [129], the spin current may be generated as a result of asymmetric spin-dependent scattering across the NiFe film, possibly due to non-homogeneous film properties across its thickness and to subsequent asymmetric spin relaxation at the various interfaces. From these data, at T ~ 95 K, the self-induced conversion of the NiFe can be as efficient as that observed with Pt. We also note that although spin-charge conversion in NiFe is inefficient close to 300 K and only relates to ISHE in the Pt layer, self-induced spin diffusion still occurs. This effect creates asymmetry in the conversion and may contribute to the observed difference in I_C measured at 300 K due to the inversion of the Pt growth order. Inverting the growth order also modifies the electric properties of the Pt layer and interfaces. For example, we measured a conductivity of $\sigma_{xx,Pt}$=4x10^6 S.m^{-1} and 5x10^6 S.m-1 for the capping and buffer layer, respectively, corresponding to reasonable $l_{sf,Pt}$ values (~ 3-4 nm) for the spin diffusion length [151]. We note that, if $J_{S,self}$ were omitted, $\Theta_{ISHE,Pt}$ $l_{sf,Pt}$ at 300 K could be calculated using the following equation:

$$\Theta_{ISHE,Pt}\cdot l_{sf,Pt} = \frac{I_c}{h_{rf}^2}\frac{1}{w\tanh[t_{Pt}/(2l_{sf,Pt})]}\frac{8\pi\alpha^2}{2e g_{eff}^{\uparrow\downarrow}\gamma^2}\frac{(4\pi M_S\gamma)^2+4\omega^2}{4\pi M_S\gamma+\sqrt{(4\pi M_S\gamma)^2+4\omega^2}}, \qquad \text{Eq. II-11}$$

where the spin mixing conductance is calculated from: $g_{eff}^{\uparrow\downarrow} = 2\sqrt{3}\,M_S\gamma\, t_{NiFe}\Delta H^{pump}/(g\,\mu_B\,\omega)$, with $\Delta H^{pump} = \Delta H_{pp,NiFe/Pt} - \Delta H_{pp,NiFe}$ for the capping Pt layer case and $\Delta H^{pump} = \Delta H_{pp,Pt/NiFe} - \Delta H_{pp,NiFe}$ for the buffer layer [121]. Using the parameters measured separately, M_S = 700 emu.cm^{-3}, γ =18.5 MHz.Oe^{-1}, $\Delta H_{pp,NiFe/Pt}$ = 57 Oe, $\Delta H_{pp,Pt/NiFe}$ = 48 Oe, $\Delta H_{pp,NiFe}$ = 29 Oe, we determined $g_{eff}^{\uparrow\downarrow}$ = 27 and 18 nm^{-2} for the capping and buffer Pt layer cases, respectively. The tanh(t_{Pt}/2$l_{sf,Pt}$) can be approximated to 1. When further considering the values of I_C/h_{rf}^2 returned from the data in Figure 38 at 300 K, we calculated $\Theta_{ISHE,Pt}$ $l_{sf,Pt}$ = 0.23 and 0.52 nm for the capping and buffer Pt layer cases, respectively. These data give the expected order of magnitude for Pt [151]. The discrepancy between the two values tends to confirm that $J_{S,self}$ should not be neglected when determining $\Theta_{ISHE,Pt}$ [128], although stacking order-dependent interfacial spin asymmetry and spin flip scattering parameters may also contribute [151].

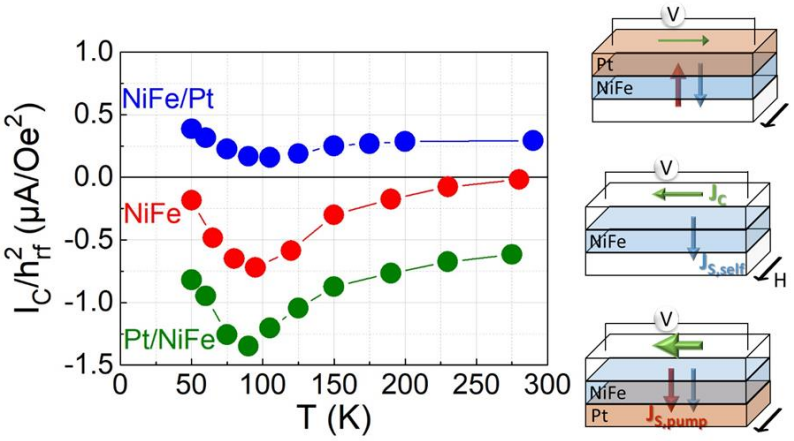

Figure 38 : *T*-dependence of I_C generated in Si/SiO$_2$//Pt(10)/NiFe(8)/Cu(6)/Al(2)O$_x$ (buffer Pt), Si/SiO$_2$//Cu(6)/NiFe(8)/Pt(10)/Al(2)O$_x$ (capping Pt), and Si/SiO$_2$//Cu(6)/NiFe(8)/Cu(3)/Al(2)O$_x$ (nm) stacks. Right panel: Representations of the spin and charge currents in the stacks.

We finally considered how the effect was affected by the NiFe layer thickness. The contributions of the Cu layer and contacts were taken into account by considering the charge current rather than just the voltage drop, thus it was relevant to compare several NiFe thicknesses. We found that the position of maximum conversion, $I_{C,95K}$, was thickness-independent (Figure 39(a)). This observation is also in agreement with the bulk origin of the effect. We further observed that the amplitude of $I_{C,95K}$ showed a similar thickness-dependence to $I_{C,300K}$ (Figure 39(b)). The thickness-dependence of I_C relates to t^*/α^2, where $1/\alpha^2$ accounts for the spin pumping efficiency, and t^* describes the thickness-dependence of the spin-charge conversion efficiency [121]. The former parameter was found to increase with thickness in a linear fashion. This behavior is due to the decreasing role played by interfaces, and the subsequent decrease of α for thick layers [60]. For the conversion efficiency, in this case, the spin-sink is also the NiFe spin current generator. Considering that the spin current is due to asymmetric spin relaxation at the various interfaces, we get a situation similar to the case of a spin-sink receiving the spin current from a third party and can thus consider that $t^* = l_{sf,NiFe}\tanh[t_{NiFe}/(2l_{sf,NiFe})]$ [121]. $l_{sf,NiFe}$ was estimated by combining our measurements of longitudinal conductivity in the following relation [152]: $l_{sf,NiFe} = 0.91\sigma_{xx,NiFe}\ \mathrm{x}10^{-12}$. The values calculated for $l_{sf,NiFe}$ at T =100 K ranged between 2.9 nm for 8-nm-thick NiFe films to 5.3 nm for the 32-nm-thick film, in agreement with [153]. Plotting t^*/α^2 vs T (inset of Figure 39(b)) revealed a nearly linear behavior, corroborating the results of the thickness-dependence of I_C.

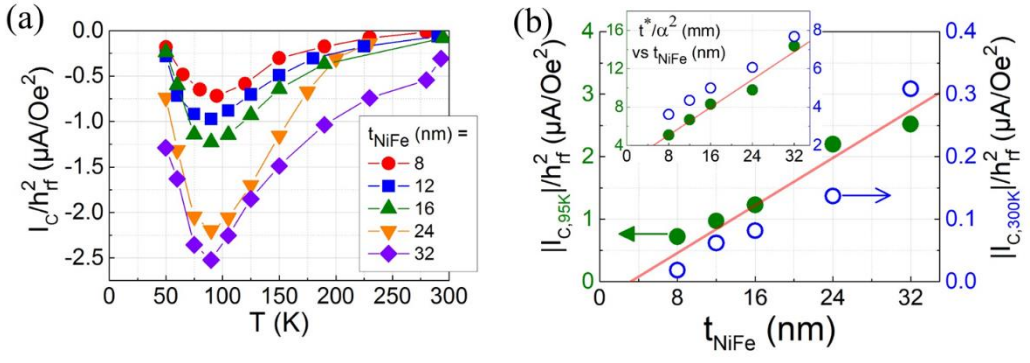

Figure 39 : (a) *T*-dependence of I_C measured in Si/SiO$_2$//Cu(6)/NiFe(t_{NiFe}=8;12;16;24;32)/Cu(3)/Al(2)O$_x$ (nm) stacks. (b) NiFe thickness-dependence of I_C measured at 95 and 300 K. Inset: corresponding thickness-dependences of t^*/α^2.

Summary

In summary, the main contribution of this study is that it presents systematic evidence of a self-induced ISHE in FMR experiments. Our findings were supported by distinct sets of *T*-, thickness-, angular-, and stack-dependent experimental data encompassing the main features of the self-induced ISHE. The experimental findings were corroborated by first-principle calculations. Most importantly, similar amplitudes but opposite signs for the bulk skew scattering and the side-jump plus intrinsic contributions to the *T*-dependent spin Hall conductivity in permalloy could explain why the SOI-related transverse voltage was observed to display non-monotonous *T*-dependence. The findings from this study contribute to our understanding of a previously overlooked and incompletely understood effect. The results further indicate that self-induced conversion within the NiFe ferromagnet can be as efficient as that recorded with noble metals such as Pt, and thus needs to be carefully considered when investigating SO-related effects in materials destined for use in spintronics. It is worthy mentioning that we have experimentally observed a similar non-monotonous *T*-dependence of the self induced ISHE in a Co single layer. Experiments and theoretical calculations are currently under further investigation in the group.

Following this extensive study on a self-induced ISHE in NiFe, in the remaining of this chapter we will focus on spin-charge conversion specific to antiferromagnets. For that purpose, based on the above findings, it became clear that NiFe can be used as a spin injector if one wants to study ISHE properties of antiferromagnets at room temperature. Conversely, it needs to be replaced by a low spin-orbit material like CoFeB if one wants to study temperature-dependent ISHE behaviors like those related to the antiferromagnetic to paramagnetic phase transition.

II.3 Inverse spin Hall effect from GHz and THz spin currents in antiferromagnets

II.3.1 Inverse spin Hall effect in antiferromagnets

The inverse spin Hall effect was initially observed in non-magnetic metals such as Pt, Ta, and Pd [112,154]. Since some of the physical principles is independent of the magnetic order (see also § II.2), this phenomenon was naturally observed in the case of antiferromagnets as well. It was extensively reported ever since, especially in MnX alloys, with X=Ir, Fe, Pt, Pd [155–164].

Here I remind § I.2.2 and Ref. [2] where we have discussed electronic and magnonic transport regimes. The electronic transport regime considers spins carried by conduction electrons and the magnonic transport regime refers to the excitation of localized-magnetic-moments. Whereas magnetic insulators only allow magnonic transport, and non-magnetic metals only permit electronic transport, both types of transport regimes can coexist in magnetic metals. Interconversion between the two types of transport occurs at interfaces [165], thus ensuring continuity of the spin flow across the heterostrutures if the conversion rate in sufficiently efficient. The contribution of electronic and magnonic transport in antiferromagnetic metals is challenging to distinguish, and a few results have yet been published on this specific point. Using spin pumping and measuring the inverse spin Hall effect Saglam *et al* [90] have studied the spin current transport through the metallic FeMn in NiFe/FeMn/W stacks (inset of Figure

40). Accordingly, they took advantage of relatively large magnitude and the opposite sign of spin Hall angle in W compared to FeMn to detect when the spin currents reach the W layer for FeMn above the electronic spin diffusion length or, in other words, when magnonic transport is responsible for the spin current transport across the FeMn layer. The dependence of W_{ISHE} with t_{FeMn} (Figure 40) is in contrast to the previous measuremens as obtained in NiFe/Cu/FeMn bilayers [156], which show a monotonic increase of W_{ISHE} with t_{FeMn} and saturation above 6 nm. This way, the authors managed to disentangle electronic (< 2 nm) and magnonic (~ 9 nm) transport-related penetration depths in FeMn. Authors speculate that those length scales are different because the electronic spin transport is limited by the spin diffusion length, while magnons can propagate over long distances [90,165].

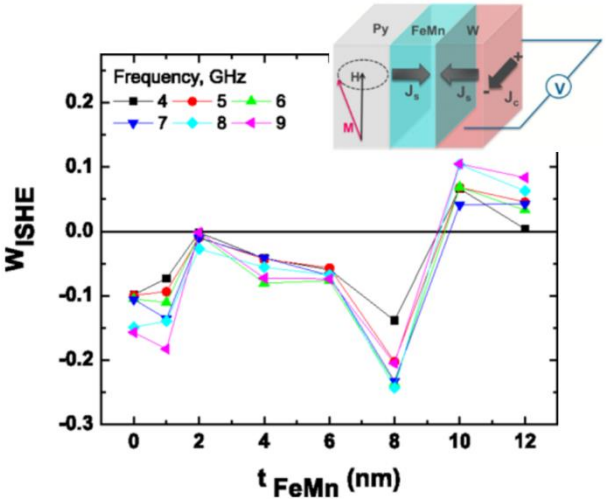

Figure 40 : FeMn thickness (t_{FeMn}) dependence of W_{ISHE} measured at room temperature for various frequencies, where W_{ISHE} represents the ISHE to AMR contribution to the total signal: $W_{ISHE}=1/(1+V_{AMR}/V_{ISHE})$ (see § II.1.2 of the present manuscript). Inset: Schematic representation of the spin and charge currents in NiFe/FeMn/W trilayers. Adapted from Ref. [90].

Remarkably, using an atomistic spin model the excitation of spin waves in an antiferromagnet was studied. The magnonic spin transport characteristic length (~ 5 nm) was studied considering the IrMn antiferromagnet [89] and it confirms the expected longer spin diffusion length for magnons when compared to the experimentally determined electronic spin diffusion length (~ 2.2 nm) [84]. Note that due to the interfacial characteristic of exchange bias, a strong excitation at the interfacial layer is expected. Oppositely, the strong anisotropy in the IrMn antiferromagnet reduces the strength of such excitations away from the interface.

The experiments discussed in the previous paragraph were performed in the GHz regime. In the study below we have tackled the influence of frequency on spin current injection, propagation, and spin-charge conversion specifically in the THz regime comparing its characteristic lengths with the values obtained in the GHz regime. The THz radiation is extremely useful for numerous applications and is currently gaining interest in spintronics [166,167]. Concerning ultrafast spin transport in antiferromagnets, so far, only a few studies focused solely on THz regime [168] and sub-THz dynamics [169,170]. Interestingly, we have found a strong influence of the interfaces that is unique to the THz regime. Our results also indicate a change on the nature of the spin transport when transiting from GHz to THz regime.

II.3.2 GHz vs THz spin currents [5]

This section is adapted from Ref. [5]. The experiments involving optical spin pumping were carried out by our collaborators in FHI Berlin - Ref. [5]: R. L. Seeger (equal first), O. Gueckstock (equal first), T. S. Seifert, S. Auffret, S. Gambarelli, J. Kirchhof, K. Bolotin, V. Baltz, T. Kampfrath, and L. Nádvorní, ArXiv:2011.04191v1 (2021).

The full stacks used in this study were (from substrate to surface): NiFe(t_{NiFe})/IrMn(t_{IrMn})/N(3)/Al(2)O_x (nm) and N(3)/IrMn(t_{IrMn})/NiFe(t_{NiFe})/Al(2)O_x (nm), with N = Pt, W or Ta. t_{IrMn} is the thicknesses of the IrMn layer and was varied between 0 and 12 nm; t_{NiFe} is the thicknesses of the NiFe layer and was chosen depending on constraints specific for each experiment, t_{NiFe} = 3 or 8 nm. Note that a 3 nm thick NiFe is optimized for THz experiments, while a 8 nm thick NiFe is needed for GHz experiments because finite size effects on damping makes the 3 nm thick NiFe more than 4 times inefficient to inject spins. Besides that, as discussed in Figure 38, the self-induced spin-charge conversion in NiFe in negligible at 300 K. The stacks were deposited at room temperature by dc-magnetron sputtering on glass (for THz experiments) or Si/SiO_2(500) (nm) (for GHz experiments) substrates. The NiFe layer was deposited from a $Ni_{81}Fe_{19}$ (at. %) permalloy target and the IrMn layer was deposited from an $Ir_{20}Mn_{80}$ (at. %) target. An Al cap was deposited to form a protective passivating AlO_x film.

Our methodology is based on measuring the spin-charge conversion signal due to spin current injected from a NiFe ferromagnet into a bilayer of IrMn and a heavy metal (Pt, W or Ta) (Figure 41(a,b)). Spin angular momentum is injected at two different frequencies by two different techniques: spin pumping at 9.6 GHz (defined by the FMR in NiFe, Figure 41(a)) and a ultrafast spin-voltage generation at 0.1-30 THz (defined by the temporal duration of the optical excitation, Figure 41(b)).

The GHz experiment was carried out using the continuous-wave electron paramagnetic resonance spectrometer fitted with a three-loop-two-gap resonator operating at 9.6 GHz, as described in Figure 31. The THz experiments are based in electro-optic sampling of the THz pulse with a co-propagating probe pulse (0.6 nJ, 10 fs) in a 10 μm-thick ZnTe(110) crystal under ambient conditions (further description of the technique can be found in Refs. [166,171]). The resulting spin current is converted to an charge current and, thus, an electric field in both N (after passing through a thin IrMn layer) and IrMn (in case of thicker layer than the spin propagation length) layer. Note that the spin Hall angle of IrMn has the same signal as the one of Pt and opposite signal with respect of W or Ta [112,156]. Concerning the effective spin current propagation lengths (λ_{eff}) in IrMn at the different regimes it is expected to be a purely electronic (governed by the mean free path) in case of THz experiments, and combination of electronic (electronic spin diffusion length) and magnonic (magnonic spin diffusion length) in case of GHz experiments.

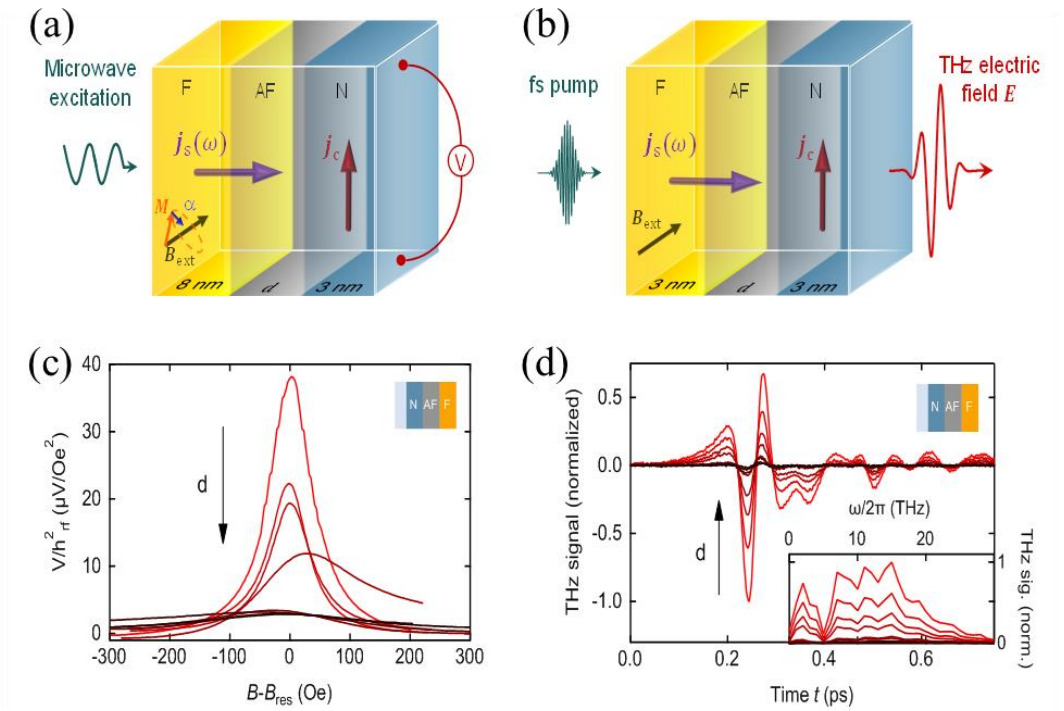

Figure 41 : Measuring inverse spin Hall effect at GHz and THz frequencies. (a) Schematic of the GHz experiments in Si/SiO_2//Pt(3)/IrMn(*d*)/NiFe(8)/Al(2)O_x (nm) stacks. The sample dimensions were: l = 2.46 mm and w = 0.46 mm. Both sides of the samples were connected to electrodes using Al-wire-bonding. The microwave excitation of amplitude h_{rf} ~ 0.5 Oe triggers the precession of magnetization in a ferromagnetic (F) layer and, due to spin pumping, launches a spin current through the antiferromagnetic (AF) layer IrMn of thickness *d* into a heavy metal (N) layer where it is converted into a detectable dc charge current via the inverse spin Hall effect. (b) The analogous experiments performed at THz frequencies in glass//Pt(3)/IrMn(*d*)/NiFe(3)/Al(2)O_x (nm) stacks. A femtosecond optical pulse triggers an ultrafast spin current between the F and the AF. The converted charge current serves as a source of an emitted THz pulse. Typical normalized raw experimental data from the GHz (c) and THz (d) experiments for different *d* (black arrows indicate increase of *d*). Note: for the GHz experiments, *V* is made of a symmetric and an antisymmetric contribution (see discussion in Figure 31). Only the symmetric contribution was considered in the rest of the manuscript for the spin-charge conversion signal. Note that $Z(\omega)$ is corrected from layers' absorption via calibration measurements. Inset: amplitude spectrum of the corresponding THz temporal waveforms.

Figure 41(c,d) shows the raw data for several IrMn thicknesses in the GHz and THz regimes, respectively. A decrease in the voltage amplitude is observed with increasing the IrMn thickness *d*. Note that the bandwidth of the THz emission signal is large enough to capture sub-ps dynamics. An analysis on the sub-ps dynamics deserves further investigation, which is above the scope of this manuscript. Figure 42 shows a complete set of raw data for the GHz experiments (THz counterparts are not shown here). Here I recall the discussion of § II.1.2, which describes the voltage signal in the GHz experiments comprises symmetric (Sym) and antisymmetric (Antisym) contributions which can be disentangled by fitting data using Eq. II-9. For the spin-charge conversion signal, the V_{sym} is averaged for $H > 0$ and $H < 0$ and it is normalized by h_{rf}^2, taking into account any variability due to *rf*-to-material coupling. Concerning the THz experiments, the detected signal can be described as: $E(\omega) = eZ(\omega)I_C(\omega)$. $E(\omega)$ is the transversal electric field detected as the amplitude of the THz waveform, i.e., the ISHE signal, $Z(\omega)$ is the impedance, and $I_C(\omega)$ is the transversal electric current. $I_C(\omega)$ originates not only from spin-charge conversion in N and IrMn layers but also from interfacial contributions [174,175].

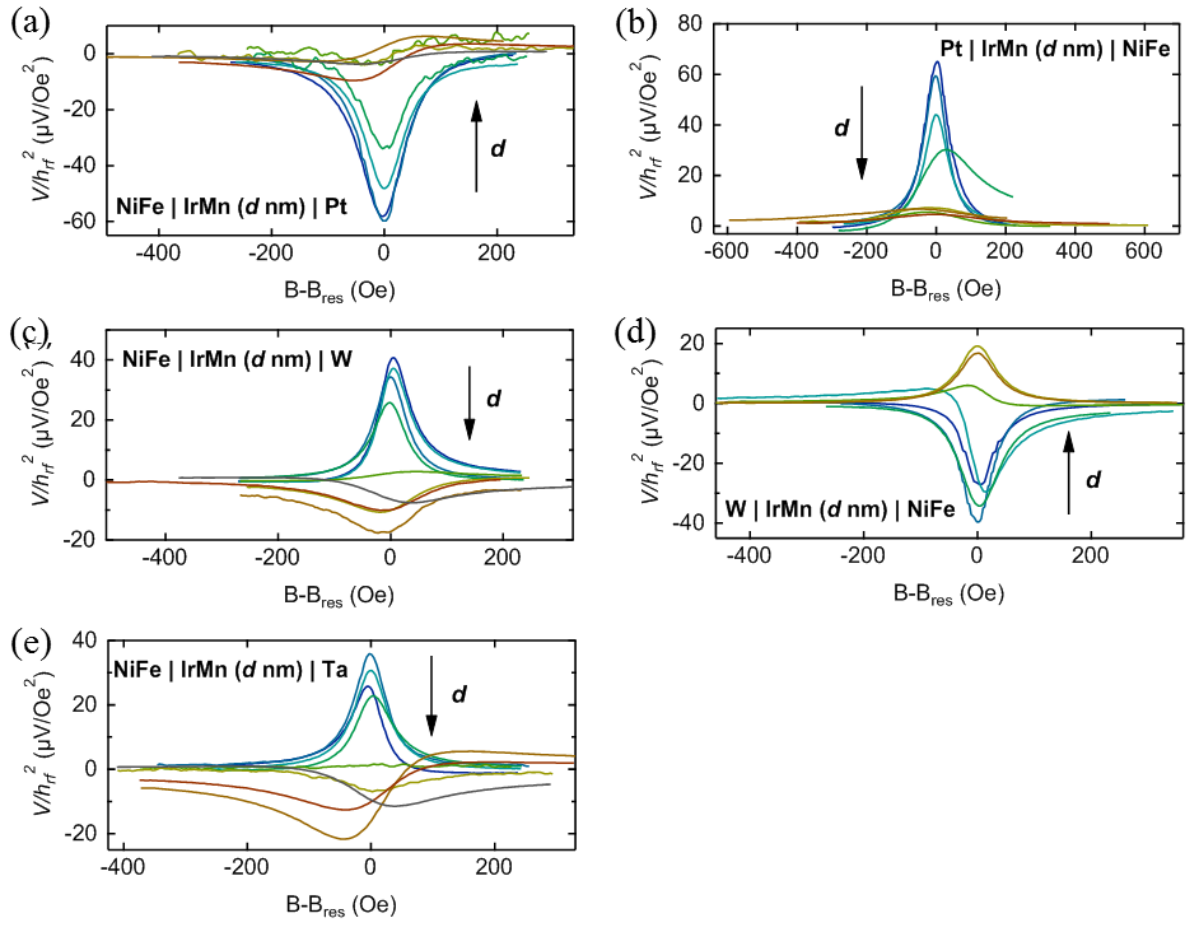

Figure 42 : Raw data from all samples as measured in the GHz range experiments. All samples were grown in Si/SiO_2 substrates and the compositions were: (a) //NiFe(8)/IrMn(*d*)/Pt(3)/Al(2)O_x, (b) //Pt(3)/IrMn(*d*)/NiFe(8)/Al(2)O_x, (c) //NiFe(8)/IrMn(*d*)/W(3)/Al(2)O_x, (d) //W(3)/IrMn(*d*)/NiFe(8)/Al(2)O_x, (e) //NiFe(8)/IrMn(*d*)/Ta(3)/Al(2)O_x (nm). Additional experiments on //Ta(3)/IrMn(*d*)/NiFe(8)/Al(2)O_x (nm) stacks are ongoing in order to complete this set of data. The experiments were carried out for different *d* (black arrows indicate increase of *d*).

To gain further insight into the characteristic lengths specific for each frequency range we have plotted the spin-charge conversion signal (S2C amplitude), as shown in Figure 43. Note that the S2C amplitude is normalized to the amplitude measured in a NiFe/Pt stack for both GHz and THz experiments. For $d = 0$, we assume spin-charge conversion in N. The changes of signs and similar amplitudes for Pt and W(or Ta) are consistent with the expected values reported in literature [112]. For large thicknesses, $d > 5$ nm, the polarity of S2C is the same for GHz and THz experiments and saturates at +7.5% (THz) and +8% (GHz) of the respective conversion in pure NiFe/Pt. Besides, the conversion only in IrMn displays same sign as Pt, consistent with literature [156]. The spin-charge conversion efficiency in IrMn stays the same when comparing the GHz and THz frequencies, see comparison in Figure 44.

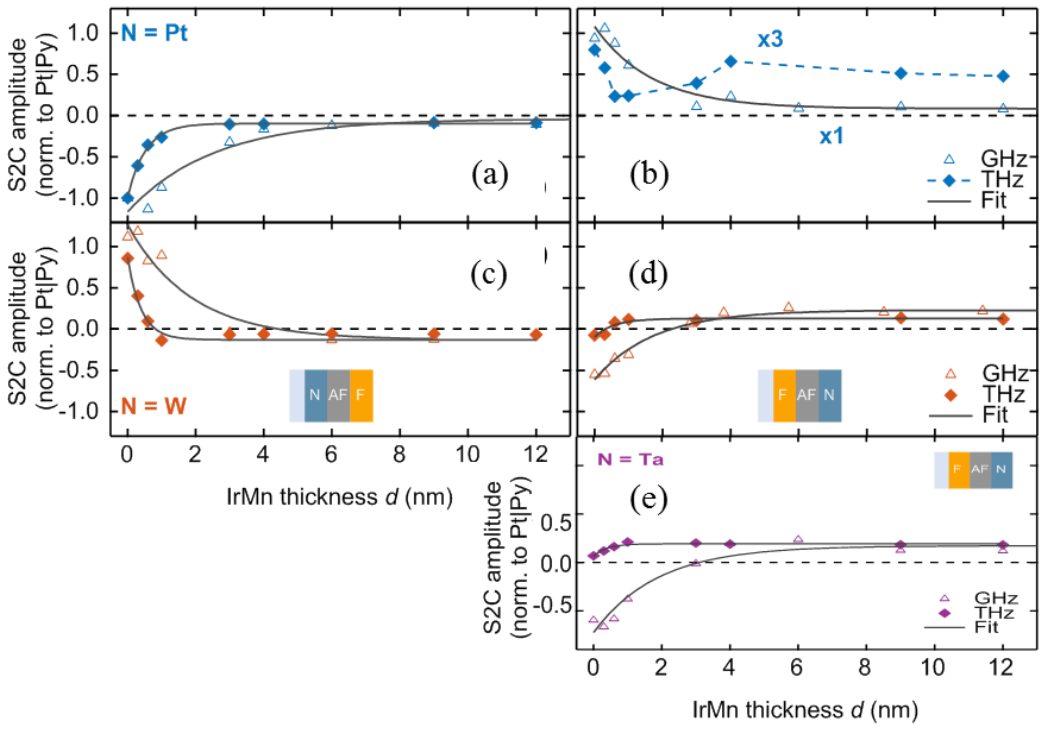

Figure 43 : Propagation lengths of spin currents in IrMn. Signal amplitudes proportional to the converted charge current as a function of the thickness of IrMn in (a) //Pt(3)/IrMn(*d*)/NiFe(8)/Al(2)O_x and (b) //W(3)/IrMn(*d*)/NiFe(8)/Al(2)O_x at both frequency ranges (GHz: open triangles, THz:closed diamonds). Data are normalized to signals from //Pt/IrMn(*d* = 0)/NiFe for GHz and THz sets. (c, d) Analogic to (a, b) but for reverse layer order (c) //NiFe(8)/IrMn(*d*)/Pt(3)/Al(2)O_x, (d) //NiFe(8)/IrMn(*d*)/W(3)/Al(2)O_x, and (e) //Ta(3)/IrMn(*d*)/NiFe(8)/Al(2)O_x (nm). Photonic and electronic effects unrelated to the spin-to-charge conversion that vary with thickness are removed. Fits are mono-exponentials, and return the characteristic propagation lengths in IrMn.

As the spin-charge conversion signal is much smaller in IrMn compared to N, it is possible to extract an effective spin current propagation length ($\lambda_{\text{eff, IrMn}}$) by fitting the *d*-dependence considering a mono-exponential function, see solid lines in Figure 43. Detailed values for all samples are summarized in Table 2. Note that in the frame of this work we have considered only a mono-exponential decay, while the real *d*-dependence in multilayers is more complex. It can be strongly affected by the spin transport properties of both IrMn and N layers and spin mixing conductances of all interfaces, as described in Refs. [172,173], which makes it challenging to obtain reliable parameters from fitting experimental data. Moreover, the simulations in Ref. [173] do not consider any interfacial parameter, such as spin memory loss or interfacial spin dependent scattering. Considering the effective values returned from our fitting, in average, it returns $\lambda^{\text{IrMn}}_{\text{eff, GHz}} \sim (2.2\pm0.5)$ nm and $\lambda^{\text{IrMn}}_{\text{eff, THz}} \sim (0.6\pm0.1)$ nm, in the GHz and THz regimes, respectively. The larger spin propagation length at GHz frequencies might indicate a different regime of spin transport. It agrees with the expectation of purely electronic transport in cases of THz experiments and a combination of electronic and magnonic in case of GHz experiments.

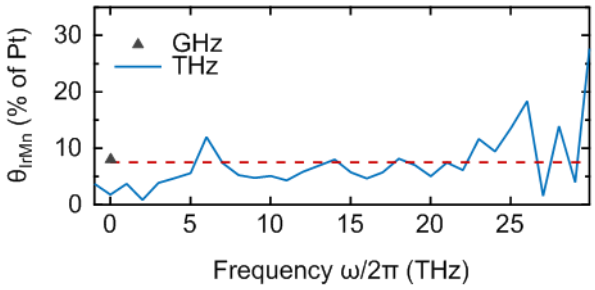

Figure 44 : Relative spin Hall angle θ_{IrMn} (ω) of IrMn with respect to Pt as a function of frequency $\omega/2\pi$ that is extracted from the THz (curve) and GHz measurements (triangle) on //Pt(3)/IrMn(*d*)/NiFe(8)/Al(2)O_x (nm) series shown in Figure 43(a). The dotted red line depicts the mean value of θ_{IrMn} from the THz experiment.

Stack	$\lambda_{eff,THz}^{IrMn}$ (nm)	$\lambda_{eff,GHz}^{IrMn}$ (nm)
Pt/IrMn(*d*)/NiFe	0.6 ± 0.1	2.5 ± 0.7
W/IrMn(*d*)/NiFe	0.4 ± 0.1	1.9 ± 0.5
NiFe/IrMn(*d*)/**Pt**	-	1.7 ± 0.5
NiFe/IrMn(*d*)/**W**	0.5 ± 0.2	1.7 ± 0.3
NiFe/IrMn(*d*)/**Ta**	0.4 ± 0.1	1.9 ± 0.5

Table 2 : Effective spin current propagation lengths λ_{eff}^{IrMn} *in IrMn as obtained from fitting the data shown in Figure 43. Note that the THz data for the NiFe/IrMn/Pt series is missing due to its non-monotonic shape (Figure 43(b)).*

Before concluding this section, we want to comment on the stacking order influence on the spin-charge conversion signal amplitude. Interestingly, by reversing the stacking order, one would expect perfectly reversed THz waveforms since the spin current flows oppositly. Deviations from this behavior are normally ascribed to the interfacial spin-charge conversion and interfacial quality [174,175]. While the GHz data behave as expected in sign, the THz look very different. In Figure 43 one can observe that by increasing *d* a sign switching is visible in W-based series and no sign switching in Pt-based series, as expected. However, the Ta-based series, shown in Figure 43(e), do not display a sign change while increasing *d*. In contrast to what was expected due to the opposite spin Hall angle between Ta and IrMn. It might indicate the role played by interfacial spin-charge conversion in this series of samples and deserves further investigation.

Following the studies in linear spin fluctuations, described in § I.2, and the observation of the self-induced ISHE in NiFe, in the remaining of this chapter we will focus on spin-charge conversion specific to antiferromagnets aiming to probe non-linear spin fluctuations using ISHE.

II.4 Inverse spin Hall effect as a probe for non linear spin fluctuations

II.4.1 Mechanisms for Hall effects when spins fluctuate in disordered metals

In § I.2 I have discussed the theoretical framework and shown results probing linear fluctuations through spin pumping experiments. I recall here data the non-local damping α^{P} is connected to the spin mixing conductance [49]. Alternatively to the original theoretical formulation for spin pumping [48,49], in a linear-response formalism it was found to be linked to the dynamical transverse spin susceptibility of the spin-sink (see Eq. I-20) [80]. Concerning magnetotransport near critical temperatures, anomalies on the AHE signal were experimentally observed and theoretically addressed [176]. Recently, it has also been observed that the ISHE signal displays an anomaly in ferromagnetic metals near T_C [177], which was theoretically explained by Gu *et al* [178] considering non-linear spin fluctuations. The following of this paragraph is dedicated to a discussion about non-linear spin fluctuations and its relation to the inverse spin Hall effets.

In order to start the discussion on the non-linear spin fluctuations we define the susceptibilities as the expansion of the magnetic order parameter m in terms of the magnetic field h as [177]:

$$m = m_0 + \chi^{(0)}h + \chi^{(1)}h^2 + \chi^{(2)}h^3. \qquad \text{Eq. II-12}$$

Note that in § I.2, the dynamic transverse spin susceptibility of the spin sink layer (χ_k^R), which is linked to α^{P}, is the linear susceptibility $\chi^{(0)}$ of Eq. II-12. Therefore, the measurement of the spin injector damping is a way to probe linear spin fluctuations. The high order terms, $\chi^{(1)}$ and $\chi^{(2)}$, can be accessed by measurements of the AHE and ISHE, respectively [177].

Figure 45(a) illustrates a picture to understand higher-order terms emerging from the interaction considering four-spin correlations [179]. Essentially, one needs to consider the exchange energies between all the angular momenta that are at stake. In simple words, when an electron, carrying a spin angular momentum by nature, flows (orbital angular momentum due to its trajectory) near a localized magnetic moment (spin and angular momentum), several types of interactions can take place, namely, spin-spin interactions, orbital-orbital interactions, and spin-orbital interactions. The combination of all those interactions makes it to higher-order energy terms which eventually contribute to either the AHE or ISHE effects. Figure 45(b) show a schematic image of the ISHE of a weak ferromagnetic material near T_C. The spin Hall resistivity is governed by four-spin correlations. As the second-order non-linear susceptibility ($\chi^{(2)}$) relate to fourth-order correlations, the ISHE is also expected to scale as $\chi^{(2)}$ [179]. Figure 45(c) illustrates the expected dip and peak in the ISHE for weak ferromagnets around T_C.

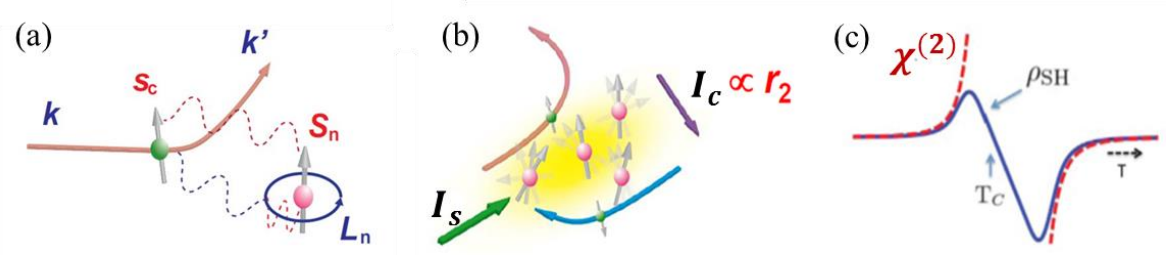

Figure 45 : (a) Schematic representation of the different type of interactions considering four-spin correlations. (b) Schematic representation of the ISHE of a weak ferromagnet near a critical temperature. (c) Schematic representation of the scaling of the ISHE with the second-order non-linear uniform susceptibility. Adapted from Refs. [177–179].

II.4.2 Experimental search for non linear spin fluctuations in IrMn

Although the model mentioned above considers a weak ferromagnet spin sink, we sought to explore the *T*-dependence of the ISHE signal at the magnetic phase transition in the IrMn antiferromagnet. In addition to the enhancement of the spin pumping (as shown in § I.2) we expect to observe the typical dip and peak signal that related to non-linear spin fluctuations (Figure 45(c)). To this end, we have replaced the NiFe spin injector layer for a CoFeB layer to avoid the self-induced ISHE signal of NiFe (discussed in § II.2). As illustrated in Figure 36(h), the amplitude of the self-induced ISHE signal in CoFeB is negligible when compared to the amplitude we have observed in NiFe. This behavior is expected since spin-orbit coupling in CoFeB is negligible compared to NiFe.

The full stacks used in this study were (from substrate to surface): Cu(4)/IrMn(1.2)/Cu(3)/CoFeB(8)/Al(2)O_x (nm) (short name: IrMn/Cu/CoFeB) and Cu(4)/IrMn(1.2)/CoFeB(8)/Al(2)O_x (nm) (short name: IrMn/CoFeB) multilayers. Stacks were deposited at room temperature by sputtering on Si/SiO_2(500) (nm) substrates at a pressure of 2.3 x 10^{-3} mbar under argon. A seed layer of Cu was deposited to ensure the growth quality of a thin IrMn layer. For this reason the stacking order of spin injector and spin-sink/spin-charge converter layer was reversed compared to our previous studies as discussed in § I.2.2. The thickness of IrMn was chosen to give a magnetic phase transition within the temperature range accessible in our setup. It is worthy mentioning that a maximum spin-charge conversion is obtained for IrMn thickness larger than the spin diffusion length. Therefore, it is close to the lower limit for the IrMn antiferromagnet, which is around 1 nm [84]. The CoFeB layer was deposited from a $Co_8Fe_{72}B_{20}$ (at. %) target. A 2-nm-thick Al cap was deposited to form a protective Al(2)O_x film after oxidation in air. The sample dimensions were: l = 2.46 mm and w = 0.46 mm. Both sides of the samples were connected to electrodes using Al-wire-bonding.

Figure 46 summarizes our preliminary results. Figure 46(a,b) shows the *T*-dependence of the total Gilbert damping (α). In the IrMn/CoFeB sample we observe that *T*-dependence of α displays a bump. As discussed in Figure 19(b), this is the direct consequence of the enhanced dynamical transverse spin susceptibility of IrMn when spins fluctuate near the paramagnetic-to-antiferromagnetic phase transition for the IrMn layer. The bump is not evidenced in IrMn/Cu/CoFeB sample. As observed in Figure 19(a), the peak gets larger and with reduced amplitude as the IrMn layer is thicker in structures without a Cu spacer. We have changed the orientation of the sample (θ = + 90° and θ = - 90°) to check that the potential *T*-dependent change in the direction of anisotropy can be ruled out as the data sumperimposes. The same can be concluded from the *T*-dependence of H_{res} (Figure 46(c,d). The behavior is known to results from rotational anisotropy and was already discussed in Figure 19(e,f). We then observed the

charge current deduced from our experimental data for the IrMn/Cu/CoFeB and IrMn/CoFeB samples (Figure 46(e,f)): $I_C = [V_{sym,\theta=-90°} - V_{sym,\theta=90°})]/(2R)$, where R is the resistance of the slab (as described in § II.2). In both cases, we observe a discontinuity near the transition temperature of a 1.2 nm thick IrMn layer. We emphasize that the observed discontinuties at ~ 120 K are in agreement with our previous results discussed in Figure 19.

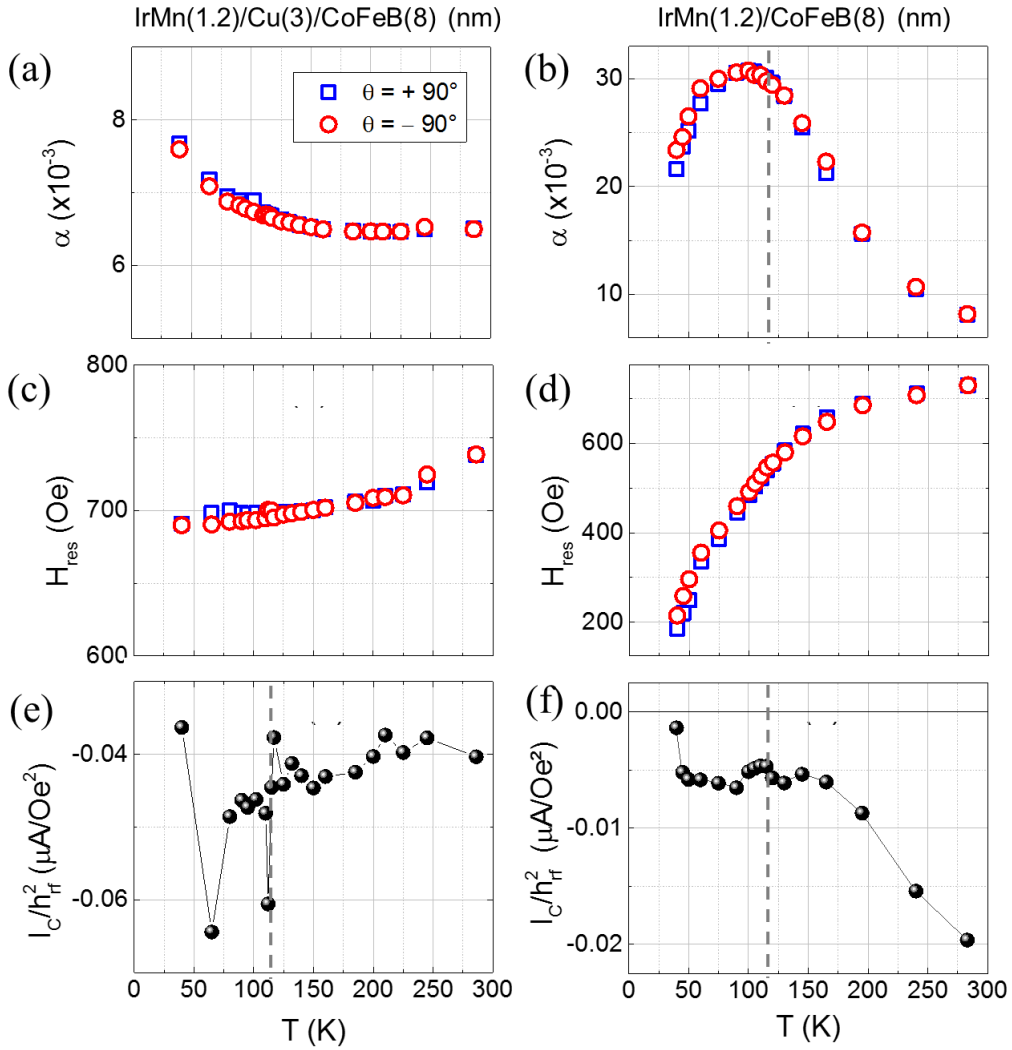

Figure 46 : Temperature (T)-dependence of the CoFeB layer's Gilbert damping (α) (a,b), the resonance field (H_{res}) (c,d), and of I_C (e,f) as measured for a Cu(4)/IrMn(1.2)/Cu(3)/CoFeB(8)/Al(2)O_x (nm) and Cu(4)/IrMn(1.2)/CoFeB(8)/Al(2)O_x (nm) samples. Vertical lines in (b,e,f) at T ~120K.

These preliminary data in search for the impact of non-collinear spin fluctuations on the ISHE in the IrMn antiferromagnet opened perspectives for further investigations. The next step in this study is to take advantage of the known thickness-dependence of the critical temperature of IrMn, as shown in Figure 19, in order to confirm that the anomaly obtained in the spin-charge conversion signal coincides with the expected phase transition for a given thickness. Also, other samples, e.g. made of spin-glass and weak ferromagnets, which are expected to show larger spin fluctuations near the phase transitions are being studied in the framework of the PhD project of Miina Leiviskä (2021-2024).

Chapter III

Charge transport specific to antiferromagnetic spin structures

This chapter deals with charge transport in antiferromagnets, compared to spin transport discussed in the previous chapters. Here the magnetotransport in epitaxial thin films of the Mn_5Si_3 antiferromagnet is extensively studied. We were particularly interested in the spontaneous Hall effect in this compound.

In § III.1 I recall the conceptual and experimental framework of charge Hall effects with a focus on antiferromagnets. It aims at introducing the mechanisms giving rise to a spontaneous Hall contribution in this class of magnetic materials.

§ III.1.1 is devoted to results that have revealed a spontaneous Hall effect in the collinear Mn_5Si_3 antiferromagnet. Mn_5Si_3 offers a vast playground for studies linking antiferromagnetic spintronics and topological structures since it has a collinear and a non-collinear antiferromagnetic phase at different temperatures. The experimental results were interpreted in terms of a novel time revesal ($\mathcal{T}$) symmetry breaking mechanism arising in a collinear antiferromagnet with a staggered Zeeman spin-splitting.

III.1 Introduction to Hall effects

In § II.1 I have introduced the mechanism giving rise to both spin Hall and anomalous (or spontaneous) Hall conductivities. In the context of the so called spontaneous Hall effect, one of the most prominent effect relies on the break of the required symmetries by ferromagnetic ordering [111]. In the past decade, much progress has been done in the identification of magnetic orderings beyond conventional anomalous Hall effect (AHE) in ferromagnets. Depending on the energy landscape of the magnetic system, it might favor magnetic moments to form an angle, which opened the path for novel magnetotransport properties in antiferromagnets.

III.1.1 Hall effects in ferromagnets

As far as ferromagnets are concerned, the relation for the Hall effect comprises two terms, one for the ordinary Hall contribution due to the external magnetic field H_z (Figure 47(a)) [13], and a second term due to AHE due to the magnetization M_z (Figure 47(b)) [14]: $\rho_{xy} = R_0H_Z+R_SM_Z$, here R_0 and R_S are ordinary and anomalous Hall coefficients, respectively [111]. The ordinary Hall effect is due to the deflections of carriers caused by the Lorentz force, which

leads to a charge accumulation resulting in a Hall voltage. Note that there is no spin accumulation because the number of spin up and down is the same. The AHE results from spin-dependent deflection of carriers, which produces a Hall voltage. For a long time, an anomalous Hall contribution was attributed solely to the $\mathcal{T}$-symmetry breaking due to the magnetization (M_Z) in ferromagnets and spin orbit interactions (SOI). In antiferromagnets, it was expected to vanish due to the compensation moments of the opposite sublattices. In simple collinear antiferromagnets, characterized by the antiparallel alignment of neighboring moments that are pointing along the same axis, this picture was accepted since the combination of the required symmetries results in a zero AHE contribution when the magnetic order is considered as a vector placed on the magnetic atoms sites. Throughout this chapter I will show that this have changed recently with developments on the microscopic understanding in the frame of antiferromagnetic spintronics due to the discovery of new macroscopic $\mathcal{T}$-symmetry breaking mechanisms in collinear antiferromagnets [180,181]. Note that an intrinsic contribution to Hall effect may be driven by the bulk band structure and has been expressed in terms of the Berry curvature (as discussed in § II.1). Moreover, recent studies have suggested that a huge AHE signal may emerge in frustrated magnets due to spin clusters [182] and in paramagnetic structures due to localized magnetic moments [183]. In such cases, the extrinsic skew-scattering mechanism dominates.

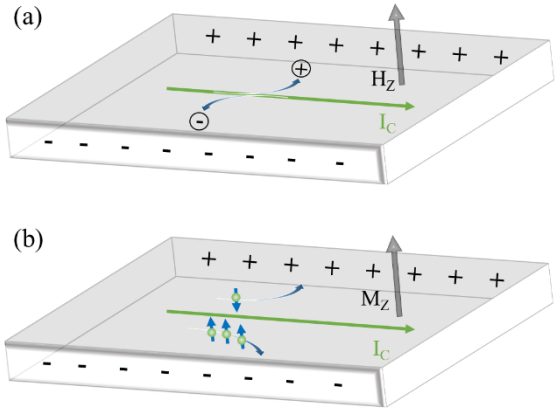

Figure 47 : Schematic illustration of: (a) the ordinary Hall effect (OHE) due to a external magnetic field and (b) the anomalous Hall effect (AHE) due to the magnetization in a ferromagnet.

III.1.2 Hall effects in antiferromagnets

III.1.2.1 Non-collinear antiferromagnets

Remarkbly, in the last decade it was shown that the breaking of the required symmetries can take place in coplanar non-collinear antiferromagnets with zero net magnetization [28,29,184]. It is noteworthy that in non-collinear antiferromagnetism, the moments are not aligned along the same axis, but they are still compensated. As discussed in § II.1.1.1, an intrinsic contribution to the Hall effect may be driven by the bulk band structure and has been expressed in terms of the Berry curvature (see Eq. II-2) [113]. Transposing to the discussion here, the $\mathcal{T}$-symmetry breaking is manifested by a non-zero Berry curvature, which itself acts as a ficticious magnetic field in reciprocal space. It finally results in a modification on the magnetotransport properties, resulting in a Hall contribution, when conduction electrons move across the Fermi surface. In non-collinear antiferromagnets, large AHE conductivities were initially observed experimentally in Mn_3Sn and Mn_3Ge with vanishing magnetization, as shown in Figure 48(a,b) [185,186].

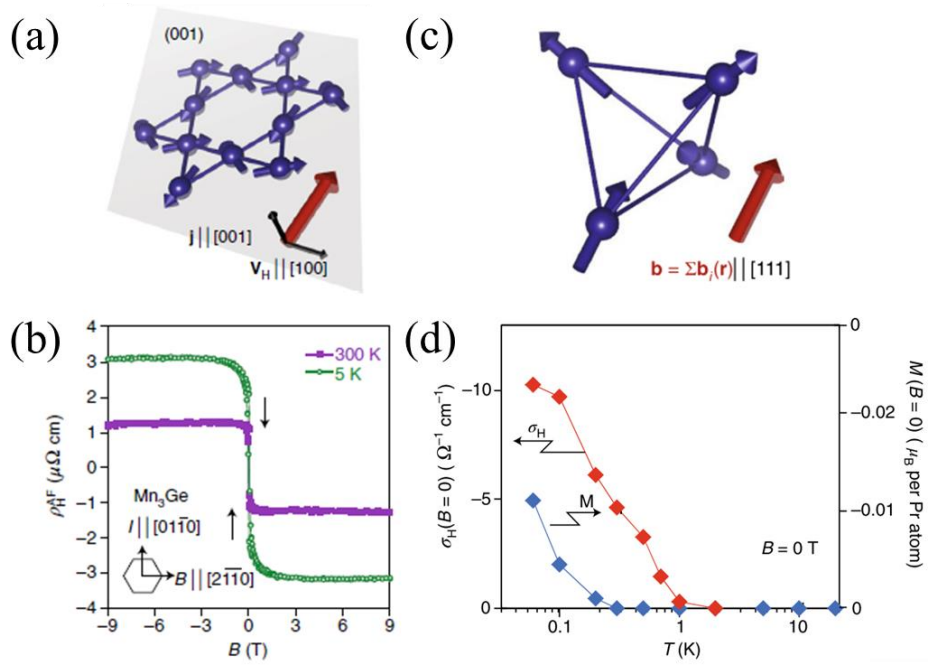

Figure 48 : (a) Spin structure of Mn_3Ge where the coplanar non-collinear magnetic order on the kagome lattice produce a large in-plane anomalous Hall effect, due to the 'topology' of the band structure in reciprocal space. (b) The measured Hall resistivity ρ_H^{AF} in Mn_3Ge. (c) Topological Hall effect generated by the real space chirality originated from the non-coplanar magnetic moments. (d) Temperature (T)-dependence of the topological Hall conductivity σ_H measured in a chiral spin liquid. Adapted from Refs. [28,186,187].

III.1.2.2 Non-coplanar antiferromagnets

Alternatively, in systems with non-coplanar spin arrangements, the spin chirality can induce a finite Berry phase and an associated ficticious magnetic field, which generates a Hall contribution also named topological (see Figure 48(c,d)) [187]. In such a case, the energy landscape of the magnetic systems favors a non-collinear and non-coplanar spin arrangement. Concerning the electronic transport in a material containing such magnetic arrangement, due to spin-spin interactions the spin tends to align to each moment locally. Due to the nonzero spin chirality, the electrons acquire a Berry phase. Here the $\mathcal{T}$-symmetry breaking takes place in the real space, because the electrons are moving by a spin arrangement in real space. Another important characteristic of the topological Hall effect is that it can be observed even without SOI, since the Berry phase is acquired by the electrons due to spin-spin interactions [28]. We can call this real space Berry phase in order to differentiate from that reciprocal Berry phase discussed above. The characteristic signature of the topological Hall effect on the resistivity is a bump for certain magnetic field range, for which the non-coplanar spin arrangement is stable. Such a Hall contribution with a topological origin was initially reported in the chiral spin liquids of pyroclore iridates [187] and then in the Mn_5Si_3 chiral antiferromagnetic alloy [188–190]. In Mn_5Si_3 policrystilline films, the effect manifest by a nonlinearity in the Hall resistivity observed when the antiferromagnetic order changes from a collinear to a non-coplanar spin arrangement with decreasing temperature. Such type of observation will also be discussed in more details in § III.2.2.2. Beyond antiferromagnets, magnetic materials where the non-collinear and non-coplanar spin texture required to generate the nonzero spin chirality include skyrmions. Such a topological Hall effect from a skyrmion is associated with a topological winding number of the skyrmion. Note that it differs from the skyrmion Hall effect which describes the deflection of the skyrmion center due to the Magnus force. As matter of fact, in antiferromagnetic skyrmions, the Magnus forces acting on either sublattice compensate one

another, meaning that antiferromagnetic skyrmions might move in straight lines [191]. On a sepatare topic, we will discuss experimental data in search for skyrmions in antiferromagnets in § IV.2.3.

It is important to highlight that the spin chirality is nonzero in non-coplanar (and non-collinear) spin arrangements and it vanishes in coplanar (and non-collinear) antiferromagnets, e.g., in the non-collinear antiferromagnetic structures of Mn_3Sn and Mn_3Ge.

III.1.2.3 Collinear antiferromagnets

As mentioned above, in collinear antiferromagnets, a spontaneous Hall contribution was expected to vanish. Recently, however, an alternative mechanism giving rise to a spontaneous Hall contribution was proposed theorethically [29,180] and detected experimentally [192] in RuO_2, which is a collinear antiferromagnet. Essentially, the symmetry breaking mechanism discussed so far (illustrated on Figure 48) can be catched considering the the magnetic ordering as a vector placed on the magnetic atoms sites. By the analysis of the spin vectors and spatial configurations of the magnetic atoms alone, there is no expected spontaneous Hall contribution in RuO_2. Alternatively, the breaking of the required symmetries is generated by the antiferromagnetism combined with the position of nonmagnetic atoms in the crystal, i.e., the crystal structure is responsible for the symmetry breaking of instead of the magnetic order (see Figure 49(a)). Figure 49(b) illustrates the crystal $\boldsymbol{\mathcal{T}}$-symmetry breaking generated in a collinear antiferromagnetic, where the position of the oxygen atoms produces an asymmetry of the magnetization density in diffent Ru lattices. Note that only when the complete magnetization density shape is taken into account, the $\boldsymbol{\mathcal{T}}$-symmetry breaking is observed, distinct from the usual AHE mechanisms. Figure 49(c) shows the Hall conductivity calculations of the crystal and anomalous parts. The last one arises by a small net moment arising from canting moments, analogous to the usual AHE in ferromagnets.

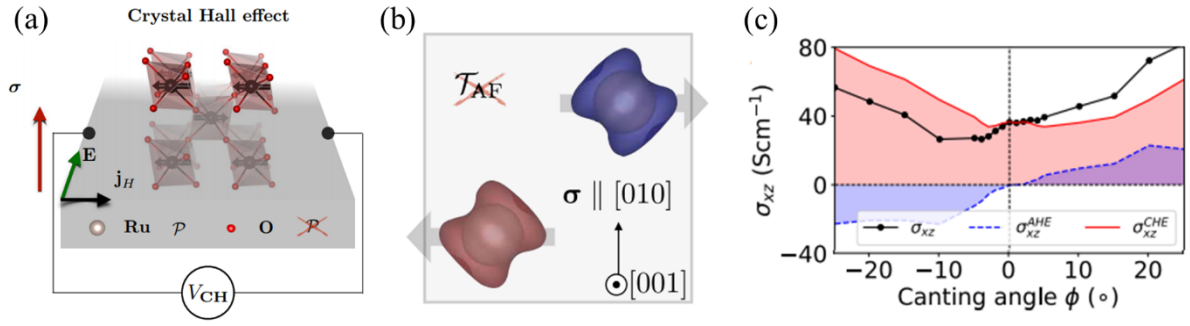

Figure 49 : (a) Illustration of the crystal Hall effect in a collinear antiferromagnet RuO_2. (b) Assimetry of the magnetization density due to the arrangement of oxygen atoms. (c) The dependence on the canting angle of the Hall conductivity and its separation into the anomalous and crystal parts, which are related to ferromagnetic and antiferromagnetic contributions, respectively. Adapted from Ref. [180].

It is worthy mentioning that several studies on thin film antiferromagnets have been interpreted based on the bulk spin structure. However, some results suggest that the spin structure of magnetic thin films might be different from the expected spin structure of bulks due to strain and high density of defects [193–195]. In most cases, the spin structure is not possible to be detected via conventional microscopy techniques in thin films.

In the following of this section we discuss experimental results showing the presence of a spontaneous Hall effect in epitaxial layers of the Mn_5Si_3 antiferromagnet with a vanishing net magnetization. Remarkably, it displays a remanent Hall conductivity on the order of

approximately 10 S.cm^{-1}. At the end of the paragraph, our experimental results are discussed in terms of a novel model considering a $\mathcal{T}$-symmetry breaking of itinerant Bloch electrons with an unconventional anisotropic spin-momentum interaction, whose straggered nature leads to the formation of two ferromagnetic-like valleys in the momentum space with opposite spin splittings. For consistency, this type of alternative mechanism for spontaneous Hall effect in antiferromagnets is not discussed in this section but rather in § III.2.2.1, after the experimental findings are shown.

III.2 Spontaneous Hall effect in the Mn_5Si_3 antiferromagnet [6]

The following of this chapter is adapted from Ref. [6] where the main findings can be found. It should be noted here that the results were obtained in the frame of a collaboration involving SPINTEC Grenoble (nanofabrication, electrical transport), CINaM Marseille (growth, structural characterization), TU Dresden / Uni. Konstanz (nanofabrication, electrical and thermal transport), JGU Mainz (theory), and FZU & Charles Uni. Prague (theory and optical measurements) - Ref. [6]: H. Reichlova (equal first), R. L. Seeger (equal first), R. González-Hernández, I. Kounta, R. Schlitz, D. Kriegner, P. Ritzinger, M. Lammel, M. Leiviskä, V. Petricek, P. Dolezal, E. Schmoranzerova, A. Bad'ura, A. Thomas, V. Baltz, L. Michez, J. Sinova, S. T. B. Goennenwein, T. Jungwirth, and L. Šmejkal, ArXiv:2012.15651v2 (2021). In the frame of this collaboration, I had the opportunity to make several stays in Dresden for experiments using a superconducting vector magnet.

III.2.1 Epitaxial crystal growth of Mn_5Si_3 thin films

The Mn_5Si_3 epilayers used in this study were grown by I. Kounta and L. Michez in Marseille. The epilayers were grown by ultrahigh-vacuum molecular beam epitaxy (MBE) with a base pressure of less than 10^{-10} Torr. The Si(111) substrates surface were cleaned by using a modified Shiraki method, for details reader is refered to Ref. [196]. A final oxide layer is then chemically formed to protect the Si surface from oxidation in air. Before depositing the epilayers, such oxide layer is thermally removed by annealing at 900° C in the MBE chamber. Subsequently, a buffer layer of 10 nm thick Si is deposited at 600° C, ensuring a high quality of the starting surface. The surface of the sample was monitored *in situ* by the reflection high energy electron diffraction (RHEED) technique that revealed an atomically flat surface with well developed (7×7) reconstruction (Figure 50(a)). The deposition of Mn and Si is performed at 170° C. High purity Mn and Si are evaporated using conventional high temperature effusion sublimation cells. The cell fluxes were calibrated by using the RHEED oscillations and a quartz microbalance in order to obtain the desired stoichiometry of the layers with a total growth rate in the range of 0.1-0.2 Å/s. The first monolayers exhibited the typical signature of a Mn_5Si_3-type crystal, a $(\sqrt{3}\times\sqrt{3})$R30° reconstruction [197]. Crystal quality was further improved by thermal annealing, the quality degree was monitored by RHEED pattern (see Figure 50(b)). Different growth parameters, such as the nominal thickness of the Mn/Si layers, the Mn and Si deposition rates and the growth temperatures, were optimized to minimize the presence of the spurious MnSi phase. We note that the Curie temperature of MnSi is around 30 K and therefore, cannot contribure to the measured signal up to 240 K, as will be discussed in Figure 51. Note that this is typical for Mn-based oxides which usually have low critical temperature. The

amount of the spurious phase can be controlled and its impact on the transport properties will be discussed in Figure 55. Figure 50(c) presents a TEM image showing the orientation of the Mn_5Si_3 on the Si substrate. It confirms the epitaxial relationships, as indicated on the figure, and reveals the location of MnSi at the interface between the Si substrate and Mn_5Si_3.

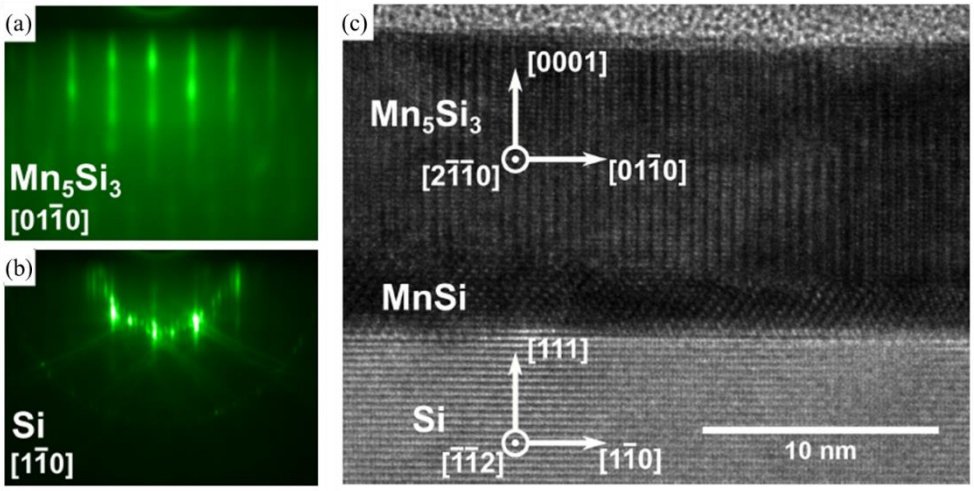

Figure 50 : Reflection high-energy electron diffraction patterns taken along (a) Mn_5Si_3 [01$\bar{1}$0] and (b) Si [1$\bar{1}$0] azimuths showing the reconstruction observed during the growth of a Mn_5Si_3 film. (c) High resolution transmission electron microscopy (TEM) image showing an approximately 12 nm thick Mn_5Si_3 film. The thin layer of MnSi formed at the substrate interface is indicated. Adapted from supplementary information of Ref. [6].

III.2.2 Magnetotransport and demonstration of the effect

To perform the magnetotransport measurements, the thin films were patterned into H-bars (measuring 8 µm wide and 180 µm long) by laser lithography and plasma etching. An optical image of the resulting H-bar is shown in Figure 51(a). Electrode contacts were created using aluminum wire-bonding on 150 x 200 µm² contact pads, it allows the transversal and longitudinal resistivity to be measured simultaneously. Electrical parameters were then measured using standard four-point current-voltage geometries, applying an electric current of +0.1 mA and -0.1 mA and the measured resistance values are averaged (delta method). This method compensates voltage offsets arising from possible thermoelectric contributions.

III.2.2.1 Temperature dependence of resistivity and magnetic structure of Mn_5Si_3

The temperature (T-)dependent longitudinal resistivity, ρ_{xx}, shown in Figure 51(b) indicates a metallic character of our Mn_5Si_3 films. Note that its magnitude is similar to the one reported in thicker sputtered layers of Mn_5Si_3 [188]. Previous reports on bulk and thicker layers identified a non-coplanar antiferromagnetic phase AF_1 below the transition temperature T_{N1} ~ 70 K and a collinear antiferromagnetic phase AF_2 between T_{N1} ~ 70 K and T_{N2} ~ 100 K [188–190,198–200]. In our samples, we also observe two kinks in the longitudinal resistivity. Such behavior is better resolved by plotting the temperature derivative of ρ_{xx}, signaling the transition between the different phases. The first transition corresponds to T_{N1} from the literature and mentioned above. Remarkably, we observe a significant enhancement of T_{N2} ~ 240 K in our epitaxial thin films. We attribute the enhancement of T_{N2} to a sizeable strain in the epilayers as evidenced by our T-dependent XRD and TEM studies. Figure 51(c) shows the T-dependence of the lattice constants obtained from the XRD measurements. The lattice constant a_{Si} of the cubic silicon substrate exhibits only a weak temperature dependence. The out-of-plane constant c of the

Mn_5Si_3 epilayer is in the whole temperature range smaller than the corresponding values obtained in bulk crystals [198]. This demonstrates the presence of epitaxial strain which can stabilize the antiferromagnetic ordering in our epilayers up to higher temperatures [201]. In Figure 51(c), we see that the collinear antiferromagnetic phase in bulk Mn_5Si_3 is stabilized for c smaller than ~ 4.8 Å (dotted line in Figure 51(c)) which corresponds to a temperature range between 70 and 100 K, marked as $AF_{2,bulk}$. Our strained epilayers exhibit a lattice constant c smaller than 4.8 Å in a wider temperature range marked as AF_2. This potentially explains the enhancement of T_{N2}.

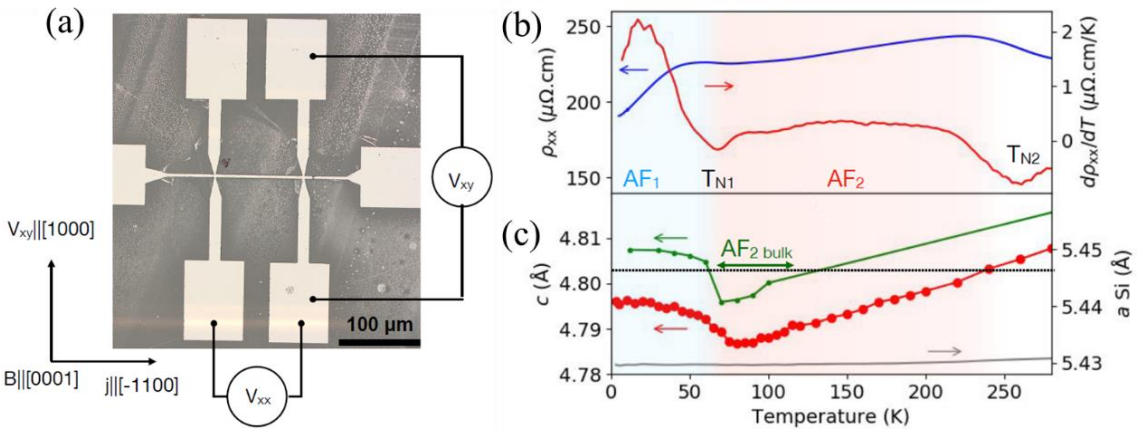

Figure 51 : (a) Optical micrograph of the litographically patterned H-bar, orientation of the crystal, and applied magnetic field H. (b) Temperature (T-)dependent longitudinal resistivity ρ_{xx} and its derivative $d\rho_{xx}/dT$ reveal two antiferromagnetic phases, AF_1 and AF_2 (see discussion on the text). (c) Lattice constant c || [0001] obtained from T-dependent XRD compared to bulk Mn_5Si_3 (green) taken from Ref. [198].

It is worthy emphasizing that in the temperature range of 80 to 300 K, the measured out-of-plane lattice parameter of our films exhibits only a weak change of its linear slope near T_{N2} without abrupt changes (Figure 51(c)). This indicates that the hexagonal unit cell is preserved over this wide temperature range and suggests that our epilayers do not exhibit the antiferromagnetic doubling of the unit cell, as observed in bulk samples below T_{N2} [198,200], and strain-relaxed single crystals [189]. The antiferromagnetic doubling makes the system invariant under a $t\mathcal{T}$-symmetry (t represents partial unit cell translation) which explains the reported absence of the AHE between T_{N1} and T_{N2} in bulk crystals [189]. The unit cell doubling in bulk is accompanied by an orthorhombic symmetry lowering which, as mentioned above, is not observed in our epilayers. Correspondingly, we do not expect the $t\mathcal{T}$-symmetry in our epilayers in the antiferromagnetic phase below T_{N2} which opens the possibility for observing the AHE signature of macroscopic $\mathcal{T}$-symmetry breaking in our antiferromaget, as will be further discussed in § III.2.2.1. It further confirms that ordering temperatures in thin films may be different from the bulk value. For example, residual strain may vary depending on substrate, thickness, and deposition conditions. Below, we experimentally confirm this expectation and show that the anomalous Hall signal and vanishing magnetization are consistent with the collinear checkerboard ordering.

III.2.2.2 Longitudinal and transversal resistivities

Figure 52(a) shows the raw longitudinal resistance data with a magnetic field applied perpendicular to the film plane for selected temperatures. Figure 52(b) shows the T-dependence of the longitudinal magnetoresistance ΔR_{xx} for different magnetic fields. The fact

that the ΔR_{xx} is clearly suppressed in the high temperature collinear phase will be further discussed below.

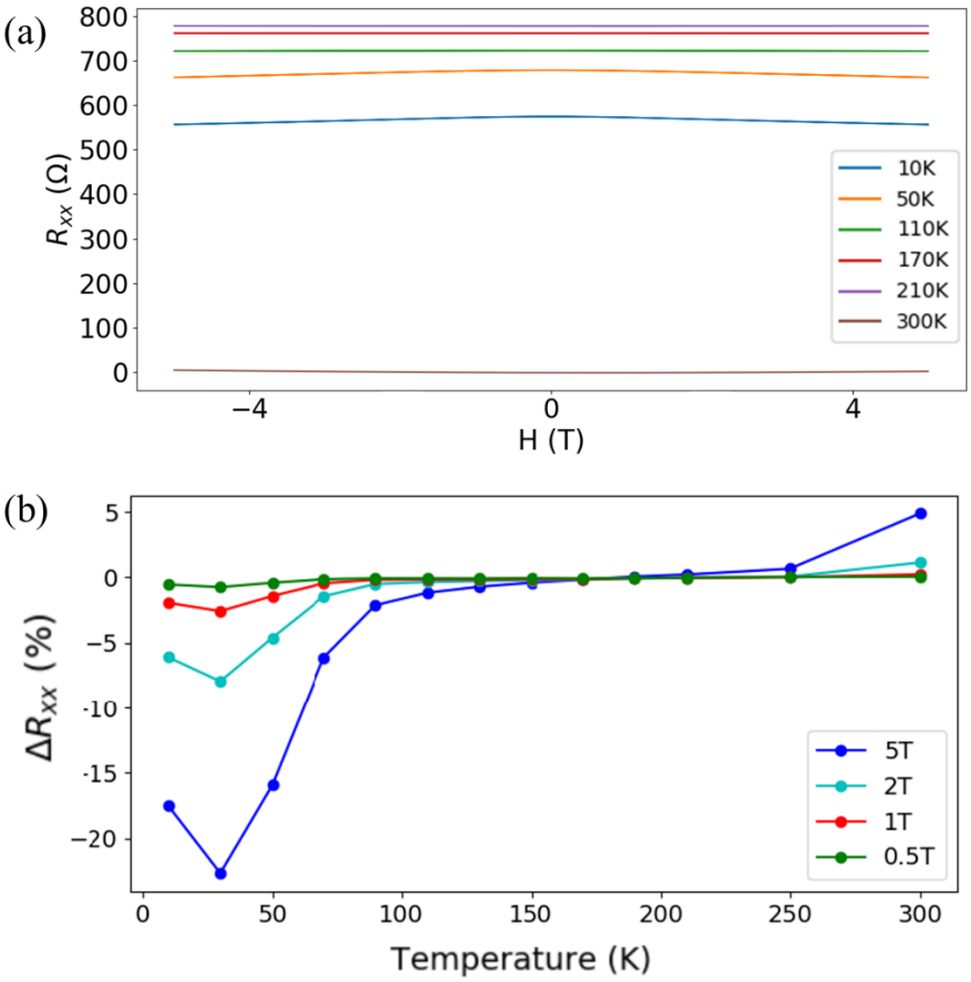

Figure 52 : (a) Longitudinal resistance measured at several temperatures under a magnetic field applied in the out-of-plane. (b) *T*-dependent longitudinal magnetoresistance recorded with an out-of-plane magnetic field of 0.5, 1, 2, and 5 T. (a) is adapted from supplementary information of Ref. [6].

Simultaneously, we measure the total transversal (or Hall) resistivity ρ_{xy}^{total} (see Figure 53(a) for raw transversal resistance R_{xy} for selected temperatures). By fitting the linear in-field ordinary Hall resistivity contribution, we determine the ordinary Hall coefficient, R_H ~ 1-4 × 10^{-10} m^3C^{-1}, which corresponds to a metallic carrier density, n ~ 10^{22} cm^{-1} assuming a single-band model. The Hall resistivity after subtracting the linear ordinary Hall effect signal is shown in Figure 53(b) for T = 50 K. It is written as $\rho_{xy}^{AF} = \rho_{xy}^{total} - R_H H_z$. We observe in the whole temperature range below 240 K a sizable anomalous Hall resistivity, confirming the presence of magnetic ordering. The anomalous Hall resistibity ρ_{xy}^{AF} exhibits a large coercive fields of approximately 2 T. It is consistent with the presence of magnetic order in our weakly spin-orbit coupled Mn_5Si_3. Moreover, our magnetometry measurements show a negligible remanent magnetization of a magnitude below the detection limit of approximately 0.01 μ_B per unit cell, as shown in Figure 54. This is also consistent with the picture of a compensated antiferromagnetic phase below T_{N2}. It illustrates that the diamagnetic contribution from the Si substrate dominates the signal in the entire temperature range, except from a subtle nonlinear contrinution near zero field. We emphasize that there is no feature close to the high coercive

fields observed in the anomalous Hall resistibity. Note that no other signal from spurious moments were found within our measurement sensitivity.

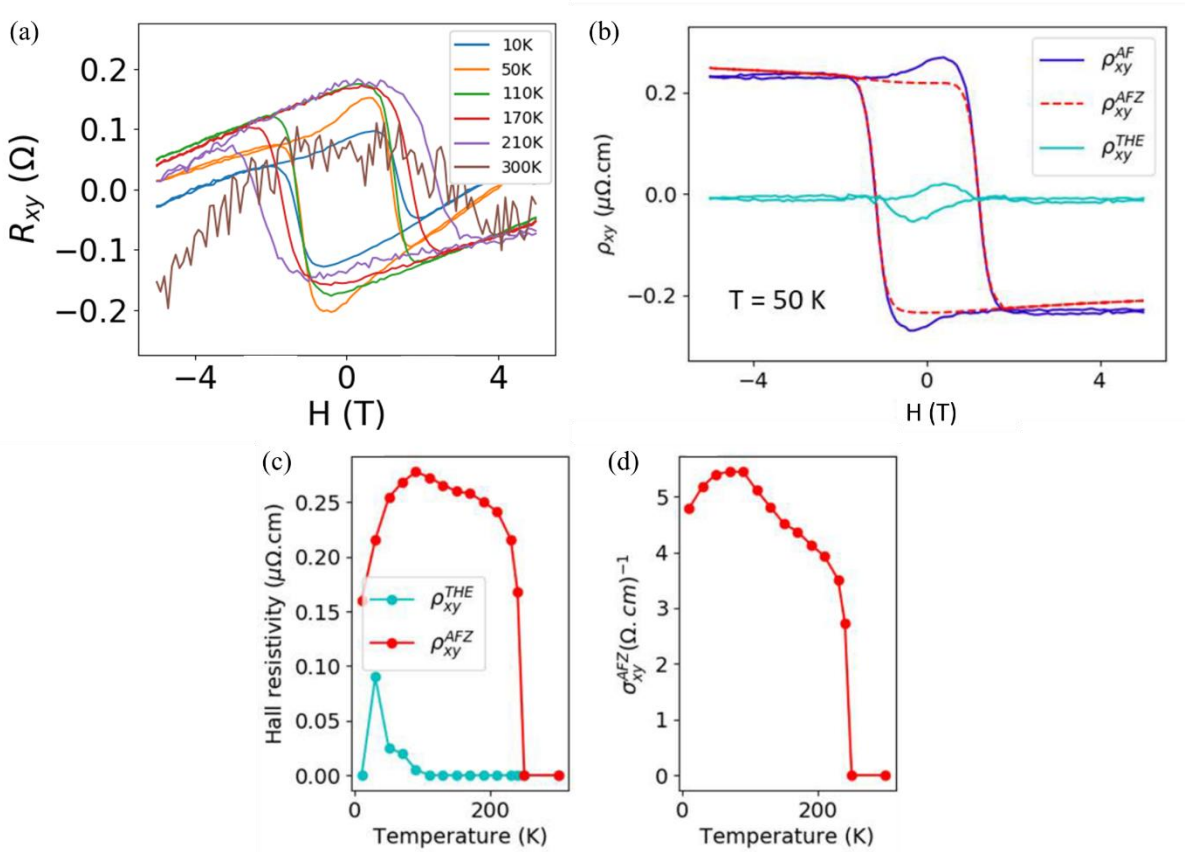

Figure 53 : (a) Transversal resistance measured at several temperatures with under an magnetic field applied in the out-of-plane. (b) Decomposition of the Hall resistivity into a collinear (ρ_{xy}^{AFZ}) and non-collinear (ρ_{xy}^{THE}) componenets as measured for 50 K. *T*-dependence of anomalous Hall resistivity (c), decomposed into the collinear and non-collinear components, and of the anomalous Hall conductivity (d). (a) is adapted from supplementary information of Ref. [6].

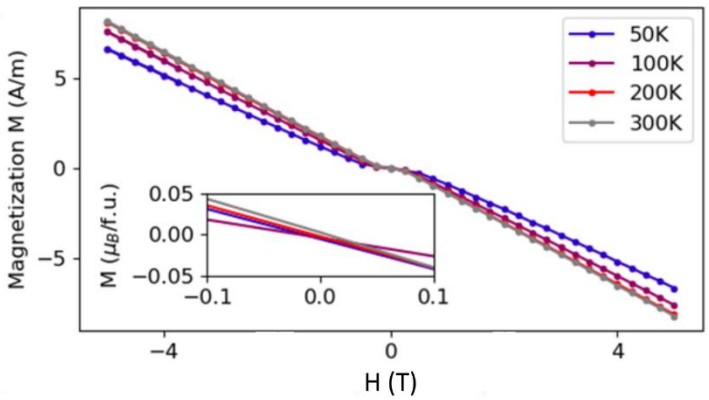

Figure 54 : Magnetization as a function of the magnetic field. The inset shows vanishing remanent magnetization and a small slope at low magnetic fields.

After removing the linear slope, i.e. the ordinady Hall effect, the resulting data is separated into symmetric (V^{sym} = (V(+H)-V(-H))/2) and antisymmetric ($V^{antisym}$ = (V(+H)+V(-H))/2) components. In particular, the antisymmetic part is the Hall signal, while the symmetric part is an artifact. This procedure removes small constant offsets in the transverse resistivity caused by misalignments of the Hall contacts, which produces a symmetric signal as the longitudinal resistivity. In Figure 53(b) only the antisymmetric part is shown. In Figure 53(b) the

antiferromagnetic related Hall resistivity is decomposed into two contributions: $\rho_{xy}^{AF} = \rho_{xy}^{AFZ} + \rho_{xy}^{THE}$. The anomalous Hall (AFZ, also named antiferromagnetic Zeeman contribution, see § III.2.3) and topological Hall (THE) resistivities are extracted by fitting a cosh function, where the anomalous Hall contribution is taken from the amplitude of the cosh fit. The ρ_{xy}^{THE} apprears below T_{N1} and displays a bump-like hysteresis, reaching 0.09 μΩ.cm. It is consistent with the topological Hall effect due to a non-coplanar spin structure [188–190], as reported on the literature for sputtered films of Mn_5Si_3 with $\rho_{xy}^{THE} \sim 0.02\text{-}0.04$ μΩ.cm [190], see also § III.1.2.2. The transition from a collinear antiferromagnetic phase above T_{N1} to an additional non-coplanar spin component below T_{N1} is corroborated in our films by the enhancement of the longitudinal magnetoresistance is the low-T range, as shown in Figure 52(b) [202,203]. In constrast, the high temperature magnetic phase exhibits a very small magnetoresistance, in agreement with the presence of collinear antiferromagnetism. It is worthy highlighting that the magnetoresistance in the low-T phase is sizable even for small applied magnetic fields of 0.5 T, where the topological Hall effect is maximal. We observe that the ρ_{xy}^{AFZ} dominates the signal over the entire temperature range, 10-240 K (see Figure 53(c,d)). We ascribe this Hall resistivity, observed below T_{N2}, to the collinear antiferromagnetic projection of the moments even in the low temperature non-coplanar phase. It dominates the signal over the entire temperature range. Remarkably it shows a spontaneous value at remanence reaching 0.2-0.7 μΩ.cm. Figure 53(d) we show the anomalous Hall conductivity $\sigma_{xy}^{AFZ} = \rho_{xy}^{AFZ} / \rho_{xx}^{2} \, (H = 0)$ in the whole temperature range in which the samples are magnetically ordered.

III.2.2.3 Crystal quality impact on the spontaneous Hall resistivity

We will now comment on the crystal quality impact on the spontaneous Hall resistivity. We remark that in policrystalline films the Hall resistivity can also vanish due to the compensation from domains with opposite Néel vector unlike in our epitaxial films [188,190]. In Figure 55 we illustrate the fact that the magnitude of the spontaneous Hall effect decays with lowering the crystal quality. Figure 55(a) shows the T-dependence of the spontaneous Hall resistivity for four samples of different crystal quality. The magnitude of σ_{xy}^{AFZ} reaches values between 5 and 20 $S.cm^{-1}$ (Figure 55(b)). While different samples with varying quality exhibit variation in the Hall resistivity amplitude, the general trend, non-zero spontaneous Hall resistivity until aproximatelly 240 K and zero above, persists. The measured Hall resistivity is clearly correlated with the samples quality, see Figure 55(c). Higher quality, indicated by a higher ratio of Mn_5Si_3/MnSi phases extracted from XRD data, corresponds to higher Hall resistivity. This excludes an impurity origin of our signal and is in general in contrast to the behavior expected of the anomalous Hall effect in simple ferromagnets [111].

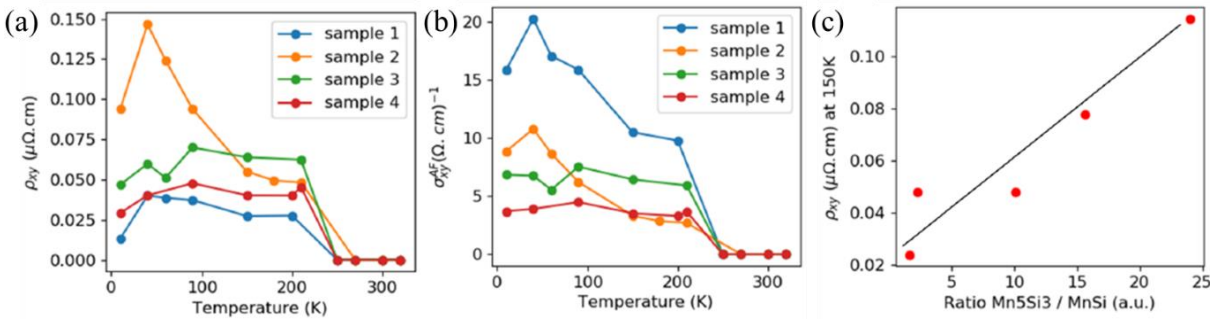

Figure 55 : Spontaneous Hall effect for various samples of different quality. *T*-dependence of anomalous Hall resistivity (a) and of the anomalous Hall conductivity (b). (c) Correlation of the measured Hall resistivity with samples quality. Sample quality is estimated by using the ratio of Mn_5Si_3/MnSi phase extracted from XRD data [6].

III.2.3 Theoretical interpretation of the experimental results

As far as individual atoms are concerned, breaking of $\mathcal{T}$-symmetry by an applied magnetic field leads to the Zeeman spin-splitting of the energy levels of the electron orbitals. The ordinary Hall effect, discussed in § III.1, which is measured when a conductor is subjected to an applied magnetic field arises as consequence of the Zeeman spin-splitting. In ferromagnets, the magnetic order of atoms makes the $\mathcal{T}$-symmetry breaking spontaneous. In this case, the Zeeman effect occurs due to the internal electronic exchange couping rather than an externally applied magnetic field. Electrically, it can be probed by the anomalous Hall effect (in the limit of zero magnetic field it is also called spontaneous Hall effect).

As already mentioned in § III.1, the spontaneous Hall effect (and also the Zeeman-split bands and other $\mathcal{T}$-symmetry breaking phenomena) has been considered to be excluded in antiferromagnets with an antiparallel alignment of atomic moments in the crystal [28,184]. Recently, relativistic spin-orbit interaction [204] or anisotropic magnetization densities [180,181,205] were predicted to split bands in antiferromagnets. In our work, it is discussed in terms of a macroscopic $\mathcal{T}$-symmetry breaking in an antiferromagnet with a staggered Zeeman spin splitting. For a description at the model Hamiltonian level reader is refered to Refs. [6,206]. Figure 56 shows the hexagonal unit cell of a paramagnetic crystal of Mn_5Si_3. Neutron scattering data in bulk crystals showed that 4 out of 6 $Mn^{(2)}$ sites in the unit cell are antiferromagnetically ordered in the temperature range of 70-100 K. The remaining 6 Mn and 6 Si atoms are nonmagnetic. There are three different possible permutations of the 4 antiferromagnetic moments: two stripy orderings ($\uparrow\downarrow$ and $\uparrow\uparrow$), and one checkerboard ordering ($\begin{smallmatrix}\uparrow & \downarrow\\ \downarrow & \uparrow\end{smallmatrix}$) with all nearest-neighbour interactions antiferromagnetic. The magnetization density isosurfaces (Figure 56) were calculated without relativistic spin-orbit interaction and are nearly isotropic around the atomic sites. Remarkably, a recent study considering symmetry and topology classification have established a new class of magnetic materials called altermagnets [206]. Considering altermagnetism and linking spin symmetry groups and physical properties, it possible to show that Mn_5Si_3 belongs to a spin symmetry group predicted to show spontaneous Hall effect.

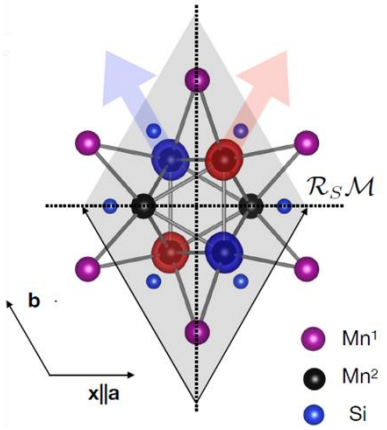

Figure 56 : Magnetization density isosurfaces of Mn_5Si_3 where red and blue indicate opposite spin polarizations [6].

Figure 57 shows first principles calculations evidencing the anisotropic staggered Zeeman interaction on the band structure of a collinear antiferromagnet Mn_5Si_3. Remarkably, the checkerboard ordering, with all nearest neighbourhood antiferromagnetic, breaks the $\boldsymbol{\mathcal{PT}}$-symmetry. This opens the possibility of generating the $\boldsymbol{\mathcal{T}}$-symmetry breaking in the band structure, while preserving zero net magnetization. Figure 57 shows the spin polarized energy bands calculated in the antiferromagnetic phase without (a) and with (b) spin-orbit interaction. Therefore, it is observed that the effect of the spin-orbit coupling on energy scales of the valleys and their Zeeman splitting is negligible, owing to the combined effect of light Mn and Si elements and the Coulomb-exchange origin of the staggered spin-momentum interaction.

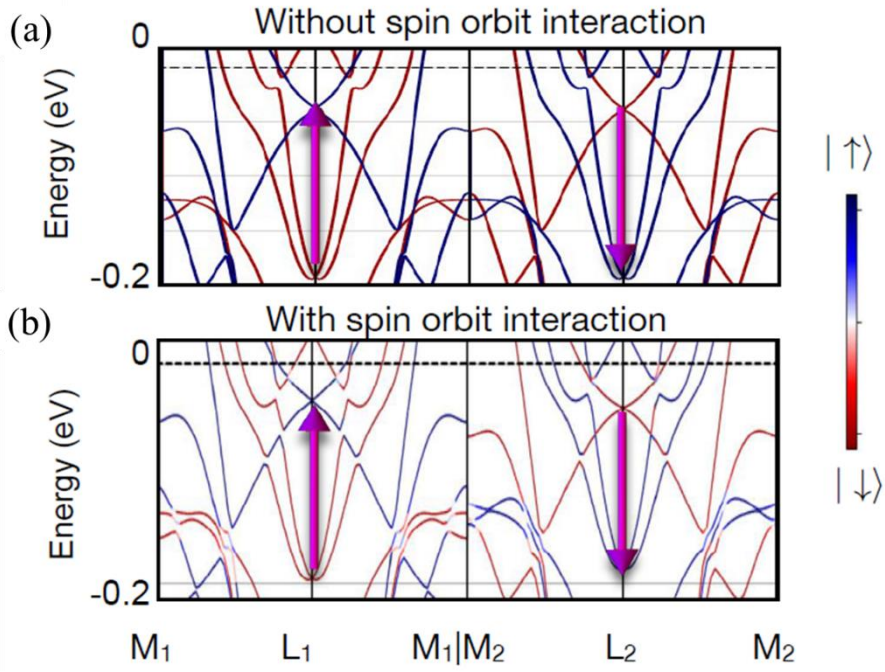

Figure 57 : Energy band and spin polarization along the two valleys calculated without (a) and with (b) spin-orbit interaction [6].

It is next demonstrated that the macroscopic $\boldsymbol{\mathcal{T}}$-symmetry breaking arising from the unconventional staggered spin-momentum can be observed in magnetransport experiments. Figure 58(a) shows the Berry curvature calculations for a model of our antiferromagnet Mn_5Si_3. For details on the relativist DFT theory used to derived the Berry curvature reader is refered to Ref. [6]. Figure 58(b) shows the Berry curvature intergrated over the Brillouin zone

which is proportional to the intrinsic contribution, independent of scattering, of the anomalous Hall conductivity σ_{xy} [111]. Such calculations illustrate that the Hall conductivity can reach values comparable to typical ferromagnets. A sizable σ_{xy} ~ 5-20 S.cm^{-1} within an approximately 100 meV energy window around the Fermi level was thus predicted by the theoretician collaborators. Note that this value is in excellent agreement with the Hall conductibity we have obtained experimentally in our epitaxial thin films of Mn_5Si_3 (see Figure 55(b)).

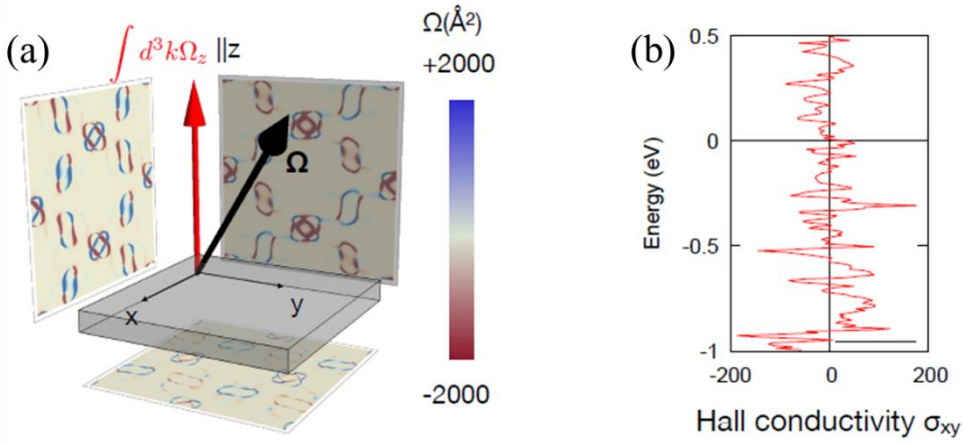

Figure 58 : (a) The hall vector and and crystal momentum resolved Berry curvature. (b) Calculated anomalous Hall conductivity [6].

Summary

In summary, the magnetotransport in epitaxial thin films of the Mn_5Si_3 antiferromagnet have experimentally been studied. Various contributions to the measured transversal signal were carefully disentangled, showing that the signal is dominated by a robust spontaneous Hall contribution, which persists at zero magnetic field. By showing structural, magnetization and magnetotransport results in a sample series we discuss the role crystalline quality in addition to magnetic symmetries on our results. The experimental results are interpreted in terms of a model considering a $\mathcal{T}$-symmetry breaking of itinerant Bloch electrons with an unconventional anisotropic spin-momentum interaction.

Before concluding this chapter, we want to emphasize that the macroscopic $\mathcal{T}$-symmetry arising from the unconventional staggered spin-momentum interaction might open the doors in spin physics and applications. Among the new perspectives in spintronics applications, it opens new possibilities for efficient spin-charge conversion for spintronics information technologies. As an example, it can facilitate the realization of the antiferromagnetic analogues of giant (or tunneling) magnetoresistance and spin transfer torque, making antiferromagnets active elements for memory applications. Ref. [207] presents theoretical models for GMR and TMR considering staggered spin-momentum interaction in collinear antiferromagnets. This theoretical study is directly related to the experimental findings shown in § III.2.

Besides possible applications, there is considerable amount of work to be done in the epitaxial thin films of Mn_5Si_3. First, as shown in Figure 51(c) the transition from non-collinear to collinear structure occurs concomitantly with an abrupt decrease of the out-of-plane constant *c*. Therefore, the spin structure is intimately related to crystal symmetries. It opens the possibility to manipulate the magnetic order by strain application. To perform experiments of this kind, Mn_5Si_3 will tentatively be grown on piezoelectric substrates capable of imposing strain by voltage control. Second, scanning thermal gradient magnetometry experiments are planned

within the consortium. Such experiments are based on a focused laser spot that is scanned across the sample surface [208]. The laser light heats the sample locally, generating a thermal gradient along the film normal. By recording the Nernst voltages induced by the thermal gradient it is possible to infer the local magnetic orientation. With this experiments, the aim is to study the local magnetic orientation in the Mn_5Si_3 films. Third, studies of the magnetothermoelectric experiments in Mn_5Si_3 will be attempted. For this we have prepared on-chip heater and thermometer structures to perform sensitive measurements as described in Ref. [209].

Moreover, there are other aspects of the magnetotransport experiments to be better explored. In the supplementary information of Ref. [6] the magnetic anisotropy energy was studied for different orientation of the Néel orientation. This suggest an anisotropy of the AHE signal. To tackle this question, we have prepared devices with H-bars along different orientations. Other points that are currently being studied are the mechanism of magnetic order reversal and anisotropies in the system. Those studies are being carried out across the consortium mentioned at the beginning of § III.2. It includes, at SPINTEC, the framework of the PhD project of Miina Leiviskä (2021-2024)

Chapter IV

Charge transport specific to magnetic spin textures

This chapter deals with charge transport in ferromagnet and antiferromagnet spin textures. While § III focused on magnetotransport specific to the antiferromagnetic arrangement of the spin textures, the purpose of this chapter is to evaluate whether magnetic textures in antiferromagnets matter for transport, and to what extend it is possible to control textures in antiferromagnets for the purpose of performing transport experiments. Note that magnetotransport effects related to the specific arrangement of the magnetic textures, such as skyrmions, vortices and domain walls, were introduced in § III.1.2.

In § IV.1 I recall the conceptual and experimental framework of superconducting proximity effects near domain walls in ferromagnets. We discuss systematic experiments performed with ferromagnet(Pt/Co)/spacer(IrMn and Pt)/superconductor(NbN) heterostructures to observe the recovery of the superconducting critical temperature, showing how to optimize such effect. Particularly, from our experimental data, we can obtain the penetration depth of Cooper pairs in the IrMn metallic antiferromagnet. The next step is to create spin textutes in antiferromagnets and to use superconducting proximity effects near such antiferromagnetic textures.

§ IV.1.3 is therefore devoted to explore the replication of spin textures from ferromagnets in antiferromagnets using exchange bias. Using the high-spatial-resolution magnetic microscopy technique XMCD-PEEM, we observe magnetic textures within the IrMn interfacial layer from the XMCD signal of the uncompensated Mn spins at the interface.

IV.1 Superconducting transport and proximity effects [7]

This section is adapted from Ref. [7] where the main findings were published. The theoretical model used to explain the experimental findings was made by Manuel Houzet (PHELIQS, Grenoble) and Alexander Buzdin (LOMA, Bordeaux) - Ref. [7]: R. L. Seeger, G. Forestier, O. Gladii, M. Leiviskä, S. Auffret, I. Joumard, C. Gomez, M. Rubio-Roy, A. I. Buzdin, M. Houzet, and V. Baltz, Phy. Rev. B 104, 054413 (2021).

IV.1.1 Introduction to the superconducting proximity effect

Superconducting proximity effect is charactherized by the propagation of Cooper pairs from a superconductor into adjacent metallic layers [210,211]. In such cases, the coherence length of Cooper pairs characterizes the depth for which the supercoducting correlations are induced in

the otherwise non-superconducting materials. In this case, the superconducting wave function decays exponentially inside the metallic material. As Cooper pairs propagates towards the adjacent layers, the proximity effect weakens superconductivity due to the lack of paired electrons in the superconductor, resulting in a decrease of the superconducting critical temperature. Note that this process occurs whenever a superconductor is in direct contact with a metallic layer, being the interfacial quality critical for the strength of the proximity effect.

Note that the terminology 'proximity effect' applies for a rather general phenomenon beyond the superconducting phase transition on superconductor/metallic material bilayers [211]. For example, in the case of surface magnetism, the critical temperature at the surface may be higher than the bulk value, resulting in an induced magnetization nearby following the surface magnetic transition. On the other side, the bulk also affects the surface transition.

IV.1.1.1 Superconducting proximity effect in a saturated magnet

As far as bulk compounds are concerned, superconductivity and ferromagnetism do not coexist easily. The opposite spins into Cooper pairs in superconductors is naturally incompatible with ferromagnetism, in which parallel aligment of spins is favorable in order to minimize the exchange energy. In other words, ferromagnetism is a source of Cooper pair breaking. Alternatively, artificially fabricated ferromagnetic/superconductor layered stacks represent a possibility to study the interplay between magnetism and superconductivity. The Cooper pairs can penetrate into the adjacent ferromagnetic layer and induce superconductivity there with a qualitatively different behavior from that in a non-magnetic metallic material. As a consequence, a variety of phenomena have been described in ferromagnet/superconductor hybrids, such as the spin switch effect [212–214], the superconducting magnetoresistance effect [215,216], and domain wall superconductivity [217–222].

Figure 59 illustrates the schematic behavior of the propagation of the superconducting wave function into a ferromagnetic metal near a superconductor/ferromagnetic interface, indicating the relevant characteristic lengths. Inside the ferromagnet, due to the large exchange field the superconducting wave function displays an oscillatory decay [210,211,223]. In the clean limit, it can be qualitatively understood by considering a Cooper pair in a superconductor as two electrons, with opposite spin and momenta, sitting inside an exchange field. While the electron with its spin aligned along the exchange field direction has its energy decreased, the opposite electron has an energy increase by the same value. As a consequence, they start to propagate with different wave vector, and the Cooper pair as a whole acquire a momentum, and therefore the superconducting wave function oscillates. Concerning the dirty limit, the approach consist in using the Usadel equations to describe the Cooper pair motion [219,224].

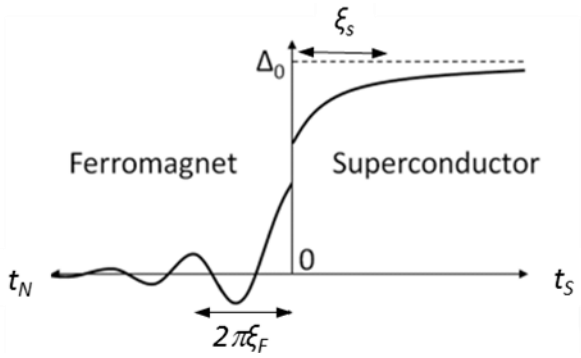

Figure 59 : Schematic behavior of the superconducting wave function near a superconductor/ferromagnet interface, the relevant characteristic lengths are indicated. Adapted from Ref. [223].

So far we have considered the ferromagnet layer as uniformly magnetized. In other words, the exchange field sampled by the Cooper pairs is uniform. With regard to proximity effect near a domain wall, a different situation takes place due to the rotation of the exchange field. As a result, we may expect a different impact on superconductivity. This scenario will be further discussed in the following paragraphs.

IV.1.1.2 Influence of domains and domain walls and open questions

Now I will comment on domain wall superconductivity. In general, the Cooper pairs experience the short range exchange field averaged over the superconducting coherence length. This phenomenon reduces the critical temperature (T_C) of the superconducting layer in superconductor/ferromagnetic bilayers. A magnetic domain wall flanked by opposite spins reduces the averaged exchange field and thus allows partial recovery of the superconducting temperature, ΔT_C. Recovery is achieved through the creation of an additional and more efficient superconducting pathway in the magnetic layer [211]. In practice, ferromagnetic domains also generate long-range dipolar magnetic fields. While nucleation of the superconductivity can occur near domain walls [217,225], dipolar fields may also cause the overall superconducting temperature to drop. This type of competition between exchange and dipolar interactions is especially significant for ferromagnets with out-of-plane anisotropy, such as [Pt/Co] multilayers [220]. Consequently, observation of the actual temperature enhancement due to the proximity effect near ferromagnetic domain walls is difficult. To overcome the inherent difficulty, the effects of two interfaces can be cumulated, for example by sandwiching a 38-nm-thick Nb superconductor between $[Co(0.6)/Pt(1.5)]_4$ and $[Co(0.4)/Pt(1.1)]_4$ (nm) ferromagnetic multilayers, as for the results shown in Figure 60. This approach allowed Zhu *et al.* [221] to demonstrate a small ferromagnetic domain wall proximity effect of $\Delta T_C/T_C = 0.6\%$. Beyound the enhacement of T_C they have studied the the impact of the of domain walls arrangement, confirming that in superconductor/ferromagnetic the superconductivity occurs in the domain wall region.

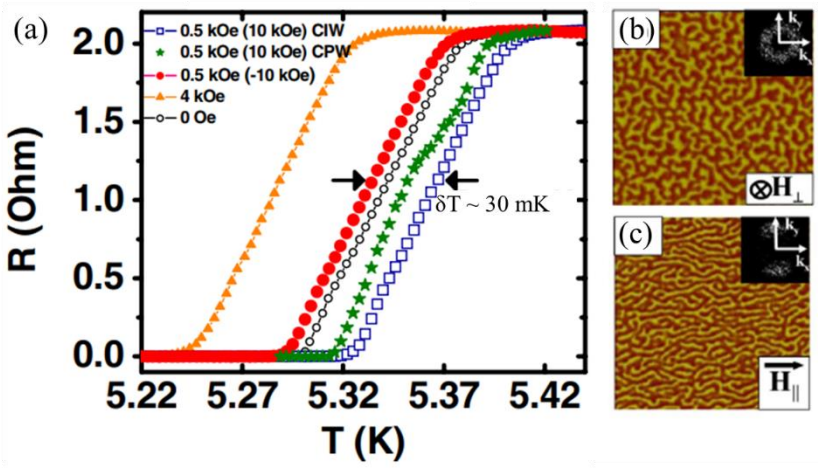

Figure 60 : (a) Temperature (*T*)-dependence of the resistance (*R*) for several magnetic configurations of a //[Co(0.6)/Pt(1.5)]$_4$/Nb(38)/[Co(0.4)/Pt(1.1)]$_4$ stack (nm). The measurements were made for different values of magnetic field applied in-plane. CIW and CPW correspond to two cases where the magnetic configuration is made of stripe domains and for which the current was applied parallel and perpendicular to the stripes, respectively. ΔT represents the critical temperarute T_C enhancement achieved by controlling the domain wall arrangement. Representative MFM images obtained at room temperature with (b) a labyrinth and (c) a stripe domains to illustrate the manipulation of the domains with *in situ* field-deposited stacks. Adapted from Ref. [221].

In superconductor/antiferromagnet heterostructures, suppression of T_C [226–229] was reported with Cr and IrMn antiferromagnets, whereas Josephson current in superconductor/antiferromagnet/superconductor trilayers [227,230–233] was observed with $Ca_{1-x}Sr_xCuO_2$, Cr, and FeMn antiferromagnets. More recently, electrical and thermal phenomena specific to antiferromagnet/superconductor junctions were theoretically predicted, as the result of combined specular reflection of holes and retroreflection of electrons [234]. Notably, the proximity effect at the interface of a non-collinear antiferromagnet with a singlet superconductor allows singlet Cooper pairs to be converted into triplet Cooper pairs, enabling spin-polarized Cooper pairs to be transported over long distances [235]. Although few experimental studies have been published on superconductor/antiferromagnet heterostructures compared to the number available for superconductor/ferromagnet systems, they could open perspectives for studies of intriguing physical phenomena and provide crucial information on the transport properties of antiferromagnets. Indeed, these properties recently attracted interest for their use in the context of spin-dependent transport [26,27]. Understanding whether antiferromagnetic spin textures influence the transport of Cooper pairs and determining the characteristic lengths promoting transport are some of the basic points that deserve to be investigated.

IV.1.2 Gradual recovery of the superconducting critical temperature in [Pt/Co]$_n$/(Pt,IrMn)/NbN multilayers

In this study, we measured the proximity effect in ferromagnet(Pt/Co)/spacer(IrMn and Pt)/superconductor(NbN) heterostructures. We created domains in the ferromagnet and varied the configurations from multi- to single-domain. While controlling the domain state, we observed its influence on the superconductor's critical temperature. By tuning the various parameters in play, e.g., superconducting coherence length-to-thicknesses ratio and domain sizes, we achieved recovery of the superconducting critical temperature $\Delta T_C/T_C$ by up to 10%. This amplitude was compatible with two types of studies that were previously impossible: i) we probed the gradual evolution of $\Delta T_C/T_C$ for all the intermediate magnetic configurations of

the ferromagnet; and, ii) we demonstrated how $\Delta T_C/T_C$ decreases gradually with the thickness of the spacer layer, thus we were able to determine the penetration depth of Cooper pairs in the IrMn antiferromagnetic spacer.

IV.1.2.1 Sample fabrication, magnetic characterization and observation of the effect

The full stacks used in this study were (from substrate to surface): $Si/SiO_2(500)//[Pt(1)/Co(0.65)]_n/spacer(t_{spacer})/NbN(t_{NbN})$ (nm) multilayers, where n is the number of repetitions of the Pt/Co heterostructure composing the ferromagnet. The value of n was varied between 4 and 25, corresponding to a variation of the nominal thickness between 6.6 and 41.25 nm. The thickness of the spacer layer (IrMn or Pt), t_{spacer}, was varied between 1 and 60 nm; t_{NbN} is the thickness of the NbN superconducting layer and was set to 15, 30, or 60 nm. Stacks were deposited at room temperature by dc-magnetron sputtering on $Si/SiO_2(500)$ (nm) substrates under argon at a pressure of 2.3×10^{-3} mbar. The IrMn layer was deposited from an $Ir_{20}Mn_{80}$ (at. %) target. The superconducting NbN layers were prepared by reactive sputtering of Nb under N_2 gas at a partial pressure of 5×10^{-3} mbar. The stacks were deposited at SPINTEC by Stéphane Auffret and NbN layers at CIME Nanotech by Christelle Gomez. During deposition, the main error relates to the number of significant digits allowed when programming the deposition time. The error with our system is of 50 ms. Based on the deposition rates, which we calibrated separately for all targets using standard x-ray reflectivity on calibration samples, we calculated that the error for the thickness of the layers was always smaller than the size of the symbols in the figures. The thin films were patterned into H-bars (measuring 200 µm wide and 5 mm long) by laser lithography and plasma etching. An optical image of the resulting H-bar is shown in Figure 61(a). Electrode contacts were created using aluminum-wire bonding on 200 x 200 µm² contact pads. Electrical parameters were then measured using standard four-point current-voltage geometries, applying an ac current (lock-in detection) of amplitude 0.5 mA and frequency 13.65 Hz.

By measuring the transverse voltage between contacts V_1 and V_3 (Figure 61(a)), the anomalous Hall contribution from the stack was determined. This contribution is known to be proportional to the perpendicular component of magnetization, M [236]. Representative data showing how normalized M ($m=M/M_S$) depends on an external magnetic field, H, applied out-of-plane for a $Si/SiO_2//[Pt(1)/Co(0.65)]_{15}/IrMn(3)/NbN(15)$ (nm) stack are plotted in Figure 61(b). Data-points were measured at 12 K after demagnetizing the sample by applying an alternating field of decreasing amplitude, from 10 kOe to 0 kOe at a rate of 50 $Oe.s^{-1}$. Subsequently, distinct field sequences were applied to produce different magnetic states for the Pt/Co ferromagnet. For example, the symbols in Figure 61(b) indicate that the demagnetized (red square, for $m=M/M_S \sim 0$) and saturated (blue circle, for $m=M/M_S \sim 1$) states can both be accessed at a remanent field of H = 0.5 kOe. These states were used throughout the study. Magnetic force microscopy (MFM) performed at room temperature (Figure 61(d)) [237] revealed that the demagnetized state consists of maze domains, with a typical width $w_{Pt/Co}$ = 47 nm. This width was determined from the power spectral density profile of the two-dimensional Fourier transform of the MFM image (Inset in Figure 61(d)). The domains are separated by domain walls ($\delta_{Pt/Co}$) measuring (11.5 ± 1.5) nm thick. $\delta_{Pt/Co}$ was calculated from $\delta_{Pt/Co}=\pi(A/K)^{1/2}$, where $A = (3.4 \pm 0.4) \times 10^{-7}$ erg cm^{-2} and $K = (1.5 \pm 0.2) \times 10^6$ erg cm^{-3} were determined by applying the Kaplan model [238]. This model will be further discussed below (see Figure 65(c) and discussion therein). The full hysteresis loop given in Figure 61(b) is also consistent with the

preferential formation of maze domains, caused by competition between exchange and magnetostatic energies [239]. It should be noted that the saturated state was only accessible here at a remanent field of 0.5 kOe. Thinner Pt/Co ferromagnets produce hysteresis loops with shape closer to a square, and can thus be used to access all states in zero applied field. Nevertheless, § IV.1.2.2 presents a discussion of some of the considerations to be taken into account when choosing thicker vs thinner Pt/Co ferromagnets for this type of study.

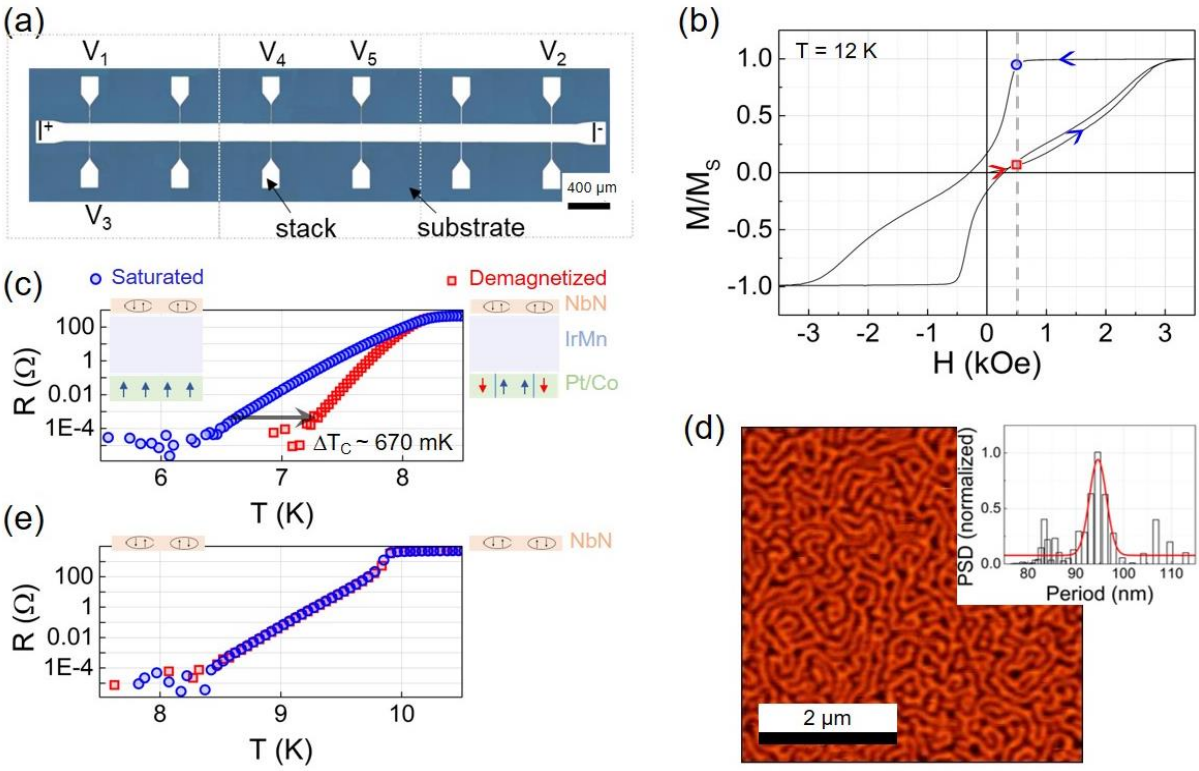

Figure 61 : (a) Optical image of a typical device used to perform transport measurements. The complete image is reconstructed from three optical images (indicated by the dotted squares). (b) Normalized magnetization M/M_S starting from a demagnetized state measured at 12 K for a Si/SiO_2//$[Pt(1)/Co(0.65)]_{15}$/IrMn(3)/NbN(15) (nm) ferromagnetic/spacer/superconductor stack. (c) Representative data showing the T-dependence of R, for the same sample as in (b), prepared in two distinct magnetic states: saturated and demagnetized, through two procedures involving field-cycling and cooling (see text). ΔT_C (here, systematically measured at R = 0.5 mΩ) represents the difference in superconducting critical temperature between the saturated and demagnetized states ($\Delta T_C = T_{c,\text{demagnetized state}} - T_{c,\text{saturated state}}$). (d) MFM image taken at room temperature, for the sample used in (b) and (c), showing maze domains after demagnetization. (Inset) PSD profile of the MFM image. (e) Control experiment with a bare Si/SiO_2//NbN(15) (nm) stack subjected to the two procedures used for (c). Data in (c) and (e) were measured for an applied field H = 0.5 kOe. The symbols in (b) represent the two magnetic states, demagnetized (square) and saturated (circle).

The superconducting critical temperature, T_C, of the NbN layer was determined from temperature(T)-dependent measurements of the stacks' resistance, R, based on the longitudinal voltage between contacts V_1 and V_2 (Figure 61(c,e)). Slant in the R vs T curves points to an inhomogeneous state that is inherent to the NbN superconductor (Figure 61(e)). It should be noted that we used a log scale for the y-axis. While this makes the basal ΔT_C more visible, it also artificially exacerbates slant in the curves. To allow data comparison, T_C was defined throughout as the temperature for which R dropped to 0.5 mΩ, i.e., above the noise level. More details about the sample holder and about the reproducibility of $\Delta T_C/T_C$ will be further discussed in Figure 68. Typical R vs T measurements for H = 0.5 kOe are shown in Figure 61(c) for $[Pt/Co]_n$/IrMn/NbN multilayers with the Pt/Co ferromagnet in a demagnetized or saturated state, and in Figure 61(e) for a single layer of NbN subjected to the same field-cycling protocol. These data for the NbN monolayer were used to verify that the NbN superconductor is not

intrinsically sensitive to field-cycling procedures. Subsequent findings could thus be confidently interpreted. Comparing Figure 61(c) and (e), T_C was observed to be approximately 20% smaller in the $[Pt/Co]_n$/IrMn/NbN multilayer (T_C ~ 6.5 K when the Pt/Co ferromagnet is saturated) than in the monolayer of NbN (T_{C0} ~ 8.4 K). This weakening of superconductivity is caused by the exchange field sampled by the Cooper pairs travelling across the spacer layer, inducing effective pair-breaking [219]. The fact that the 3-nm-thick IrMn spacer layer is transparent for the transport of Cooper pairs will be addressed specifically when discussing the results shown in Figure 67. The results shown in Figure 61(c) confirmed that the presence of domains and the resulting domain walls in the demagnetized Pt/Co ferromagnet led to weaker Cooper pair-breaking effects, as expected from the theory [219]. This effect resulted in a larger T_C (~7.2 K) than that recorded for the saturated state (~ 6.5 K). Thus, relative recovery of T_C, defined as $\Delta T_C/T_C = (T_{c,\text{demagnetized state}} - T_{c,\text{saturated state}}) / T_{c,\text{saturated state}}$, was up to ~10% - an order of magnitude larger than the ~0.6% reported previously (see Figure 60) [221]. In fact, to observe this effect, several parameters (superconducting coherence length, ξ_{NbN}, vs layer thicknesses, t_{NbN}, t_{IrMn}, $t_{Pt/Co}$, vs magnetic domain width, $w_{Pt/Co}$, and domain walls width, $\delta_{Pt/Co}$) must be appropriately adjusted with respect to each other. For example: i) optimizing proximity effects requires the ξ_{NbN}/t_{NbN} ratio to be maximized, but minimizing finite-size effects on superconductivity imposes a lower limit on t_{NbN}, or ii) optimizing the influence of a domain wall on superconductivity imposes that $\delta_{Pt/Co}$ be of the same order of magnitude as ξ_{NbN}. The *ad hoc* adjustment of several parameters produced the reported $\Delta T_C/T_C$, up to ~10%. Specifically, the results shown in Figure 61 were obtained with a sample in which: t_{NbN} = 15 nm, ξ_{NbN} = 15 nm, $\delta_{Pt/Co}$ = 11.5 nm, $w_{Pt/Co}$, = 47 nm, $t_{Pt/Co}$ = 41.25 nm, and t_{IrMn} = 3 nm. Parameter tuning will be discussed in the following of this paragraph.

It is interesting to note that a similar recovery of T_C was measured when using contacts V_4 and V_5 instead of V_1 and V_2 for the measurements (Figure 61(a)), i.e., when the total number of domains probed was reduced but the overall maze arrangement remained the same. This result confirms the reproducibility of our data and also that it is the maze arrangement that produces the observed effect, such control experiments will be further discussed in Figure 70.

It should also be noted that experimental observations (Figure 61(c)) point to an inhomogeneous state in the ferromagnet, on the length scale of the superconducting coherence length. More specifically, the magnetic state seems to affect more the temperature at which the stack reaches the zero resistance state rather than the onset of superconducting correlations. Figure 62 shows the normalized ΔT_C dependence on R in $[Pt/Co]_n$/IrMn/NbN multilayers for different thicknesses of the NbN superconductor. It indicates that the NbN thickness does not play a role on the process at stake here. In other words, the zero resistance state is controlled by the magnetic layer state. Note that, to allow that comparison, ΔT_C was normalized by extrapolating the raw data to get the value for which R = 0 for the different NbN thicknesses.

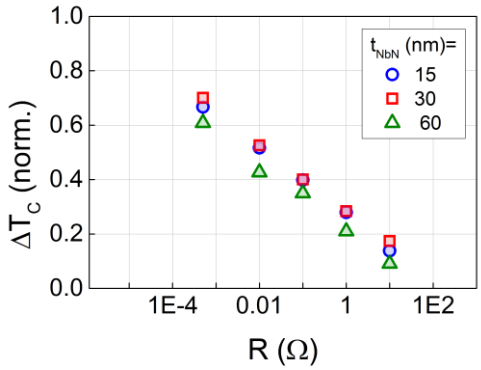

Figure 62 : Normalized ΔT_C dependence on R as measured for Si/SiO_2//[Pt(1)/Co(0.65)]$_{15}$/IrMn(3)/NbN(t_{NbN}) (nm) stacks. R indicates the value for which T_C is obtained in the R vs T sweeps.

We will now comment more on the influence of the thickness of the NbN superconductor on the recovery of T_C in [Pt/Co]$_n$/IrMn/NbN multilayers. The data presented in Figure 63(a) show that ΔT_C decreases when t_{NbN} increases, confirming the interfacial nature of the effect observed [219]. We gained further insights into the thickness-dependence of the NbN properties from series of measurements of R vs T for several applied fields. The resulting H-dependences of T_C (Figure 63(b)) were fitted using Ginzburg-Landau (GL) theory, which is expected to apply in the perpendicular field configuration for type II superconductors. Specifically, we deduced the superconducting coherence length, ξ_{NbN}, using the following equation [240]:

$$H = \phi_0(1 - T/T_{C,H=0})/(2\pi\xi^2_{GL,T=0}) \qquad \text{Eq. IV-1}$$

where Φ_0 is the magnetic flux quantum ($\Phi_0 = h/(2e)$), and ξ_{GL} is the GL coherence length, with $\xi_{GL,T=0} = \xi_{NbN}\ \pi/2$. It should be remembered that, in the dirty limit, $\xi_{NbN} = \sqrt{\hbar D_{NbN}/2\pi k_B T_C}$, where D_{NbN} is the diffusion constant (see also discussion in the Appendix of Ref. [7]). Data derived from the fits of H vs T for several t_{NbN} were plotted for [Pt/Co]$_n$/IrMn/NbN and NbN stacks Figure 63(c). The corresponding t_{NbN}-dependences of $T_{C,H=0}$ and ξ_{NbN} are known to be related to finite-size effects taking weakened interfacial superconductivity into account [240]. Most importantly, measurements of the finite-size effect on ξ_{NbN} were used to produce the data presented in Figure 63(d), where $\Delta T_C/T_C$ can be observed to scale linearly with ξ_{NbN}/t_{NbN}. This relationship further supports the interfacial nature of the proximity effect involved here.

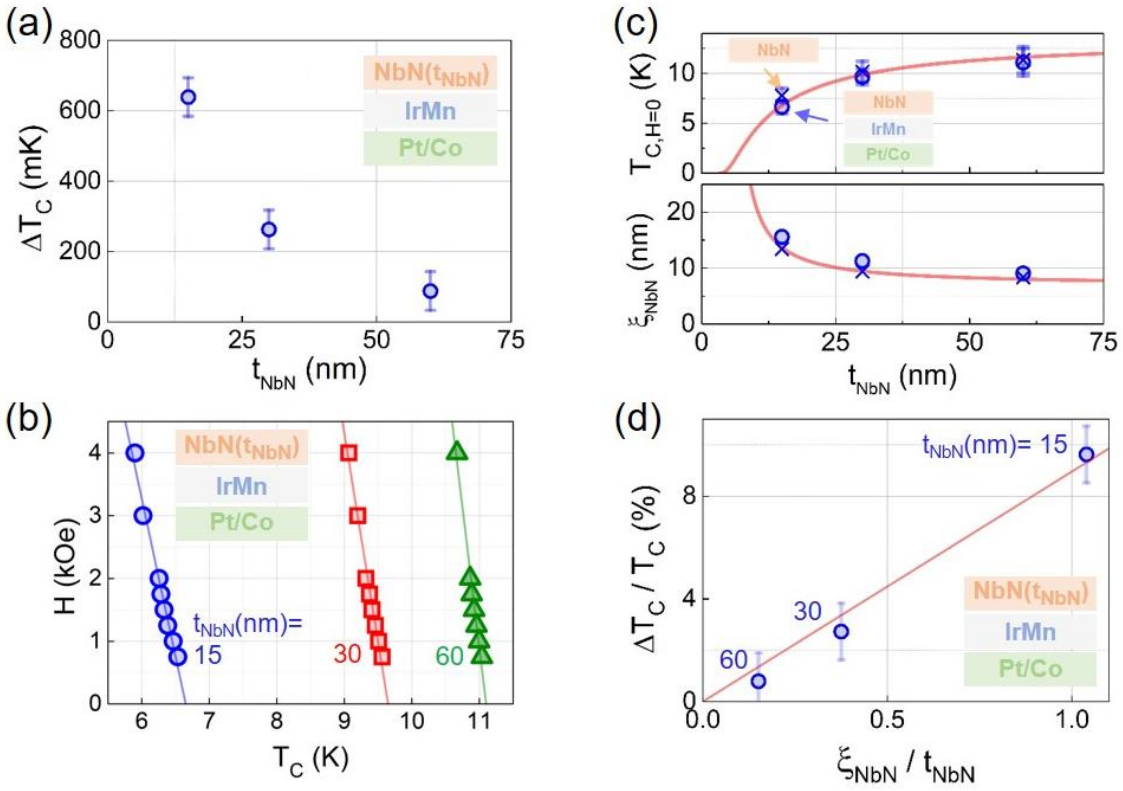

Figure 63 : (a) NbN thickness (t_{NbN}) dependence of ΔT_C. (b) Representative data showing H vs. T_C as measured for Si/SiO_2//[Pt(1)/Co(0.65)]$_{15}$/IrMn(3)/NbN(t_{NbN}) (nm) stacks. These data were used to calculate the superconducting coherence length, ξ_{NbN} and the zero-field superconducting temperature, $T_{C,H=0}$. Lines were fitted to the data with Eq. IV-1. (c) Corresponding t_{NbN}-dependences of ξ_{NbN} and $T_{C,H=0}$ in comparison to data obtained for bare Si/SiO_2//NbN(t_{NbN}) (nm) stacks. The lines serve as visual guide. The error bars were obtained from the fits of the data shown in (b). (d) Dependence of $\Delta T_C/T_C$ with the superconducting coherence length to thickness ratio (ξ_{NbN}/ t_{NbN}). The line is a linear fit to the data constrained to pass through (0,0). Figure 68 shows the results used to estimate the error bars from (a) and (d).

IV.1.2.2 Influence of ferromagnetic domains

As the temperature recovery observed here in [Pt/Co]$_n$/IrMn/NbN multilayers was considerable, it was possible to explore how $\Delta T_C/T_C$ evolved for several ferromagnetic configurations of the Pt/Co multilayer. Intermediate configurations, between the demagnetized and saturated states discussed in Figure 61, were obtained as illustrated in Figure 64(a). Specifically, an incremental sequence of minor hysteresis loops was applied at 12 K. Starting from a demagnetized state, the magnetic field was raised to H_i and then reduced to 0.5 kOe. The symbols in Figure 64(a) indicate the magnetic states that we considered. The gradual increase in $m=M/M_S$ for the intermediate states accounts for the partial remagnetization and gradual evolution of the domain configuration in the Pt/Co multilayer. After each step of the sequence in field, the T_C of the superconductor was deduced from an R vs T scan at H = 0.5 kOe (Figure 64(b)). The plot of $\Delta T_{C,i}/T_C = (T_{c,\text{intermediate state}} - T_{c,\text{saturated state}}) / T_{c,\text{saturated state}}$ vs $1\text{-}M/M_S$ (Figure 64(c)) shows how the magnetic domain arrangement in the Pt/Co ferromagnet influenced superconductivity recovery in the NbN film. In particular, we observed that gradually reducing the domain size, from infinite in the saturated state ($1\text{-}M/M_S \sim 0$) to 45 nm in the demagnetized state ($1\text{-}M/M_S \sim 1$) led to progressive recovery of superconductivity, from $\Delta T_{C,i}/T_C \sim 0$ to 10%. Overall, this behavior can be explained by a theoretical model, which is detailed below. We note that the error bar for $\Delta T_{C,i}/T_C$ in the figures corresponds to 1.1%. This error was estimated using several measurements for the same sample (see discussion in Figure 68).

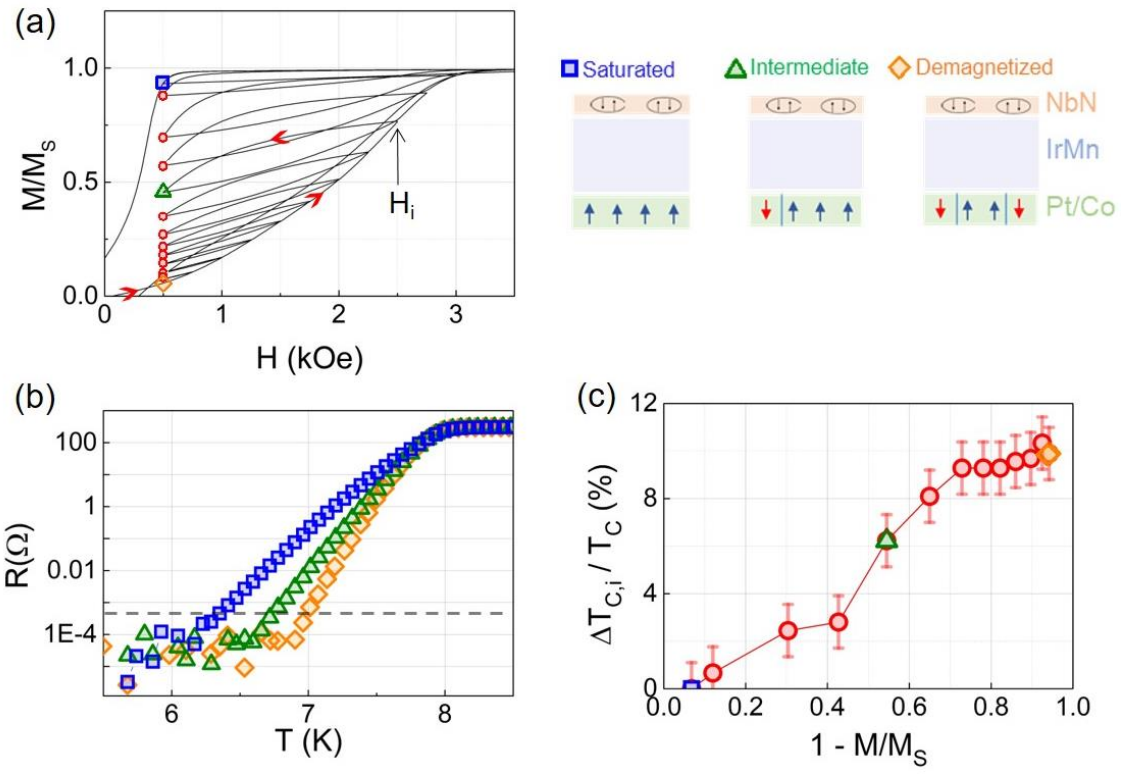

Figure 64 : (a) Normalized magnetization M/M_S of a Si/SiO_2//[Pt(1)/Co(0.65)]$_{15}$/IrMn(3)/NbN(15) (nm) stack for field cycling series. Measurements were performed at 12 K starting from a demagnetized state. Selected magnetic configurations are labeled as: (1) Saturated; (2) Intermediate; and (3) Demagnetized. (b) Data showing the T-dependences of R for the three magnetic states examined. (c) Dependence of $\Delta T_C/T_C$ with 1-M/M_S, , where $\Delta T_{C,i}$ represents the difference in superconducting critical temperature between any state and the saturated state.

Before coming to the model, we considered how superconductivity recovery was affected by the thickness of the Pt/Co ferromagnet. Figure 65(a) shows that the gradual increase in $\Delta T_{C,i}/T_C$ as the magnetic domain configuration of the Pt/Co multilayer shifted from saturated to demagnetized appeared to follow a universal trend that is independent of $t_{Pt/Co}$. However, the maximum value, corresponding to $\Delta T_C/T_C = (T_{c,\text{demagnetized state}} - T_{c,\text{saturated state}}) / T_{c,\text{saturated state}}$, did significantly depend on $t_{Pt/Co}$ (Figure 65(b)), leveling out from n = 15. This number of Pt/Co layers corresponds to a nominal $t_{Pt/Co}$ thickness of 24.75 nm. We note that data in Figure 65(b) were measured for both H = 0.5 kOe and 1.3 kOe, to allow exploration of larger $t_{Pt/Co}$ values. Indeed, for larger values, saturation can only be reached with a 1.3-kOe field (see § IV.1.2.1). Data for H = 0.5 kOe naturally show larger values than data for H = 1.3 kOe as superconducting properties are weakened when a stronger field is applied. The $t_{Pt/Co}$-dependence of $\Delta T_C/T_C$ is undoubtedly driven by several parameters. First, superconducting properties are more affected by a thicker ferromagnet, as long as $t_{Pt/Co}$ remains shorter than the Cooper pair coherence length, $\xi_{Pt/Co}$. However, this effect should not be involved here, as the coherence length is known to be a few nanometers in ferromagnets. Second, since the size of the domains decreases down to a threshold thickness corresponding to about 47 nm (Figure 65(c)), the density of domain walls increases and then levels out, resulting in a similar shape for $\Delta T_C/T_C$ vs $t_{Pt/Co}$. Specifically, the size of the domains in the demagnetized state, $w_{Pt/Co}$, changes with the number of layers, n, making up the [Pt/Co]$_n$ multilayer (i.e., with $t_{Pt/Co}$). The thickness-dependence of $w_{Pt/Co}$ is known to obey Kaplan's model, which accounts for the fact that the cost in domain wall energy was compensated by the gain in demagnetizing energy as the film thickness increased [238]. For $w_{Pt/Co} / t_{Pt/Co} > 1.5$, the thickness-dependence of $w_{Pt/Co}$ is given by: $\text{Ln}(w_{Pt/Co} / t_{Pt/Co}) = \pi w_0 / (2t_{Pt/Co})+a$, with $a=\text{Ln}(\pi)-1+\mu(0.5-\text{Ln}(2))$; $\mu=1+2\pi M_S^2/K$. Considering M_S equal to 550 emu cm^{-}

[3] ($M_S = M_{Co}t_{Co}/(t_{Co}+t_{Pt})$), data-fitting returned w_0 = (19.8 ± 2) nm and an anisotropy of K = (1.5 ± 0.2) x 106 erg.cm^{-3}. These values are in agreement with previous findings [237]. The domain wall energy σ_w = (5.5 ± 0.5) erg.cm^{-2}, the exchange stiffness A = (3.4 ± 0.4) x 10^{-7} erg cm^{-2}, and the domain wall width $\delta_{Pt/Co}$ = (11.5 ± 1.5) nm were subsequently calculated by applying the following relations: $\sigma_w=4(AK)^{1/2}=2\pi M_S^2\, w_0$ and $\delta_{Pt/Co}=\pi(A/K)^{1/2}$ [238].

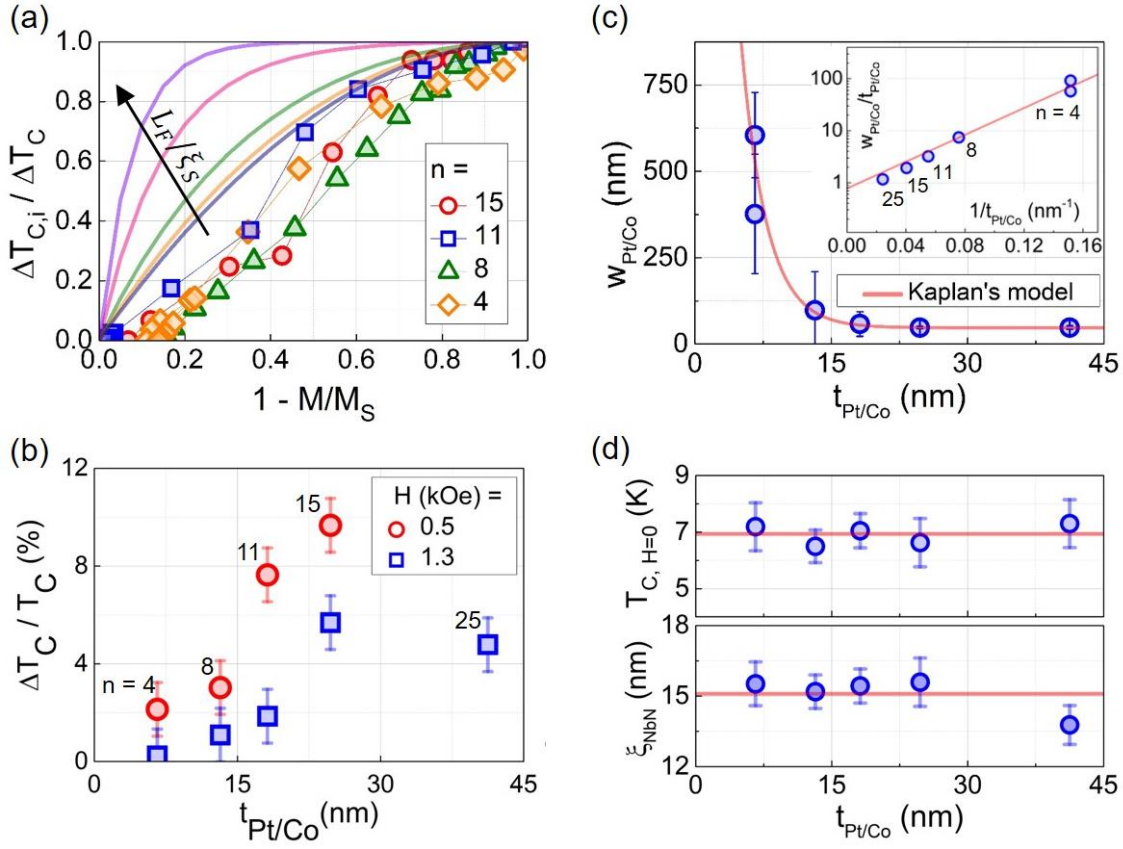

Figure 65 : Dependence of $\Delta T_{C,i}/\Delta T_C$ on 1-M/M_S for Si/SiO$_2$//[Pt(1)/Co(0.65)]$_n$/IrMn(3)/NbN(15) (nm) stacks (n = 4, 8, 11, 15), measured while applying an external field of H = 0.5 kOe. Lines were calculated using the model described in the text (Eq. IV-2), for L_F/ξ_S≈0.25;2.5;5;12.5;and 25. (b) Corresponding dependence of $\Delta T_C/T_C$, corresponding to ($T_{c,\text{demagnetized state}} - T_{c,\text{saturated state}}$) / $T_{c,\text{saturated state}}$) on the total thickness ($t_{Pt/Co}$) of the [Pt/Co]$_n$ multilayer, measured at H = 0.5 and 1.3 kOe. (c) $t_{Pt/Co}$-dependence of the domain sizes ($w_{Pt/Co}$), deduced from MFM images taken at room temperature after demagnetization, ie for M/M_S ~ 0. (Inset) Semilogarithmic-scale dependence of $w_{Pt/Co}$ on $1/t_{Pt/Co}$. Lines were fitted to the data using a model described in the text. (d) Control measurements for ξ_{NbN} and $T_{C,H=0}$ vs $t_{Pt/Co}$.

Because the NbN layer was grown on top of the multilayers, for which the thicknesses varied significantly, we verified that its superconducting properties were not significantly altered as a result of growth issues. ξ_{NbN} and $T_{C,H=0}$ were therefore extracted using the same procedure and equations as described in Figure 63(b) and corresponding text. These data confirmed negligible variability in NbN properties across samples (Figure 65(d)).

We next sought to develop a theoretical model supporting the experimental findings. The model considers that Cooper pairs feel a reduced effective exchange field that is spatially uniform over the surface of the demagnetized ferromagnet. Within the quasiclassical diffusive theory for superconducting heterostructures, we derived an expression for the critical temperature of a superconductor/ferromagnet bilayer in the presence of a periodic magnetic domain structure (for details on the derivation reader is refered to the Appendix of Ref. [7]). Thus, assuming a thin superconducting layer ($t_S \ll \xi_S(T_C)$ with S=NbN) in good electrical contact with a thick ferromagnetic layer ($t_F \gg \xi_F$ with F=Pt/Co), and narrow domain walls ($\delta_F \ll \xi_S$), we found:

$$\frac{\Delta T_{C,i}}{\delta T_C} = \frac{T_C(m) - T_C(m=1)}{\delta T_C} = \qquad \text{Eq. IV-2}$$

$$1 - m^2 - \frac{2(L_F/\xi_S)^4}{7\pi^6\zeta(3)} \sum_{p=1}^{\infty} \frac{\sin^2\left[\frac{\pi}{2}(m+1)p\right]}{p^6} \left[\frac{\pi^4 p^2}{(L_F/\xi_S)^2} + \Psi\left(\frac{1}{2}\right) - \Psi\left(\frac{1}{2} + \frac{2\pi^2 p^2}{(L_F/\xi_S)^2}\right) \right]$$

for an arbitrary ratio L_F/ξ_S. Here ζ and ψ are the Riemann zeta and digamma functions, respectively, and L_F is the period of the domain structure ($L_F = 2w_F$).

It should be noted that the most restrictive condition for the application of our theory to the interpretation of the experimental data is a thin S layer approximation $t_S \ll \xi_S(T_C)$, where $\xi_S(T_C) \sim \xi_S (T_{C0}/(T_{C0}-T_C))^{1/2}$. Taking $\xi_S = \xi_{NbN} = 15$ nm and $T_{C0} \sim 8.4$ K for the NbN monolayer, and $T_C \sim 7.2$ K (from Figure 61), we estimate $\xi_S(T_C) \sim 40$ nm. Therefore, our theoretical approach should provide a reasonable description of the experimental situation for $t_{NbN} = 15$ nm.

The domain structure consists of alternating majority and minority stripe domains, the relative lengths of which determine the reduced magnetization, $m=M/M_S$. The maximal shift was obtained for $L_F \ll \xi_S$, given by $\Delta T_C = \delta T_C$ with:

$$\delta T_C = \frac{T\zeta(3)}{4\pi^2} \frac{\tilde{h}^2}{k_B^2 T_{C0}}. \qquad \text{Eq. IV-3}$$

Here, T_{C0} is the critical temperature of the bare superconducting layer, and $\tilde{h}$ is an effective exchange field. This field can be related to the exchange field h acting on the electron spins in the ferromagnetic layer as follows:

$$\tilde{h} = \frac{\hbar\sigma_F D_S}{2\sigma_S t_S} \sqrt{\frac{h}{\hbar D_F}} \qquad \text{Eq. IV-4}$$

with the conductivities σ_S and σ_F, and the diffusion constants D_S and D_F in the superconducting and ferromagnetic layers, respectively. From Figure 65(a) it emerges that Eq. IV-2 for $L_F \lesssim \xi_S$, where it approximates to $\Delta T_{C,i} = (1-m^2)\delta T_C$, qualitatively describes the experiment for $0 \le m \ll 1$. Deviations for $1-m \ll 1$ are attributed to the limitations of the model close to saturation, when the domain structure is very different from periodic stripes. Close to the saturation, instead of the regular domain structure we should expect the existence of the small minority domains separated by very large majority domains. Naturally in this situation our theoretical model is not applicable, because the condition $L_F \ll \xi_S$ fails and the superconductivity appears near the domain walls only (or above the whole minority domain if its thickness starts to be smaller than ξ_S). The superconducting regions in this case are well separated from each other; their presence provides only a small impact on the overall resistance of the sample.

As the ratio L_F/ξ_S increases, the ΔT_C shift is progressively reduced. Ultimately, for $L_F \gg \xi_S$, Cooper pairs mostly feel single domains, making both the demagnetized and saturated states detrimental, and producing similar depairing efficiency. For $L_F \gg \xi_S$, Eq. IV-2 yields:

$$\Delta T_C = \frac{(2^{7/2}-1)\zeta(7/2)}{\sqrt{2}\pi^2} \frac{\tilde{h}^2}{k_B^2 T_{C0}} \frac{\xi_S}{L_F} \qquad \text{Eq. IV-5}$$

The above equation qualitatively describes the suppression of ΔT_C as the ferromagnetic layer gets thinner and $L_F = 2w_F$ concomitantly increases (Figure 65(b,c)).

As L_F increases further, the assumption of a superconducting order parameter that is almost spatially uniform - used to derive Eq. IV-2 - breaks down. This happens when the transition takes place in the domain wall superconducting (DWS) phase, according to [219]. In this case, the increase in critical temperature between demagnetized and saturated configurations can be determined as follows:

$$\Delta T_C = \frac{\left(8\sqrt{2}-1\right)^2 \zeta^2(7/2)}{8\pi^6} \frac{\tilde{h}^2}{k_B^4 T_{C0}^3} \qquad \text{Eq. IV-6}$$

This relationship requires the walls to be sufficiently distant from each other on the characteristic DWS length scale [219], i.e., $(1\text{-}m)\, L_F \geq \xi_{DWS}(T)$, with $\xi_{DWS}(T) = \xi_S\, T_{C0}/(T_{C0}\text{-}T)$. As $T_{C0}\text{-}T \approx \tilde{h}^2/(k_B^2\, T_{C0})$ in this regime, Eq. IV-5 and Eq. IV-6 can be seen to match parametrically at m=0 (i.e., $L_F \approx \xi_{DWS}(T_C)$). Note that the DWS phases overlap extensively at $L_F \approx \xi_{GL}(T_C)$, where $\xi_{GL}(T) = \pi/2\,\xi_S\sqrt{T_{C0}(T_{C0}-T)}$ is the GL coherence length.

When superconducting and magnetic state related inhomogeneities observed experimentally (from slant in the R vs T curves and R-dependent recovery of T_C (Figure 61) were not taken into account in this simplified model, it should be noted that it captures the physics of the proximity-effect related phenomenon observed experimentally. In a refined and complex model, the use of a distribution of exchange field could for example account for these inhomogeneities, with the aim to model refined transition mechanism, involving for example percolation-like behaviors.

IV.1.2.3 Influence of the nature, thickness, and domain state of the spacer layer

We next investigated the influence of the spacer thickness on the recovery of superconductivity. More particularly, we took advantage of the proximity effect in our ferromagnet/antiferromagnetic-spacer/superconductor heterostructures to study the transport properties of Cooper pairs in the IrMn antiferromagnet and to further deduce characteristic properties that could be of interest for any electronic transport-related study, e.g., for antiferromagnetic spintronics [26,27]. How $\Delta T_C/T_C$ depends on the IrMn spacer thickness is shown in Figure 66(a) for two values of applied field. It should be noted that the superconducting properties of NbN, ξ_{NbN} and $T_{C,H=0}$ were tested in this set of samples. These data indicated that the variability in ξ_{NbN} and $T_{C,H=0}$ across samples was negligible (not shown), in line with the data presented in Figure 63(d) and the related discussion. The overall reduction of $\Delta T_C/T_C$ with t_{IrMn} (Figure 66(a)) relates to the coherence length of Cooper pairs in the metallic spacer of the IrMn antiferromagnet, ξ_{IrMn}. The fact that the overall signal only entirely vanished when the t_{IrMn} thickness reached ~ 40 nm indicates that a thin IrMn layer (e.g., 3 nm as considered in the previous sections) will be completely transparent for the electronic transport of Cooper pairs. This finding can be explained by the fact that an antiferromagnetic exchange length of a few nanometers is much shorter than the superconducting coherence length of a few tens of nanometers. As a result, the different directions of the moments are sampled simultaneously by a Cooper pair, and the antiferromagnet is viewed as a non-magnetic layer in the Cooper pair reference frame. We note that the spin structure in polycrystalline IrMn

thin films like the ones used in our samples resembles a disordered phase (γ-phase) of the non-collinear structure of the bulk $L1_2$-$IrMn_3$ antiferromagnet . When considering the diffusion of Cooper pairs, we took $\Delta T_C/T_C \propto \exp[-k_{spacer}\, t_{spacer}]$ - expected from quasiclassical theories in the diffusive limit - with a wavevector of the form $k_{spacer} = 1/\xi_{spacer}$. Fitting these relations to the data shown in Figure 66, we obtained a coherence length of $\xi_{IrMn} = (6.7 \pm 1)$ nm for the IrMn antiferromagnet. In comparison, a value of (12.4 ± 2) nm was obtained for the non-magnetic Pt layer. The expected result was $\xi_{spacer} \propto (D_{spacer}\, \tau_{spacer})^{1/2}$, where D_{spacer} is the electron diffusion constant, and τ_{spacer} is the depairing time for Cooper pairs in the metallic spacer layer, which includes contributions from spin relaxation processes [241].

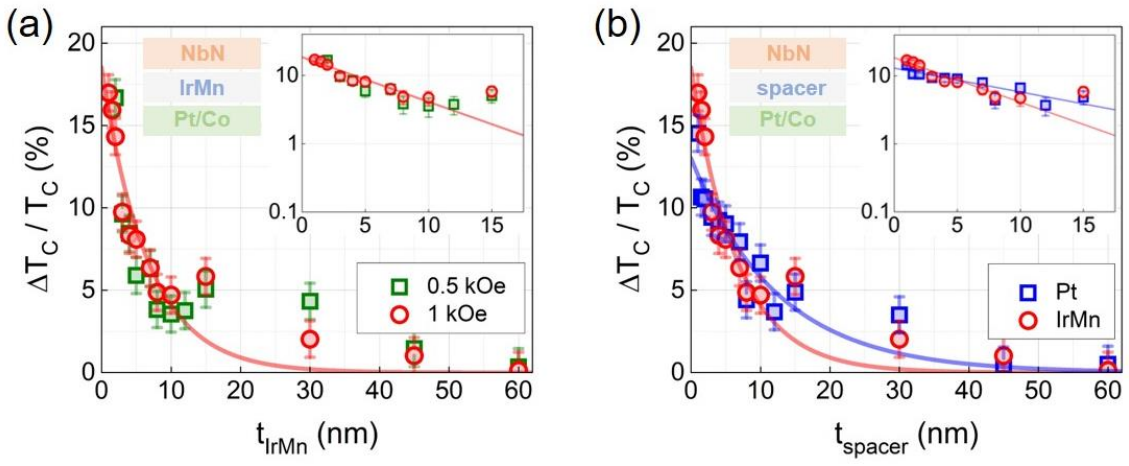

Figure 66 : (a-b) t_{spacer}-dependence of $\Delta T_C/T_C$ measured for Si/SiO_2//[Pt(1)/Co(0.65)]$_{15}$/spacer(t_{spacer})/NbN(15) (nm) stacks, for IrMn and Pt spacers. Lines correspond to exponential fits of the data (see text). (Inset) Corresponding semilogarithmic scale dependence of $\Delta T_C/T_C$ on t_{spacer}.

We finally considered whether the magnetic state of the IrMn antiferromagnet influenced superconductivity. We took advantage of the strong exchange bias interaction between the IrMn bottom interface and the adjacent Pt/Co ferromagnet to imprint ferromagnetic configurations in the IrMn antiferromagnet [242]. Initially, exchange bias interaction was quenched by raising the sample's temperature to 400 K, i.e., above the blocking temperature (T_B) for the ferromagnet/antiferromagnet bilayer (Figure 67(a)). In these conditions, the IrMn antiferromagnetic layer lost its ability to pin the magnetization of the adjacent Pt/Co ferromagnet. Consequently, this layer can be considered to be a single-layer ferromagnet in which different magnetic state types - demagnetized, saturated, or any intermediate state - can be nucleated by conventional means (see Figure 64(a) and corresponding text). Subsequently, the bilayer was cooled below T_B, (here, down to $T = 12$ K), causing the moments in the antiferromagnet to align with those of the ferromagnet due to exchange bias coupling. Indeed, below the blocking temperature, the moments in the antiferromagnet remained pinned regardless of the direction of the moments in the ferromagnet; at 12 K this effect produced a hysteresis loop shift, H_E. This procedure was demonstrated to be robust and has been used elsewhere to imprint multi-domain states and magnetic textures in antiferromagnets an will be further discussed in the following of this paragraph (see Figure 74). Thus, for example, exchange bias was shown to allow several spin arrangements to be imprinted across the core of antiferromagnets, at least across 8 nm for exchange springs in IrMn layers [243], or 3 nm for textures such as vortices in CoO and NiO layers [244]. Figure 67(a) shows the blocking temperature distribution for a Si/SiO_2//[Pt(1)/Co(0.65)]$_4$/IrMn(3)/NbN(15) (nm) stack. This distribution was obtained following a proven specific process according to which H_E is recorded

after each step in an incremental field-cooling procedure starting from an annealing temperature T_a (see discussion in Figure 79(a)). The procedure is extensively described elsewhere [245,246] and will be further discussed in § IV.2.1. Most importantly, the data presented in Figure 67(a) indicate that the magnetic configuration of the Pt/Co ferromagnet can be stabilized in the IrMn antiferromagnet by cooling from 400 K down to 12 K, as the whole distribution of blocking temperatures was measured below 400 K. Using the domain replication approach mentioned above, we stabilized several states at T = 12 K in the IrMn antiferromagnet of a Si/SiO_2//[Pt(1)/Co(0.65)]$_{15}$/IrMn(3)/NbN(15) (nm) stack (Figure 67(b)). This stabilization made it possible to obtain a hysteresis loop for which the shift along the H-axis depended on the magnetic state of the antiferromagnet [242]. For every antiferromagnetic state (pinned at 12 K), we reproduced the procedure detailed in Figure 64(a) and related text, using sequences of minor hysteresis loops, driven by H_i, to scan $\Delta T_C/T_C$ for several ferromagnetic configurations, from demagnetized to saturated. Figure 67(c) shows the corresponding normalized magnetization ($m = M/M_S$) vs H_i. The shift observed on these curves is a direct consequence of the fact that the IrMn antiferromagnet was prepared in three distinct states. Figure 67(d) shows the gradual enhancement of $\Delta T_C/T_C$ as a function of the magnetic domain configuration of the Pt/Co for several IrMn arrangements. These results demonstrate that the recovery of superconductivity, driven by the ferromagnetic configuration of the Pt/Co multilayer (Figure 64 and corresponding text), is independent of the domain arrangement in the IrMn antiferromagnet. This finding is consistent with the fact that a 3-nm-thick IrMn layer is transparent for the electronic transport of Cooper pairs, due to simultaneous sampling of the different directions of the moments.

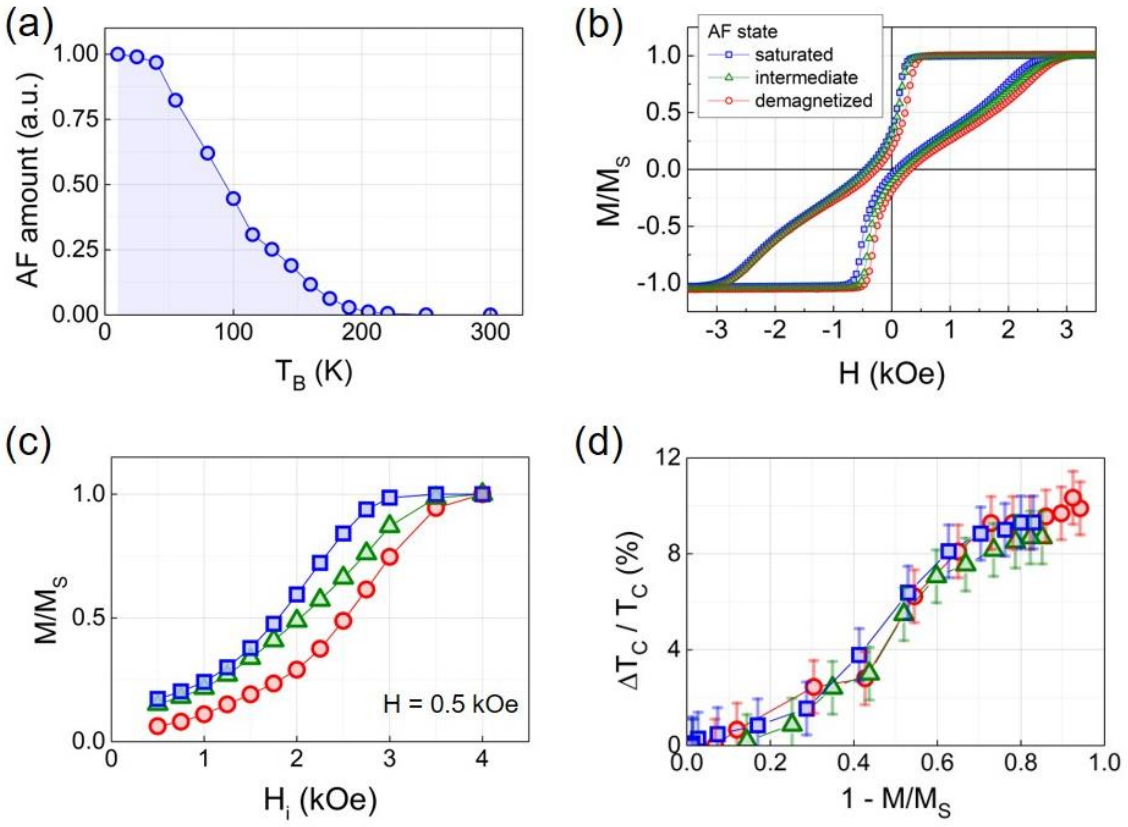

Figure 67 : (a) Blocking temperature distribution measured for a Si/SiO_2//[Pt(1)/Co(0.65)]$_4$/IrMn(3)/NbN(15) (nm) stack. (b) Normalized magnetization M/M_S, measured at 12 K for a Si/SiO_2//[Pt(1)/Co(0.65)]$_{15}$/IrMn(3)/NbN(15) (nm) stack, after stabilizing several states in the IrMn antiferromagnet as describe in the text. (c) Corresponding normalized magnetization at the remanent state for H = 0.5 kOe. (d) Dependence of $\Delta T_{C,i}/T_C$ on 1-M/M_S.

IV.1.2.4 Reproducibility, polarity independence and density of domain walls influence on proximity effects

We next investigate the reproducibility of $\Delta T_C/T_C$ (the main parameter for our findings) for a set of several measurements. Aiming to accurately measure the sample temperature we have used sample holders equipped with on-board thermometers, as shown in Figure 68(a), for all the experiments shown in this chapter. We estimate the error bars for $\Delta T_C/T_C$ of 1.1 % corresponding to the maximum difference obtained between several measurements, see Figure 68(b). We point out that the above determined value of 1.1 % of error on the determination of $\Delta T_C/T_C$ is in line with data shown in Figure 67(d), where the same set of over 10 ferromagnetic states was measured 3 times after stabilizing 3 states in the antiferromagnet. We also note that because $\Delta T_C << T_C$, the error in $\Delta T_C/T_C$ is mainly driven by the error in ΔT_C and not by the error in T_C, therefore making the findings robust against slight shifts in the determination of the temperature. For example, the red pair of curves in Figure 68(b) is shifted in comparison to the other pairs of curves and $\Delta T_C/T_C$ is still reliable. In this sense, each measurement can be considered as self-referenced. Further, it is worthy reminding that T_C was defined throughout as the temperature for which R dropped to 0.5 mΩ at the onset the temperature for that the zero resistance state was achieved (see discussion in Figure 61 and Figure 62). Therefore, the corresponding power dissipation of less than 0.15 μW ensures that no issues related to Joule heating are encountered in the determination of T_C.

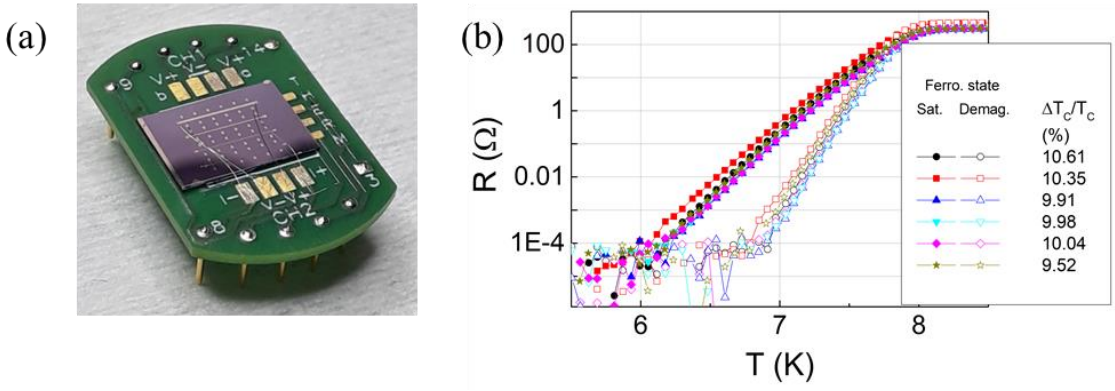

Figure 68 : (a) Typical sample mounted next to the on-board thermometer, THERM. The sample holder is a standard 'Rotator ACT Sample Board' for the Physical Property Measurement System from Quantum Design. (b) Set of several measurements of the temperature-dependence of the stack's resistance to estimate the reproducibility on the determination of $\Delta T_C/T_C$. Data taken for a Si/SiO_2//$[Pt(1)/Co(0.65)]_{15}$/IrMn(3)/NbN(15) (nm) stack, prepared in two distinct magnetic states: saturated (closed symbols) and demagnetized (open symbols), through two procedures involving field-cycling and cooling as discussed in IV.1.2.1.

We have verified the polarity independence of proximity effects to further support that the determination of T_C is not sensitive to the field-cycling procedures, see Figure 69. A single-domain configuration is imprinted in the IrMn antiferromagnet on cooling from above the blocking temperature to 5 K from a positively (negatively) saturated configuration of the [Pt/Co] ferromagnet (for more details on the imprinting procedure see § IV.2.1, Figure 74(a,b)). A magnetic field of +10 kOe (-10 kOe respectively) was applied to saturate the ferromagnet at 200K and reduced to +0.5 kOe (-0.5 kOe respectively) before cooling to 5K.

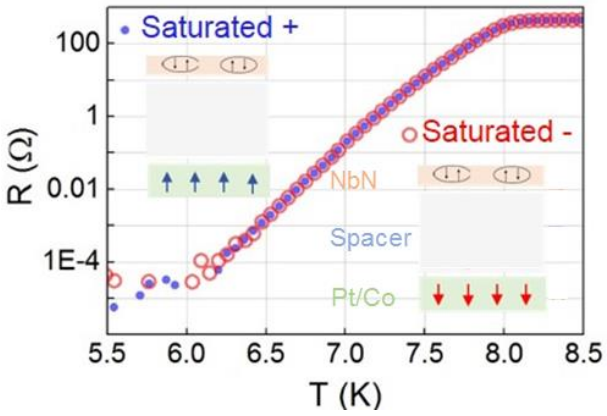

Figure 69 : Polarity independence of proximity effects. Temperature (T)-dependence of the resistance R of a Si/SiO_2//$[Pt(1)/Co(0.65)]_{15}$/IrMn(3)/NbN(15) (nm) stack for two magnetic configurations named *Positive* and *Negative*.

Figure 70 further confirms the reproducibility of our data, even when the contacts and total resistance of the stack are purposely changed. A similar recovery of T_C was measured when using contacts V_4 and V_5 instead of V_1 and V_2 for the measurements. As already mentioned in § IV.1.2.1, doing so we can change the total number of domains probed while the overall maze arrangement of the domains remains the same. This result confirms that our self-referenced approach is a crucial advantage of the technique we have used, based on the comparison of $\Delta T_C/T_C$ between several samples as opposed to a comparison of absolute T_C values.

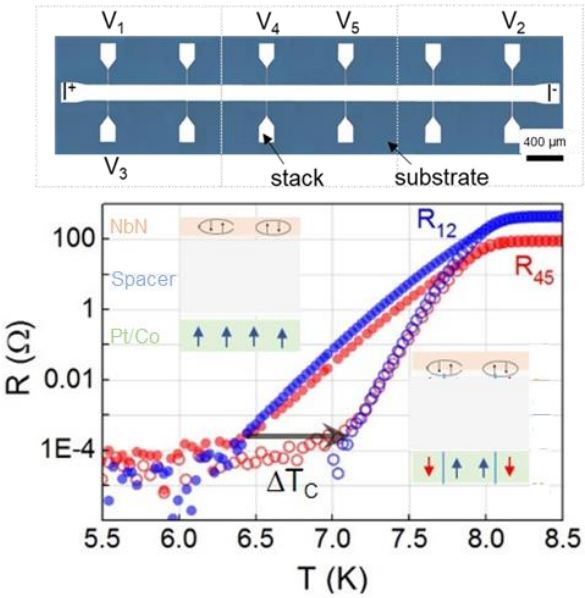

Figure 70 : Density vs amount of domain walls. Temperature (T) dependence of the resistance of a Si/SiO_2//$[Pt(1)/Co(0.65)]_{15}$/IrMn(3)/NbN(15) (nm) stack, single-domain (closed symbols) vs. multi-domain configurations (open-symbols). The case for which the resistance was measured between contacts 1 and 2 is compared to that for which contacts 3 and 4 were used, i. e. when the total amount of domains walls was reduced while keeping the same density.

Before concluding this section, it is worthy mentioning that an attempt was made in order to study the impact of the domain walls arrangement on T_C, similar to the experiments discussed in Figure 60. Zhu *et al.* [221] have deposited stacks with an *in situ* magnetic field applied in the sample plane in order to obtain stripe domains for which the current was applied either parallel or perpendicular to the stripes. Doing so, they manage to show anisotropic superconducting properties with T_C being larger when the current is applied along the stripe direction. In the stacks we have used in our study the formation of maze domains is favorable,

as shown in the MFM image (Figure 61(d)). In our experiments, in order to enhance the possibility of forming stripes, we have cooled the [Pt/Co] ferromagnet from 400 K in the presence of a large in-plane magnetic field (+10 kOe) and at 12 K the sample is demagnetized by applying a decreasing, alternating out-of-plane magnetic field. By using this annealing procedure we did not observe any anisotropy on superconducting properties of the NbN superconductor. A possible reason might be that by annealing it did not change sufficiently the anisotropies into play in order to form stripe instead of maze domains. This could be overcomed by growing the [Pt/Co] ferromagnet with an *in situ* magnetic field applied in the sample plane and it deserves further investigation.

Summary

In summary, this work presents a systematic investigation of the superconducting proximity effect in ferromagnet(Pt/Co)/spacer(IrMn and Pt)/superconductor(NbN) heterostructures. The findings presented indicate that by tuning the various parameters in play, the recovery of the superconducting critical temperature in the presence of ferromagnetic domains and domain walls can be maximized to a degree that makes it possible to carry out two types of studies that were previously impossible. We were therefore able to: i) probe how the recovery of the superconducting critical temperature gradually evolves with all the intermediate magnetic configurations of the ferromagnet; and, ii) determine that the recovery of the superconducting critical temperature gradually reduces with the thickness of the metallic spacer layer. Most importantly, these experiments allowed us to evaluate the penetration of Cooper pairs in the IrMn metallic antiferromagnet, information which is crucial for electronic transport, and up to now has been difficult to access experimentally for antiferromagnets. The results presented therefore open a new pathway for the investigation of electronic transport in antiferromagnetic materials for spintronics.

IV.1.2.5 Critical current enhancement

We will now consider the critical current (I_C) enhancement. When I_C is reached the NbN layer transits to its high-resistance normal state [247]. In other words, the critical current is the maximum electrical current that the superconductor is able to maintain without resistance. This critical value is temperarute dependent, increasing as the temperature is reduced below T_C. We have used the same field-cycling procedure as described in Figure 61 to obtain the demagnetized and saturates states in the [Pt/Co] ferromagnet. The V vs I data obtained for those two magnetic states by ramping the current from low to high values are shown in Figure 71(a). It shows that 0.5 mA stands far below the critical current for superconducting to normal state transition (> 6 mA), further confirming the reliability of our measurements discussed so far. We measured a critical current enhancement of $\Delta I_C/I_C \sim 13\%$, in satisfactory agreement with the critical temperature enhancement $\Delta T_C/T_C \sim 10\%$ obtained by the R vs T experiments.The oscillations in voltage are ascribed to back and forth normal to superconducting transition. Figure 71(b) indicates that the measurement is perturbed due to thermal fluctuations that follows the oscillations of V. At the normal state, part of the current is shunted by the $[Pt/Co]_n$/IrMn metallic layers. This reduces the current injected in the NbN layer to a value below I_C and the NbN layer transits back to its zero-resistance state and so on and so forth until the current is sufficient to maintain the NbN layer in its normal state. We have observed the same oscillations in Pt/NbN samples further confirming the shunting mechanism, results not shown. At the normal state, we have reached the ohmic behavior, i.e. the relationship between V and I is linear. An accurate determination when scanning the current is perturbed by the

oscillatory behavior described above, making measurements with a fixed bias current, as the ones discussed in previous results of this chapter, more reliable.

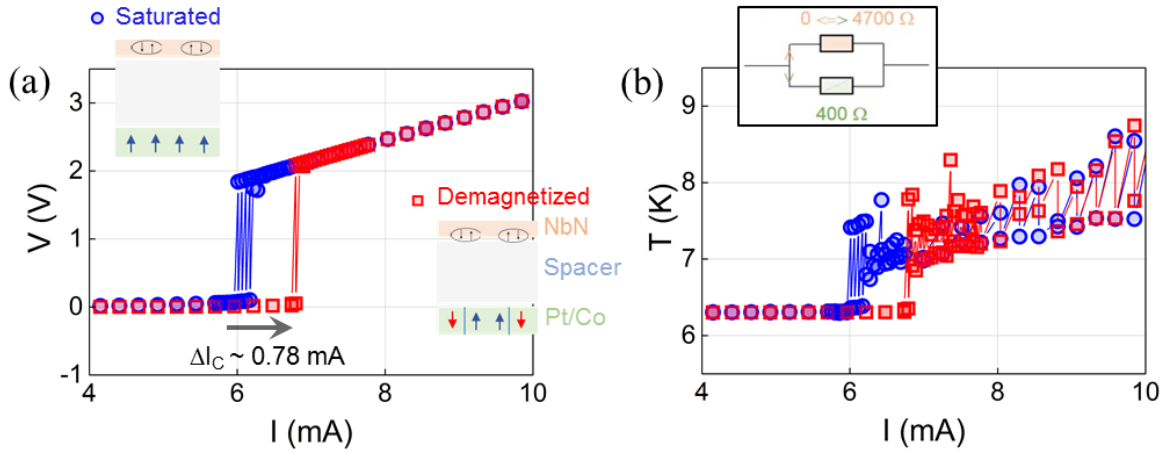

Figure 71 : (a) Critical current enhancement due to domain walls. Current (I) dependence of the voltage of a Si/SiO_2//[Pt(1)/Co(0.65)]$_{15}$/IrMn(3)/NbN(15) (nm) stack, single-domain vs. multi-domain configurations. During the measurement T = 6.3 K and H = 0.5kOe. The critical currents correspond to current densities of around 0.2 MA/cm^2. We measured a critical current enhancement of $\Delta I_C/I_C$ ~ 13%, in satisfactory agreement with the critical temperature enhancement $\Delta T_C/T_C$ ~ 10%, as shown in Figure 61. (b) T-dependence with I indicates that the measurement is perturbed by thermal fluctuations right after the superconducting transition to the high-resistance state. We note that the temperature was obtained with the on-board thermometer.

To gain further insight on the critical current, we have studied R vs I curves for several temperatures and for saturated and demagnetized state of the [Pt/Co] ferromagnet, as shown in Figure 72(a). We have selected the temperature interval from 3 K to T_C. It shows that the R vs I curves display an abrupt change from the superconducting to the normal state behavior at a defined current (I_C) for all $T < T_C$. The temperature dependence of the critical current is presented in Figure 72(b). One can observed that in the entire temperature range I_C is larger for the demagnetized than the saturated state. From the Ginzburg–Landau theory, it is possible to calculate the expected T-dependence of the critical current as follows [248,249]:

$$I = I_{C,0}\left(1-t^2\right)^{3/2}\left(1+t^2\right)^{1/2}, \qquad \text{Eq. IV-7}$$

with $t = T/T_C$. I_C values obtained experimentally follow the theoretical expression over the entire temperature range. Fitting this expression to the data shown in Figure 72(b), we obtained T_C = 9.3 K; $I_{C,0}$ = 10.1 mA (Saturated) and T_C = 9.5 K; $I_{C,0}$ = 10.6 mA (Demagnetized). It corresponds to $\Delta T_C/T_C$ ~ 2.1% and $\Delta I_C/I_C$ ~ 4.9%. The difference between the values for the critical current and critical temperature recovery between the saturated and demagnetized states could be explained by the proximity effects near the domain walls, as already described in Figure 61. Discrepancies in the values are ascribed to error in determining I_C due to the thermal fluctuations right after the superconducting transition to the high-resistance state. Besides that, it is possible to observe from Figure 72(a) that along with the abrupt change from the superconducting to normal ohmic behavior, there is a smoth evolution in the curvature with increasing temperature. It is worthy mentioning that considering domains in a ferromagnet, the interaction between stray field and magnetic flux can pin the vortex in an adjacent superconductor, resulting in an improvement on the critical current density, as already reported in the literature [250]. This behavior deserves further studies to properly understand the impact of the domains on I_C.

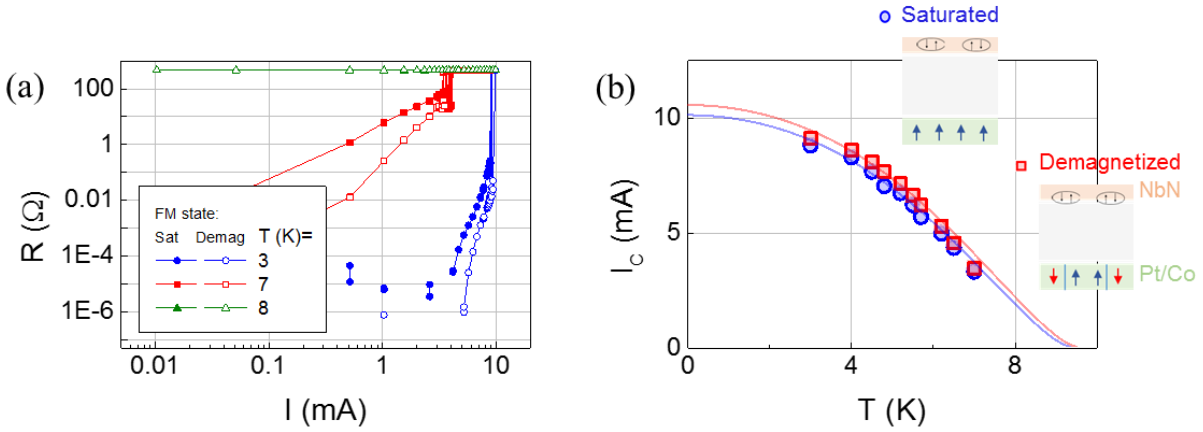

Figure 72 : (a) R vs I curves of a Si/SiO_2//[Pt(1)/Co(0.65)]$_{15}$/IrMn(3)/NbN(15) (nm) stack, single-domain vs. multi-domain configurations for selected temperatures. I is plotted in a semilogarithmic scale. I_C is determined here by the current value for which R = 0.5 mΩ. (b) Critical current dependence with temperature. Lines correspond to fits of the data considering Eq. IV-7.

In the experiments discussed above we have observed that a metallic IrMn layer is transparent to Cooper pairs transport, see Figure 66 and discussion therein. Taking advantage of the exchange bias coupling to a ferromagnet at the bottom interface and procedures involving domain imprinting, we have also shown that the recovery of superconductibity is independent of the magnetic state in the IrMn antiferromagnet (Figure 67). Before concluding this section, I will discuss preliminary experiments for an antiferromagnetic insulator/superconductor interface.

IV.1.3 Exploring NiO/NbN bilayers

The full stacks used in this study were (from substrate to surface): a-Al_2O_3(0001)//NiO(111)-50nm/NbN-15nm multilayers. NiO is grown by pulse laser deposition, and NbN is grown by dc-magnetron sputtering. The samples were deposited at SPEC (Ormes des Merisiers) by Jean-Batiste Moussy and Michel Viret and at CIME Nanotech by Christelle Gomez. Electrode contacts were created using aluminum-wire bonding directly on sample surface, as shown in Figure 73(a). Electrical parameters were then measured using standard four-point current-voltage geometries, applying an ac current (lock-in detection) of amplitude 0.5 mA and frequency 13.65 Hz. The superconducting critical temperature, T_C, of the NbN layer was determined from temperature(T)-dependent measurements of the stacks' resistance. As discussed in § IV.1.2.1, T_C was defined as the temperature for which R dropped to 0.5 mΩ.

Due to the crystal structure and spin arrangements in the easy-plane antiferromagnet NiO, domains are expected since in bulk NiO crystals spins are allowed to rest in different directions [251]. Figure 73(b) shows the critical temperature T_C of the superconducting layer as function of the field cooling angle, θ (sketched in Figure 73(a)). Before each measurement, the temperature is raised to 400 K and then it is field cooled down to 10 K under a 5 T magnetic field along different angles. Note that the sample is placed always in the same position ($\theta = 0°$) before performing a R vs T sweep. This is to avoid differences in thermalization of the sample and sample holder depending on the position inside the chamber that may generate errors in T_C determination. We experimentally measured this type of error and it can be as large as 250 mK. Depending on the angle of the field cooling, the antiferromagnetic domains might be stabilized in different states. The red-cross show the value of T_C after zero-field cooling. Preliminary results indicate that the critical temperature of the adjacent NbN superconducting layer is independent on the domain state of the NiO antiferromagnet (Figure 73(b)). The formation of

disctinct domain arrangements in a NiO upon such field cooling procedure is to be confirmed by NV-center microscopy. More systematic transport measurements are required to confirm these very preliminary data. Moreover, the parameters in play, such as superconducting coherence length-to-thicknesses ratio with respect to the expected domain and domain wall sizes in NiO, must be optimized to favor the observation of the effect.

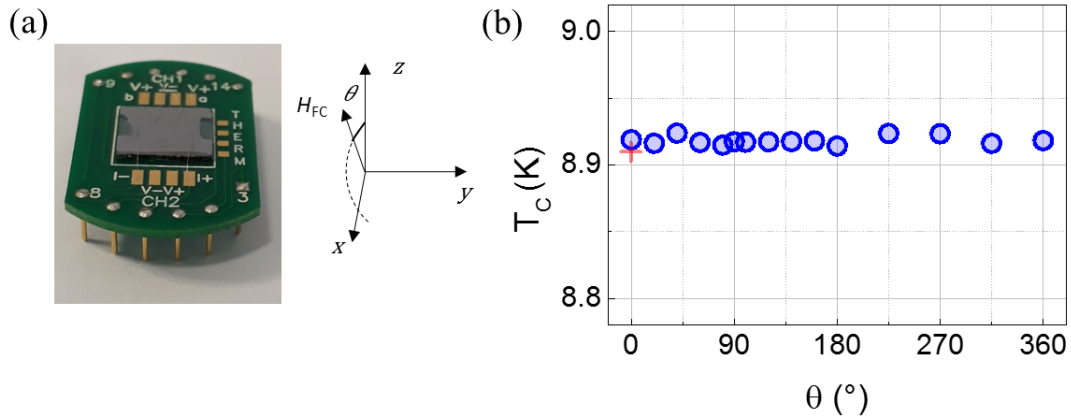

Figure 73 : (a) Picture of sample mounted. The sketch on the right illustrates the direction along which a magnetic field was applied for field cooling. (b) T_C vs θ curves of an a-Al_2O_3(0001)//NiO(111)-50nm/NbN-15nm stack. The red-cross point indicates T_C after zero-field cooling.

In the frame of the experiments described in Figure 67, different magnetic states were imprinted in the IrMn antiferromagnet by using the exchange bias interaction between the antiferromagnet and an adjacent ferromagnet. Nuances in the magnetization curves (Figure 67(c)) indicate the spin texture replication from the ferromagnet into the antiferromagnet [242]. In the following we will further discuss the impression of spin textures in antiferromagnets, as well as experimental techniques that can be used to directly observe such spin textures.

IV.2 Imprinting spin textures in antiferromagnets

Spin textures in antiferromagnets may offer new functionalities for spintronics devices compared to their ferromagnetic analogs [191]. More specifically skyrmions in antiferromagnets [191,252], also known as antiferromagnetic skyrmions, may present several advantages due to interesting physical properties emerging in antiferromagnets. Indeed they combine key features for applications in the field of spintronics as: (i) they produce no dipolar fields, making them stable at the nanometer scale in zero external magnetic field; (ii) they are robust against perturbation due to magnetic fields, which is beneficial for data retention; (iii) they exhibit zero net topological charge [28,252], thus eliminating the unwanted transverse velocity related to the skyrmion Hall effect [253,254]. Hence, it ensures a straight skyrmion trajectory with enhanced mobility [252]. However, since they lack net magnetization the experimental observation and nucleation of antiferromagnetic skyrmions is challenging. Nevertheless, direct observation of antiferromagnetic spin textures can be achieved [255], but in large-scale facilities with element-sensitive techniques like X-ray absorption spectroscopy [243,244,256], specific local probe techniques such as spin-polarized scanning tunneling microscopy [257,258] and quantum sensing with single spins (nitrogen vacancies) in diamond [259–261], or optical second harmonic generation [262] and thermal gradient microscopy [208]. Antiferromagnetic domains and domain walls in NiO [256,263],

$BiFeO_3$ [259,262], Cr_2O_3 [260], CuMnAs [261] and Mn_3Sn [208], and vortex states in IrMn [243] and NiO [255] layers were for example investigated in those ways. Recently, fractional antiferromagnetic skyrmion lattices in bulk $MnSc_2S_4$ were also observed at cryogenic temperature using neutron scattering experiments [264] as well as antiferromagnetic half-skyrmion and bimerons in α-Fe_2O_3 at room temperature [265], where the transition over magnetic phases using low temperature cycling was used to nucleate the spin textures. The current bottleneck is the nucleation of skyrmions in antiferromagnets. Application of an external magnetic field, like in ferromagnetic [266] or synthetic antiferromagnetic [267] films, is ineffective for actual antiferromagnets. We note that, for the case of synthetic antiferromagnets, the low antiferromagnetic coupling between two ferromagnetic skyrmions makes these skyrmions sensitive to external magnetic field. An antiferromagnet is also more robust against dynamical torque deformation, since its spin structure relies on strong interatomic exchange interactions.

IV.2.1 Introduction to magnetic imprint via exchange bias coupling

An alternative way to manipulate the order parameter of an antiferromagnet, is to take advantage of the strong exchange bias interaction [268] between the antiferromagnet and an adjacent ferromagnet [242] to imprint a ferromagnetic configuration in the antiferromagnet [26]. The imprinting procedure is schematically described in Figure 74 and it has been extensively used at SPINTEC for earlier studies. In a first step, exchange bias interaction is quenched by raising the sample temperature above the blocking temperature (T_B) of the ferromagnet/antiferromagnet bilayer. The antiferromagnetic layer loses its ability to pin the magnetization of the adjacent ferromagnet. The latter can then be considered as a ferromagnetic single layer in which it is possible to nucleate different types of spin textures by conventional means. In a second step, the bilayer is cooled below T_B in zero external magnetic field, causing the moments in the antiferromagnet to align with those of the ferromagnet due to the exchange bias coupling.

The hysteresis loops after a positive (negative) field cooling process results in a loop shifted towards the negative (positive) fields, as shown in Figure 74(a,b) [268]. An interesting feature is observed in the hysteresis loop after zero field cooling process from a demagnetized state (Figure 74(c)). Demagnetization is achieved by applying a decreasing, alternating magnetic field. It displays a double-loop shifted, with one sub-loop shifted towards negative fields and the other towards positive fields, indicating that the magnetic structure of the antiferromagnet is divided into two regions which are opositelly coupled with the ferromagnet, as illustrated on the left handside sketh of Figure 74(c). Indeed, for a demagnetized state in the [Pt/Co] ferromagnet we have observed maze domains (Figure 61) with an equal proportion of up and down magnetization. Therefore, during the impression of the domain structure, equal areas with opposite magnetic structure are created in the antiferromanget. Figure 74(d) illustrates the fact that the sub-loop shifted curves can be obtained for variable magnetization amplitudes by cooling in different magnetization states. In such intermediate state, after demagnetization a small field is applied during cooling. Doing so, it is possible to tune the hysteresis from a double-loop shifted to a single-loop shifted. This procedure was used to imprint multidomain states in antiferromagnets, by preparing the ferromagnet above T_B in a specific magnetic configurations [242,269] (as applied in study discussed in § IV.1.1.2).

In addition to the impression of multidomain states in antiferromagnets described in Figure 74, other magnetic textures such as vortex states were imprinted and observed experimentally in antiferromagnetic nanostructures [243,244].

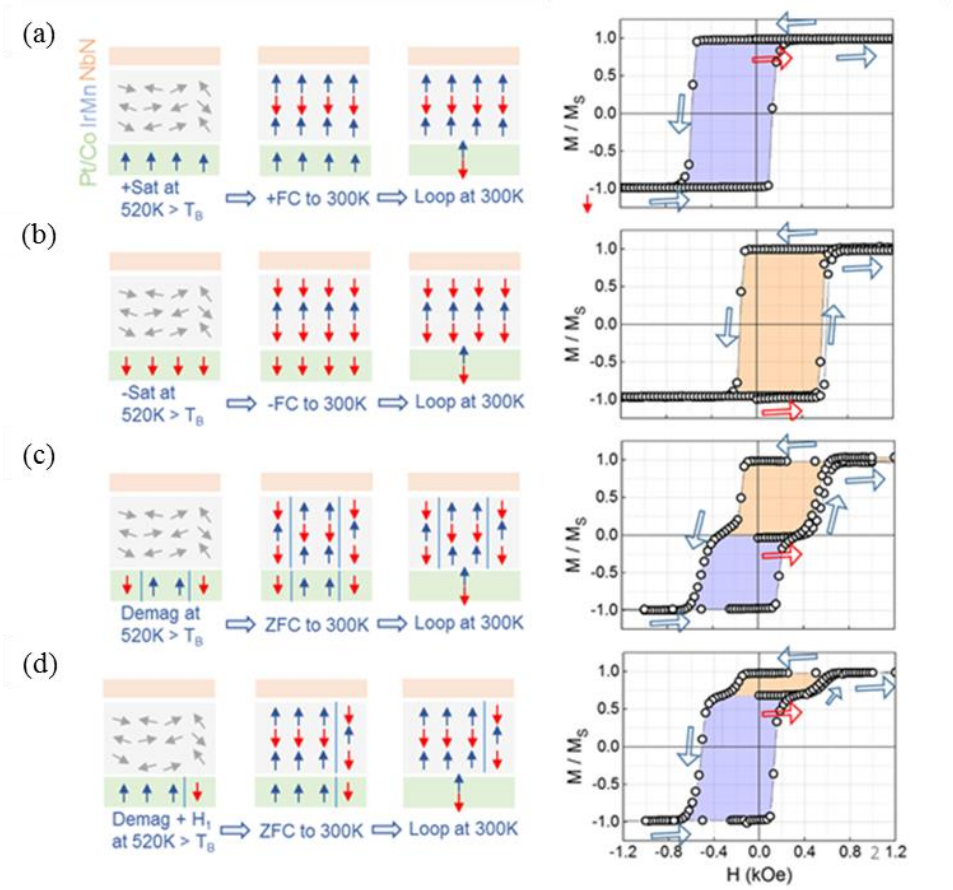

Figure 74 : Hysteresis loops measured at 300 K for a Si/SiO2//[Pt(2)/Co(0.65)]4/IrMn(5)/Pt(2) (nm) stack. The field was applied along the out-of-plane direction. The film was prepared in different magnetic configurations, as illustrated on the left handside.

IV.2.2 Imaging domain walls in the IrMn antiferromagnet by nitrogen-vacancy magnetometry

Due to the lack of net magnetization in antiferromagnets, the experimental observation of textures in antiferromagnets is challenging. One possible way to do so consists in using quantum sensing with nitrogen vacancies (NV) in diamond to measure the stray fields. Note that in antiferromagnets, uncompensated magnetic moments arise due to symmetry breaking at surfaces or domain walls, providing a way to map it by magnetic field imaging. The NV center is an atomic-scale defect in diamond hosting a spin that can be detected optically. In a NV-magnetometer, the NV center is incorporated in a scanning probe microscope. It combines, therefore, a large field sensitivity with nanometer spatial resolution. An extensive description of the technique can be found in Refs. [259–261].

The NV-magnetometry experiments, shown in Figure 75, were performed on our samples by the group of Vincent Jacques at the Laboratoire Charles Coulomb in Montpellier.

The samples used in this study consist of a Si/SiO_2//[Pt(1)/Co(0.65)]$_4$/IrMn(5)/Pt(2) (nm) stack. Such stacking was designed for NV-magnetometry experiments at room temperature that

requires: i) thin capping layer to bring the NV probe closer to the sample ensuring sufficient resolution, ii) 100% remanence at the $[Pt/Co]_n$ ferromagnet to probe stray fields from the IrMn antiferromagnet only, and iii) blocking temperature distributed across 300 K to be able to get IrMn domain walls at 300 K. Before performing the experiments, a rf line has to be defined on top of the $[Pt/Co]_n$/IrMn/Pt (nm) stack which is used for radiofrequency excitation required for the experiments. For this, the thin films were patterned into lines (measuring 5 µm wide and 250 µm long) by laser lithography. Then a Ti(5)/Al(5)/Au(50) (nm) stack is evaporated to define an antenna. Figure 75(a) shows an optical image of the resulting device. Contact electrodes were created with 500 x 2000 µm² contact pads.

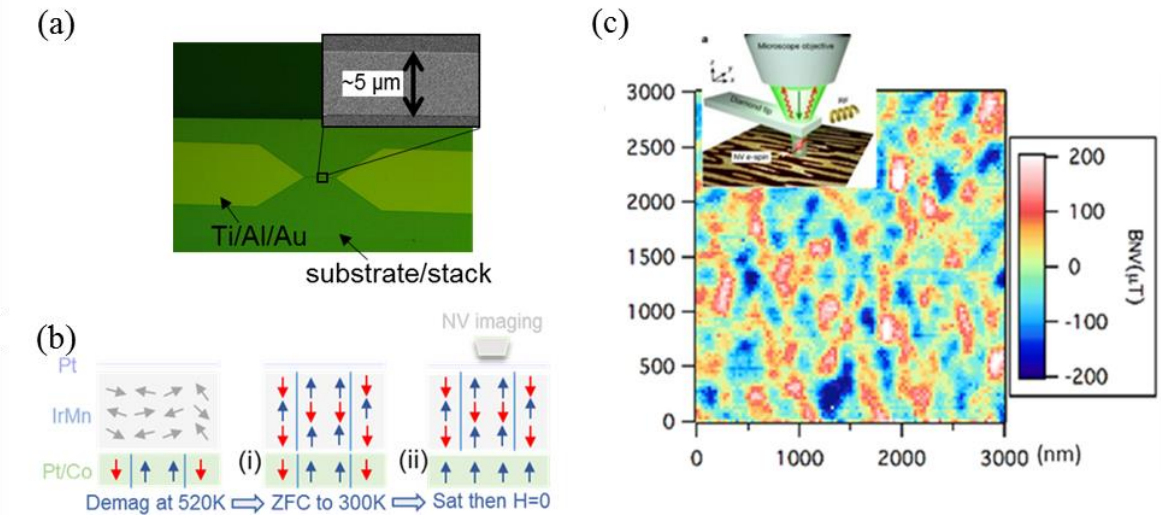

Figure 75 : (a) Optical image of a typical rf line used to perform the measurements. (b) Schematic representation of the cooling procedure performed to prepare the IrMn layer in a demagnetized state. (c) Representative measurement showing the distribution of the stray field obtained by NV-magnetometry in a $Si/SiO_2//[Pt(2)/Co(0.65)]_4/IrMn(5)/Pt(2)$ (nm) stack at 300 K.

Figure 75(b) illustrates the magnetic state preparation of the $[Pt/Co]_n$/IrMn/Pt (nm) stack before the experiments. We have employed the procedure discussed in Figure 74 to prepare magnetic domains and domains walls in the IrMn antiferromagnet. The [Pt/Co] ferromagnet is saturated to avoid a contribution coming to the stray field generated at ferromagnetic domain walls. Figure 75(c) shows the image the stray field distribution of the IrMn top interface. The technique can measure the small magnetic stray field, of the order of 100 µT here, created by the uncompensated moments located at the surface of the antiferromagnet. It indicates that the field cycling and cooling procedure can imprint the demagnetized state from the [Pt/Co] ferromagnet into the 5 nm-thick IrMn antiferromagnet. Additional measurements are currently being conducted to ensure that the observed signal does not come from spatial magnetic inhomogeneities, like anisotropy, in the bottom ferromagnet. Besides that, NV-magnetometry experiments at low temperature are being attempted.

As mentioned above, the nucleation of skyrmions in antiferromagnets is highly desired. In the following we will discuss experimental where we have employed the impression approach aiming to nucleate skyrmions in an antiferromagnetic layer.

IV.2.3 In search of skyrmions in an exchange-biased thin film of the IrMn antiferromagnet [8]

This section is adapted from Ref. [8] where the main findings can be found - Ref. [8]: K. G. Rana, R. L. Seeger, S. Ruiz-Gómez, R. Juge, Q. Zhang, V. T. Pham, M. Belmeguenai, S.

Auffret, M. Foerster, L. Aballe, G. Gaudin, V. Baltz, and O. Boulle, Appl. Phys. Lett. **119**, 192407 (2021).

Using the imprinting approach described in Figure 74, we show that spin textures can be stabilized at zero field and room temperature in an IrMn antiferromagnet. The IrMn layer was exchange-coupled to a ferromagnetic layer hosting magnetic skyrmions. Our goal was to nucleate the skyrmions in the IrMn antiferromagnet, the skyrmionic spin texture in the ferromagnet was replicated by annealing above the blocking temperature of the ferromagnetic/antiferromagnetic bilayer. Using the high spatial resolution magnetic microscopy technique XMCD-PEEM, we observe the imprinted spin textures within the IrMn layer from the XMCD signal of the uncompensated Mn spins.

The sample used in this study consisted of a (from substrate to surface) Ta(3)/Cu(3)/IrMn(5)/Pt(0.5)/Co(0.3)/NiFe(0.87)/Al(2) (nm) multilayer. The polycrystalline stack was deposited at room temperature by magnetron sputtering on a Si/SiO_2(500) wafer at a pressure of 2.3 x 10^{-3} mbar under argon. The IrMn antiferromagnet was deposited from an $Ir_{20}Mn_{80}$ (at. %) target and the NiFe ferromagnet was deposited from a $Ni_{81}Fe_{19}$ (at. %) permalloy target. A Ta(3)/Cu(3) seed bilayer was used to promote the growth of the antiferromagnetic (111)-textured fcc phase of the IrMn alloy. The composition of the stack was carefully optimized in order to stabilize skyrmions in the Co/NiFe layer [270] and allow for their observations using X-ray magnetic microscopy. The ultra-thin intermediate bilayer of Pt(0.5)/Co(0.3) allows us to achieve large perpendicular magnetic anisotropy as well as a large interfacial DMI [266,270] without magnetically decoupling the IrMn and NiFe layers. This thickness of the NiFe layer was chosen in the vicinity of the planar-to-perpendicular anisotropy transition of the ferromagnet, therefore allowing us to promote the formation of skyrmions [266]. The choice of the stacking order for the IrMn and NiFe layers, combined with the reduced thickness of the NiFe layer, was such that the sensitivity of photoemission electron microscopy to Mn spins at the IrMn surface was most favorable. A 2-nm-thick Al cap was finally deposited to form a protective and transparent $Al(2)O_x$ film after oxidation in air.

To achieve exchange bias, the sample temperature was first raised to 250°C, above T_B [26], kept for 30 minutes and cooled to room temperature in an external magnetic field applied along the out-of-plane direction – field cooling (see discussion on magnetic textures imprinting using exchange bias in § IV.2.1). The amplitude of the external field was of 5.7 kOe, i.e. sufficient to saturate the NiFe ferromagnetic layer. Upon cooling across T_B, the moments in the IrMn antiferromagnet align out-of-plane due to exchange bias coupling and freeze out below T_B, regardless of the direction of the moments in the NiFe ferromagnet. This favours a parallel alignment of the magnetic moments of the ferromagnet and antiferromagnet at the interface [268]. The saturated configuration of the IrMn layer at the interface, due to the field cooling procedure, creates an internal magnetic field sufficient to make magnetic skyrmions stable in the NiFe layer, in zero external magnetic field [270]. Following the initial field-cooling procedure, the sample temperature was raised a second time to 250°C for 30 minutes, but it was then cooled in a zero-field – zero-field cooling. As a result, the interfacial magnetic moments in the antiferromagnet are expected to align with those of the ferromagnet due to exchange bias coupling, which results in an expected replication of skyrmions in the antiferromagnet, similar to vortex replication [243,244]. Since the contribution to exchange bias pinning of the newly formed spin textures in the antiferromagnet is marginal, the out-of-plane magnetic field-dependence of the Kerr signal measured after zero field cooling remained

unchanged (Figure 76(a)). The out-of-plane magnetic-field-dependence of the Kerr signal as measured at room temperature (Figure 76(a)) is shifted with respect to zero-field by an exchange bias field, of around 500 Oe. The linear and anhysteretic reversal of the signal further indicates stripe domain reversal.

To extract the Dzyaloshinskii-Moriya interaction (DMI), we carried out Brillouin light scattering experiments. The principle of the technique is the following [271]: the magnetisation is saturated in the film plane by an external magnetic field and spin waves (SW) propagating along the direction perpendicular to this field are probed by a laser with a well-defined wave vector k_{SW}. The DMI introduces a preferred handedness and therefore leads to an energy difference between two spin waves propagating with opposite wave vectors. This energy difference corresponds to a shift in frequency : $\Delta F(k_{SW}) = F_S(k_{SW}) - F_{AS}(k_{SW})$ where F_S and F_{AS} are the Stokes (a SW is created) and Anti-Stokes (a SW was absorbed) frequencies respectively. This frequency shift is directly related to the DMI value D [271]: $\Delta F(k_{SW}) = 2\gamma k_{SW} D/(\pi M_S)$ with γ the gyromagnetic ratio. Figure 76(b) shows the frequency of the Stokes and Anti-stokes peaks as a function of k_{SW} performed for several wave vectors. The shift in frequency ΔF scales linearly with k_{SW} (Figure 76(b)), which allows us to extract $D = -0.30$ mJ/m^2 using $M_{s,eff} = 8.73 \times 105$ A.m^{-1} measured separately by SQUID magnetometry and $\gamma/(2\pi) = 31$ GHz/T. In these Brillouin light scattering experiments, a negative value for D indicates a left-handed chirality, consistently with results from the literature [266,270]. The critical D associated with the Bloch to Néel domain wall transition writes [272]: $D_C = 4\ \mu_0 M_S^2 t\ \ln 2/2\pi^2$, with t the film thickness, which can be estimated to be $D_C = 0.16$ mJ/m² in our stack. Thus, $D > D_C$ and the domain wall and skyrmions in our samples are expected to be of the chiral left handed Néel type.

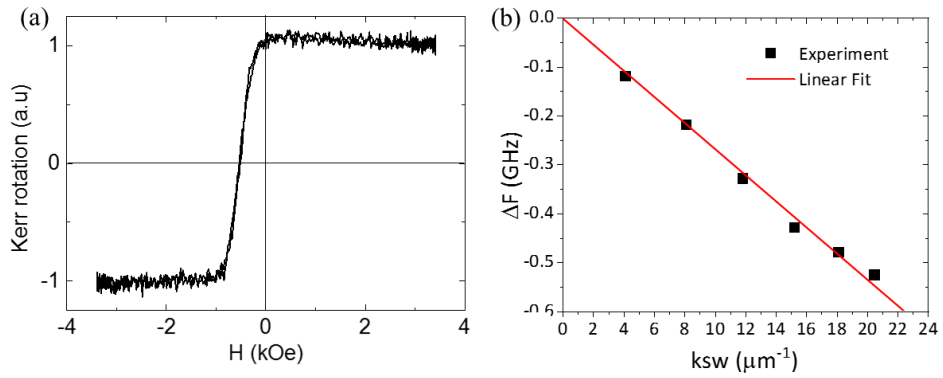

Figure 76 : (a) Out-of-plane magnetic-field-dependence of the Kerr signal as measured at room temperature for a //Ta(3)/Cu(3)/IrMn(5)/Pt(0.5)/Co(0.3)/NiFe(0.7)/Al(2) (nm) stack after the annealing procedure. (b) Frequency shift ΔF versus the in-plane k-vector, k_{SW}, for an in-plane field of $H = 8$ kOe as a result of Brillouin light scattering experiments for a //Ta(3)/Cu(3)/IrMn(5)/Pt(0.5)/Co(0.3)/NiFe(0.87)/Al(2) (nm) multilayer.

To gain insight into the impression of spin textures at the IrMn layer interface through exchange bias replication, element-specific X-ray magnetic circular dichroism photoemission electron microscopy (XMCD-PEEM) experiments were subsequently carried out at room temperature and in zero external magnetic field. These experiments were performed on the SPELEEM III microscope (Elimtec GmbH) at the CIRCE beamline in the ALBA synchrotron [273]. Typical X-ray absorption spectra (XAS) integrated over an area of about 300 µm^2 are given in Figure 77(a) (circular polarization) and Figure 77(b) (linear polarization). The X-ray magnetic circular dichroism (XMCD) in Figure 77(a) shows the existence of a small net magnetic

moment in IrMn, ascribed to the frozen uncompensated spins after the cooling procedure. The corresponding X-ray magnetic linear dichroism (XMLD) spectra (Figure 77(b)) indicates that the overall orientation of the Mn spins is tilted out-of-plane [274], in agreement with what is expected from the cooling procedure.

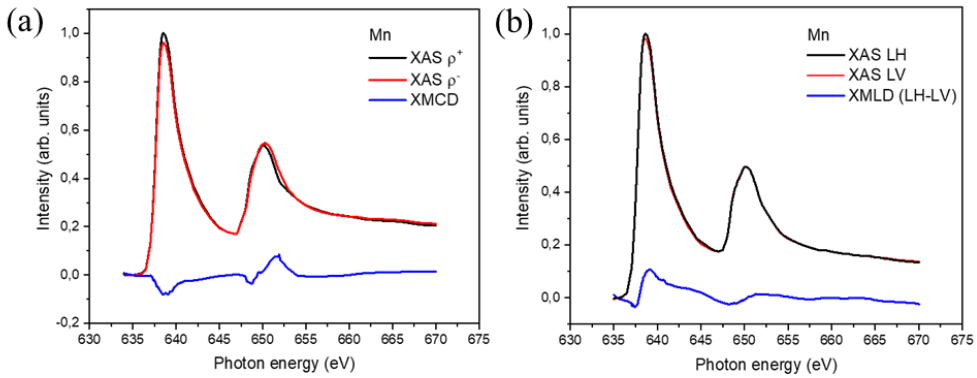

Figure 77 : Energy absorption spectra corresponding to X-ray magnetic (a) circular and (b) linear dichroism photoemission electron experiments for a //Ta(3)/Cu(3)/IrMn(5)/Pt(0.5)/Co(0.3)/NiFe(0.87)/Al(2) (nm) stack. Two polarities are shown. In (a), ρ^+ and ρ^- stands for circular right and circular left polarization respectively. XMCD is the difference of the ρ^+ and ρ^- signal; its amplitude is multiplied by a factor 2. In (b), LH and LV stands for linear horizontal and linear vertical polarization. The energy window is focused in the vicinity of the L-edges of the Mn element.

Spatially resolved XMCD-PEEM images were recorded at the Fe, and Mn L-edges for right- and left-circularly polarized X-rays. The resulting magnetic contrast image at the Fe edge (Figure 78(a)) indicates that magnetic skyrmions are stabilized in zero external magnetic field in the NiFe layer. Images at the Mn edge (Figure 78(b)) provide information on the non-compensated Mn spins at the top interface of the IrMn layer. For some regions, spin textures can clearly be observed, whose shape and position coincide with the skyrmions in the NiFe ferromagnet (Figure 78(c)). These results demonstrate that the skyrmionic spin texture in the NiFe ferromagnet is replicated in the interfacial Mn spins of the IrMn antiferromagnet. Although we cannot conclude on the penetration depth of the spin texture due to the complex spin structure of the IrMn antiferromagnet [26] combined with the weighted depth-sensitivity of the measurement, we note that earlier works have shown that exchange bias made it possible to imprint other spin textures in the depth of the antiferromagnet, down to at least 3 nm for vortices in CoO and NiO, [244] and exchange springs in IrMn [274] layers.

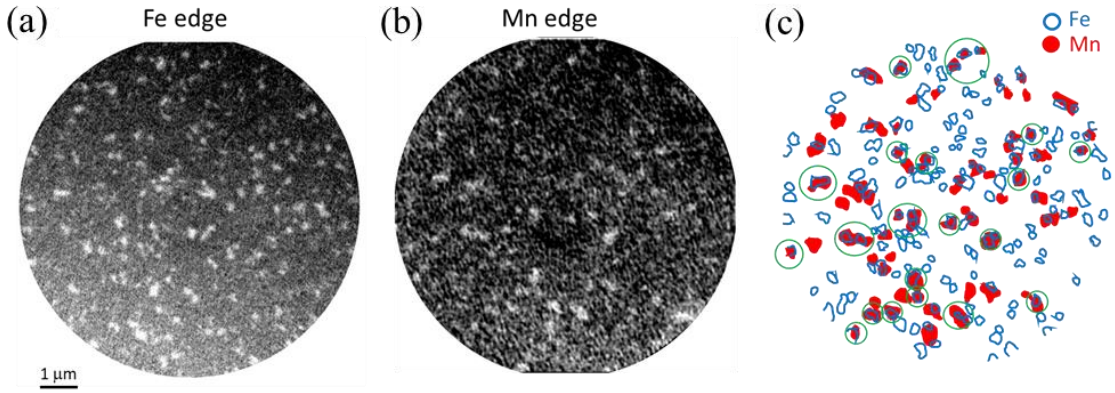

Figure 78 : Images corresponding to the NiFe and IrMn magnetic contrasts for a //Ta(3)/Cu(3)/IrMn(5)/Pt(0.5)/Co(0.3)/NiFe(0.87)/Al(2) (nm) stack. The images are obtained at room temperature and in zero external magnetic field, by XMCD-PEEM at the L-edges of the energy absorption spectra of (a) the Fe and (b) the Mn elements, respectively. (c) Superposition of the contours of textures for the Fe (open, blue) and for the Mn (filled, red) elements. The green circles indicate area where an overlap between Fe and Mn bubbles is observed. Measurements follow a two-step

annealing procedure used to stabilize bubbles in the NiFe ferromagnet in zero-field and subsequently imprint these textures in the IrMn antiferromagnet.

Additional experiments show that the spin texture in the ferromagnet is replicated in the IrMn even after the first field cooled annealing step. Furthermore, we note that the domain structure of the interfacial Mn spins follows the one of the ferromagnet when the latter is modified by an external magnetic field. These observations point to the role of the exchange interaction with the ferromagnetic layer in the stabilization of the replicated texture in the IrMn.

From Figure 78(c), we can also observe that conformity between the ferromagnetic and antiferromagnetic spin textures does not hold everywhere. For some areas, skyrmions in the NiFe layer are not replicated in the IrMn layer, and for other areas, textures in the IrMn layer are replicated but are no more facing textures in the NiFe layer. These results can be accounted for the known spatial distribution of blocking temperature (DT_B) [245,268]. In this standard procedure, the sample is first field-cooled from above the maximum blocking temperature (here, 520 K) down to 10 K under a positive field. This cooling causes the magnetic phases of the IrMn antiferromagnetic (AF) layer in contact with the ferromagnetic layer to align in the positive direction. Then, the sample's temperature is raised to an intermediate annealing temperature, T_a, and the sample is subsequently field-cooled under a negative field down to 10 K. This cooling step results in a negative reorientation of the magnetic phases of the antiferromagnetic layer in contact with the ferromagnet when the blocking temperature is lower than T_a. Finally, a hysteresis loop is measured at 10 K. These steps are repeated for a range of T_a and the variation in the exchange field, H_E, with T_a is recorded (Figure 79(a)). Since the increase in the exchange field with T_a is related to the negative repolarization of the magnetic phases of the antiferromagnetic layer, the derivative, dH_E/dT_a (Figure 79(b)) is linked to the blocking temperature distributions of these magnetic phases [246,275,276]. It is acknowledged that the volume distribution of grains in the antiferromagnet in direct contact with the ferromagnet gives rise to a high-temperature peak, and that additional magnetically frustrated phases spatially distributed over the interface result in a low-temperature contribution [245,276,277].

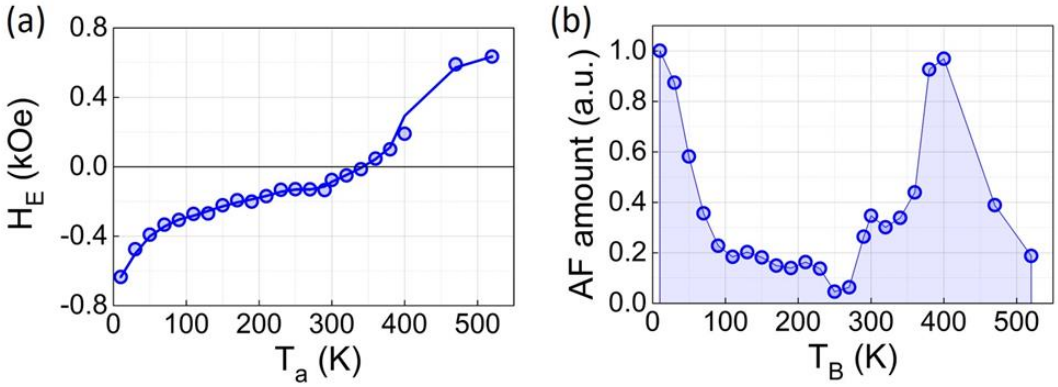

Figure 79 : (a) Variation of H_E vs. T_a for a //Ta(3)/Cu(3)/IrMn(5)/Pt(0.5)/Co(0.3)/NiFe(0.87)/Al(2) (nm) multilayer. The full line is a smooth interpolation of the data. (b) Blocking temperature distribution, corresponding to the derivative dH_E/dT_a vs. T_a from the data interpolation.

Most importantly, the results shown in (Figure 79(b)) indicate that the blocking temperatures of the various areas composing the IrMn/NiFe interface are distributed on both sides of 300 K. As a result, for areas where $T_B \geq 300$ K, the magnetic configuration of the NiFe ferromagnet can be stabilized in the 5 nm-thick IrMn antiferromagnet at 300 K by a cooling procedure from T_B to 300 K, in contrast to areas where $T_B < 300$ K, in which case, textures cannot be stabilized

in this way in the IrMn antiferromagnet [276,278]. Note that there has been so far only indirect insights on such spatial distributions, for example through the correlation between disordered magnetic phases spread above ferromagnetic/antiferromagnetic thin films and device-to-device variability of exchange bias in spintronic applications, after patterning the thin film [279]. Here, our observation would provide a direct observation of spatial distribution of blocking temperature in an exchange-biased stack.

Summary

In summary, we demonstrate the the impression from ferromagnetic skyrmions into a sputtered IrMn antiferromagnetic thin films, at room temperature and in zero external magnetic field. Such spin textures were nucleated by replicating the skyrmionic spin texture of an adjacent exchange biased ferromagnet by annealing above the blocking temperature of the ferromagnet/antiferromagnet bilayer. Element-specific X-ray magnetic microscopy allows the direct observation of the imprited spin textures at the interface of the antiferromagnet, from the uncompensated Mn spins at the interface. This study paves the way for future advances, since several spin-dependent transport effects in antiferromagnetic skyrmions, like topological Hall [280] or spin-orbit torque effects [281], have been theoretically predicted and have yet to be experimentally demonstrated, along with the closely related promising applications opening up a path for logic and memory devices based on skyrmion manipulation in antiferromagnets.

Conclusion and perspectives

In order to fully exploit the physical properties of antiferromagnets for spintronics applications, a better understanding on the spin and charge transport mechanisms in antiferromagnetic spin structures and spin textures is needed. In spite of the development of the condensed matter physics understanding concerning antiferromagnets during the last decade, there is much to be done to realize the long-sought pure antiferromagnet-based devices. Aiming to contribute to this field, in my thesis we have investigated the spin and charge transport in ferro- and antiferromagnets using different experimental approaches.

Initially we have used the spin pumping by means of ferromagnetic resonance to probe the magnization dynamics of a ferromagnetic layer in structures containing a ferromagnetic and an adjacent spin sink layer [2,3]. Such technique allows the extraction of relevant physical parameters for spintronics. Doing so, we studied the spin transport in ferro- and antiferromagnets of different electrical states, and considering different nature of spin current transport. The observed enhancement of the spin absorption at the phase transition is related to linear spin fluctuations. Currently, experiments are envisaged in the group, aiming to explore superconducting spin sinks. Electronic spin injection and dynamics in superconductors are of central fundamental interest and also relevant in the emerging field of super-spintronics. Beyond spin pumping, we have conducted an experiment-oriented study on the impact of eddy currents below the microwave magnetic skin-depth [1]. Remarkbly, it explains the line shape assymetries and phase lags reported in stripline experiments.

Following the study in spin pumping, we have explored spin-charge conversion in ferro- and antiferromagnets. Specifically in ferromagnets, we have observed experimentally a self-induced inverse spin Hall effect in NiFe [4]. Such spin-charge conversion in a metallic ferromagnet displays a non-monotonous temperature-dependence and our results indicated that self-induced conversion within the NiFe ferromagnet can be as efficient as that recorded with noble metals such as Pt. We compared our experimental resuls with first-principle calculations to explain the origin of the non-monotonicity. Therefore, self-induced spin-charge conversion needs to be carefully considered when investigating SO-related effects in materials destined for use in spintronics. Currently, more systematic studies are conducted in the group, following the observation of a similar effect in Co, in order to better understand a possible universal behavior for metallic ferromagnets. Concerning spin-charge conversion in antiferromagnets, we have compared spin transport and spin-charge conversion in the GHz and THz frequency ranges [5]. Besides, we have shown preliminary data on the search of the impact of non-linear spin fluctuations in the spin-charge conversion signal. There ongoing experiments are being made to confirm that the anomaly obtained in the spin-charge conversion signal relates to such effect. For this, we take advantage

of the known thickness-dependence of the critical temperature of IrMn. Besides that, other samples, which are expected to show larger spin fluctuations near the phase transitions are being studied, for example a larger signal is expected in spin glass binary alloys.

Next, we have explored charge transport specific to antiferromagnets. We have observed and exploited a spontaneous Hall effect in epitaxial thin films of Mn_5Si_3 governed by crystal and magnetic symmetries [6]. By presenting structural, magnetization and magnetotransport results in several samples we discuss the role of epitaxial growth on our results. These results are interpreted in terms of a novel $\mathcal{T}$ symmetry breaking mechanism arising in a collinear antiferromagnet with a staggered Zeeman spin-splitting. They are a promising path for the realization of giant magnetoresistance and spin transfer torque in antiferromagnets. On thermoelectric effects, such as the Nernst effect, new devices comprising on-chip heater structures are being implemented.

In the last chapter, we studied charge transport specific to magnetic textures of ferro- and antiferromagnets. We have performed a systematic study of the recovery of the superconducting critical temperature in ferromagnet/spacer/superconductor heterostructures observed when the ferromagnetic layer is set to a multi-domain state [7]. After optimizing several parameters into play, we used it as a technique to extract information of the Cooper-pair characteristic lengths on the spacer layer. Particularly, we were interested in extracting the Cooper pair penetration depth of metallic antiferromagnets. Besides that, we have shown preliminary data of proximity effects in an antiferromagnetic insulator/superconductor interface, which is a topic that deserves further investigation. In parallel with these studies, we have taken advantage of the exchange coupling to replicate spin textures from ferromagnets in antiferromagnets. Specifically, we have used this approach in the search of the transport properties of skyrnions in antiferromagnets [8].

During my thesis I have studied several systems using various experimental techniques, which broaden my knowledge in experimental spintronics [1–8]. I have been trained to perform experiments using the spin pumping technique in a cavity resonator down to low temperature and broadband stripline experiments. These techniques are extensively used for the results involving spin pumping enhancement and spin-charge conversion presented in § I and II, respectively. I have also used more conventional magnetotransport properties of thin films, including complex epitaxial antiferromagnets and heterostructures containing superconductors, as presented in § III and IV, respectively. For such experiments, I was trained at the cleanroom to prepare H-bar devices using laser lithography. Besides magnetotransport, I have also used extensively VSM, SQUID and magnetic force microscopy techniques for sample characterization.

Bibliography

[1] O. Gladii*, R. L. Seeger*, L. Frangou, G. Forestier, U. Ebels, S. Auffret, and V. Baltz, Appl. Phys. Lett. **115**, 032403 (2019), * equal first.

[2] O. Gladii, L. Frangou, G. Forestier, R. L. Seeger, S. Auffret, I. Joumard, M. Rubio-Roy, S. Gambarelli, and V. Baltz, Phys. Rev. B **98**, 094422 (2018).

[3] O. Gladii, L. Frangou, G. Forestier, R. L. Seeger, S. Auffret, M. Rubio-Roy, R. Weil, A. Mougin, C. Gomez, W. Jahjah, J. P. Jay, D. Dekadjevi, D. Spenato, S. Gambarelli, and V. Baltz, Appl. Phys. Express **12**, 023001 (2019).

[4] O. Gladii, L. Frangou, A. Hallal, R. L. Seeger, P. Noël, G. Forestier, S. Auffret, M. Rubio-Roy, P. Warin, L. Vila, S. Wimmer, H. Ebert, S. Gambarelli, M. Chshiev, and V. Baltz, Phys. Rev. B **100**, 174409 (2019).

[5] O. Gueckstock*, R. L. Seeger*, T. S. Seifert, S. Auffret, S. Gambarelli, J. Kirchhof, K. Bolotin, V. Baltz, T. Kampfrath, and L. Nádvorní, ArXiv:2011.04191v1 (2021), *equal first.

[6] H. Reichlova*, R. L. Seeger*, R. González-Hernández, I. Kounta, R. Schlitz, D. Kriegner, P. Ritzinger, M. Lammel, M. Leiviskä, V. Petricek, P. Dolezal, E. Schmoranzerova, A. Bad'ura, A. Thomas, V. Baltz, L. Michez, J. Sinova, S. T. B. Goennenwein, T. Jungwirth, and L. Šmejkal, ArXiv:2012.15651v2 (2021), * equal first.

[7] R. L. Seeger, G. Forestier, O. Gladii, M. Leiviskä, S. Auffret, I. Joumard, C. Gomez, M. Rubio-Roy, A. I. Buzdin, M. Houzet, and V. Baltz, Phy. Rev. B **104**, 054413 (2021).

[8] K. G. Rana, R. L. Seeger, S. Ruiz-Gómez, R. Juge, Q. Zhang, V. T. Pham, M. Belmeguenai, S. Auffret, M. Foerster, L. Aballe, G. Gaudin, V. Baltz, and O. Boulle, Appl. Phys. Lett. **119**, 192407 (2021).

[9] C. Chappert, A. Fert, and F. N. V. Dau, Nat. Mater. **6**, 813-823 (2007).

[10] S. Bhatti, R. Sbiaa, A. Hirohata, H. Ohno, S. Fukami, and S. N. Piramanayagam, Mater. Today **20**, 530-548 (2017).

[11] A. Hirohata, K. Yamada, Y. Nakatani, I. L. Prejbeanu, B. Dieny, P. Pirro, and B. Hillebrands, J. Magn. Magn. Mater. **509**, 166711 (2020).

[12] W. Thomson, Proc. R. Soc. London **8**, 546-560 (1856).

[13] E. H. Hall, Am. J. Math. **2**, 287-292 (1879).

[14] E. H. Hall, Proc. Phys. Soc. London **4**, 325 (1880).

[15] M. N. Baibich, J. M. Broto, A. Fert, F. N. Van Dau, F. Petroff, P. Etienne, G. Creuzet, A., Friederich, and J. Chazelas, Phys. Rev. Lett. **61**, 2472 (1988).

[16] G. Binasch, P. Grünberg, F. Saurenbach, and W. Zinn, Phy. Rev. B **38**, 4828 (1989).

[17] B. Dieny, J. Magn. Magn. Mater. **136**, 335-359 (1994).

[18] J. S. Moodera, L. R. Kinder, T. M.Wong, and R. Meservey, Phys. Rev. Lett. **74**, 3273 (1995).

[19] J. C. Slonczewski, J. Magn. Magn. Mater. **159**, L1-L7 (1996).

[20] L. Berger, Phy. Rev. B **54**, 9353 (1996).

[21] Z. D., Z. Li, S. Wang, Y. Ding, A. Panchula, E. Chen, L.-C. Wang, and H. Yiming, J. Phys. Condens. Matter **19**, 165209 (2007).

[22] D. C. Ralph and M. D. Stiles, J. Magn. Magn. Mater. **329**, 1190-1216 (2008).

[23] I. M. Miron, K. Garello, G. Gaudin, P.-J. Zermatten, M. V. Costache, S. Auffret, S. Bandiera, B. Rodmacq, A. Schuhl, and P. Gambardella, Nature **476**, 189 (2011).

[24] K. Garello, I. M. Miron, C. O. Avci, F. Freimuth, Y. Mokrousov, S. Blugel, S. A. Ret, O. Boulle, G. Gaudin, and P. Gambardella, Nat. Nanotechnol. **8**, 587 (2013).

[25] L. Liu, C. F. Pai, Y. Li, H. W. Tseng, D. C. Ralph, and R. A. Buhrman, Science (80-.). **336**, 555-558 (2012).

[26] V. Baltz, A. Manchon, M. Tsoi, T. Moriyama, T. Ono, and Y. Tserkovnyak, Rev. Mod. Phys. **90**, 015005 (2018).

[27] T. Jungwirth, X. Marti, P. Wadley, and J. Wunderlich, Nat. Nanotechnol. **11**, 231-241 (2016).

[28] L. Šmejkal, Y. Mokrousov, B. Yan, and A. H. MacDonald, Nat. Phys. **14**, 242-251 (2018).

[29] L. Šmejkal, A. H. MacDonald, J. Sinova, S. Nakatsuji, and T. Jungwirth, ArXiv:2107.03321 (2021).

[30] L. Landau and E. Lifshitz, Perspect. Theor. Phys. **169**, 51-65 (1992).

[31] T. L. Gilbert, IEEE Trans. Magn. **40**, 3443-3449 (2004).

[32] J. C. Slonczewski, J. Appl. Phys. **44**, 1759-1770 (1973).

[33] V. V. Volkov and V. A. Bokov, Phys. Solid State **50**, 199-228 (2008).

[34] D. V. Berkov and J. Miltat, J. Magn. Magn. Mater. **320**, 1238-1259 (2008).

[35] S. Azzawi, A. T. Hindmarch, and D. Atkinson, J. Phys. D. Appl. Phys. **50**, 473001 (2017).

[36] J. A. C. Bland and B. Heinrich, *Ultrathin Magnetic Structures III* (Springer, New York, 2005).

[37] B. Heinrich, D. Fraitová, and V. Kamberský, Phys. Status Solidi **23**, 501-507 (1967).

[38] V. Kamberský, Phys. Rev. B **76**, 134416 (2007).

[39] K. Gilmore, Y. U. Idzerda, and M. D. Stiles, Phys. Rev. Lett. **99**, 027204 (2007).

[40] K. Gilmore, M. D. Stiles, J. Seib, D. Steiauf, and M. Fähnle, Phys. Rev. B **81**, 174414 (2010).

[41] H. Suhl, IEEE Trans. Magn. **34**, 1834-1838 (1998).

[42] B. Heinrich, R. Urban, and G. Woltersdorf, J. Appl. Phys. **91**, 7523-7525 (2002).

[43] M. A. W. Schoen, J. M. Shaw, H. T. Nembach, M. Weiler, and T. J. Silva, Phys. Rev. B **92**, 184417 (2015).

[44] M. M. Qaid, T. Richter, A. Müller, C. Hauser, C. Ballani, and G. Schmidt, Phys. Rev. B **96**, 184405 (2017).

[45] V. Flovik, F. Macià, A. D. Kent, and E. Wahlström, J. Appl. Phys. **117**, 143902 (2015).

[46] V. Flovik, B. H. Pettersen, and E. Wahlström, J. Appl. Phys. **119**, 163903 (2016).

[47] S. Mizukami, Y. Ando, and T. Miyazaki, Jpn. J. Appl. Phys. **40**, 580-585 (2001).

[48] Y. Tserkovnyak, A. Brataas, and G. E. W. Bauer, Phys. Rev. B **66**, 224403 (2002).

[49] Y. Tserkovnyak, A. Brataas, G. E. W. Bauer, and B. I. Halperin, Rev. Mod. Phys. **77**, 1375-1421 (2005).

[50] K. Ando, Semicond. Sci. Technol. **29**, 043002 (2014).

[51] M. V. Costache, S. M. Watts, C. H. Van Der Wal, and B. J. Van Wees, Phys. Rev. B **78**, 064423 (2008).

[52] K. Xia, P. J. Kelly, G. E. W. Bauer, A. Brataas, and I. Turek, Phys. Rev. B **65**, 2204011(R) (2002).

[53] S. Maekawa, S. O. Valenzuela, E. Saitoh, and T. Kimura, *Spin Current* (Oxford University Press, 2011).

[54] C. Kittel, Phys. Rev. **73**, 155-161 (1948).

[55] C. E. Patton, J. Appl. Phys. **39**, 3060-3068 (1968).

[56] E. Schlömann, Phys. Rev. **182**, 632-645 (1969).

[57] S. S. Kalarickal, P. Krivosik, M. Wu, C. E. Patton, M. L. Schneider, P. Kabos, T. J. Silva, and J. P. Nibarger, J. Appl. Phys. **99**, 093909 (2006).

[58] I. S. Maksymov and M. Kostylev, Phys. E Low-Dimensional Syst. Nanostructures **69**, 253-293 (2015).

[59] A. Ghosh, J. F. Sierra, S. Auffret, U. Ebels, and W. E. Bailey, Appl. Phys. Lett. **98**, 052508 (2011).

[60] A. Ghosh, S. Auffret, U. Ebels, and W. E. Bailey, Phys. Rev. Lett. **109**, 127202 (2012).

[61] O. Mosendz, J. E. Pearson, F. Y. Fradin, G. E. W. Bauer, S. D. Bader, and A. Hoffmann, Phys. Rev. Lett. **104**, 046601 (2010).

[62] E. Montoya, T. McKinnon, A. Zamani, E. Girt, and B. Heinrich, J. Magn. Magn. Mater. **356**, 12-20 (2014).

[63] W. Heinrich, IEEE Trans. Microw. Theory Tech. **41**, 45-52 (1993).

[64] M. Bailleul, Appl. Phys. Lett. **103**, 192405 (2013).

[65] F. J. Dyson, Phys. Rev. **98**, 349-359 (1955).

[66] A. J. Berger, E. R. J. Edwards, H. T. Nembach, A. D. Karenowska, M. Weiler, and T. J. Silva, Phys. Rev. B **97**, 094407 (2018).

[67] K. J. Kennewell, M. Kostylev, N. Ross, R. Magaraggia, R. L. Stamps, M. Ali, A. A. Stashkevich, D. Greig, and B. J. Hickey, J. Appl. Phys. **108**, 073917 (2010).

[68] W. E. Bailey, C. Cheng, R. Knut, O. Karis, S. Auffret, S. Zohar, D. Keavney, P. Warnicke, J. S. Lee, and D. A. Arena, Nat. Commun. **4**, 2025 (2013).

[69] V. Vlaminck, J. E. Pearson, S. D. Bader, and A. Hoffmann, Phys. Rev. B **88**, 064414 (2013).

[70] M. Krakowski, Arch. Für Elektrotechnik **64**, 307-311 (1982).

[71] K. Fuchs, Math. Proc. Cambridge Philos. Soc. **34**, 100-108 (1938).

[72] E. H. Sondheimer, Adv. Phys. **1**, 1-42 (1952).

[73] S. P. Dash, S. Sharma, J. C. Le Breton, J. Peiro, H. Jaffrès, J. M. George, A. Lemaître, and R. Jansen, Phys. Rev. B **84**, 054410 (2011).

[74] R. W. Sanders, D. Paquette, V. Jaccarino, and S. M. Rezende, Phys. Rev. B **10**, 132-138 (1974).

[75] S. Andrieu, A. Neggache, T. Hauet, T. Devolder, A. Hallal, M. Chshiev, A. M. Bataille, P. Le Fèvre, and F. Bertran, Phys. Rev. B **93**, 094417 (2016).

[76] M. A. W. Schoen, D. Thonig, M. L. Schneider, T. J. Silva, H. T. Nembach, O. Eriksson, O. Karis, and J. M. Shaw, Nat. Phys. **12**, 839-842 (2016).

[77] K. Klein, B. Hauer, B. Stoib, M. Trautwein, S. Matich, H. Huebl, O. Astakhov, F. Finger, R. Bittl, M. Stutzmann, and M. S. Brandt, Rev. Sci. Instrum. **84**, 103911 (2013).

[78] S. Il Kim, M. S. Seo, and S. Y. Park, J. Appl. Phys. **115**, 17C501 (2014).

[79] W. R. Hagen, *Biomolecular EPR Spectroscopy* (CRC Press, 2008).

[80] Y. Ohnuma, H. Adachi, E. Saitoh, and S. Maekawa, Phy. Rev. B **89**, 174417 (2014).

[81] L. Frangou, S. Oyarzún, S. Auffret, L. Vila, S. Gambarelli, and V. Baltz, Phys. Rev. Lett. **116**, 077203 (2016).

[82] W. Lin, K. Chen, S. Zhang, and C. L. Chien, Phys. Rev. Lett. **116**, 186601 (2016).

[83] Z. Qiu, J. Li, D. Hou, E. Arenholz, A. T. N'Diaye, A. Tan, K. I. Uchida, K. Sato, S. Okamoto, Y. Tserkovnyak, Z. Q. Qiu, and E. Saitoh, Nat. Commun. **7**, 12670 (2016).

[84] P. Merodio, A. Ghosh, C. Lemonias, E. Gautier, U. Ebels, M. Chshiev, H. Béa, V. Baltz, and W. E. Bailey, Appl. Phys. Lett. **104**, 032406 (2014).

[85] T. Yamaoka, M. Mekata, and H. Takaki, J. Phys. Soc. Japan **31**, 301 (1971).

[86] M. Inoue, M. Ichioka, and H. Adachi, Phys. Rev. B **96**, 024414 (2017).

[87] L. Frangou, G. Forestier, S. Auffret, S. Gambarelli, and V. Baltz, Phys. Rev. B **95**, 054416 (2017).

[88] D. Petti, E. Albisetti, H. Reichlová, J. Gazquez, M. Varela, M. Molina-Ruiz, A. F. Lopeandía, K. Olejník, V. Novák, I. Fina, B. Dkhil, J. Hayakawa, X. Marti, J.

Wunderlich, T. Jungwirth, and R. Bertacco, Appl. Phys. Lett. **102**, 192404 (2013).

[89] S. Jenkins, R. W. Chantrell, and R. F. L. Evans, J. App. Phys. **128**, 033903 (2020).

[90] H. Saglam, W. Zhang, M. B. Jungfleisch, J. Sklenar, J. E. Pearson, J. B. Ketterson, and A. Hoffmann, Phys. Rev. B **94**, 140412 (R) (2016).

[91] M. Henkel, S. Andrieu, P. Bauer, and M. Piecuch, Phys. Rev. Lett. **80**, 4783-4786 (1998).

[92] R. Zhang and R. F. Willis, Phys. Rev. Lett. **86**, 2665-2668 (2001).

[93] J. McCord, R. Mattheis, and D. Elefant, Phys. Rev. B **70**, 094420 (2004).

[94] J. Dubowik, F. Stobiecki, I. Gościańska, Y. P. Lee, A. Paetzold, and K. Röll, Eur. Phys. J. B **45**, 283-288 (2005).

[95] H. Xi, R. M. White, Z. Gao, and S. Mao, J. Appl. Phys. **92**, 4828 (2002).

[96] S. M. Rezende, A. Azevedo, M. A. Lucena, and F. M. De Aguiar, Phys. Rev. B **63**, 214418 (2001).

[97] A. Mougin, C. Dufour, K. Dumesnil, P. Mangin, and G. Marchai, J. Magn. Magn. Mater. **165**, 168-171 (1997).

[98] B. Khodadadi, J. B. Mohammadi, C. Mewes, T. Mewes, M. Manno, C. Leighton, and C. W. Miller, Phys. Rev. B **96**, 054436 (2017).

[99] Y. Ou, D. C. Ralph, and R. A. Buhrman, Phys. Rev. Lett. **120**, 097203 (2018).

[100] A. Michels, J. P. Bick, R. Birringer, A. Ferdinand, J. Baller, R. Sanctuary, S. Philippi, D. Lott, S. Balog, E. Rotenberg, G. Kaindl, and K. M. Döbrich, Phys. Rev. B **83**, 224415 (2011).

[101] J. Yue, S. Jiang, D. Zhang, H. Yuan, Y. Wang, L. Lin, Y. Zhai, J. Du, and H. Zhai, AIP Adv. **6**, 056120 (2016).

[102] E. N. Abarra, K. Takano, F. Hellman, and A. E. Berkowitz, Phys. Rev. Lett. **77**, 3451-3454 (1996).

[103] C. Boeglin, O. Ersen, M. Pilard, V. Speisser, and F. Kronast, Phy. Rev. B **80**, 035409 (2009).

[104] D. Hou, Z. Qiu, J. Barker, K. Sato, K. Yamamoto, S. Vélez, J. M. Gomez-Perez, L. E. Hueso, F. Casanova, and E. Saitoh, Phys. Rev. Lett. **118**, 147202 (2017).

[105] D. Alders, L. Tjeng, F. Voogt, and T. Hibma, Phys. Rev. B **57**, 11623-11631 (1998).

[106] W. Lin and C. L. Chien, Phys. Rev. Lett. **118**, 067202 (2017).

[107] M. I. Dyakonov and V. I. Perel, Phys. Lett. A **35A**, 459-460 (1971).

[108] J. E. Hirsch, Phys. Rev. Lett. **83**, 1834-1837 (1999).

[109] Y. K. Kato, R. C. Myers, A. C. Gossard, and D. D. Awschalom, Science (80-.). **306**, 1910-1913 (2004).

[110] J. Sinova, S. O. Valenzuela, J. Wunderlich, C. H. Back, and T. Jungwirth, Rev. Mod. Phys. **87**, 1213-1260 (2015).

[111] N. Nagaosa, J. Sinova, S. Onoda, A. H. MacDonald, and N. P. Ong, Rev. Mod. Phys. **82**,

1539-1592 (2010).

[112] A. Hoffmann, IEEE Trans. Magn. **49**, 5172-5193 (2013).

[113] D. Xiao, M. C. Chang, and Q. Niu, Rev. Mod. Phys. **82**, 1959-2007 (2010).

[114] Y. Shiomi, *Anomalous and Topological Hall Effects in Itinerant Magnets* (Springer Japan, 2013).

[115] G. Y. Guo, S. Murakami, T. Chen, and N. Nagaosa, Phys. Rev. Lett. **100**, 096401 (2008).

[116] G. Vignale, J. Supercond. Nov. Magn. **23**, 3-10 (2010).

[117] J. Smit and J. Volger, Lett. to Ed. 1576-1577 (1953).

[118] J. Smit, Physica **24**, 39-51 (1958).

[119] L. Berger, Phys. Rev. B **2**, 4559-4566 (1970).

[120] D. Wei, M. Obstbaum, M. Ribow, C. H. Back, and G. Woltersdorf, Nat. Commun. **5**, 3768 (2014).

[121] K. Ando, S. Takahashi, J. Ieda, Y. Kajiwara, H. Nakayama, T. Yoshino, K. Harii, Y. Fujikawa, M. Matsuo, S. Maekawa, and E. Saitoh, J. Appl. Phys. **109**, 103913 (2011).

[122] M. Harder, Y. Gui, and C. M. Hu, Phys. Rep. **661**, 1-59 (2016).

[123] R. Iguchi and E. Saitoh, J. Phys. Soc. Japan **86**, 011003 (2017).

[124] H. J. Juretschke, J. Appl. Phys. **31**, 1401 (1960).

[125] Y. Otani, M. Shiraishi, A. Oiwa, E. Saitoh, and S. Murakami, Nat. Phys. **13**, 829-832 (2017).

[126] F. Hellman, M. S. Division, L. Berkeley, A. Hoffmann, G. S. D. Beach, E. E. Fullerton, A. H. Macdonald, and D. C. Ralph, Rev. Mod. Phys. **89**, 025006 (2017).

[127] B. F. Miao, S. Y. Huang, D. Qu, and C. L. Chien, Phys. Rev. Lett. **111**, 066602 (2013).

[128] A. Azevedo, O. A. Santos, R. O. Cunha, R. Rodríguez-Suárez, and S. M. Rezende, Appl. Phys. Lett. **104**, 152408 (2014).

[129] A. Tsukahara, Y. Ando, Y. Kitamura, H. Emoto, E. Shikoh, M. P. Delmo, T. Shinjo, and M. Shiraishi, Phys. Rev. B **89**, 235317 (2014).

[130] C. Ciccarelli, K. M. D. Hals, A. Irvine, V. Novak, Y. Tserkovnyak, H. Kurebayashi, A. Brataas, and A. Ferguson, Nat. Nanotechnol. **10**, 50-54 (2015).

[131] K. Kanagawa, Y. Teki, and E. Shikoh, AIP Adv. **8**, 055910 (2018).

[132] Y. Omori, E. Sagasta, Y. Niimi, M. Gradhand, L. E. Hueso, F. Casanova, and Y. Otani, Phys. Rev. B **99**, 014403 (2019).

[133] W. Wang, T. Wang, V. P. Amin, Y. Wang, A. Radhakrishnan, A. Davidson, S. R. Allen, T. J. Silva, H. Ohldag, D. Balzar, B. L. Zink, P. M. Haney, J. Q. Xiao, D. G. Cahill, V. O. Lorenz, and X. Fan, Nat. Nanotechnol. **14**, 819-824 (2019).

[134] A. Azevedo, R. O. Cunha, F. Estrada, O. Alves Santos, J. B. S. Mendes, L. H. Vilela-Leão, R. L. Rodríguez-Suárez, and S. M. Rezende, Phys. Rev. B **92**, 024402 (2015).

[135] K. M. D. Hals and A. Brataas, Phys. Rev. B **91**, 214401 (2015).

[136] F. Freimuth, S. Blügel, and Y. Mokrousov, Phys. Rev. B **92**, 064415 (2015).

[137] J. C. Rojas-Sánchez, M. Cubukcu, A. Jain, C. Vergnaud, C. Portemont, C. Ducruet, A. Barski, A. Marty, L. Vila, J. P. Attané, E. Augendre, G. Desfonds, S. Gambarelli, H. Jaffrès, J. M. George, and M. Jamet, Phys. Rev. B **88**, 064403 (2013).

[138] I. Miccoli, F. Edler, H. Pfnür, and C. Tegenkamp, J. Phys. Condens. Matter **27**, 223201 (2015).

[139] J. F. Sierra, V. V. Pryadun, F. G. Aliev, S. E. Russek, M. García-Hernández, E. Snoeck, and V. V. Metlushko, Appl. Phys. Lett. **93**, 172510 (2008).

[140] J. Smit and H. G. Beljers, Philips Res. Rep. **10**, 113-130 (1955).

[141] H. Ebert, D. Ködderitzsch, and J. Minár, Reports Prog. Phys. **74**, 096501 (2011).

[142] H. Ebert, J. Braun, D. Ködderitzsch, and S. Mankovsky, Phys. Rev. B **93**, 075145 (2016).

[143] Y. Tian, L. Ye, and X. Jin, Phys. Rev. Lett. **103**, 087206 (2009).

[144] A. Fert and P. M. Levy, Phys. Rev. Lett. **106**, 157208 (2011).

[145] P. M. Levy, H. Yang, M. Chshiev, and A. Fert, Phys. Rev. B **88**, 214432 (2013).

[146] S. Y. Huang, W. G. Wang, S. F. Lee, J. Kwo, and C. L. Chien, Phys. Rev. Lett. **107**, 216604 (2011).

[147] M. Weiler, M. Althammer, F. D. Czeschka, H. Huebl, M. S. Wagner, M. Opel, I. M. Imort, G. Reiss, A. Thomas, R. Gross, and S. T. B. Goennenwein, Phys. Rev. Lett. **108**, 106602 (2012).

[148] P. Noël, M. Cosset-cheneau, V. Haspot, V. Maurel, C. Lombard, M. Bibes, A. Barthelemy, L. Vila, and J.-P. Attané, **127**, 163907 (2020).

[149] M. Isasa, E. Villamor, L. E. Hueso, M. Gradhand, and F. Casanova, Phys. Rev. B **91**, 024402 (2015).

[150] Y. Wang, P. Deorani, X. Qiu, J. H. Kwon, and H. Yang, Appl. Phys. Lett. **105**, 152412 (2014).

[151] J. C. Rojas-Sánchez, N. Reyren, P. Laczkowski, W. Savero, J. P. Attané, C. Deranlot, M. Jamet, J. M. George, L. Vila, and H. Jaffrès, Phys. Rev. Lett. **112**, 106602 (2014).

[152] E. Sagasta, Y. Omori, M. Isasa, Y. Otani, L. E. Hueso, and F. Casanova, Appl. Phys. Lett. **111**, 082407 (2017).

[153] G. Zahnd, L. Vila, V. T. Pham, M. Cosset-Cheneau, W. Lim, A. Brenac, P. Laczkowski, A. Marty, and J. P. Attané, Phys. Rev. B **98**, 174414 (2018).

[154] E. Saitoh, M. Ueda, H. Miyajima, and G. Tatara, Appl. Phys. Lett. **88**, 182509 (2006).

[155] J. B. S. Mendes, R. O. Cunha, O. Alves Santos, P. R. T. Ribeiro, F. L. A. Machado, R. L. Rodríguez-Suárez, A. Azevedo, and S. M. Rezende, Phys. Rev. B **89**, 140406 (R) (2014).

[156] W. Zhang, M. B. Jungfleisch, W. Jiang, J. E. Pearson, A. Hoffmann, F. Freimuth, and Y. Mokrousov, Phys. Rev. Lett. **113**, 196602 (2014).

[157] J. Sklenar, W. Zhang, M. B. Jungfleisch, W. Jiang, H. Saglam, J. E. Pearson, J. B. Ketterson, and A. Hoffmann, AIP Adv. **6**, 055603 (2016).

[158] V. Tshitoyan, C. Ciccarelli, A. P. Mihai, M. Ali, A. C. Irvine, T. A. Moore, T. Jungwirth, and A. J. Ferguson, Phys. Rev. B **92**, 214406 (2015).

[159] S. M. Wu, W. Zhang, A. Kc, P. Borisov, J. E. Pearson, J. S. Jiang, D. Lederman, A. Hoffmann, and A. Bhattacharya, Phys. Rev. Lett. **116**, 097204 (2016).

[160] Y. Ou, S. Shi, D. C. Ralph, and R. A. Buhrman, Phys. Rev. B **93**, 220405 (R) (2016).

[161] S. Fukami, C. Zhang, S. Duttagupta, A. Kurenkov, and H. Ohno, Nat. Mater. **15**, 535-541 (2016).

[162] Y. C. Lau, D. Betto, K. Rode, J. M. D. Coey, and P. Stamenov, Nat. Nanotechnol. **11**, 758-762 (2016).

[163] A. Van Den Brink, G. Vermijs, A. Solignac, J. Koo, J. T. Kohlhepp, H. J. M. Swagten, and B. Koopmans, Nat. Commun. **7**, 10854 (2016).

[164] W. J. S. Garcia, R. L. Seeger, R. B. Silva, and A. Harres, J. Magn. Magn. Mater. **441**, 392-397 (2017).

[165] A. V. Chumak, V. I. Vasyuchka, A. A. Serga, and B. Hillebrands, Nat. Phys. **11**, 453-461 (2015).

[166] T. Seifert, S. Jaiswal, U. Martens, J. Hannegan, L. Braun, P. Maldonado, F. Freimuth, A. Kronenberg, J. Henrizi, I. Radu, E. Beaurepaire, Y. Mokrousov, P. M. Oppeneer, M. Jourdan, G. Jakob, D. Turchinovich, L. M. Hayden, M. Wolf, M. Münzenberg, M. Kläui, and T. Kampfrath, Nat. Photonics **10**, 483-488 (2016).

[167] K. Jhuria, J. Hohlfeld, A. Pattabi, E. Martin, A. Ygnacio, A. Córdova, X. Shi, R. Lo Conte, S. Petit-watelot, J. C. Rojas-sanchez, G. Malinowski, S. Mangin, A. Lemaître, M. Hehn, J. Bokor, R. B. Wilson, and J. Gorchon, Nat. Electron. **3**, 680-686 (2020).

[168] M. Chen, R. Mishra, Y. Wu, K. Lee, and H. Yang, Adv. Opt. Mater. **6**, 1800430 (2018).

[169] J. Li, C. B. Wilson, R. Cheng, M. Lohmann, M. Kavand, W. Yuan, M. Aldosary, N. Agladze, P. Wei, M. S. Sherwin, and J. Shi, (n.d.).

[170] P. Vaidya, S. A. Morley, J. van Tol, Y. Liu, R. Cheng, A. Brataas, D. Lederman, and E. del Barco, Science (80-.). **368**, 160 (2020).

[171] M. Meinert, B. Gliniors, O. Gueckstock, T. S. Seifert, L. Liensberger, M. Weiler, S. Wimmer, H. Ebert, and T. Kampfrath, Phys. Rev. Appl. **14**, 064011 (2020).

[172] C. T. Boone, H. T. Nembach, J. M. Shaw, and T. J. Silva, J. Appl. Phys. **113**, 153906 (2013).

[173] W. Zhang, M. B. Jungfleisch, W. Jiang, J. Sklenar, F. Y. Fradin, J. E. Pearson, J. B. Ketterson, and A. Hoffmann, J. Appl. Phys. **117**, 172610 (2015).

[174] T. S. Seifert, N. M. Tran, O. Gueckstock, S. M. Rouzegar, L. Nadvornik, S. Jaiswal, G. Jakob, V. V. Temnov, M. Münzenberg, M. Wolf, M. Kläui, and T. Kampfrath, J. Phys. D. Appl. Phys. **51**, 364003 (2018).

[175] O. Gueckstock, L. Nádvorník, M. Gradhand, T. S. Seifert, G. Bierhance, R. Rouzegar, M. Wolf, M. Vafaee, J. Cramer, M. A. Syskaki, G. Woltersdorf, I. Mertig, G. Jakob, M.

Kläui, and T. Kampfrath, Adv. Mater. **33**, 2006281 (2021).

[176] J. Kondo, Prog. Theor. Phys. **27**, 772-792 (1962).

[177] D. H. Wei, Y. Niimi, B. Gu, T. Ziman, S. Maekawa, and Y. Otani, Nat. Commun. **3**, 1058 (2012).

[178] B. Gu, T. Ziman, and S. Maekawa, Phys. Rev. B **86**, 241303 (R) (2012).

[179] Y. Niimi, D. Wei, and Y. Otani, J. Phys. Soc. Japan **86**, 011004 (2017).

[180] L. Šmejkal, R. González-Hernández, T. Jungwirth, and J. Sinova, Sci. Adv. **6**, eaaz8809 (2020).

[181] L. Yuan, Z. Wang, J. Luo, E. I. Rashba, and A. Zunger, Phys. Rev. B **102**, 14422 (2020).

[182] S.-Y. Yang, Y. Wang, B. R. Ortiz, D. Liu, J. Gayles, E. Derunova, R. Gonzalez-Hernandez, L. Šmejkal, Y. Chen, S. S. P. Parkin, S. D. Wilson, E. S. Toberer, T. McQueen, and M. N. Ali, Sci. Adv. **6**, eabb6003 (2020).

[183] D. Maryenko, A. S. Mishchenko, M. S. Bahramy, A. Ernst, J. Falson, Y. Kozuka, A. Tsukazaki, N. Nagaosa, and M. Kawasaki, Nat. Commun. **8**, 14777 (2017).

[184] L. Šmejkal and T. Jungwirth, in *Topol. Magn.* (Springer, 2018), pp. 267–298.

[185] S. Nakatsuji, N. Kiyohara, and T. Higo, Nature **527**, 212-215 (2015).

[186] N. Kiyohara, T. Tomita, and S. Nakatsuji, Phys. Rev. Appl. **5**, 064009 (2016).

[187] Y. Machida, S. Nakatsuji, S. Onoda, T. Tayama, and T. Sakakibara, Nature **463**, 210-213 (2010).

[188] C. Sürgers, W. Kittler, T. Wolf, and H. V. Löhneysen, AIP Adv. **6**, 055604 (2016).

[189] C. Sürgers, T. Wolf, P. Adelmann, W. Kittler, G. Fischer, and H. V. Löhneysen, Sci. Rep. **7**, 42982 (2017).

[190] C. Sürgers, G. Fischer, P. Winke, and H. v. Löhneysen, Nat. Commun. **5**, 3400 (2014).

[191] O. Gomonay, V. Baltz, A. Brataas, and Y. Tserkovnyak, Nat. Phys. **14**, 213-216 (2018).

[192] Z. Feng, X. Zhou, L. Smejkal, L. Wu, Z. Zhu, H. Guo, R. González-Hernández, X. Wang, H. Yan, P. Qin, X. Zhang, H. Wu, H. Chen, C. Jiang, M. Coey, J. Sinova, T. Jungwirth, and Z. Liu, ArXiv:2002.08712 (2020).

[193] C. L. Gao, U. Schlickum, W. Wulfhekel, and J. Kirschner, Phys. Rev. Lett. **98**, 107203 (2007).

[194] C. L. Gao, A. Ernst, A. Winkelmann, J. Henk, W. Wulfhekel, P. Bruno, and J. Kirschner, Phys. Rev. Lett. **100**, 237203 (2008).

[195] D. Sanders, J. Phys. Condens. Matter **16**, R603 (2004).

[196] A. Ishizaka and Y. Shiraki, J. Electrochem. Soc. **133**, 666 (1986).

[197] S. Olive-Mendez, A. Spiesser, L. A. Michez, V. Le Thanh, A. Glachant, J. Derrien, T. Devillers, A. Barski, and M. Jamet, Thin Solid Films **517**, 191 (2008).

[198] M. Gottschilch, O. Gourdon, J. Persson, C. De La Cruz, V. Petricek, and T. Brueckel, J. Mater. Chem. **22**, 15275 (2012).

[199] J. Leciejewicz, B. Penc, A. SzytuŁa, A. Jezierski, and A. Zygmunt, Acta Phys. Pol. A **113**, 1193-1203 (2008).

[200] P. J. Brown and J. B. Forsyth, J. Phys. Condens. Matter **7**, 7619-7628 (1995).

[201] A. Ney, T. Hesjedal, L. Däweritz, R. Koch, and K. Ploog, J. Magn. Magn. Mater. **288**, 173-177 (2005).

[202] B. Gopalakrishnan, C. Sürgers, R. Montbrun, A. Singh, M. Uhlarz, and H. v. Löhneysen, Phy. Rev. B **77**, 104414 (2008).

[203] T. Higo, D. Qu, Y. Li, C. L. Chien, Y. Otani, and S. Nakatsuji, Appl. Phys. Lett. **113**, 202402 (2018).

[204] K. Yamauchi, P. Barone, and S. Picozzi, Phy. Rev. B **100**, 245115 (2019).

[205] S. Hayami, Y. Yanagi, and H. Kusunose, J. Phys. Soc. Japan **88**, 123702 (2019).

[206] L. Šmejkal, J. Sinova, and T. Jungwirth, ArXiv:2105.05820v1 (2021).

[207] L. Šmejkal, A. B. Hellenes, R. González-Hernández, J. Sinova, and T. Jungwirth, ArXiv:2103.12664v1 (2021).

[208] H. Reichlova, T. Janda, J. Godinho, A. Markou, D. Kriegner, R. Schlitz, J. Zelezny, Z. Soban, M. Bejarano, H. Schultheiss, P. Nemec, T. Jungwirth, C. Felser, J. Wunderlich, and S. T. B. Goennenwein, Nat. Commun. **10**, 5459 (2019).

[209] R. Schlitz, P. Swekis, A. Markou, H. Reichlova, M. Lammel, J. Gayles, A. Thomas, K. Nielsch, C. Felser, and S. T. B. Goennenwein, Nano Lett. **19**, 2366 (2019).

[210] Y. A. Izyumov, Y. N. Proshin, and M. G. Khusainov, Physics-Uspekhi **45**, 109-148 (2002).

[211] A. I. Buzdin, Rev. Mod. Phys. **77**, 935-976 (2005).

[212] L. R. Tagirov, Phys. Rev. Lett. **83**, 2058-2061 (1999).

[213] J. Y. Gu, J. S. Jiang, J. Pearson, and S. D. Bader, Phys. Rev. Lett. **89**, 267001 (2002).

[214] A. Potenza and C. H. Marrows, Phys. Rev. B **71**, 180503 (R) (2005).

[215] R. Steiner and P. Ziemann, Phys. Rev. B **74**, 094504 (2006).

[216] D. Stamopoulos, E. Manios, and M. Pissas, Supercond. Sci. Technol. **20**, 1205-1222 (2007).

[217] A. Y. Aladyshkin, A. I. Buzdin, A. A. Fraerman, D. A. Ryzhov, and A. V Sokolov, Phys. Rev. B **68**, 184508 (2003).

[218] A. Y. Rusanov, M. Hesselberth, and J. Aarts, Phys. Rev. Lett. **93**, 057002 (2004).

[219] M. Houzet and A. I. Buzdin, Phy. Rev. B **74**, 214507 (2006).

[220] A. Singh, C. Sürgers, and H. Löhneysen, Phys. Rev. B **75**, 024513 (2007).

[221] L. Y. Zhu, T. Y. Chen, and C. L. Chien, Phys. Rev. Lett. **101**, 017004 (2008).

[222] M. Z. Cieplak, Z. Adamus, M. Kończykowski, L. Y. Zhu, X. M. Cheng, and C. L. Chien, Phys. Rev. B **87**, 014519 (2013).

[223] G. Miao, in *Supercond. - New Dev.* (InTechOpen, 2015).

[224] A. I. Buzdin and A. S. Mel'nikov, Phy. Rev. B **67**, 020503 (2003).

[225] Z. Yang, M. Lange, A. Volodin, R. Szymczak, and V. V. Moshchalkov, Nat. Mater. **3**, 793-798 (2004).

[226] Y. Cheng and M. B. Stearns, J. App. Phys. **67**, 5038 (1990).

[227] M. Hübener, D. Tikhonov, I. AGarifullin, K. Westerholt, and H. Zabel, J. Phys. Condens. Matter **14**, 8687 (2002).

[228] B. L.Wu, Y. M. Yang, Z. B. Guo, Y. H.Wu, and J. J. Qiu, Appl. Phys. Lett. **109**, 152602 (2013).

[229] J. J. Hauser, H. C. Theuerer, and N. R. Werthamer, Phys. Rev. **142**, 118 (1966).

[230] I. V. Bobkova, P. J. Hirschfeld, and Y. S. Barash, Phys. Rev. Lett. **94**, 037005 (2005).

[231] B. M. Andersen, I. V. Bobkova, P. J. Hirschfeld, and Y. S. Barash, Phys. Rev. Lett. **96**, 117005 (2006).

[232] P. Komissinskiy, G. A. Ovsyannikov, I. V. Borisenko, Y. V. Kislinskii, K. Y. Constantinian, A. V. Zaitsev, and D. Winkler, Phys. Rev. Lett. **99**, 017004 (2007).

[233] C. Bell, J. Tarte, G. Burnell, W. Leung, D. J. Kang, and G. Blamire, Phys. Rev. B **68**, 144517 (2003).

[234] M. F. Jakobsen, K. B. Naess, P. Dutta, A. Brataas, and A. Qaiumzadeh, Phy. Rev. B 140504 (2020).

[235] K.-R. Jeon, B. K. Hazra, K. Cho, A. Chakraborty, J.-C. Jeon, H. Han, H. L. Meyerheim, T. Kontos, and S. S. P. Parkin, Nat. Mater. **7**, 3870 (2021).

[236] C. Canedy, X. Li, and G. Xiao, Phys. Rev. B **62**, 508-519 (2000).

[237] V. Baltz, A. Marty, B. Rodmacq, and B. Dieny, Phy. Rev. B **75**, 014406 (2007).

[238] B. Kaplan and G. A. Gehring, J. Magn. Magn. Mater. **128**, 111-116 (1993).

[239] P. D. Johnson, Rep. Prog. Phys. **60**, 1217-1304 (1997).

[240] de G. P.-G., *Superconductivity of Metals and Alloys* (CRC Press, 1999).

[241] F. S. Bergeret, M. Silaev, P. Virtanen, and T. T. Heikkilä, Rev. Mod. Phys. **90**, 41001 (2018).

[242] S. Brück, J. Sort, V. Baltz, S. Suriñach, J. S. Muñoz, B. Dieny, M. D. Baró, and J. Nogués, Adv. Mater. **17**, 2978 (2005).

[243] G. Salazar-Alvarez, J. J. Kavich, J. Sort, A. Mugarza, S. Stepanow, A. Potenza, H. Marchetto, S. S. Dhesi, V. Baltz, B. Dieny, A. Weber, L. J. Heyderman, J. Nogues, and P. Gambardella, Appl. Phys. Lett. **95**, 012510 (2009).

[244] J. Wu, D. Carlton, J. S. Park, Y. Meng, E. Arenholz, A. Doran, A. T. Young, A. Scholl, C. Hwang, H. W. Zhao, J. Bokor, and Z. Q. Qiu, Nat. Phys. **7**, 303-306 (2011).

[245] V. Baltz, B. Rodmacq, A. Zarefy, L. Lechevallier, and B. Dieny, Phys. Rev. B **81**, 052404 (2010).

[246] S. Soeya, T. Imagawa, K. Mitsuoka, and S. Narishige, J. Appl. Phys. **76**, 5356 (1994).

[247] D. Dew-Hughes, Low Temp. Phys. **27**, 713 (2001).

[248] A. Engel, H. Bartolf, A. Schilling, K. Il'in, M. Siegel, A. Semenov, and H. W. Hübers, J. Phys. Conf. Ser. **97**, 012152 (2008).

[249] A. Semenov, B. Günther, U. Böttger, H. W. Hübers, H. Bartolf, A. Engel, A. Schilling, K. Ilin, M. Siegel, R. Schneider, D. Gerthsen, and N. A. Gippius, Phys. Rev. B **80**, 054510 (2009).

[250] Z. Li, W. Wang, L. Zhang, Z. Yang, M. Tian, and Y. Zhang, Sci. Rep. **5**, 18601 (2015).

[251] S. M. Rezende, A. Azevedo, and R. L. Rodríguez-suárez, **126**, 151101 (2019).

[252] J. Barker and O. A. Tretiakov, Phys. Rev. Lett. **116**, 147203 (2016).

[253] W. Jiang, X. Zhang, G. Yu, W. Zhang, X. Wang, B. M. Jungfleich, J. E. Pearson, X. Cheng, O. Heinonen, K. L. Wang, Y. Zhou, A. Hoffmann, and S. G. E. te Velthuis, Nat. Phys. **13**, 162-169 (2017).

[254] R. Juge, S.-G. Je, D. de S. Chaves, L. D. Buda-Prejbeanu, J. Peña-Garcia, J. Nath, I. M. Miron, K. G. Rana, L. Aballe, M. Foerster, F. Genuzio, T. O. Mente, A. Locatelli, F. Maccherozzi, S. S. Dhesi, M. Belmeguenai, Y. Roussigné, S. Auffret, S. Pizzini, G. Gaudin, J. Vogel, and O. Boulle, Phys. Rev. Appl. **12**, 44007 (2019).

[255] S.-W. Cheong, M. Fiebig, W. Wu, L. Chapon, and V. Kiryukhin, Npj Quantum Mater. **5**, 3 (2020).

[256] N. B. Weber, H. Ohldag, H. Gomonaj, and F. U. Hillebrecht, Phys. Rev. Lett. Lett. **91**, 237205 (2003).

[257] M. Bode, E. Y. Vedmedenko, K. von Bergmann, A. Kubetzka, P. Ferriani, S. Heinze, and R. Wiesendanger, Nat. Mater. **5**, 477-481 (2006).

[258] S. Loth, S. Baumann, C. P. Lutz, D. M. Eigler, and A. J. Heinrich, Science (80-.). **335**, 196 (2012).

[259] I. Gross, W. Akhtar, V. Garcia, L. J. Martínez, S. Chouaieb, K. Garcia, C. Carrétéro, A. Barthélémy, P. Appel, P. Maletinsky, J.-V. Kim, J. Y. Chauleau, N. Jaouen, M. Viret, M. Bibes, S. Fusil, and V. Jacques, Nature **549**, 252-256 (2017).

[260] T. Kosub, M. Kopte, R. Hu, P. Appel, B. Shields, P. Maletinsky, O. G. Schmidt, and D. Makarov, Nat. Commun. **8**, 13985 (2017).

[261] M. S. Wörnle, P. Welter, Z. Kašpar, K. Olejník, V. Novák, R. P. Campion, P. Wadley, T. Jungwirth, C. L. Degen, and P. Gambardella, ArXiv.1912.05287 (2019).

[262] J.-Y. Chauleau, E. Haltz, C. Carrétéro, S. Fusil, and M. Viret, Nat. Mater. **16**, 803 (2017).

[263] M. Fiebig, D. Fröhlich, T. Lottermoser, V. V. Pavlov, R. V. Pisarev, and H.-J. Weber, Phys. Rev. Lett. **87**, 137202 (2001).

[264] S. Gao, H. D. Rosales, F. A. G. Albarracín, V. Tsurkan, G. Kaur, T. Fennell, P. Steffens, M. Boehm, P. Čermák, A. Schneidewind, E. Ressouche, D. C. Cabra, C. Rüegg, and O. Zaharko, Nature **586**, 37-41 (2020).

[265] H. Jani, J.-C. Lin, J. Chen, J. Harrison, F. Maccherozzi, J. Schad, S. Prakash, C.-B. Eom,

A. Ariando, T. Venkatesan, and P. G. Radaelli, Nature **590**, 74-79 (2021).

[266] O. Boulle, J. Vogel, H. Yang, S. Pizzini, D. de S. Chaves, A. Locatelli, T. O. Menteş, A. Sala, L. D. Buda-Prejbeanu, O. Klein, M. Belmeguenai, Y. Roussigné, A. Stashkevich, S. M. Chérif, L. Aballe, M. Foerster, M. Chshiev, S. Auffret, I. M. Miron, and G. Gaudin, Nat. Nanotechnol. **11**, 449-454 (2016).

[267] W. Legrand, D. Maccariello, F. Ajejas, S. Collin, A. Vecchiola, K. Bouzehouane, N. Reyren, V. Cros, and A. Fert, Nat. Mater. **19**, 34-42 (2020).

[268] J. Nogués and I. K. Schuller, J. Magn. Magn. Mater. **192**, 203-232 (1999).

[269] I. V. Roshchin, O. Petracic, R. Morales, Z.-P. Li, X. Batlle, and I. K. Schuller, Europhys. Lett. **71**, 297-303 (2005).

[270] K. G. Rana, A. Finco, F. Fabre, S. Chouaieb, A. Haykal, L. D. Buda-Prejbeanu, O. Fruchart, S. Le Denmat, P. David, M. Belmeguenai, T. Denneulin, R. E. Dunin-Borkowski, G. Gaudin, V. Jacques, and O. Boulle, Phys. Rev. Appl. **13**, 044079 (2020).

[271] M. Belmeguenai, J.-P. Adam, Y. Roussigné, S. Eimer, T. Devolder, J.-V. Kim, S. M. Cherif, A. Stashkevich, and A. Thiaville, Phy. Rev. B **91**, 180405 (2015).

[272] A. Thiaville, S. Rohart, É. Jué, V. Cros, and A. Fert, EPL Eur. Lett. **100**, 57002 (2012).

[273] L. Aballe, M. Foerster, E. Pellegrin, J. Nicolas, and S. Ferrer, J. Synchrotron Radiat. **22**, 745-752 (2015).

[274] Y. Y. Wang, C. Song, G. Y. Wang, F. Zeng, and F. Pan, New J. Phys. **16**, 123032 (2014).

[275] V. Baltz, B. Rodmacq, A. Zarefy, L. Lechevallier, and B. Dieny, Phys. Rev. B **81**, 052404 (2010).

[276] G. Lhoutellier, D. Ledue, R. Patte, and V. Baltz, J. Appl. Phys. **120**, 193902 (2016).

[277] K. Takano, R. H. Kodama, A. E. Berkowitz, W. Cao, and G. Thomas, J. App. Phys. **83**, 6888 (1998).

[278] V. Baltz, J. Sort, B. Rodmacq, B. Dieny, and S. Landis, Phy. Rev. B **72**, 104419 (2005).

[279] K. Akmaldinov, L. Frangou, C. Ducruet, C. Portemont, J. Pereira, I. Joumard, B. Dieny, J. Alvarez-Hérault, and V. Baltz, IEEE Magn. Lett. **6**, 3000404 (2015).

[280] C. A. Akosa, O. A. Tretiakov, G. Tatara, and A. Manchon, Phys. Rev. Lett. **121**, 97208 (2018).

[281] C. Jin, C. Song, J. Wang, and Q. Liu, Appl. Phys. Lett. **109**, 182404 (2016).

Summary

The emerging field of antiferromagnetic spintronics consists in exploring spin-dependent properties of antiferromagnetic materials. This class of magnetic materials might offer a number of advantages in terms of new physics and device performance due to: i) robustness against external magnetic fields, ii) zero net magnetization which produces no stray field, and iii) high frequency dynamics, typically close to THz frequencies. Besides the interesting features mentioned above, antiferromagnets are found to show a wide variety of properties. As far as electrical properties are concerned, they can be metals, insulators, semimetals, semiconductors and also superconductors. This makes antiferromagnets interesting for spintronic devices and intense research effort have been carried out recently in order to demonstrate the specific properties of antiferromagnets. In this thesis manuscript, we present how we explored experimentally novel spin and charge transport mechanism in ferromagnetic and antiferromagnetic spin structures and spin textures. Via the spin pumping technique, we unravelled the spin transport mechanisms associated with magnetic ordering transitions in materials with different electrical states and have studied the role of the electronic or magnonic nature of the spin current. In addition to that, we have studied spin-charge conversion in ferromagnets and antiferromagnets. We also used magnetotransport experiments to demonstrate spin-dependent properties specific to the antiferromagnetic arrangement of spins, where we have observed a spontaneous Hall effect that relies in crystal and magnetic symmetries. Finally, we evaluated whether magnetic textures in antiferromagnets matter for transport, whether it be single electron or Cooper pair transport. Particularly, we have used the proximity effect to study Cooper pair characteristic lengths in antiferromagnets. We have also explored the replication of spin textures from ferromagnets to antiferromagnets to reveal to what extend it is possible to control those textures in antiferromagnets.

Résumé

Le domaine émergent de la spintronique antiferromagnétique consiste à explorer les propriétés dépendantes du spin des matériaux antiferromagnétiques. Cette classe de matériaux magnétiques pourrait offrir un certain nombre d'avantages en termes de nouvelle physique et de performances des dispositifs en raison de : i) leur robustesse face aux champs magnétiques externes, ii) leur aimantation nette nulle qui ne produit aucun champ magnétique parasite, et iii) leur dynamique à haute fréquence, typiquement proche des fréquences THz. Outre les caractéristiques mentionnées ci-dessus, les matériaux antiferromagnétiques présentent une grande variété de propriétés. En ce qui concerne les propriétés électriques, ils peuvent faire partie de la catégorie des métaux, des isolants, des semi-métaux, des semi-conducteurs et également des supraconducteurs. Cela rend les matériaux antiferromagnétiques particulièrement intéressants pour les dispositifs spintroniques et un effort de recherche intense a été mené récemment afin de démontrer leurs propriétés spécifiques. Ce manuscrit présente comment nous avons exploré expérimentalement de nouveaux mécanismes de transport de spin et de charge dans des structures et des textures de spin ferromagnétiques et antiferromagnétiques. Grâce à la technique de pompage de spin, nous avons étudié les mécanismes de transport de spin associés aux transitions d'ordre magnétique dans des matériaux présentant différents états électriques. Nous avons notamment étudié le rôle de la nature électronique ou magnonique du courant de spin. Par ailleurs, nous avons étudié la conversion spin-charge dans les matériaux ferromagnétiques et antiferromagnétiques. Nous avons également utilisé des expériences de magnétotransport pour étudier les propriétés dépendantes du spin liées spécifiquement à l'arrangement antiferromagnétique des spins, où nous avons observé un effet Hall spontané qui repose sur les symétries cristallines et magnétiques. Enfin, nous avons évalué si les textures magnétiques dans les antiferromagnétiques sont importantes pour le transport, qu'il s'agisse du transport d'un électron unique ou d'une paire de Cooper. En particulier, nous avons utilisé l'effet de proximité pour étudier les longueurs caractéristiques des paires de Cooper dans les antiferromagnétiques. En complément, nous avons utilisé la méthode d'impression de textures de spin dans un antiferromagnétique à partir d'un ferromagnétique dans le but d'évaluer dans quelle mesure il est possible de contrôler ces textures dans les antiferromagnétiques.